CORA Cork Open Research Archive
Cartlann Taighde Oscailte Chorcaí

| | |
|---|---|
| Title | Energy harvesting system design and optimization for wireless sensor networks |
| Authors | Wang, Wensi S. |
| Publication date | 2014 |
| Original Citation | Wang, W. 2014. Energy harvesting system design and optimization for wireless sensor networks. PhD Thesis, University College Cork. |
| Type of publication | Doctoral thesis |
| Rights | © 2014, Wensi Wang. - http://creativecommons.org/licenses/by-nc-nd/3.0/ |
| Download date | 2026-11-03 00:37:31 |
| Item downloaded from | https://hdl.handle.net/10468/1410 |



UCC
University College Cork, Ireland
Coláiste na hOllscoile Corcaigh

Ollscoil na hÉireann

# Energy Harvesting System Design and Optimization for Wireless Sensor Networks

A thesis presented to the
National University of Ireland, Cork
for the degree of Doctor of Philosophy

by

Wensi Wang, M.Eng.Sc.

Supervisors: Dr. Cian O'Mathuna, Dr. Ningning Wang

Head of Department: Dr. Nabeel A. Riza







Tyndall National Institute,
National University of Ireland, Cork

Spring, 2014

# Abstract

Wireless sensor networks (WSN) are becoming widely adopted for many applications including complicated tasks like building energy management. However, one major concern for WSN technologies is the short lifetime and high maintenance cost due to the limited battery energy. One of the solutions is to scavenge ambient energy, which is then rectified to power the WSN.

The objective of this thesis was to investigate the feasibility of an ultra-low energy consumption power management system suitable for harvesting sub-mW photovoltaic and thermoelectric energy to power WSNs.

To achieve this goal, energy harvesting system architectures have been analyzed. Detailed analysis of energy storage units (ESU) have led to an innovative ESU solution for the target applications. Battery-less, long-lifetime ESU and its associated power management circuitry, including fast-charge circuit, self-start circuit, output voltage regulation circuit and hybrid ESU, using a combination of super-capacitor and thin film battery, were developed to achieve continuous operation of energy harvester.

Low start-up voltage DC/DC converters have been developed for 1mW level thermoelectric energy harvesting. The novel method of altering thermoelectric generator (TEG) configuration in order to match impedance has been verified in this work.

Novel maximum power point tracking (MPPT) circuits, exploring the fractional open circuit voltage method, were particularly developed to suit the sub-1mW photovoltaic energy harvesting applications. The MPPT energy model has been developed and verified against both SPICE simulation and implemented prototypes.

Both indoor light and thermoelectric energy harvesting methods proposed in this thesis have been implemented into prototype devices. The improved indoor light energy harvester prototype demonstrates 81% MPPT conversion efficiency with 0.5mW input power. This important improvement makes light energy harvesting from small energy sources (i.e. credit card size solar panel in 500lux indoor lighting conditions) a feasible approach. The 50mm $\times$ 54mm thermoelectric energy harvester prototype generates 0.95mW when placed on a 60$^o$C heat source with 28% conversion efficiency. Both prototypes can be used to continuously power WSN for building energy management applications in typical office building environment.

In addition to the hardware development, a comprehensive system energy model has been developed. This system energy model not only can be used to predict the available and consumed energy based on real-world ambient conditions, but also can be employed to optimize the system design and configuration. This energy model has been verified by indoor photovoltaic energy harvesting system prototypes in long-term deployed experiments.

# Acknowledgments

First and foremost I would like to express my sincere thanks to my supervisors Dr. Ningning Wang, Dr. Terence O'Donnell and Professor Cian *Ó* Mathúna for all the effort, time and patience they have put into the five years of my Ph.D studies.

I am grateful to have the invaluable opportunity to learn from their knowledge, experience and their attention to detail. I could not have asked for better role models.

Especially, I would like to thank Dr. Ningning Wang for his support and guidance in my research and for the monumental effort of correcting the revisions of revisions of this thesis. Indeed, without his guidance, I would not be able to put this thesis together.

I am very grateful to MAI group senior program manager Mike Hayes for his advice and help in all the projects we have been through. His encouragement allows me to take part in great experiences beyond what is traditionally thought of as Ph.D. studies.

I would like to extend thanks to members of Microsystems group at Tyndall for the collaboration and help during my studies: Brendan O'Flynn, Victor Cionca, Wassim Magnin, John Barton, Santosh Kulkarni, Saibal Roy, Ju Xu, Alan Mathewson, Mark Gaffney, Rosemary O'Keeffe, Marco Belcastro and Liam Moore.

I would like to also thank Professor Mary Ann Ingram of Georgia Institute of Technology, her students Jin Woo Jung and Jian Lin for the long term collaboration and for their support during my visiting programme to Atlanta.

I also like to thank my former Tyndall colleagues, Shunpu Li, Brice Jamieson, Luca Ribetto, Matteo Piovanelli, Jan Kubik, Jan Vcelak and Vanessa Smet for all the great suggestions both in research and in life.

Furthermore, I am extremely grateful to my friends, they have always been a constant source of support. In particular, Ye Wang, thank you for your support when I have needed it the most. Min Yang, Ying Feng, Zixiang Cong, Liqiang Zheng, Tingcong Ye, Xiaoju Nong, Xiao Chen, Shuo Su, Fei Wang, Wenbin Chen and Wen Wu, thank you for sharing these years with me.

Last but not least, I would like to thank my mother Professor Liming Liu and my father Professor Ning Wang for their infinite support throughout everything.

Declaration: I hereby declare that, except where otherwise indicated, this document is entirely my own work and has not been submitted in whole or in part to any other university.

Signed: ..... Date: .....

# Contents

**Abstract** **i**

**Acknowledgments** **iii**

**List of Figures** **xvi**

**List of Tables** **xviii**

**List of Publications** **xix**

**1 Background and Motivation** **1**

1.1 Wireless Sensor Networks . . . . . 1

1.2 Energy Harvesting System . . . . . 2

1.2.1 Definition of Energy Harvesting System . . . . . 3

1.2.2 Terms Regarding Energy Harvesting System . . . . . 4

1.2.3 Power Level of Energy Harvesting System . . . . . 5

1.2.4 Research Objectives . . . . . 6

1.3 Thesis Layout . . . . . 10

**2 Literature Review** **11**

2.1 Introduction . . . . . 11

2.2 Wireless Sensor Networks . . . . . 11
2.3 Power Management Circuits for Energy Harvesting Applications . . 16
2.3.1 MPPT for Photovoltaic EH . . . . . 16
2.3.1.1 Indoor Light Energy Harvesting Summary Table . . 26
2.3.2 Low Voltage Converter for Thermoelectric EH . . . . . 29
2.3.2.1 Charge Pump Low Voltage Converters . . . . . 31
2.3.2.2 Coupled Inductor Based Low Voltage Step-up Converter . . . . . 33
2.3.3 Energy Storage Unit . . . . . 35
2.3.3.1 Super-capacitors . . . . . 36
2.3.3.2 Thin Film Solid State Battery . . . . . 38
2.3.3.3 ESU Power Management Circuits . . . . . 40
2.3.4 System Simulation of Energy Harvesting Systems . . . . . 43
2.4 Conclusion . . . . . 44

**3 Energy Storage Unit and Conditioning Circuits 47**

3.1 Introduction . . . . . 47
3.2 ESU Characterisations . . . . . 48
3.2.1 Equivalent Series Resistance . . . . . 48
3.2.2 Leakage Current . . . . . 51
3.2.3 Charge Efficiency Characterization . . . . . 53
3.3 ESU Simulation Model . . . . . 58
3.3.1 Charge/Discharge Model . . . . . 58
3.3.2 Simulink Model Implementation . . . . . 61
3.4 ESU Power Regulation . . . . . 63

3.4.1 Output Voltage Regulation . . . . . 64
3.4.2 ESU Fast Charge Circuit . . . . . 70
3.4.3 Self-Start Circuit for ESU . . . . . 75
3.5 Hybrid Energy Storage . . . . . 79
3.6 Conclusion . . . . . 82

**4 Thermoelectric Energy Harvesting 85**

4.1 Introduction . . . . . 85
4.2 Thermoelectric Module Characterizations . . . . . 86
4.2.1 Thermoelectric Module Structures and Energy Transfer Model 86
4.2.2 TEG Device Characterization . . . . . 92
4.2.2.1 Thermoelectric Characterization Test Setup . . . . 92
4.2.2.2 TEGs Thermoelectric Parameters . . . . . 93
4.2.2.3 TEG Electrical Characterization . . . . . 97
4.3 TEG Power Management . . . . . 100
4.3.1 Transformer Based Boost Converter . . . . . 101
4.3.1.1 Ultra-low Voltage Boost Converter . . . . . 102
4.3.2 Charge Pump and Boost Converter Power Management . . . 106
4.3.2.1 Charge Pump and Boost Converter . . . . . 108
4.3.2.2 TEG Impedance Matching Configuration . . . . . 110
4.4 Prototype Implementation and Experimental Results . . . . . 112
4.5 Conclusion . . . . . 118

**5 Low Intensity Light Energy Harvesting** **121**

5.1 Introduction . . . . . 121

5.2 Indoor Light Photovoltaic Cell Characterization . . . . . 123

5.2.1 Test Setup . . . . . 123

5.2.2 PV Cell Electric Model . . . . . 123

5.2.3 COTS Photovoltaic Cell Characterizations . . . . . 127

5.3 Maximum Power Point Tracking . . . . . 128

5.3.1 Buck Converter FVOC MPPT . . . . . 130

5.3.1.1 MPPT Design . . . . . 130

5.3.2 Synchronized Boost Converter MPPT . . . . . 146

5.4 Indoor Photovoltaic EHM Powered WSN Operation Model . . . . . 160

5.4.1 Energy Harvesting WSN Case Study . . . . . 163

5.5 Conclusion . . . . . 166

**6 Conclusion and Future Work** **169**

6.1 Suggestions for Future Work . . . . . 172

**A** **175**

A.1 CAP-XX Super-capacitor Models and Design Aid Calculator . . . . 175

A.2 Tyndall Wireless Sensor Node Power Consumption Test Results . . . 178

**Bibliography** **193**

# List of Figures


1.1 Global Energy Consumption in term of U.S. Dollars in 2011 . . . . . 2

1.2 Simple Energy Harvester Powered WSN . . . . . 3

1.3 Energy Harvesting Powered WSN System Example . . . . . 4

1.4 Power Levels Synopsis of Portable Devices . . . . . 5

1.5 Sanyo AM1815 Solar Cell Current-Voltage and Power-Voltage Characteristics in Office Environment (light intensity 200-600lux) . . . . 7

1.6 Marlow industries EHA-PA1AN1 generator Output Power when placed on $50^oC/45^oC/40^oC$ hot surface (room temperature $=20^oC$) . . . . . 8

1.7 Power Management for Energy Harvesting Systems . . . . . 10

2.1 Wireless Sensor Node (Mote) Block Diagram . . . . . 12

2.2 Typical Power Consumption Profile of a "duty cycling" WSN Mote . 12

2.3 Tyndall Mote Current Consumption Profile . . . . . 15

2.4 "semi-MPPT" method: choose rechargeable battery with operating voltage (2.7-3.0V) near PV cell MPP voltage (2.7-2.9V) . . . . . 17

2.5 Energy Harvesting System with PFM controlled Buck Converter MPPT 18

2.6 Low power light sensor based MPPT system . . . . . 19

2.7 MPPT Energy Harvestor for Outdoor Applications with Tmote . . . 19

2.8 Voltage "Window" Semi-MPPT for Low Power Light EH . . . . . 22

2.9 WSN Discontinuous Operation with "Voltage Window" Semi-MPPT Energy Harversting . . . . . 22

2.10 PWM MPPT for Wind Energy Harvesting . . . . . 23

2.11 Indoor light and thermal hybrid energy harvesting power management module with MPPT function . . . . . 25

2.12 Light Energy Harvesting Powered WSN Technologies Summary Table 1 . . . . . 27

2.13 Light Energy Harvesting Powered WSN Technologies Summary Table 2 . . . . . 28

2.14 Measured Wasted Heat on the Surface of An Air Compressor Unit . 29

2.15 Bulk Material based Thermoelectric Generator . . . . . 30

2.16 Operation of Charge Pump Circuit . . . . . 31

2.17 10-stage Startup/Operation Dual-mode Low Voltage Charge Pump with 0.12V Minimum Input Voltage . . . . . 32

2.18 Seiko Instruments S-882Z Charge Pump External ($V_{CC}$) Capacitor Charge/Discharge Process . . . . . 32

2.19 Coupled Inductors based Low Voltage Converter Design . . . . . 33

2.20 Linear Technologies LTC3108/3109 Ultra-low Voltage Boost Converter with 1:100 Ratio Transformer . . . . . 34

2.21 Datasheet Efficiency Comparison between two COTS low voltage converters: Linear Technologies LTC3108 v.s. Seiko Instruments S-882Z 35

2.22 Electrochemical Double Layer Capacitor Charge Separations . . . . 37

2.23 Thin Film Micro Energy Cell, TFB Structure . . . . . 38

2.24 Cold Start Circuit for piezoelectric energy harvester . . . . . 42

2.25 Simplified PV Energy Harvesting Simulation Model for Active RFID Applications . . . . . 44

3.1 ESU ESR Equivalent Circuit . . . . . 49

3.2 Measured Voltage Drop Due to ESR During (high current) Active Mode 50

3.3 Measured Voltage Drop Due to Parallel Connected super-capacitors ESR During (high current) Active Mode . . . . . 50

3.4 super-capacitors Discharge Test Over 24 Hours . . . . . 51

3.5 super-capacitor Charging Tests. From Bottom to Top: Charging Current Equals to 0.3mA, 0.5mA, 0.6mA, 0.7mA, 0.75mA and 0.8mA . 55

3.6 super-capacitor Charging Efficiency . . . . . 56

3.7 High Gain Amplifier Circuit for TFB Voltage Monitoring . . . . . 57

3.8 Charging Efficiency of TFB . . . . . 57

3.9 Simplified Equivalent Circuit of ESU . . . . . 59

3.10 super-capacitor Charge/discharge Simulink Model . . . . . 62

3.11 super-capacitor Simulink Model Simulation Results (Screen Capture) (a) Without Charge Efficiency and Leakage Current Effects; (b) Considering Charge Efficiency and Leakage Current Effects . . . . . 62

3.12 Super-capacitor Simulink Model Simulation Result Verification: Charging . . . . . 63

3.13 Super-capacitor Simulink Model Result Verification: Discharging . . 63

3.14 DC/DC Converter Voltage Threshold and Wasted Energy Analysis . 65

3.15 Sourcemeter Set-up for Conversion Efficiency Tests . . . . . 66

3.16 Output Regulation Schematic Using TI TPS61220 . . . . . 66

3.17 Measured DC/DC Converter Efficiency between 0.5V and 3V Input Voltage in 3 Current Consumption Modes . . . . . 67

3.18 Revised DC/DC Converter Threshold Voltage and Wasted Energy Simulation with Consideration of Conversion Efficiency Variations . 68

3.19 Buck and buck/boost Converters: Total Energy Utilization Ratio for Different ESU Voltage Rating (WSN load: D=0.1% duty cycle) . . . 69

3.20 Parallel and Series Connection Configuration of PV cells . . . . . 71

3.21 Charging current of Parallel and Series Configurations . . . . . 72

3.22 Fast Charge Circuit Schematics . . . . . 72

3.23 Fast Charge Experiment Charge Time Results (including the energy consumption of the switching circuits) . . . . . 74

3.24 Initial Phase of Fast Charge Experiment (Difference between Fast Charge and Parallel Configurations is due to the power consumption of the switching circuits) . . . . . 74

3.25 PV Cell Energy Harvester Self Start Circuits Schematics . . . . . 76

3.26 Screen Capture of Start Up Process in a PV Cell Energy Harvester Based on Self Start Circuits (measured with Pico Tech Data Logger) 77

3.27 Thermoelectric Energy Harvester Self Start Circuits Schematics . . . 78

3.28 Schematics of hybrid ESU power management circuits . . . . . 80

3.29 (a) Hybrid energy storage unit discharge experiment with a Tyndall WSN mote. (b) 1 week long charge/discharge test with 0.5mW PV cell and a Tyndall WSN mote. Black: super-capacitor Voltage; Blue: TFB Voltage; Red: super-capacitor charges TFB function ON/OFF 81

4.1 (a) Typical Thermoelectric Generator Structure and (b) Equivalent Circuit with resistive load . . . . . 86

4.2 Thermoelectric Module Typical Structure and Key Parameters . . . 87

4.3 MEMS based TEG Microscope Photo and Illustrated Cross-Section (Thermo-element length $\approx 35\mu$m) . . . . . 88

4.4 Temperature Variations on TEG and Substrates . . . . . 90

4.5 Equivalent Circuit of Thermoelectric Generator and Load . . . . . 91

4.6 Test setup of thermoelectric module characterization . . . . . 93

4.7 Wafer Photograph of Micropelt Thermo-elements . . . . . 94

4.8 Heat sinks for MEMS and Bulk TEG Modules . . . . . 96

4.9 Temperature Difference on TEGs ($50-80^oC$ heat source) Due to Heat Sink Cooling; MEMS TEG: Micropelt; Conventionally machined: Thermonamic . . . . . 96

4.10 I-V Characteristics of MEMS TEGs for different load resistance . . . 97

4.11 Power Characteristics of MEMS TEGs for different load resistance . 97

4.12 I-V Characteristics of Bulk Thermo-element TEG for load resistance between 1Ω and 1kΩ . . . . . 99

4.13 Power Characteristics of Bulk Thermo-element TEG . . . . . 99

4.14 Conceptual circuit design of the thermoelectric energy harvesting power management . . . . . 101

4.15 Ultra low voltage step up DC/DC converter . . . . . 103

4.16 Regulation Loop of Ultra low voltage step up DC/DC converter . . . 104

4.17 Ultra Low Voltage DC/DC Converter Start-up Process . . . . . 104

4.18 Ultra low voltage boost converter efficiency measurements . . . . . 105

4.19 TEG Charge-Pump / Boost-Converter Two-Stage Power Management v.s. Boost Converter Single Stage Power Management . . . . . 107

4.20 TEG Impedance Matching . . . . . 107

4.21 Schematics of Charge pump/Boost Converter Power Management . . 109

4.22 Equivalent Input Resistance of the two stage power management circuit . . . . . 110

4.23 TEG Configurations Voltage Analytic Model Simulation Results . . 111

4.24 TEG Internal Resistance and Power Management Input Resistance Matching for $\Delta T = 4^oC$ . . . . . 112

4.25 Thermoelectric Powered WSN Prototype . . . . . 113

4.26 TEG Start-up Performance ($60^oC$ Hot Surface, $\Delta T = 4$ kelvin) . . . 113

4.27 TEG I-V Characteristics ($60^oC$ Hot Surface, $\Delta T = 4$ kelvin) . . . . 114

4.28 TEG Power-Current Characteristics ($60^oC$ Hot Surface, $\Delta T = 4$ kelvin) . . . . . 114

4.29 TEG Prototype Charges 2.5F Super-Capacitor . . . . . 116

4.30 TEG power management circuit conversion efficiency (super-capacitor load) compares with Linear Technology LTC3108 . . . . . 117

4.31 Duty Cycle Limits of WSN When Powered From Thermoelectric Energy Harvester . . . . . 118

5.1 Indoor Light Energy Harvester for WSN System Block Diagram . . . 122

5.2 PV cell illumination tests: (a) Samples tests setup;(b) Integrating sphere with halogen lamp light source . . . . . 123

5.3 Equivalent Electric Circuit of PV cells . . . . . 124

5.4 Diode 1 and series resistance curve fitting and measured dark I-V characteristics . . . . . 125

5.5 Diode 2 and shunt resistance curve fitting and measured dark I-V characteristics . . . . . 126

5.6 Simulated and measured dark I-V characteristics . . . . . 126

5.7 Measured I-V Characterizations and MPPT error (100-500 lux) . . . 129

5.8 Buck Converter based MPPT . . . . . 130

5.9 Simplified MPPT Implementation with Single Stage Buck Converter 131

5.10 Upper and Lower Threshold of Proposed Comparator . . . . . 132

5.11 Buck converter based MPPT equivalent circuit . . . . . 132

5.12 Buck converter based MPPT Inductor current . . . . . 134

5.13 Buck Converter MPPT SPICE Model for Power Loss Analysis . . . 138

5.14 SPICE Simulation Results of Buck Converter MPPT PV voltage and Inductor Current(1mH inductor and $47\mu F$ input capacitor) . . . . . 139

5.15 Input and Output Voltage Simulation Result (screen capture) . . . . 141

5.16 Buck MPPT conversion efficiency with different super-capacitor voltages . . . . . 141

5.17 Buck MPPT input capacitance/inductance and Simulated conversion efficiency . . . . . 142

5.18 Buck converter MPPT and indoor light energy harvester implementation . . . . . 142

5.19 Buck converter MPPT Measurement Results: MPPT operation $V_{MPP} = 3.87V$ (1mF $C_{IN}$ configuration) . . . . . 143

5.20 Buck converter MPPT Measurement Results: MPPT Circuit Charging Test Capacitor(100mF) . . . . . 144

5.21 Power Gain from MPPT compared to Non-MPPT Configuration (Simulated vs. Measured Results) with 10F super-capacitor . . . . . 145

5.22 Schematics of Maximum Power Point Tracking . . . . . 147

5.23 Converter SPICE simulation and control signals of SW1, SW2 and SW3 . . . . . 148

5.24 (a) On-stage ($t_0$-$t_1$) equivalent circuit (b) OFF-stage ($t_1$-$t_2$) equivalent circuit and Idle-stage ($t_2$-$t_3$) equivalent circuit . . . . . 149

5.25 Boost Converter MPPT with (top) 2% MPP voltage error; (bottom) 10% MPP voltage error . . . . . 155

5.26 Indoor Photovoltaic Energy Harvester with Boost Converter MPPT and Hybrid Energy Storage Schematics . . . . . 156

5.27 Picture of indoor light EH powered WSN prototype . . . . . 157

5.28 Boost Converter MPPT Results (Oscilloscope screen capture) . . . . 157

5.29 MPPT conversion efficiency in sub-1mW power conditions (100-1000 $\mu W$) . . . . . 158

5.30 Measured Power Loss Factors and Output Power Results ($40cm^2$ PV cell in typical office environment) . . . . . 159

5.31 Simulink Simulation of Energy Harvesting Module Powered WSN System . . . . . 162

5.32 EH powered WSN Deployment Case Study . . . . . 163

5.33 Light intensity measurement and simulation . . . . . 164

5.34 EH Powered WSN Deployment Measurement Results . . . . . 166

A.1 Cap-XX Design-Aid Calculators . . . . . 177

# List of Tables


1.1 Abbreviations and Terms used in Energy Harvesting System Architecture . . . . . 5

1.2 Energy Storage Units Lifetime and Re-charge Cycles . . . . . 9

2.1 Power Consumption and Profile Summary of WSNs [1] †Including temperature and light sensors; ⋆Transmission Power = 0dBm; ♣Transmission Power = 17dBm; ♠Transmission Power = 20dBm . . . . . 13

2.2 The power Consumption of a Tyndall BEM mote at 3.3V (Sleep mode is 300 seconds, i.e. 5 minutes measurement interval) . . . . . 15

2.3 Comparisons of State of the art (SOTA) Energy Storage Units . . . 40

2.4 DC/DC Converters and Characterizations . . . . . 41

3.1 super-capacitor and TFB Average Leakage Current Over 24 Hours and Leakage Correlation $\rho_{leak}$ . . . . . 52

3.2 Characterizations Summary of super-capacitors and Thin Film Battery . . . . . 58

3.3 Significance of terms in Equation 3.10 . . . . . 60

3.4 Components Parameters of Self Start Circuit . . . . . 77

4.1 Symbol and Definition of Thermal Effect Parameters . . . . . 89

4.2 Micropelt Thermoelectric Module Parameters Summary . . . . . 94

4.3 Conventional Machined Thermoelectric Module Parameters Summary 95

4.4 Micropelt TEG Characterization and Simulation at Matched Load . 98

4.5 Thermonamic Bulk TEG Characterizations and Simulation at Matched Load . . . . . 99

4.6 TEG Module performance comparison at $60^oC$ source temperature . 100

4.7 Component Selection for Thermoelectric Energy Harvester . . . . . 108

4.8 TEG Power Management Energy Transfer . . . . . 115

5.1 Dark Characterization of Tyndall GaAs cells . . . . . 127

5.2 Measured Dark Characterization and Active Area Parameters Summary 127

5.3 Power Density at 500 lux light intensity . . . . . 128

5.4 Simulated Inductor Current and Control Signal Frequency with 0.9mW Input Power . . . . . 140

5.5 Power Loss Analysis in Buck Converter MPPT in 1 Duty Cycle (1mH inductor; $47\mu F$ input capacitor; super-capacitor voltage 2.0V) . . . . 140

5.6 Power Loss Analysis in Boost Converter MPPT in 1 Duty Cycle (1mH inductor; $14\mu F$ input capacitor) . . . . . 154

5.7 Simulation Results of Energ Loss due to MPPT Error (Sanyo 1815 Cell 55mm $\times$ 40mm Cell) . . . . . 155

5.8 sub-1mW to 50mW Input Power MPPT Results . . . . . 159

5.9 System Simulation Parameters . . . . . 161

5.10 EH powered WSN System Configurations . . . . . 165

# List of Publications

## A. Journal Publications and Book Chapters:

1. Wang, W., O'Donnell, T., Wang, N., Hayes, M., O'Flynn, B. and O'Mathuna, C. (2010). "Design considerations of sub-mW indoor light energy harvesting for wireless sensor systems." ACM J. Emerg. Technol. Comput. Syst. 6(2): 1-26.

2. Wang, W., Wang, N., Hayes, M., O'Flynn, B. and O'Mathuna, C. (2012). "Power management for sub-mW energy harvester with adaptive hybrid energy storage." SAGE Journal of Intelligent Material Systems and Structures, on-line first

3. Wang, W., Wang, N., Hayes, M., O'Flynn, B. and O'Mathuna, C. (2011). "Thermoelectric Powered Autonomous Wireless Sensor Module for Temperature Monitoring." Applied Mechanics and Materials 63: 978-982.

4. Wang, W., Cionca, V., Wang, N., Hayes, M., O'Flynn, B., and O'Mathuna, C. (2013). "Thermoelectric Energy Harvesting for Building Energy Management Wireless Sensor Networks." Accepted by Journal of Distributed Sensor Networks

5. O'Donnell, T. and Wang, W. (2009). "Power Management, Energy Conversion and Energy Scavenging for Smart Systems." Book Chapter in Ambient Intelligence with Microsystems: 241-266.

## B. Invention Disclosures:

6. "Autonomous energy harvester design and implementation for wireless sensor networks", WS. Wang, T. O'Donnell, N. Wang, M. Hayes, IDF number: IE-UCC-1215

7. "Hybrid energy storage unit design for low power energy harvester", WS. Wang, N. Wang, M. Hayes, IDF number: IE-UCC-1318

## C. Conference Proceedings:

8. [Selected Best Paper] WS Wang, N Wang, M Hayes, B O'Flynn, C O'Mathuna (2010). "Autonomous Smart Sensing System for Building Energy Metering". Smart Systems Integration, 4th European Conference and Exhibition on Integration Issues of Miniaturized Systems, Como, Italy, Mar 23-24

9. WS Wang, T O'Donnell, L Ribetto, B O'Flynn, M Hayes, C O'Mathuna (2009). "Energy harvesting embedded wireless sensor system for building environment applications". Wireless VITAE 2009. IEEE Conference on, Aalborg, Denmark, May 17-20

10. WS Wang, N Wang, M Hayes, B O'Flynn, C O'Mathuna (2011). "Hybrid energy storage for energy harvesting powered wireless sensor networks". Smart Systems Integration, 5th European Conference and Exhibition on Integration Issues of Miniaturized Systems, Dresden, Germany, Mar 22-23

11. WS Wang, N Wang, M Hayes, B O'Flynn, C O'Mathuna (2012). "Power Management Circuits Design for Low Intensity Indoor Light Powered Wireless Sensor Nodes". Smart Systems Integration, 6th European Conference and Exhibition on Integration Issues of Miniaturized Systems, Zurich, Switzerland, Mar 21 - 22

12. WS Wang, N Wang, M Hayes, B O'Flynn, C O'Mathuna (2010). "Autonomous wireless sensor network based Building Energy and Environment Monitoring system design". Environmental Science and Information Application Technology, International Conference on, IEEE. Wuhan, China, July 10-13

13. WS Wang, W Magnin, N Wang, M Hayes, B O'Flynn, C O'Mathuna (2011). "Bulk material based thermoelectric energy harvesting for wireless sensor applications." Journal of Physics: Conference Series, Sensors and their Applications XVI,

307(1): 012030, Cork, Ireland, Sep 12-14

14. WS Wang, R O'Keeffe, N Wang, M Hayes, B O'Flynn and C O'Mathuna (2011) "Practical Wireless Sensor Networks Power Consumption Metrics for Building Energy Management Applications", 23rd European Conference Forum Bauinformatik, Cork, Ireland, Sep 10-11

15. WS Wang, V Cionca, D O'Mahony, N Wang, M Hayes, B O'Flynn, C O'Mathuna (2012), "Design Considerations of Wireless Monitoring Networks for Concentrated Photovoltaic Power Plant Applications", Smart Grid Technology, Economics and Policies conference, Nuremberg, Germany, Dec 3 - 4

16. M Hayes , WS Wang, T O'Donnell, B O'Flynn, C O'Mathuna (2009) "Energy Harvesting for Practical Deployment of Wireless Sensor Networks in Building Energy Management (BEM) Applications", Proc. NanoPower Forum, nPF '09, San Jose, US, May 18-20

17. J Jung, WS Wang, MA Ingram (2011) "Cooperative Transmission Range Extension for Duty Cycle-Limited Wireless Sensor Networks," Wireless VITAE. IEEE Conference on, Chennai, India, 28 Feb - 2 Mar

18. J Essa, B O'Flynn, C O'Mathuna, WS Wang, "Design of miniaturized wireless sensor mote and actuator for building monitoring and control", Telecommunications (ICT), IEEE 17th International Conference on, Doha, Qatar, Apr 4-7

19. L Zheng, WS Wang, A Mathewson, B O'Flynn, M Hayes (2010) "An Adaptive Transmission Power Control Algorithm for Wireless Sensor Networks", 21st Irish Signals and Systems Conference, Cork, Ireland, Jun 23 - 24

## D. Invited Talk:

20. Wensi Wang, "Energy Harvesting Design Model and Implementation" Energy Harvesting and Storage Conference and Exposition 2011, Munich, Germany, June

21-23

## E. Workshops and Technology Reports:

21. Member of technical committee - Knowledge Transfer Networks, Sensing Technology WiSIG Workshop. Birmingham, U.K. Sep 28-29, 2010

22. WS Wang, M Hayes, T O'Donnell, B O'Flynn and C O'Mathuna, (2008) "Energy Harvesting Technologies for Wireless Sensor Systems", Poster Presentation at IET Sensors Instrumentation Workshop, London, UK, Nov 25

23. UK Knowledge Transfer Networks Technology Report: "Energy harvesting technologies to enable remote and wireless sensing", WS Wang, T O'Donnell, J Barton, Jun 2008

## F. Citation and H-Index:

Citations: 79, Jun 2009 - Feb 2013. H-Index: 5. I10-Index: 3.



Change photo

wensi wang Edit

Tyndall National Institute, Ireland Edit

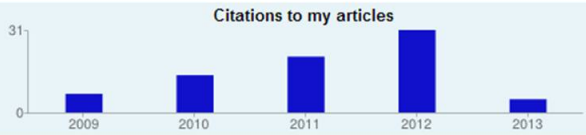
Energy Harvesting - Wireless Sensor Networks - Smart Grid - Maximum Power Point Tracking Edit

Verified email at tyndall.ie Edit

My profile is public Edit Link Add homepage

**Citation indices**

| | All | Since 2008 |
|---|---|---|
| Citations | 79 | 78 |
| h-index | 5 | 4 |
| i10-index | 3 | 3 |




Select: All, None Actions 1-18

| Title / Author | Cited by | Year |
|---|---|---|
| Design considerations of sub-mW indoor light energy harvesting for wireless sensor systems<br>WS Wang, T O'Donnell, N Wang, M Hayes, B O'Flynn, C O'Mathuna<br>ACM Journal on Emerging Technologies in Computing Systems (JETC) 6 (2), 6 | 16 | 2010 |
| Energy harvesting embedded wireless sensor system for building environment applications<br>WS Wang, T O'Donnell, L Ribetto, B O'Flynn, M Hayes, C O'Mathuna<br>Wireless Communication, Vehicular Technology, Information Theory and ... | 12 | 2009 |
| Autonomous wireless sensor network based Building Energy and Environment Monitoring system design<br>W Wang, N Wang, E Jafer, M Hayes, B O'Flynn, C O'Mathuna<br>Environmental Science and Information Application Technology (ESIAT), 2010 ... | 9 | 2010 |

# Chapter 1

# Background and Motivation

## 1.1 Wireless Sensor Networks

A Wireless Sensor Network (WSN) is a concept that has gradually emerged in the last two decades. It was first introduced in 1991 by Dr. Mark Weiser, who now is widely considered as the father of ubiquitous computing. In his *Scientific American* article titled *"The Computer for The* $21^{st}$ *Century"*, he wrote *"The most profound technologies are those that disappear. They weave themselves into the fabric of everyday life until they are indistinguishable from it."* He introduced the concept of small "tabs", suggested these "tabs" will be *"the smallest components of embodied computing, sensing and visualization system"* and they are *"interconnected"*[2].

One area of greatest potential is in Building Energy Management (BEM) WSN systems [3, 4, 5]. In the International Energy Outlook 2011 report issued by United States Department of Energy, 37% of global energy usage and over 40% of $CO_2$ emissions can be attributed to the operation of residential and commercial buildings as shown in Figure 1.1 [6]. By monitoring and controlling artificial lighting, temperature, energy consumption, carbon dioxide levels, relative humidity, airflow, a substantial percentage of energy can be saved [7, 8].

It has been estimated that the usage of intelligent sensor networks can result in 15-20% savings in total energy consumption in typical office buildings [9]. If the BEM wireless sensor network technologies become as "ubiquitous" as Weiser envisaged, the benefit of utilizing BEM WSN technologies can be translated into 5-8% global

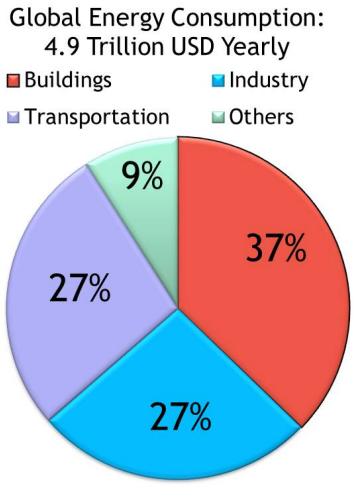



Figure 1.1: Global Energy Consumption in term of U.S. Dollars in 2011 [6]

energy savings, which is worth several trillion U.S. dollars in the coming decade, and which will have a profound impact on the global environment.

At present, this type of network normally consists of wireless sensor nodes (also known as "motes") featuring sensors data processing and communication capability. Recent advances in integrated circuit design and wireless communication research enable these motes to evolve in terms of transmit range, data throughput, processing power, sensor types and accuracy etc. WSN technologies are moving towards further miniaturization [10], smart communication [11] and ultra-low energy consumption [12, 13].

## 1.2 Energy Harvesting System

WSN development is moving towards Weiser's target of "interconnected small tabs with ubiquitous computing capability". However, one fundamental obstacle to "weave WSN into the fabric of everyday life", is the limited battery lifetime. Due to the limits on the system form factor, the physical size of battery is desired to be small, which in turn limits the capacity of the battery.

Even advanced CR2032 coin-sized batteries ($\approx 1$ cm$^3$) with very high energy densities of 300 Amp hours per litre (Ah/L) can only store approximately 2000J of energy

[14]. If a mote consumes an average power of 0.2mW (typical power consumption of a commercially available TelosB mote) [15], the lifetime of the CR2032 sized battery is only 115 days, or less than 4 months in an optimistic estimation. With the continuous development of WSN, the number of motes in a network is moving from 10s to 100s, even 1000s in the foreseeable future [16]. The mandatory requirement to replace batteries for the entire network every few months increases the maintenance efforts and costs. Such requirement also compromises the system reliability. This is one of the most significant barriers to the widespread commercial adoption of WSN for many BEM applications. Without a significant breakthrough in battery technology, alternative methods have been studied to enable longer lifetime for WSN systems.

### 1.2.1 Definition of Energy Harvesting System

To effectively prolong the lifetime of WSN systems, "energy harvesting" technologies have been proposed. "Harvesting" energy from ambient environments provides a way to not only prolong the system lifetime, but eliminates the need for battery energy storage. In simple terms, it is a process that supplies WSN with small but "infinite" environmental energy. In this way, WSN lifetime is no longer constrained by the finite local stored energy in the battery but only limited by the lifetime of energy harvesting module (EHM) and WSN electronic components.

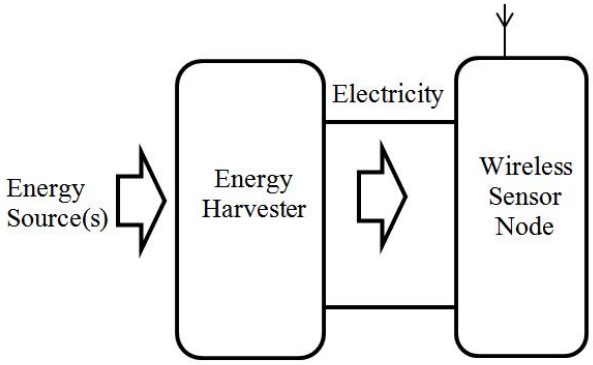



Figure 1.2: Simple Energy Harvester Powered WSN

The basic concept of energy harvesting (EH) is a system which converts ambient

energy into electricity, as shown schematically in Figure 1.2. However, although electricity is harvested from the ambient environment, without output power management, it cannot be used in this "unconditioned" form to power a wireless sensor node. Without an energy storage unit, any glitch in the ambient energy source will lead to mote power failure. Furthermore, without input power management on the energy harvesting unit, the energy conversion is not optimized and cannot deliver energy with high efficiency and reliability.

For practical application of energy harvesting techniques for wireless sensor networks, "energy harvesting" is not limited to converting ambient energy into electricity.

Energy harvesting system is a power supply which collects the energy from the ambient environment, converts it into electricity and stores the energy when necessary in order to supply WSN for a power autonomous operation.

### 1.2.2 Terms Regarding Energy Harvesting System

It is also necessary to define the terms used to describe the energy harvesting system in the introduction of this thesis as shown in Figure 1.3. The terms used in this thesis concerning the system architecture is introduced in Table 1.1.

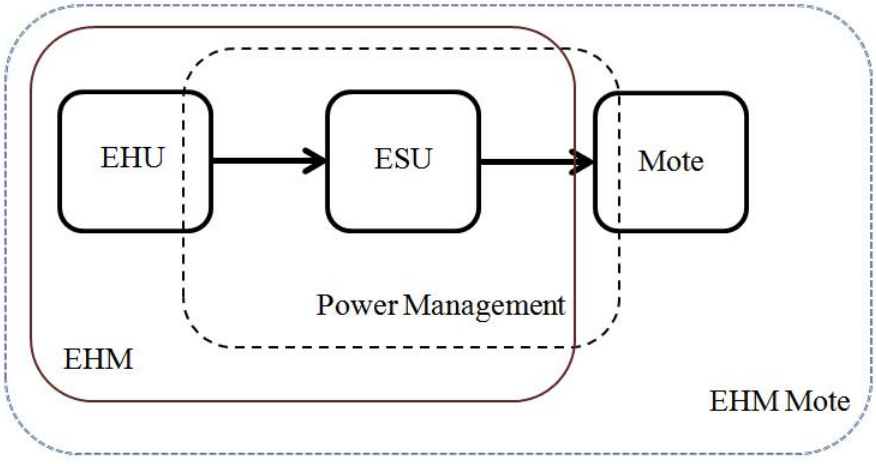



Figure 1.3: Energy Harvesting Powered WSN System Example

| Abbreviations | Name | Function & Comments |
|---|---|---|
| EHU | Energy Harvesting Unit | Converts ambient energy into electricity (e.g. Solar Panel and Thermoelectric Generator) |
| ESU | Energy Storage Unit | Stores energy (e.g. battery or capacitor) |
| Power Management | Power Mangement Circuits | The circuits conduct input/output power conditioning |
| EHM | Energy Harvesting Module | The complete energy harvesting system including EHU, ESU and Power Management |

Table 1.1: Abbreviations and Terms used in Energy Harvesting System Architecture

### 1.2.3 Power Level of Energy Harvesting System

It is worth noting that energy harvesting technology for WSN is significantly different from other applications utilizing ambient energy from the power level point of view as shown in Figure 1.4.

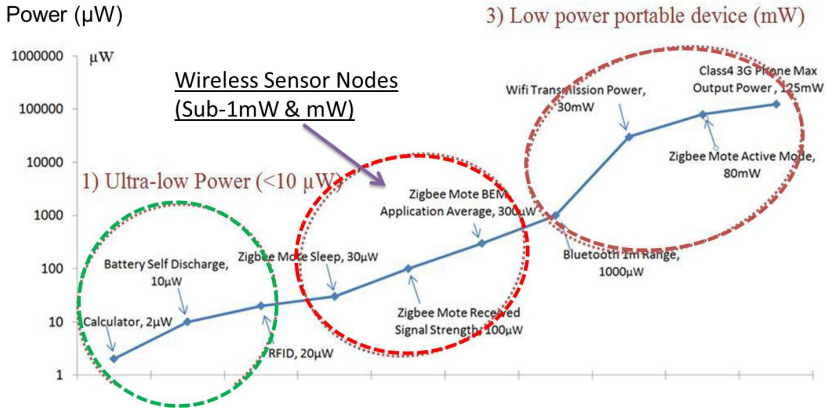



Figure 1.4: Power Levels Synopsis of Portable Devices [17]

The ultra-low power device (indicated as type 1 in Figure 1.4) such as calculators and digital clocks only consume several $\mu$W. More complicated wireless communication devices (indicated as type 3 in Figure 1.4) such as Bluetooth, Wifi communication and 3G cell phones consume 1-100mW. The average power consumption of wireless sensor networks typically falls between type 1) and 3). Attempts to directly utilize the power management methods and components previously developed and used in type 1) and 3) devices lead to either insufficient functionalities and failure to reach the overall design target, or low conversion efficiency due to inadequate

operating condition. The power management design and components selection must meet the power level requirements of energy harvesting. In this thesis, the energy harvesting system is designed for the WSN applications with power consumption in the range of 0.1-1mW.

### 1.2.4 Research Objectives

Different from energy harvesting research such as [18], [19] and [20] which primarily focus on the energy harvesting transducers, the focus of this thesis is mainly in the development of power management circuits for various types of energy harvesting transducers. The goals of this thesis are to extract the maximum power from transducers as well as to convert harvested electricity to a useful form with highest possible efficiency.

For different energy source types, many aspects of the power management circuits vary due to their distinctive energy characteristics (i.e. AC/DC, high voltage, low voltage, voltage source or current source) when they are harvested. Since ambient energy exists in many forms, ranging from vibration/motion kinetic energy, fluid/gas flow kinetic energy, ambient RF energy to thermal energy and solar/light energy, research to extract energy from these energy sources has been conducted individually. Several research groups have previously summarized the energy sources and energy harvesting technologies in detail [21], [22], [23],[24] and [25].

The general view towards the energy sources and harvesting solutions is that a "one solution fits all" does not exist at present. Each energy harvesting technology should be application-oriented with careful consideration given to the realistic environmental parameters and energy generation/consumption characteristics.

In commercial and residential building scenario, the energy source of the energy harvester should be ubiquitous in order to suit a wide range of applications. Indoor

light energy [1] can be considered as the most ubiquitous ambient energy source, although it generally has low light intensity (300lux - 500lux) as opposed to high power density outdoor lighting (>2000lux for a cloudy day [26]). The existence of thermal energy has been found in some locations in residential and commercial buildings, such as heaters, hot water pipes and air conditioning units. Hence, thermal energy harvesting and its power management are also investigated in this work.

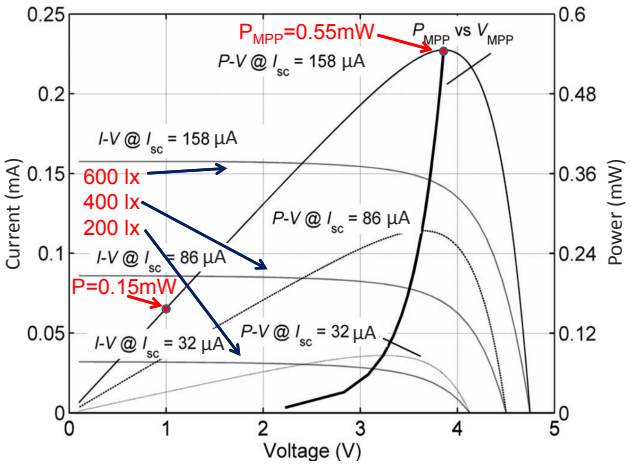



Figure 1.5: Sanyo AM1815 Solar Cell Current-Voltage and Power-Voltage Characteristics in Office Environment (light intensity 200-600lux) [27]

For energy harvester module with a device (EHU, ESU and power management circuits) size similar to credit card, solar cell such as amorphous silicon Sanyo AM1815 [27] (58mm×48mm) cells generate a maximum power of 0.55mW from 600lux. The output power and current of the solar cell are shown in Figure 1.5.

For thermoelectric energy harvesting, a commercially available thermoelectric generator (TEG), such as Marlow industries EHA-PA1AN1 generator [28] (20mm×20mm), produces a maximum power of 1.8mW with 30$^o$C module-wide temperature difference (e.g. hot side temperature 50$^o$C, room temperature 20$^o$C) when the generator operates with 100% matched impedance as shown in Figure 1.6.

In both cases of solar and thermal energy harvesting, the output power are often calculated based on theoretical maximum output power. However, in practice, when

[1]The European guideline for light intensity in office environment is: >300lux and <750lux in office, optimal light intensity 450 - 500lux; between 200 - 400lux in corridor [European Standard EN 15193:2007, Energy Performance of Buildings [9]]

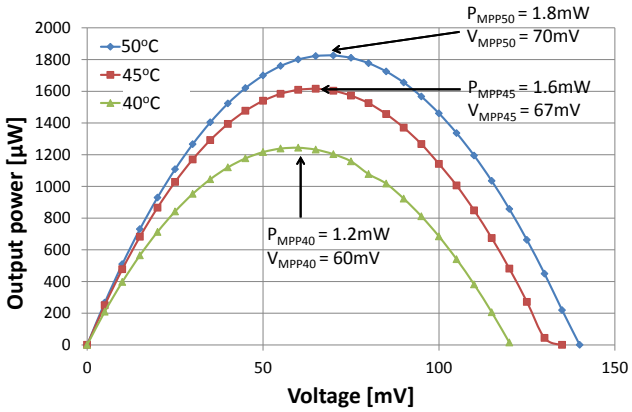



Figure 1.6: Marlow industries EHA-PA1AN1 generator[28] Output Power when placed on 50$^o$C/45$^o$C/40$^o$C hot surface (room temperature =20$^o$C)

the energy harvester is directly connected to the load without Input Power Management Circuits the solar cell and TEG will not operate at their maximum power point, i.e. the actual amount of power harvested from EHUs will be lower than the theoretical value. For example, as shown in Figure 1.5 when the Sanyo AM1815 solar cell is connected to load without input power management circuits and operates at 1V instead of its maximum power point voltage of 3.8V, only 0.15mW or 27 % of the theoretical maximum power is harvested.

Maximum power point tracking (MPPT) technologies have often been used for solar power systems with output power higher than 100mW [29]. By implementing switching regulator based MPPT techniques, the EHU will operate near its theoretical maximum power point ($P_{MPP}$) and generates power close to its highest conversion efficiency. One major challenge in energy harvesting system is how to implement this type of input power management circuit with a minimum power consumption overhead. The conventional methods of MPPT cannot be directly adopted because their power consumption is beyond the power budget of the small EH system, i.e. 1mW or even lower. In this thesis, new methods have been proposed in order to perform Ultra-low Power (sub-1mW) MPPT.

In addition to the MPPT issue, the energy harvesters often generate lower voltage than the conventional power supplies such as battery. For example, the open circuit voltage of thermoelectric generator such as aforementioned Marlow industries

EHA-PA1AN1 generator (20mm×20mm module) is only 140mV at 50$^o$C surface temperature as shown in Figure 1.6. In order to efficiently utilize the low voltage thermoelectric energy, step-up voltage conversion must be performed in order to raise the voltage to an "usable" voltage level. In this work, Ultra-low Voltage (<0.5V) DC-DC Conversion circuits have been designed in order to utilize the harvested thermoelectric energy.

Once the optimized output power of EHU is harvested, it is necessary to store the harvested energy using energy storage units (ESU). ESU such as super-capacitor, thin film battery and commercial off the shelf rechargeable battery are considered in this work. Three types of energy storage units are compared in Table 1.2 in terms of lifetime and re-charge cycles.

| ESU Type. | Typ. Lifetime (years) | Max. Re-charge Cycles |
|---|---|---|
| Super-capacitor | 10-15 y | >100,000 |
| Thin Film Battery | 10 y | >10,000 |
| COTS Li-ion Rechargeable Battery | <7 y | <1,000 |

Table 1.2: Energy Storage Units Lifetime and Re-charge Cycles [30], [31], [32]

Based on these ESUs, the related charge/discharge control circuits such as fast charge circuits, self-start circuits, output voltage regulation circuits for ESU, and hybrid ESU, combining super-capacitor and rechargeable thin film battery, power management circuits are proposed in this work.

Figure 1.7 illustrates the power management circuits proposed for energy harvesting system.

In addition to the power management circuits development, this thesis also proposes a system level simulation model for energy harvesting based on energy flow modelling. This proposed model simulates the generated power, conversion efficiency and power loss in sub-systems, and the power consumption of the WSN mote in order to 1) optimize components value and selection; 2) estimate useable energy from the energy harvesting system.

In terms of prototype development, the objective of this thesis is to design a

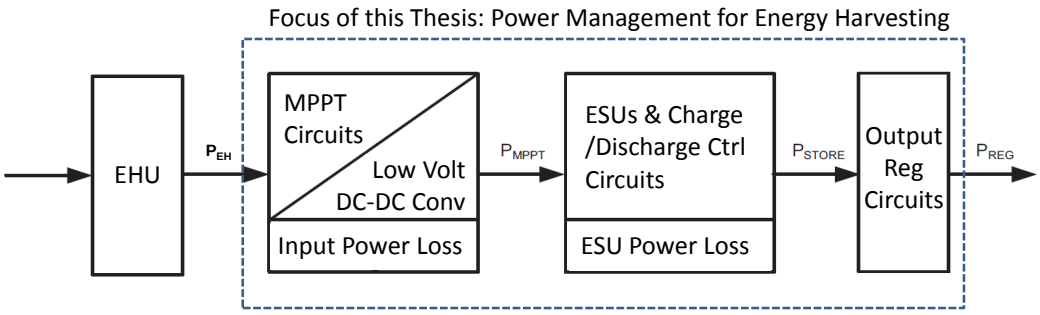



Figure 1.7: Power Management for Energy Harvesting Systems

continuous and maintenance-free power management system for energy harvester module in low duty cycle WSN applications. With a credit card form factor (less than 80mm $\times$ 50mm), the device should be able to supply the power consumption of WSN with regulated power from typical building environment. The average conversion efficiency of the power management circuits should be higher than previous state of the art and the prototypes require a minimal lifetime of 10 years.

## 1.3 Thesis Layout

This thesis is organized as follows: Chapter 2 presents an introduction to energy harvesting systems and literature reviews of important previous work. Chapter 3 analyses the energy storage units and their power management circuits. In this chapter, a detailed energy model is also created to simulate the energy storage unit operations. Chapter 4 shows the thermoelectric energy harvesting system design with an emphasis on power management circuit design and system conversion efficiency optimization. In Chapter 5, an indoor light energy harvesting system is studied with an emphasis on maximum power point tracking circuits design. Indoor light energy harvesting WSN system implementation, with system energy model, is introduced in this chapter. Chapter 6 concludes the findings of this thesis and proposes several possible directions for future work.

# Chapter 2

# Literature Review

## 2.1 Introduction

The practical application of energy harvesting (EH) considered in this thesis is in the area of wireless sensor networks (WSN) for building energy management (BEM) as introduced in Chapter 1. This thesis investigates two types of EH technologies in BEM application, low intensity light EH and thermoelectric EH.

Before developing an energy harvesting module (EHM), a review of the currently-available technologies is necessary. In this chapter, Section 2.2 introduces previous work on low power WSN and summarises their power consumption profiles. Section 2.3 introduces energy harvesting power management technologies related to this work. The final section, Section 2.4, draws conclusions from the literature review and gives the context for the research challenges addressed in this thesis.

## 2.2 Wireless Sensor Networks

The conceptual block diagram of a typical WSN mote is shown in Figure 2.1. In a WSN mote, sensors conduct measurement and transfer the data to micro-controller via sensor interfaces such as Analog-to-Digital Converter (ADC) or Inter-Integrated Circuit ($I^2C$). Micro-controller transmits the processed sensor data via radio frequency transceiver to receiver(s) in the wireless network.

WSNs have been a research focus in recent years and have seen many potential applications in the areas of building management [7][33], body sensor networks for

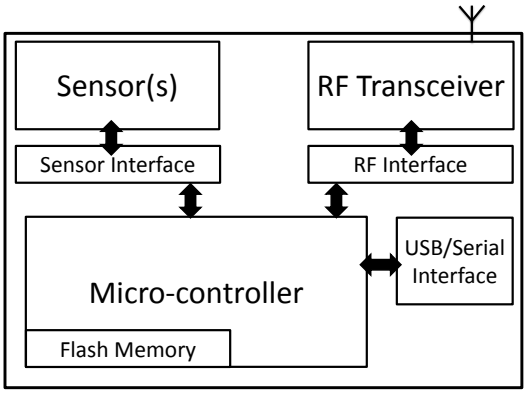



Figure 2.1: Wireless Sensor Node (Mote) Block Diagram

medical applications [34], tracking and localization [35], aircraft monitoring [36], vehicle monitoring [37], agriculture [38] and generic sensor networks [39]. Given the focus of this thesis is in the area of energy harvesting technologies for WSN applications, this literature review of WSN concentrates on the perspective of energy consumption of WSN mote.

The motes are often programmed to perform "duty cycling" operation for energy conservation, i.e. entering low power sleep mode after the high power sensing and transmission (active) mode as illustrated in Figure 2.2.

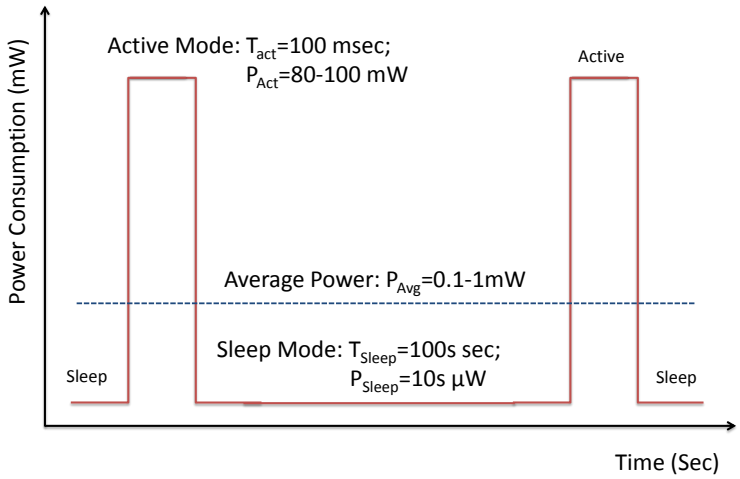



Figure 2.2: Typical Power Consumption Profile of a "duty cycling" WSN Mote

At present, the IEEE physical layer standard for short-mid range communication

WSN is IEEE 802.15.4 standard. Different physical layer specifications have been introduced based on this standard such as Zigbee, WirelessHart, 6LowPan, Zigbee-Pro and IEEE 802.15.4-Pro. The first three specifications focus on short range communication (<100 meters) with maximum transmission power of 7dBm or 10dBm. The Zigbee-Pro and IEEE 802.15.4-Pro specifications use higher transmission power radio (17dBm or 20dBm transmission power) to increase the transmission range to >1000 meters.

WSN platforms such as CrossBow MicaZ, Mica2Dot, Linear Technologies Dust Networks, Ember system-on-chip (SOC) EM250, TeloSB, Libellium Waspmote, Texas Instruments EZ430, EnOcean STM and Tyndall motes have been reviewed. These WSN motes are summarized in terms of active mode transmission current (peak current at given transmission power), sleep mode current and supply voltage $V_{CC}$ in Table 2.1.

| Wireless Sensor Node | $V_{cc}$ (V) | $I_{active}$ (mA) | $I_{sleep}$ ($\mu A$) | IEEE 802.15.4 2.4GHz Compatibility |
|---|---|---|---|---|
| CrossBow MicaZ⋆ | 2.1-3.6 | 17.4 | 20 | Yes, Zigbee |
| Ember EM250⋆ | 2.1-3.6 | 24 | 1.5 | Yes, Zigbee |
| Texas Instruments EZ430-RF2500⋆ | 1.8-3.6 | 21.2 | 0.7 | Yes, Zigbee |
| Tyndall Mote⋆ | 2.5-3.5 | 27 | 6.5 | Yes, Zigbee/6LowPan |
| Dust Networks LTC5800⋆ | 2.7-3.3 | 26 | 1.2 | Yes, WirelessHart |
| TeloSB⋆ | 2.5-3.5 | †22 | 15 | Yes, 6LowPan |
| CrossBow Mica2Dot⋆ | 2.7-3.3 | 33 | 1 | No, 868/915MHz 433/315MHz Multi-Freq |
| EnOcean STM-300⋆ | 2.6-4.5 | 24 | 0.2 | No, EnOcean 868/315MHz |
| Libellium Waspmote♣ | 3.3-4.2 | 95 | 55 | Yes, IEEE 802.15.4-Pro 1kM line-of-sight range |
| NXP Jennic JN5148-M04♠ | 2.7-3.6 | 110 | 2.6 | Yes, Zigbee-Pro 4kM line-of-sight range |

Table 2.1: Power Consumption and Profile Summary of WSNs [1] †Including temperature and light sensors; ⋆Transmission Power = 0dBm; ♣Transmission Power = 17dBm; ♠Transmission Power = 20dBm

It can be concluded from the summary table that the voltage rating of the wireless sensor nodes is generally between 1.8V and 4.5V. The active mode current

consumption is on the level of 20-30mA for short RF range (<100meters) motes, and 95-110mA for long range (>1kM) motes. The sleep mode current consumption is between 1-20 $\mu$A in most cases.

In addition to the active mode current and sleep mode current, the duty cycle of the mote shows impacts on the average power consumption. The generic equation of the mote average power consumption $P_{avg}$ is shown in Eq 2.1.

$$P_{avg} = \frac{P_{act} \times T_{act} + P_{sleep} \times T_{sleep}}{T_{act} + T_{sleep}} \tag{2.1}$$

where $P_{act}$ and $T_{act}$ are the average active mode power consumption and active mode time, respectively. $P_{sleep}$ and $T_{sleep}$ are the sleep mode power consumption and sleep mode time, respectively. The active mode duty cycle $D_{act}$ is defined in the Eq 2.2,

$$D_{act} = \frac{T_{act}}{T_{act} + T_{sleep}} \times 100\% \tag{2.2}$$

Thus, the average power consumption $P_{avg}$ in Eq 2.1 can be simplified into Eq 2.3.

$$P_{avg} = P_{act} \times D_{act} + P_{sleep} \times (1 - D_{act}) \tag{2.3}$$

Different from hardware power consumption parameters such as voltage rating and sleep/active current which are generally constants, the duty cycle is application oriented. A case study on the duty cycling power consumption profile of BEM Tyndall mote[1] was conducted and the results are shown in Figure 2.3. The operating sequence of Tyndall modes is programmed in C language. The active mode includes 5 steps: 1) System Initialization; 2) Sensing (sensors are active and being sampled through the ADC); 3) Data Payload Tx (RF transmit); 4) ACK (acknowledgement) Rx (receiving). After the ACK signal is received, the active mode is complete, the mote enters 5) Sleep Mode. The sleep mode is programmed to be 5 minutes. The measured current consumption are listed in Table 2.2.

[1]Tyndall mote has 2 sensors for BEM applications: 1) temperature/relative humidity: Sensirion SHT-75 dual function sensor; and 2)light: Avago APDS 1000lux visible light sensor

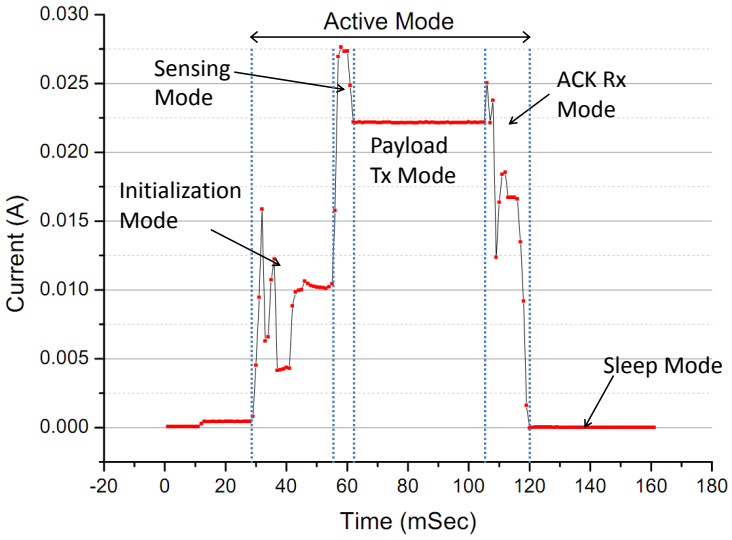



Figure 2.3: Tyndall Mote Current Consumption Profile

| Mode | Symbol. | Power (mW) | Time (mSec) | Energy (mJ) |
|---|---|---|---|---|
| 1) Initialization | $P_{Init}$ | 27.1 | 27 | 0.73 |
| 2) Sensing | $P_{Sen}$ | 82.5 | 5 | 0.41 |
| 3) RF Tx | $P_{Tx}$ | 73.2 | 42 | 3.07 |
| 4) ACK Rx | $P_{Rx}$ | 58.5 | 13 | 0.76 |
| Active Mode Average | $P_{Act}$ | 57.1 | 87 | 4.97 |
| 5) Sleep | $P_{sleep}$ | 0.033 | 300,000 | 9.9 |
| Mote Average | $P_{Avg}$ | 0.049 | 300,000.1 | 14.97 |
| Duty Cycle | $D_{Act}$ | $= 87ms/300sec = 0.029\%$ | | |

Table 2.2: The power Consumption of a Tyndall BEM mote at 3.3V (Sleep mode is 300 seconds, i.e. 5 minutes measurement interval)

The average power consumption changes significantly when the duty cycle is modified. For example, if the sleep time $T_{sleep} = 10$ seconds instead of the aforementioned 5 minutes $T_{sleep}$, the duty cycle changes to 0.87% and the mote average power consumption $P_{Avg}$ increases 10 times to 0.53mW. If the sleep time $T_{sleep}$ further reduces to 1 second, $P_{Avg}$ increases to 2.51mW.

In BEM temperature/humidity and light monitoring applications, the measurement interval of Tyndall mote was set at 10 seconds/1 minute/ 5 minutes. The

measurement interval can be re-programmed based on user requirement. In this case study, the average power consumption of Tyndall mote is measured between 0.05-0.5mW. Thus, in this thesis, the energy harvester system is designed for this level of power consumption.

## 2.3 Power Management Circuits for Energy Harvesting Applications

This section introduces the energy harvesting technologies for WSN applications with a focus on power management circuits and simulation.

### 2.3.1 MPPT for Photovoltaic EH

Re-visiting the Power-Voltage curve (P-V) shown in Figure 1.5, the $V_{mpp}$ and maximum power point are highlighted to demonstrate the maximum power point. The behaviour of the PV cell is similar to voltage controlled current source. When the voltage varies, the output power of the PV cell changes with it. The method to obtain the maximum power point (MPP) is called maximum power point tracking (MPPT).

Since the input light intensity varies with changing ambient light conditions, the P-V characteristics of PV cell also vary significantly under different light intensity. A fixed load impedance cannot respond to the changes of I-V characteristics, thus, switching regulator with controllable impedance (by adjusting the duty cycle of switching regulator control signal) is introduced to dynamically match the impedances.

Perturb and observe (P&O) method based conventional MPPT method is widely used in large scale energy generation since 1980s [40]. However, for many 1mW/sub-1mW power level small solar systems, MPPT has not been included. The main reason is: conventional P&O MPPT power consumption is too high (10-100mW

level, 2-3 orders of magnitude higher than the indoor PV cell harvested sub-1mW power) for small scale PV cells [41].

In [41], Raghunathan et al. highlighted this issue and suggested a "semi-MPPT" method: The SolarWorld 4-4.0-100 PV cell used in this paper has MPP voltage between 2.7V and 2.9V as shown in Figure 2.4. Raghunathan et al. selected a battery operating between 2.7V and 3.0V. By clamping the output terminals of the PV cell to this battery, this forces the PV cell to operate at a fixed output voltage near the MPP on its I-V curve. This approach is essentially overhead free, since the use of MPP tracking circuit is completely avoided. However, this method only applies for battery energy storage. When capacitive energy storage unit such as super-capacitor is selected, this method cannot be used since the PV cell voltage will be controlled by the super-capacitor voltage. Different from the battery type energy storage unit which has a narrow voltage range e.g. 2.7V-2.9V in this case, capacitive energy storage unit has a wide voltage range (0-5V, i.e. 0-100 % voltage rating). When directly connecting PV cell and capacitive energy storage unit, the output voltage of PV cell cannot be fixed near the MPP.

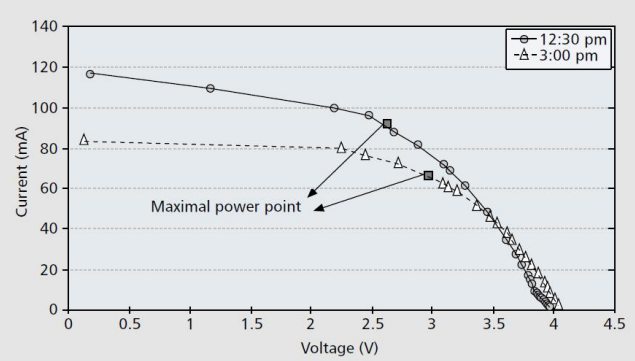



Figure 2.4: "semi-MPPT" method: choose rechargeable battery with operating voltage (2.7-3.0V) near PV cell MPP voltage (2.7-2.9V)

Farhan et.al. introduced a pulse frequency modulated (PFM) power management unit with maximum power point tracking capability as shown in Figure 2.5. The MPPT method utilizes the mote micro-controller to adjust the frequency and duty cycle to operate near the maximum power point condition [42].

This method is a very typical example of MPPT circuit design. It consists of

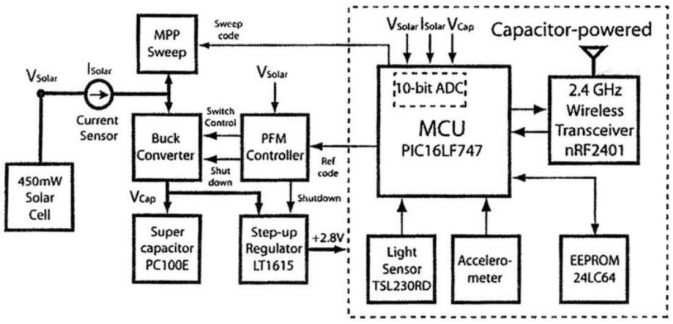



Figure 2.5: Energy Harvesting System with PFM controlled Buck Converter MPPT [42]

three key components: 1) sensor(s) to detect PV cell I-V condition. In this case, both the voltage and current of the PV cell are measured. 2) DC-DC switching regulator. The regulator switches on and off at given duty cycle and frequency in order to adjust the PV cell voltage. In this paper, a 5V to 3V buck converter is used. 3) control logic and signal generator which generate the switching regulator duty cycle/frequency signal. In this paper, the MCU is used to perform MPPT logic control. A PFM controller is used as the signal generator.

This MPPT design adopts a "perturb and observe" method[2] which requires a micro-controller to constantly monitor and adjust the frequency of the PFM control signal on the buck converter. This significantly increases the system cost and complexity. The power consumption of the current sensor and the ADC of the micro-controller are far beyond the harvestable power from indoor light. Although the system can obtain 80% efficiency when operates with 20mW input power, the adoption of this MPPT approach for indoor light energy harvesting is impractical. The less than 1mW harvestable power in indoor condition obviously cannot operate the 5mW MPPT circuitry.

In Park and Chou's paper [43] , a different sensor method is proposed for its lower power consumption. Instead of the commonly used current sensor, a light intensity sensor is used in this case to monitor light level and simulating the power

[2]In perturb and observe method, the controller continuously adjusts the voltage by a small amount from the PV cell and measures power; if the power increases, further adjustments in that direction are tried until power no longer increases.

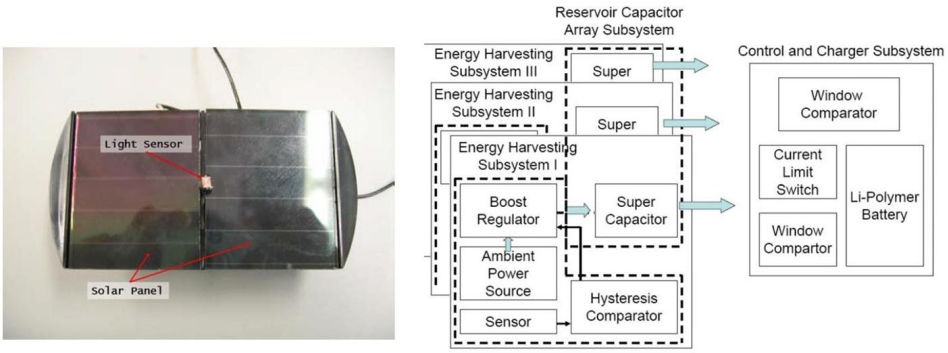



Figure 2.6: Low power light sensor based MPPT system

output instead of current sensing as shown in Figure 2.6. The micro-controller is programmed with a lookup table with relevant control modes in different light intensities. When the light condition varies, the micro-controller changes the control mode in order to maximize the harvested energy. The power consumption of this MPPT circuit is approximately 2mW, based on the efficiency calculation given in the paper.

Brunelli et. al. presented an analog comparator controlled PWM buck converter MPPT design without using complicated DSP or micro-controller in [44].

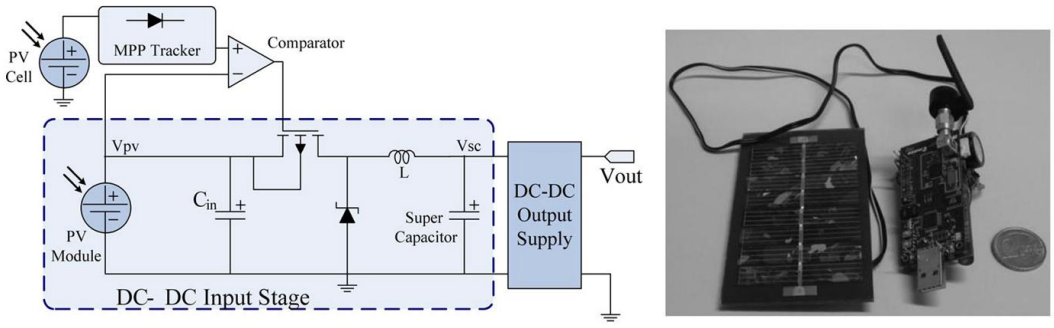



Figure 2.7: MPPT Energy Harvestor for Outdoor Applications with Tmote [45]

Different from the aforementioned Perturb and Observe method which continuously measures the output power and adjusts the output voltage of PV cell until it "finds" the MPP, in this method, the PV cell voltage is regulated to the maximum power point voltage $V_{MPP}$ based on the constant ratio to the measured open circuit voltage (VOC). Thus, this method is often called "**fractional open circuit**

**voltage**" MPPT or FVOC MPPT.

Figure 2.7 shows the schematics of this MPPT control logics. Firstly the PV cell charges input capacitor $C_{in}$ to a upper voltage threshold $V_U$; the DC-DC converter is then switched on to discharge the energy stored in input capacitor to the output capacitor (super-capacitor) until the input capacitor voltage reaches the lower voltage threshold $V_L$. The control logic (MPP Tracker and comparator) switch on/off the converter at a given frequency and duty cycle in order to repeat the charge/discharge process. Thus, the output voltage of PV cell only oscillates between the lower and upper voltage threshold, $V_L$ and $V_U$. By setting $V_L$ and $V_U$ close to the maximum power point voltage $V_{MPP}$, MPPT is performed in FVOC method.

This method simplifies the sensing requirement and control logic. Instead of constantly measuring the current and voltage in Perturb and Observe method, this method only requires the measurement on open circuit voltage.

The adoption of analog comparator based control circuits significantly reduced the power consumption in the MPPT circuits by one order of magnitude from 10-100mW to 1-10mW level. Although the conversion efficiency of 80% achieved at 10mW is similar to that in previous work which utilized Perturb and Observe method (84%) at 10mW [46], it shows the promise to a low power consumption solution to track MPP.

This group also published [45], [47] and [48] from the perspectives of simulation and components selection improvement of this method. These work analysed the power loss in a MPPT circuit and the impacts on the system conversion efficiency for **10-50mW input power applications**. The power loss is mainly attributed to the switching loss of the converter, conduction loss associated with the inductor, super-capacitors, and the diode forward voltage drop in the buck converter circuit.

These papers analysed the detailed power loss in DC/DC converter "on" and "off" states. The capacitance of the input capacitor and the inductance of the DC/DC converter inductor are included in the model to determine the optimal efficiency of the system. The most important contribution of this paper [47] is the proposed

power loss model giving in-depth theoretical understanding about the main factors impacting the efficiency of the energy harvester system. This model or similar model is frequently used in later energy harvester research. The prototype device is then tested with a Tmote-sky wireless sensor node as shown in Figure 2.7.

In [47], a 50F super-capacitor is adopted as the main energy storage unit. The large energy storage unit associates with larger capacity but also higher leakage current. (The super-capacitors typically have higher leakage current compared to other storage technologies. This will be discussed in details later in this chapter.) The feasibility of using such system in low light intensity condition is questionable. Even assuming the 50F super-capacitor operates in ideal condition without leakage current, the asynchronous MPPT DC/DC converter has average power dissipation >1mW when the "on" state inductor current flow through the diode (due to forward voltage drop). In addition, the buck converter is running at 100 kHz frequency in the continuous mode with a 22% duty cycle. Even with the optimal components selection and assuming the highest conversion efficiency, this design dissipates average power consumption more than 700$\mu$W. Although a 82% efficiency is measured at 5mW input power, it is impossible to directly use such system for sub-1mW input power energy harvesters.

In fact, Brunelli and Benini suggested that due to the power consumption in the MPPT, small PV cell is impractical to use the MPPT to improve conversion efficiency, and alternative method should be adopted instead. In [49], a semi-MPPT design with two voltage comparator is adopted as shown in Figure 2.8.

The PV cell is hard-wired to the super-capacitor, the two comparators set the thresholds of the sensor node on/off voltages. Once the super-capacitor voltage exceeds the higher threshold, the wireless sensor node starts to record the data and transmit to the base station. When the active mode of WSN continues, the high power consumption pulls down the super-capacitor voltage to the lower threshold. The WSN is then switched off. By running the super-capacitor voltage within a small range, the connected PV cell can only operate within this window. By adjusting the threshold voltages, the window is selected around the maximum power point

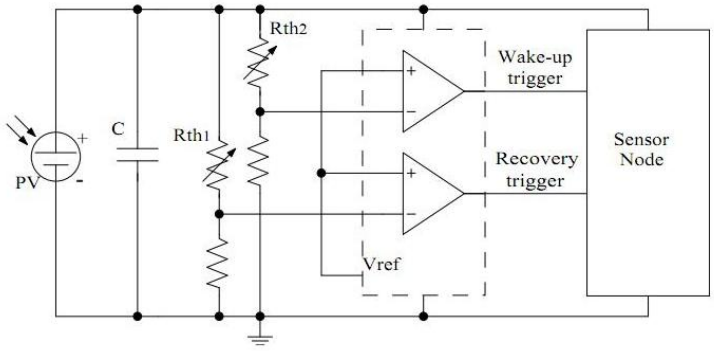



Figure 2.8: Voltage "Window" Semi-MPPT for Low Power Light EH [49]

voltage. Hence, by using this method the PV cell can operate near MPP.

Main drawbacks of this design are: Firstly, it cannot power the mote when no direct light is available. Once the capacitor voltage drops lower than threshold voltage, with no input power charging the capacitor, the mote cannot operate.

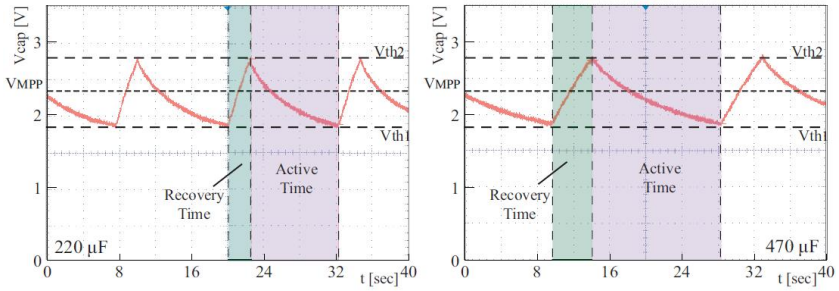



Figure 2.9: WSN Discontinuous Operation with "Voltage Window" Semi-MPPT Energy Harversting [49]

Secondly, as shown in Figure 2.9, the output voltage of this design is not a regulated voltage. The WSN mote operation time and frequency are not programmed by WSN mote, but instead relies on the input light and capacitor size. For example, in Figure 2.9, the module with 0.22mF capacitor requires 3 seconds "recovery" (charge) time before it discharges the capacitor and operates the mote for 9 seconds. When a 0.47mF capacitor is used, the charge and discharge time changes to 5 seconds and 15 seconds, respectively. With higher input power, the charge time will become shorter, i.e. the mote will operate more frequently.

This simple "semi-MPPT" method operates with high efficiency at 90% in indoor condition. However, for most BEM applications which require a constant duty cycle, e.g. WSN mote programmed to operate every 1 minutes, this method is not suitable due to its variable charge/discharge time.

Tan proposed a MPPT solution for wind EH using boost converter structure to perform impedance matching through resistance emulator method [50] as shown in Figure 2.10. This method operates the DC-DC converter with a **low frequency low duty cycle Pulse-width modulation (PWM)**. This paper has demonstrated that with 1-10mW input power, the low frequency PWM signal controlled switching regulator achieves higher dc-dc converter efficiency. It achieves a converter efficiency of 84% for 9.2mW input power (1.15V $\times$ 8.14mA). The reason for the efficiency improvement can be attributed to the negligible switching loss due to the low switching frequency (1-10Hz). In previous work such as [44], the 100 kHz switching frequency contributes approximately 45% of the total power loss. This method shows the potentials to further reduce the power consumption of MPPT into **sub-1mW power level** but was not verified by Tan and Panda due to difference in applications. One trade-off in this converter design is: the inductor required is larger (from both inductance and size perspectives) than that used in higher frequency switching regulator, e.g. the inductor used in [50] is 10mH as shown in Figure 2.10. However, for BEM application the 10mH inductor (0.7cm $\times$ 0.7cm footprint) size is not a concern.

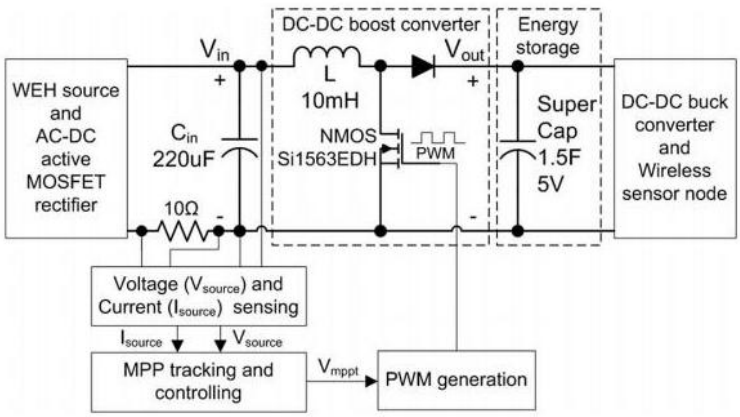



Figure 2.10: PWM MPPT for Wind Energy Harvesting [50]

This proposed system still utilizes a typical perturb and observe method. It monitors the input voltage and current through ADC and a shunt resistor type current sensor. The input I-V characteristics are then analysed in the MPP tracking and controlling unit. The MPPT control unit is a TI MSP430 micro-controller, similar to the one used in many advanced wireless sensor nodes. The MPPT control unit generates a low frequency control signal for the PWM generation unit. This MPPT control logic and the current/voltage sensors unit consume 0.36mW.

Tan's work [50] shows the **low frequency low duty cycle PWM** control signal and related DC-DC converter design lead to small power loss in the MPPT switching regulator. However, the complicated Perturb and Observe MPPT control logic in [50] still consumes considerable power (0.36mW) and requires both current and voltage sensors to monitor the solar cell. **FVOC ultra-low power analog comparator control logics** from Brunelli's work [44] shows it is possible to achieve low power consumption from this simple and low power control logic. However, the high frequency high duty cycle operation of the DC-DC converter used in [44] limits it efficiency.

These findings lead to a proposal, in this thesis, to combine the highlighted advantages of each approach in order to achieve ultra-low power consumption MPPT solution. The details of this method will be introduced in Chapter 5 of this thesis.

Tan and Panda also applied the low frequency low duty cycle PWM control method to indoor light and thermal hybrid energy harvesting with a voltage sensor based MPPT control logic in an attempt to resolve the aforementioned control logic power consumption issue as reported in [51].

In this MPPT circuit shown in Figure 2.11, the boost converter has been optimized for sub-1mW operation. The large 100mH inductor and the NMOS Si1563 switch have less than 0.5Ω internal/on resistance. The near optimal discrete component based converter shows a 91.8% conversion efficiency from 0.4mW (3.6V × 109$\mu$A) input power. In this paper, the system power loss consists of 2 parts. The first part is the power loss due to the converter efficiency, i.e. 0.4mW × (100%-91.8%)=32 $\mu$W.

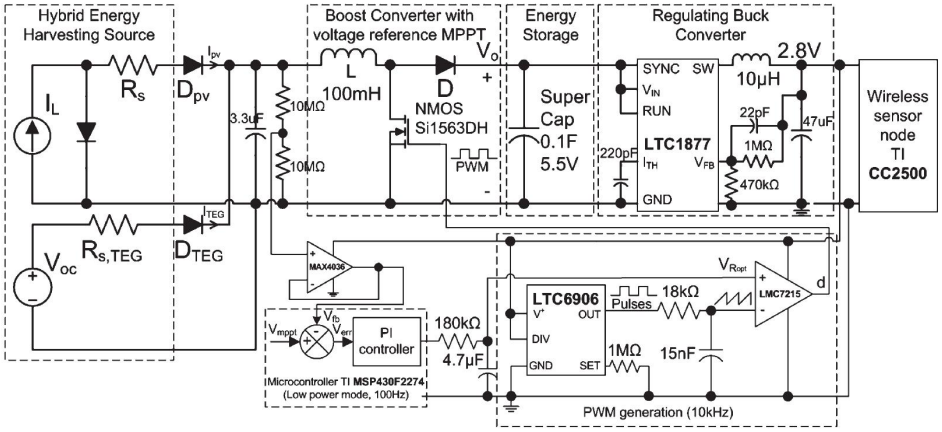



Figure 2.11: Indoor light and thermal hybrid energy harvesting power management module with MPPT function

The main attempt to reduce the power consumption is from the second part: control logic power consumption. Different from the current and voltage sensor perturb and observe method in their previous work shown in Figure 2.10 [50], this solution only uses voltage monitoring. A Texas Instrument MSP430F2274 micro-controller is used in this solution to monitor the solar cell voltage and compare to the reference voltage. The reference voltage is calculated from a light intensity sensor and a temperature sensor.

This simplified perturb and observe method reduces the power loss from the controller, sensor and PWM generator of the MPPT circuit from 0.36mW [50] to 135$\mu$W when operating in low duty cycle (low power) mode. The end-to-end conversion efficiency is 59% (i.e. 100%-(0.032mW+0.135mW)/0.4mW) from 0.4mW input solar power. This is considered as the state of the art in the sub-1mW MPPT designs.

The main drawbacks of this MPPT method are: 1) although it reduces the power consumption of the logic circuits, the 0.135mW power consumption is still considerable for sub-mW MPPT. 2) In this work, in order to acquire the open circuit voltage of the solar cell and thermoelectric generator, light sensor and temperature sensor are used to generate the light/temperature data. The data is then processed by the micro-controller and compared to the pre-stored look up table based on the measurement of the selected type of solar cell and thermoelectric generator. An algorithm

has to be created to adjust the PWM for each type of solar cell in order to response to the reference voltage. 3) Its very high system cost and complexity. The utilization of an additional 16-bit micro-controller (TI MSP430F2274 chip costs 14 Euro as of July 2013 which is even more sophisticated than the WSN micro-controller) in order to control a maximum power point tracker has only been seen in kW/MW level solar power plant applications. Together with the PWM generator, they significantly increase the total cost of the system. The needs to program and modify the micro-controller power management code for different applications makes this method much more complicated. The necessity of utilizing a 16-bit micro-controller is questionable when the analog comparator logic can achieve the same functionality. 4) Although not clarified in the paper, it also potentially poses a self-start issue for the power supply control logics, i.e. during the initial zero-power cold start phase, there is no power supply to start up the MSP430F2274 micro-controller which operates the MPPT converter. External battery voltage supply may be required to start up the MPPT system.

In this thesis, methods are proposed to investigate the possibility of avoiding the use of micro-controller for MPPT, whilst still be able to achieve MPPT and self-starting.

#### 2.3.1.1 Indoor Light Energy Harvesting Summary Table

The aforementioned works represent the developments of indoor solar MPPT circuits. This literature review selected examples of the energy harvester powered WSN systems and analysed their main design factors. The detailed review and comments are shown in the following table.

| Work, Year | Energy Source | PV-Cell Size & Targeted Power (Norm.) | Energy Storage & Lifetime | EH System Architecture | MPPT Ctrl, Converter Type, &Efficiency | MPPT Sampling /Reference | Power Management Controller | Output DC/DC Converter | Cold Start | Stable Power Supply | Sensor Node, Applications &Conditions | Design Goal & Comments |
|---|---|---|---|---|---|---|---|---|---|---|---|---|
| AmbiMax Park & Chou, 2006 | Solar & Wind | 95*63mm$^2$, 400mW @ direct sunlight | supercap 2*22F 1*Li-polymer Recharge 200mAh, Medium | EH-MPPT-Cap-Batt-WSN | FVOC, Boost, n/a | Voltage, Photodiode | Analog Comparator MPPT | Battery charger | No | Stable, Supercap & Battery Powered | Eco Node, Generic light Monitoring, Outdoor | Simplified analog MPPT w/o ADC, I/O & software |
| Sunflower, Stanley-Marbell & Marculscu 2007 | Solar | 4*Miniature PIN Photodiode (Approx. 0.5cm$^2$ each) | Supercap 0.2F, Long | EH-PM-Cap-PR-WSN | Not Used | Not Used | Fixed Duty Cycle Boost Converter Charging from Photodiode to Supercap | Boost/ LDO Due Channel Regulator 1.8V/2.7V | n/a | Stable, supercap powered | Sunflower, Acoustic monitoring with microphones, Outdoor | Miniature device, Long lifetime |
| Everlast Simjee & Chou, 2006 & 2008 | Solar | 95*58mm$^2$, 450mW @ direct sunlight | Supercap 100F, Long | EH-MPPT-Cap-PR-WSN | Hill-Climbing, Buck, Approx. 85%@50mW Approx. 60%@10mW | Current Sensor, disconnect &Sampled PV cell Voc, Voltage divider | Shared MCU for I-V tracer based on pre-measured I-V curve stored in on-board EEPROM | Linear 3.3V Step-down 2.3V | No | Stable, supercap powered w/ 3.3V for sensors, 2.3V for MCU &RF | Everlast, Light, Vibration Monitoring, Outdoor | Long lifetime, accurate and high efficiency MPPT |
| Twin-Star Zhu et al., 2009 | Solar | 1 Large Main PV Cell, 1 Small Boot Cell, n/a | Supercap n/a, Long | EH-Cap-PR-WSN | Not Used | Not Used | Analog Comparator Based Schmitt Trigger | Switching regulator (type not specified) | Yes, secondary PV cell with Schmitt trigger controlled regulator enable/shut-down pins | Stable, supercap powered 3.0V | Twin-Star, Power Characterization for WSN and leakage current monitoring, Outdoor | High reliable and repeatable cold start capability, Long lifetime, autonomous operation |
| Brunelli et al., 2009 | Solar | 112cm$^2$, 50mW @direct sunlight | Supercap, 50F, Long | EH-MPPT-Cap-PR-WSN | FVOC, Buck, Approx. 81%@50mW | Voltage Real time sampling, Pilot PV Cell as reference source | Analog Comparator MPPT | Switching regulator (type not specified) | n/a | Stable, Supercap powered | Tmotesky, Generic Monitoring, Outdoor Only | Long lifetime, Low costs, high efficiency MPPT w/o complex control mechanism |

Figure 2.12: Light Energy Harvesting Powered WSN Technologies Summary Table 1

| Work, Year | Energy Source | PV-Cell Size & Targeted Power (Norm.) | Energy Storage & Lifetime | EH System Architecture | MPPT Ctrl, Converter Type, &Efficiency | MPPT Sampling /Reference | Power Management Controller | Output DC/DC Converter | Cold Start | Stable Power Supply | Sensor Node, Applications &Conditions | Design Goal & Comments |
|---|---|---|---|---|---|---|---|---|---|---|---|---|
| Brunelli & Benini, 2009 Improved | Solar | 3cm$^2$, 600uW @indoor light | Supercap, 2*1.7F, Long | EH-Cap-PR-WSN | Voltage Window Semi-MPPT | Voltage Real time sampling, Comparator internal reference | Analog Comparator with wake-up/capacitor recovery trigger | Not Used | Natural, No Switching Regulator used | Unstable, input power dependent, w/ preset voltage range | µsolar mote, Low power communication applications, Indoor/Outdoor | Semi-MPPT design to minimize the power consumption while maintain charging voltage within MPP window. Simple and low power design |
| DuraCap Chen & Chou, 2010 | Solar | Various, 1200mW @direct sunlight | 2*supercap 200F each 1*supercap 50F (cold-boot), Long | EH-MPPT-Cap/Batt-PR-WSN | I-V Swipe, Buck, n/a | Shunt Resistor Current Sensor | Dedicated MCU for PFM Ctrl | 4* Parallel Converters 3.3V Buck & Boost 4.2V Buck & Boost | Yes, 50F booting capacitor, Programmed Priority Charging | Stable, Selectable, 3.3V/4.2V, Supercap Powered | DuraCap, n/a, Outdoor Direct Sunlight Only | Long lifetime, Self Calibrating MPPT, Fast cold booting |
| Tan & Panda, Wind 2011 | Wind | Not Used | Supercap, 1.5F, Long | EH-REC-MPPT-Cap-PR-WSN | Perturb & Observe, Boost Converter, 84% @9.4mW | Shunt Resistor Current Sensing & Voltage | Dedicated MCU for PWM Ctrl, PWM Generator for higher frequency PWM | Buck Converter 3V | n/a | Stable, supercap powered, 3.0V buck regulated | TI eZ430 mote, Generic Monitoring Applications, Wind powered | Resistor emulator based MPPT for wind energy harvester. Design concept can be adopted for low power PV cell energy harvesting with different perturb & observe ctrl |
| Tan & Panda, Hybrid 2011 | Solar & thermal | 55*30mm$^2$, Approx. 180uW @380Lux | Supercap 0.1F, Long | EH-MPPT-CAP-PR-WSN | Perturb & Observe, Boost Converter, 80~90% @180~480 uW | Shunt Resistor Current Sensing & Voltage | Dedicated MCU for PWM Ctrl, PWM Generator for higher frequency PWM | Buck Converter 2.8V | n/a | Stable, supercap powered, 2.8V buck regulated | TI CC2500 mote, Generic Monitoring Applications, Indoor/ Outdoor | Ultra-low power design for indoor PV cell applications, dedicated MCU control PWM in low duty cycle, low power mode. |

Figure 2.13: Light Energy Harvesting Powered WSN Technologies Summary Table 2

### 2.3.2 Low Voltage Converter for Thermoelectric EH

In the targeted WSN deployment scenario, the indoor light is used as the main source of energy. However, monitoring locations such as mechanical rooms which often contains the boiler, heat exchange unit, water pumps and air handling units is important for the building management applications. The mechanical room is typically dark with limited lighting for most of the time, the light intensity may be insufficient to power the WSN. In these cases, the temperature difference can be potentially high enough to be used as a source of energy for powering a WSN system. An example of such application is shown in Figure 2.14. This air compressor is a part of a vapor-compression refrigeration system used by CGI group, the largest commercial refrigeration facility in Ireland [52]. A set of temperature sensors and data acquisition system have been deployed in the refrigeration facility to study the available wasted heat for energy harvesting. The surface temperatures of the air compressor unit are measured. The hot air outlet shows a temperature of 69$^o$C, whilst the maximum surface temperature of the air compressor is measured at 62$^o$C. Concluded from both the measured results and literature, wasted heat is an important source of energy harvesting and available in many buildings and other industry environment. The typical temperature in TEG applications is between 50$^o$C and 80$^o$C [53], [54].

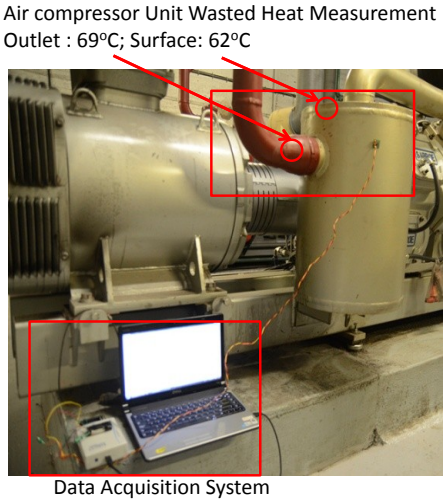



Figure 2.14: Measured Wasted Heat on the Surface of An Air Compressor Unit

The process of thermal energy to electrical energy conversion is called thermoelectric energy harvesting. In this survey, the background, previous work and design considerations of thermoelectric energy harvesting are reviewed.

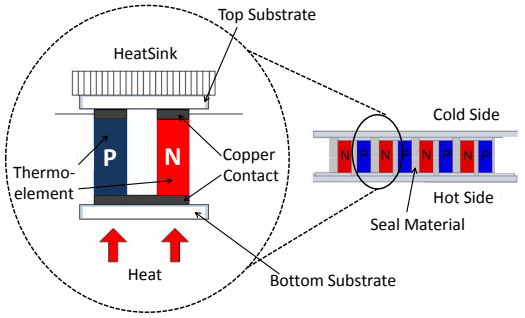



Figure 2.15: Bulk Material based Thermoelectric Generator

The basic structure of these Thermo-Electric Generators (TEGs) is presented in the Figure 2.15. A typical thermoelectric module consists of P-type and N-type semiconductor thermo-element and heat transfer substrates. When a temperature difference exists on the P-N junctions, thermoelectric electromotive force is created in the thermo-element, hence a voltage difference on the cold side of P/N thermo-element as shown in Figure 2.15. Since single P/N thermo-element pair only generates limited voltage output, most practical TEGs contain multiple series-connected P/N thermo-elements in order to generate high voltage.

Typical TEGs such as aforementioned Marlow industries EHA-PA1AN1 generator [28] (20mm×20mm module) generally deliver ultra-low voltage outputs in the range of 100-500 mV when the device is placed on $40 - 60^{o}$C surface (cooled by passive heatsink on the other side) as shown in Chapter 1 Figure 1.6.

In terms of power management circuit design, for the standard CMOS technologies, this voltage is lower than the typical threshold voltage ($V_{TH}$) of a MOSFET, and many design and efficiency issues would arise in power conversion in this deep subthreshold regions. The power management circuit is required to cold start batteryless electronic systems, and to produce much higher output voltages, suitable for operation of standard CMOS technologies and circuits[55].

Considering the low output voltage generally observed in a TEG for BEM applications, a key aspect of power management for TEG is its requirements of DC-DC converter with ultra-low input voltage capability. A literature review specifically focused on this topic will be given in this section.

#### 2.3.2.1 Charge Pump Low Voltage Converters

Charge pump is a common architecture for boost topology dc-dc converter. Charge pumps use switches to control the connection of voltages to the capacitor. As shown in Figure 2.16, a two-stage cycle can be used to generate a higher pulsed voltage from a lower-voltage supply. In the first stage of the cycle, a capacitor is connected across the supply, charging it to 5V voltage. In the second stage of the cycle, the circuit is reconfigured so that the capacitor is in series with the supply to the load. In theory, this provides an output voltage doubles the input voltage.

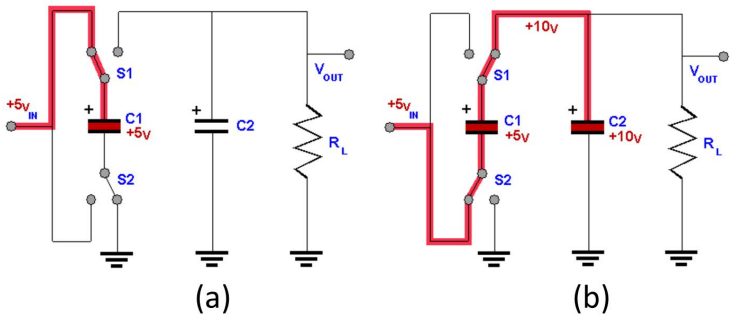



Figure 2.16: Operation of Charge Pump Circuit

The current state of the art in terms of high efficiency low voltage charge pump is [56] by Chen et.al. (see Figure 2.17). This design adopts a 10-stage start-up/operation "dual-mode" charge pump architecture. In the start-up mode, the start-up oscillator drives the clock selector with 1MHz frequency to operate the Dickson charge pump (using diode switch element). The voltage builds up in output capacitor $C_{OUT}$ until it reaches 0.3V. The voltage detector switch on the operation oscillator. The voltage on $C_{OUT}$ continuously charges up to 0.77V then the start-up charge pump is switched off. The operation charge pump uses CMOS switch as the switch element and operates with 20MHz clock frequency. This design shows a

38.8% conversion efficiency when the input voltage is 0.12V.

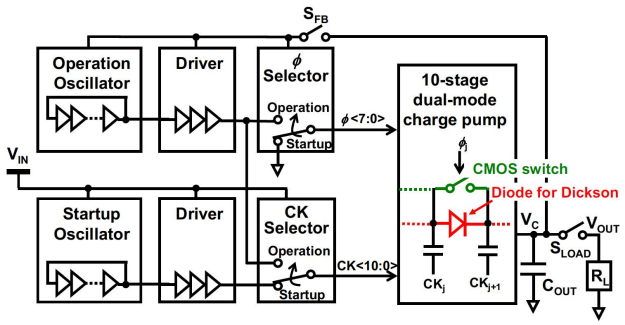



Figure 2.17: 10-stage Startup/Operation Dual-mode Low Voltage Charge Pump with 0.12V Minimum Input Voltage [56]

Commercial off-the-shelf low voltage charge pumps such as S-882Z series charge pump from Seiko Instruments are available [57]. The charge pump differs from conventional ones since it utilizes fully depleted Silicon on Insulator (SOI) technology to enable ultra-low voltage operation.

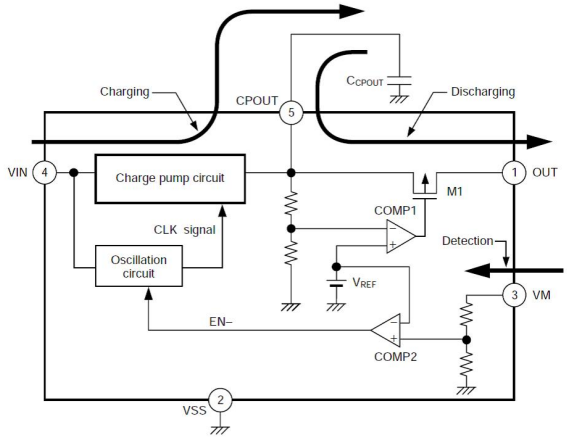



Figure 2.18: Seiko Instruments S-882Z Charge Pump External ($V_{CC}$) Capacitor Charge/Discharge Process

The S-882Z is based on a charge pump and an oscillator circuit and is capable to start conversion from input voltage of 0.15V with an external startup capacitor and deliver from 1.8 to 2.4V to the output. When a low voltage input is connected to the converter, the oscillator circuit starts operation (5MHz), then the charge pump is activated and charge the start-up capacitor, $C_{CPOUT}$, until reaching the discharge voltage level (see the operation diagram in Figure 2.18). The peak efficiency is

measured at 29% when the input voltage is 0.3V.

Due to the increased on-resistance of the CMOS switch in sub-threshold region and low switching frequency (1.5V startup charge pump often operates with 35MHz-50MHz frequency) when operates in low voltage condition, this type of charge pump is inherently low in efficiency.

#### 2.3.2.2 Coupled Inductor Based Low Voltage Step-up Converter

Another type of architecture used for energy harvesting circuits is step-up converter based on cross-coupled inductors.

The current state of the art for <0.5V input voltage step-up converter based on coupled inductor is [58] in terms of conversion efficiency. The converter uses a boost topology (see Figure 2.19): transistor T1 is the low position transistor, D1 is the high position diode. It also includes a self-start up circuit (J1 is the start-up JFET transistor) and an oscillating circuit.

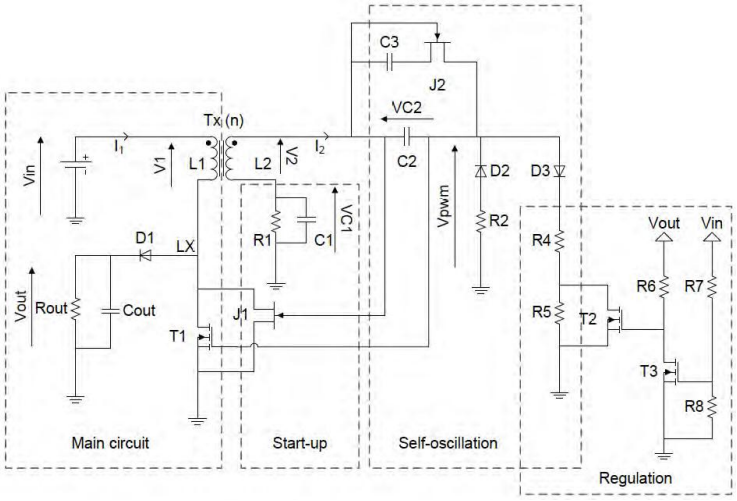



Figure 2.19: Coupled Inductors based Low Voltage Converter Design

The harvested power is 10mW under a minimum input voltage of 0.3V. A PCB prototype is realized with a measured efficiency of 74% and a maximum output voltage of about 2V depending on load conditions. For TEG energy harvester in BEM applications, the required output power is at 0.5-3mW level, which is significantly

less than 10mW. It is not clear whether this design can be used for thermoelectric power less than 5mW.

In commercial off-the-shelf ICs, LTC3108 [59] from Linear Technology (applications example shown in Figure 2.20) provides an ultra-low voltage (20mV) boost converter solution using high ratio transformer. The LTC3108 uses a normally-on MOSFET and a resonant oscillator scheme with a small external step-up transformer. This enables to boost input voltages as low as 20 mV using a 1:100 ratio transformer and provides multiple regulated output voltages for powering other circuits. The oscillator is coupled with an external charge pump capacitor, $C_2$, and a rectifier which act as a boost converter thus providing an output voltage from 2.35 to 5 V and high efficiency.

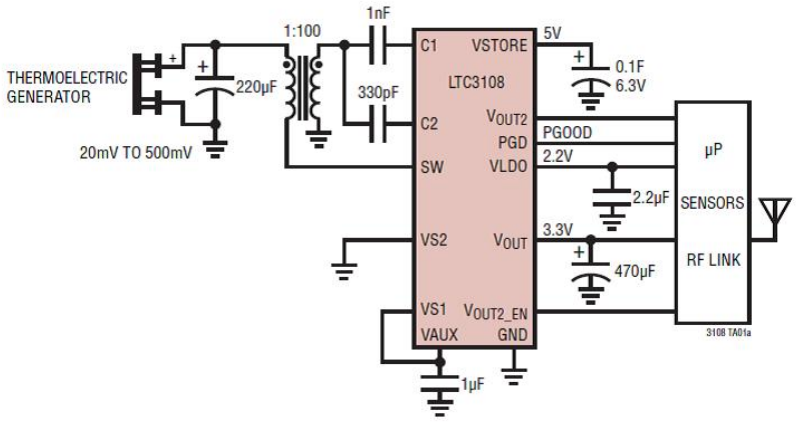



Figure 2.20: Linear Technologies LTC3108/3109 Ultra-low Voltage Boost Converter with 1:100 Ratio Transformer [59]

One generic issue related to coupled inductor based boost converter in terms of conversion efficiency is illustrated in Figure 2.21. This figure compares the conversion efficiency of the LTC3108 converter to the aforementioned Seiko Instruments S-882Z charge pump. Although the peak efficiency of LTC3108 is 40% at 70mV, the efficiency decreases to less than 15% when the input voltage is >100mV or <45mV.

This very narrow peak efficiency voltage "zone" is due to the large and fixed (1:100) transformer ratio. In scenarios which TEG operates in wide range of temperatures, the TEG will also have a wide voltage range. In practice, this issue leads to lower

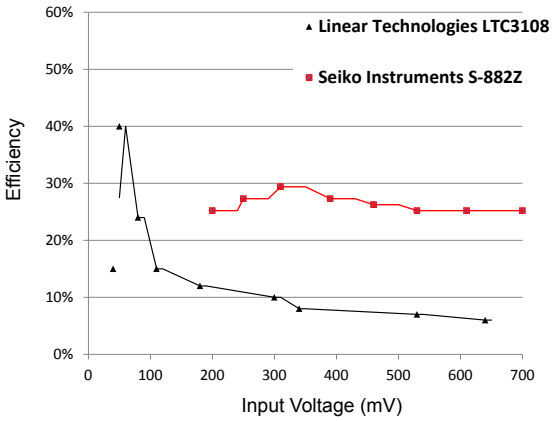



Figure 2.21: Datasheet Efficiency Comparison between two COTS low voltage converters: Linear Technologies LTC3108 v.s. Seiko Instruments S-882Z[59]

average conversion efficiency than its peak conversion efficiency. For the aforementioned charge pump architecture, the conversion efficiency is much more "flat" as shown in Figure 2.21 Seiko S-882Z charge pump. A trade-off exists between utilization of coupled inductor based boost converter and the low voltage charge pump in terms of peak conversion efficiency and average conversion efficiency. In Chapter 4 of this thesis, this trade-off and suitable solution will be addressed in details.

### 2.3.3 Energy Storage Unit

Energy storage units (ESUs) are often used in energy harvesting systems in order to temporarily store the harvested energy. Four types of ESUs have been used for energy harvesting applications: 1) electrical double layer capacitor (also known as super-capacitor or supercap), 2) thin film solid state battery (thin film battery or TFB), 3) conventional rechargeable battery and 4) Tadiran battery.

The lifetime is one of the main considerations when choosing an ESU. As shown in Table 1.2, the average lifetime of COTS rechargeable li-ion battery is limited to $<$7 years. The capacity of the conventional rechargeable battery is also subjected to high level of degradations over time. A test on a commonly-used $LiCoO_2$ cell showed that, over one year, a fully charged cell, kept at 25$^o$C, permanently lost 20% of total capacity [60]. 5 years fully charged cell kept at same temperature has accumulated

capacity loss over 70% [60].

25 years lifetime rechargeable Tadiran battery with carbon based anode, multi metal oxides cathode, organic electrolyte [61], [62] designed for wireless sensor applications has been introduced in 2012 [63]. The rechargeable batteries use a built-in super-capacitor to store the energy needed for burst current consumption of two-way communications.

In addition to the cost issue (approx. 30 USD for one 1000mAh rechargeable Tadiran cell as of August 2013), the main application concern for this type of battery is its complicated charge/discharge circuits which in turn makes its suitableness for low power applications questionable. Regulated voltage and current are required to charge the battery, both over-voltage and under-voltage protection circuits and over-temperature battery management are needed. For applications such as indoor light energy harvesting, 1) it is unclear, based on the available information, whether the cell can be charged from sub-1mW power, and 2) the power loss in the battery power management circuits may be higher than the sub-1mW harvested power.

#### 2.3.3.1 Super-capacitors

Super-capacitor are electrochemical based capacitors that demonstrate several orders of magnitude higher capacitance than electrolytic capacitors. They also obtain high power density, long lifetime, high number of charge cycles and less than 1Ω equivalent series resistance (ESR). A super-capacitor features a structure that can be viewed as electrolyte enhanced non-reactive porous plates separated by a thin dielectric layer as shown in Figure 2.22.

The two plates are the same porous carbon-based electrode material separated by a thin layer of separator (on the order of a few nanometres). With one side of the separator filled with electrolyte in addition to the capacitor electrode layer, the electrochemical properties form the so-called “electrical double layers” [64].

The combination of large surface area, A, and small charge separation, d, gives the super-capacitor higher capacitance relative to conventional capacitors. Although

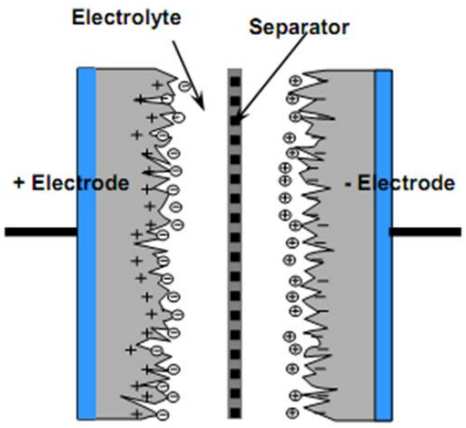



Figure 2.22: Electrochemical Double Layer Capacitor Charge Separations [30]

the super-capacitor features a structure almost identical to the battery, no chemical reactions occur in the super-capacitor charge/discharge process. Thus the energy storage mechanism of super-capacitor is purely electrostatic and completely different from conventional battery [65].

Due to the absence of chemical reactions, in theory, the electrostatic charge/discharge should operate indefinitely in super-capacitors. The commercial off-the-shelf super-capacitors data sheets often state that their charge cycles are higher than 1 million times. The claimed lifetime for COTS super-capacitors is between 10-20 years in room temperature condition [66].

The capacitance of a super-capacitor ranges from 1mF to several hundred Farads. For WSN applications, super-capacitors with capacitance in the 0.1-10 Farads range have been proven to be most suitable [67]. Based on this consideration, commercially available, high energy density super-capacitor models including Maxwell UltraCap [68], AVX BestCap [66], CapXX H series [69] are acquired and tested.

The energy density of state-of-the-art COTS (high energy density model) super-capacitor is within the 5-6Wh/kg range (10-13J/cm$^3$). The difference between the aforementioned three series of super-capacitors are less than 20% in terms of Wh/kg energy density. All tested COTS super-capacitors have DC equivalent series resistance (ESR) less than 1$\Omega$. Several super-capacitors such as CapXX H-270/290

demonstrate ESR lower than 100mΩ. The unit cost of COTS super-capacitor is between 3-10 US dollars for order quantity larger than 1000 units.

Recent research concerning graphene based electrodes demonstrated a specific energy density of 86Wh/kg in room temperature, and 136Wh/kg energy density at $80^oC$ [70, 71]. The exhibited energy density of 80-130 Wh/kg of super-capacitors in lab condition is approaching the energy density in COTS lithium-ion battery (100-250 Wh/kg). As of second quarter of 2013, graphene based super-capacitors have not entered the commercial market.

#### 2.3.3.2 Thin Film Solid State Battery

All layers of the Thin Film Solid State Battery (TFB) including: current collector, cathode, electrolyte and anode are deposited successively, from bottom to top, using chemical vapor deposition (CVD) process. The thickness of the layers range from several hundred nanometres to several microns dependent on the battery capacity requirement and CVD implementation [72]. The CVD processed thin film battery is only 10-15$\mu$m thick without packaging. The most common TFB structure is illustrated in the Figure 2.23 .

Several companies such as Infinite power solution (IPS) and Cymbet have made TFBs commercially available since 2008. Commercial off the shelf TFBs are typically 0.1-0.5mm in thickness, 1-20 $cm^2$ in footprint, and 0.1-5mAh in capacity [32].

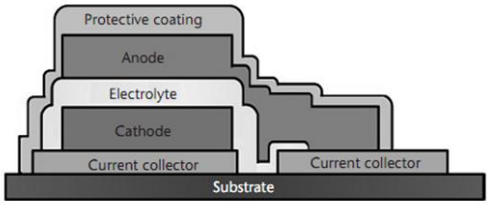



Figure 2.23: Thin Film Micro Energy Cell, TFB Structure [73]

The assembled 12.5$cm^2\times$ 200$\mu$m IPS MEC series TFB have a capacity up to 2.2mAh [74]. The equivalent capacity (35 Joules) is similar to the capacity of a 10F 2.5V super-capacitor (capacity: 32 Joules, Diameter $\times$ Height: 10.5mm $\times$ 30.5mm)

[75]. The energy density of IPS TFB is measured with 0.1mW load power. The result shows that it is one order of magnitude higher than the energy density of super-capacitor at 80Wh/kg or 145J/cm$^3$.

Due to the CVD process, the electrolyte film is more stable than the conventional batteries, the number of charge cycles the thin film battery can endure is in the range of 10,000 to 100,000 instead of less than 1000 cycles as for the Lithium-ion rechargeable batteries [32]. The thin film battery, such as IPS TFB, has a 10 years minimal lifetime [74], due to the more stable structure. However, the existing thin film battery has a considerable disadvantage of high equivalent series resistance (ESR) [76]. The 10-50Ω ESR may limit the device to low current applications (<20mA), since higher current leads to instant voltage drop over 1 volt. ESR also leads to the conduction loss especially during the active (high current) mode of WSN operation. For example, assuming in active mode a WSN mote consumes 30mA current with a 3.3V supply voltage (100mW power consumption). The conduction loss due to the 50Ω TFB ESR can be calculated as $P=I^2\times R=(0.03A)^2\times 50\Omega=45mW$.

Table 2.3 compares the state of the art super-capacitors, thin film batteries and rechargeable batteries for energy harvesting applications. They show distinctive characteristics in several perspectives. 1)Super-capacitor shows longer lifetime than both conventional rechargeable/non-rechargeable batteries. The lifetime of a super-capacitor (operating in room temperature) is between 10 to 20 years, whilst the rechargeable battery is limited to 5-7 years lifetime when operating in the same condition. 2)Charge cycles of both super-capacitor and TFB are several orders of magnitude higher than the rechargeable batteries. 3) TFB has internal resistance at 50Ω whilst the super-capacitor only has less than 1Ω internal resistance. 4) Leakage current of super-capacitor is higher than the TFB by more than 10 times.

For BEM applications, the design target of the ESU are 1) enough capacity to operate WSN mote for more than 48 hours (weekend). 2) low leakage current: less than 20$\mu$A (less than sleep mode current consumption of WSN mote). 3) low cost: ESU cost target is set to \$15 (lower than the cost of li-ion rechargeable battery).

| | Maxwell UltraCap P270 SuperCap [77] | Cap-xx H206 SuperCap [78] | Infinite Power Solutions MEC-202 TFB [74] | Energizer CA-5L Battery[79] | Tadiran TLI battery [63] |
|---|---|---|---|---|---|
| Type | SuperCap | SuperCap | TFB | Li-ion Rechargeable | Li-ion Rechargeable |
| Charge cycles | $> 500,000$ | $> 1million$ | $> 100,000$ | $< 1,000$ | $5,000$ |
| Lifetime | $> 10$ years | $> 15$ years | $> 10$ years | 5 years | $> 25$ years |
| Voltage Rating | 2.5V | 5.5V | 4.1V | 3.7V | 3.6V |
| Capacity | 10.3J (3.3F) | 9.1J (0.6F) | 36J (2.2mAh) | 15000J (1120mAh) | 15500J (1200mAh) |
| Form Factor | Dia:10mm L:21.5mm | W:39mm L:14mm H:2.4mm | W:50mm L:25mm H:0.2mm | W:45mm L:32mm H:8.1mm | Dia:14.5mm L:50.1mm |
| Energy Density | $6.1J/cm^3$ | $6.9J/cm^3$ | $145J/cm^3$ | $1300J/cm^3$ | $1900J/cm^3$ |
| Self Discharge | Max. $30\mu A$ | Max. $10\mu A$ | Max. $1\mu A$ | $< 1\%$ per month | $< 0.1\%$ per month |
| ESR | $290m\Omega$ | $70m\Omega$ | 50-75Ω | 50-200mΩ | 250mΩ |
| Operation Temperature | $-20 \sim 70^oC$ | $-40 \sim 85^oC$ | $-20 \sim 70^oC$ | $-20 \sim 70^oC$ | $-40 \sim 85^oC$ |
| Unit Cost | $2.5 | $12 | $5 | $15 | $50 |
| Comment | Low cost SOTA SuperCap | Low leakage current SuperCap | SOTA thin film battery | Low cost rechargeable battery | SOTA long lifetime battery |

Table 2.3: Comparisons of State of the art (SOTA) Energy Storage Units

#### 2.3.3.3 ESU Power Management Circuits

Based on the analysis of ESUs, the design target of energy storage for energy harvesting is to fully utilize the advantage of super-capacitor from the lifetime and charge cycle perspectives, and to minimize the negative impact of leakage current and small capacity.

The output voltage regulation is necessary for the ESU to resolve the voltage

matching issue between ESU and the WSN's required voltage. It is especially important when the capacitive ESU is used, since the voltage fluctuates depending on its state of charge. In previous literatures, the most common method of the voltage regulation is to use a buck converter or low dropout regulator (LDO) [80, 81]. However, LDO has inherent low efficiency and the efficiency is even worse when applied with high voltage conversion ratio [82]. In addition, the buck converter and LDO voltage regulation cannot operate when the ESU voltage is lower than WSN threshold voltage.

Buck-boost converters are suitable for this type of requirements due to the wider input voltage range. The main parameters for ESU output voltage regulator applications are: 1) Low minimal operation voltage. The lower operation threshold voltage allows the output regulator to extract more energy from the ESU. 2) High efficiency. Instead of the peak efficiency which is primarily criteria for most applications, the average conversion efficiency over the entire input voltage range is more important in this case. This is mainly due to the fact that super-capacitors do not have a constant voltage.

Study on the state-of-the-art in the area of low input voltage DC/DC converters show that Texas Instruments TPS61200 series, TPS61220 series[83] and OnSemi NCP1400 DC/DC converters[84] are most suitable for this voltage and power scale. These boost and buck-boost switching regulators were acquired and tested in this work.

| Manuf. | Prod. | $V_{in}$ | $V_{out}$ | $I_{out}$ (max) | Peak $\eta$(%) | Avg. $\eta$(%) |
|---|---|---|---|---|---|---|
| TI | TPS61201 | 0.3-5.5V | 3.3V | 70mA | 90% | 40% |
| TI | TPS61220 | 0.5-5.5V | 3.3V | 70mA | 94% | 75% |
| OnSemi | NCP1400 | 0.2-3.3V | 3.3V | 100mA | 92% | 50% |

Table 2.4: DC/DC Converters and Characterizations

The measured DC-DC converter performances are shown in Table 2.4. The average conversion efficiency is calculated based on efficiency measurements at different voltages when the converter is connected to a simulated WSN load. In this thesis, commercially available output regulation circuits will be used. Converter model as

part of the energy flow model will be built to predict the conversion efficiency.

The utilization of inductor based switching regulator as the output voltage regulator leads to an cold start issue. When the input pin and inductor pin of the switching regulator is directly connected to the super-capacitor, once the super-capacitor reaches its minimal start up voltage, the inductor in-rush current is high enough to pull-down the super-capacitor voltage. In this way, the super-capacitor enters an oscillation below its minimal start voltage and cannot successful start up.

Zhu et.al. [85] proposed a cold start circuit for piezoelectric energy harvester. The schematics of the cold start circuit are shown in Figure 2.24.

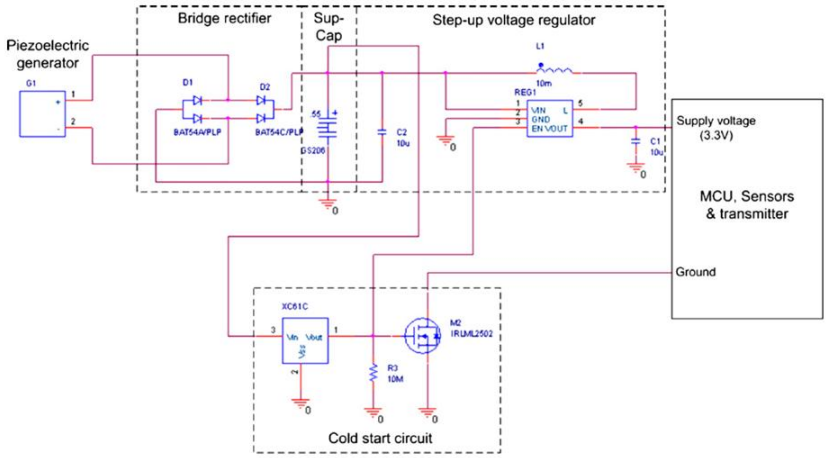



Figure 2.24: Cold Start Circuit for piezoelectric energy harvester [85]

A Torex XC61C voltage detector is used to control the "Enable" pin of the output voltage regulator. A low position switch M2 is used to enable the WSN mote when the voltage of the super-capacitor surpasses the pre-set threshold. This cold start circuit only consumes 1.4$\mu$W power.

However, directly utilization of this cold start method in the photovoltaic and thermoelectric energy harvesting is not possible. The input power management of the piezoelectric generator is a bridge rectifier with only passive components (diode) as shown in Figure 2.24. This self start circuit [85] is only suitable for the output regulation.

However, photovoltaic and thermoelectric energy harvester have switching regulators

in the input power management circuits. As opposed to solution in [85] which only requires output self start circuit, cold start circuits are also needed for the input stage.

### 2.3.4 System Simulation of Energy Harvesting Systems

Energy harvesting system simulation can be used to predict the power management circuits conversion efficiency. By modifying the components value, e.g. internal resistance, input/output capacitor, inductance etc., the conversion efficiency can be optimized before the prototype is manufactured. SPICE simulation of the power management circuit are presented in several energy harvesting systems [44, 50]. High accuracy can be obtained from the transient SPICE model [86]. However, the SPICE simulation needs a complete SPICE model library for every component in the system. In practice, SPICE models are not available for many components. It is also difficult to operate long term (longer than 1 week) SPICE model due to the limitation of the simulation tool, i.e. it requires a high simulation frequency (simulation time step in millisecond or microsecond). This high sampling rate leads to large amount of data and makes it difficult to simulate over a long period of time, e.g. 1 week long simulation with 1msec sampling rate will generate more than 600 megabyte of data.

In [87] Janek et.al. introduced the concept of energy flow model for a solar powered active RFID tag. The model consists of five main building blocks: 1) solar cell model; 2) power management model (DC/DC converter model and charge/discharge control model); 3) super-capacitor model (SuperCap1 and SuperCap2 as shown in Figure 2.25); 4) battery model; 5) RFID tag power consumption model. The output of this model is state of charge.

This long term system level "energy flow" model is created using Matlab Simulink software. For each sub-model, its conversion efficiency is calculated based on measured results. It can predict the operation of the energy harvester, i.e. the state of charge (voltage level of the super-capacitor in this case). When certain component

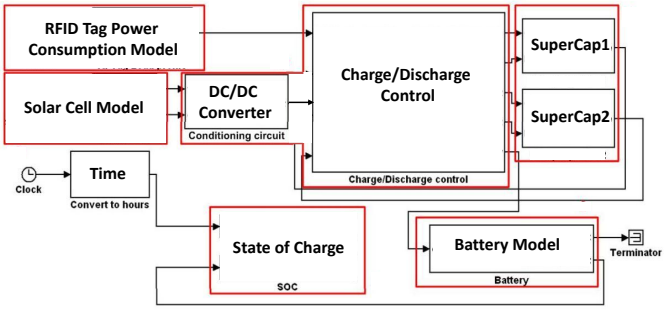



Figure 2.25: Simplified PV Energy Harvesting Simulation Model for Active RFID Applications [87]

is replaced by new part, e.g. solar cell, it only needs to make a change on the power and efficiency data.

However, this simulation lacks of the detailed understanding of each subsystem. The solar cell model, DC/DC converter model and super-capacitor model are all based on measured result "look-up table". Another drawback of this simulation is it is overly simplified, e.g. the conversion efficiency of the DC/DC converter is only considered as a constant efficiency independent from the solar cell voltage and current. In addition, the near constant RFID tag power consumption profile is different from the WSN power consumption.

Although the intended application is for active RFID devices, the concept of this model can be used to simulate energy harvesting powered WSN with significant modifications. In chapter 5, energy model of wireless sensor networks and energy harvester is created in Matlab Simulink using similar method.

## 2.4 Conclusion

The following points are the main conclusions from the literature review.

1. Stage of Developments

The developments of photovoltaic and thermoelectric energy harvesting technologies are evolving at a very fast pace. Several prototypes are starting to show promise to provide long term and maintenance free power supply for wireless sensor networks.

However, it is clear that the area of energy harvester efficiency improvements from advanced power management, energy storage, system modelling, system holistic design and energy harvesting compatible protocols are not yet mature. The large and increasing amount of publications in recent years show energy harvesting is a hot research area and many opportunities exist to develop new energy harvesting solutions.

2. System Architecture Study

There is no established analysis on the optimal system architecture of the energy harvesters especially for low power energy harvesters. With a more suitable system architecture, many previous works can be significantly improved with the same subsystem circuit design and components. The holistic design concept is only investigated from a theoretical point of view. The actual implementation is not complete and cannot reflect the advantage of the design concept.

3. Energy Storage Unit and Related Power Regulation

Energy storage unit is a key component for energy harvesting. The system lifetime of energy harvester powered WSN is mainly determined by energy storage unit. In addition, the characteristics of ESU have direct impact on the energy harvester performance, i.e. energy conversion efficiency and maximum output power. However, in the area of energy storage unit, detailed study of ESU characteristics for WSN applications has not been reported previously. Several considerations concerning the equivalent series resistance (ESR), leakage current and charge efficiency have only been addressed for high power applications.

4. Power Management for Energy Harvesting System

Power management is an essential component of energy harvesting systems. The system efficiency of the energy harvester highly relies on the functionalities and conversion efficiency of the power management subsystem. Although research on power management for large scale energy harvester system (>50mW) is well established, the power management of smaller scale energy harvester (1-10mW and sub-1mW) is not yet investigated in depth. A few publications exist in the area of sub-1mW

energy harvester power management. Although the new publications such as [50] show the promises to further increase the conversion efficiency by using optimized converter design, the power management system can still be significantly improved from control logic perspectives.

5. Power Level Mismatch

The obvious mismatch between the conventional power management/energy storage components and the novel low power energy harvester are becoming smaller over the last 5 years. However, even for the most recent power management circuit, the conversion efficiency and other functionalities are still well below the theoretical maxima.

6. System Level Model of Energy Harvester

Several types of modelling methods exist in energy harvesting studies. The more suitable one is the matlab based simulation, describing the energy transferred from component to component within energy harvester using efficiency look-up table (extracted from empirical measurements). This method can be used to simulate several weeks of performance of an energy harvester with a sampling interval of a few seconds. The second type of model is SPICE based model of each sub-system. This type of model presents detailed analysis on power loss using SPICE simulation. Although it can provide in-depth analysis on energy harvester, it is difficult to perform long term simulation due to the software limitation.

# Chapter 3

# Energy Storage Unit and Conditioning Circuits

## 3.1 Introduction

In this chapter, the energy storage unit and its conditioning circuits are investigated. This study begins with performance comparison between electrochemical double layer capacitor (super-capacitor or supercap) and thin film battery cell (TFB).

Different types of ESUs are characterized and compared from the aspects of energy density, power density, charge efficiency, leakage current and equivalent series resistance (ESR). Previous work in this area mainly focused on the energy density. The importance of other parameters are less addressed. In this work, the ESR, leakage current and charge efficiency are carefully studied.

A new Matlab Simulink based ESU simulation model is then built based on these characterizations to analyze the charge condition of the stand alone ESU. The simulation results are then verified by realistic charge/discharge experiments with a PV cell energy harvesting module (EHM).

Several practical considerations derived from the characterization and simulation model are investigated in the later part of this chapter, including the large voltage drop due to high ESR, cold start issue when ESU is fully discharged, and slow charging speed.

A new self-start circuit is also proposed in this work to restart the energy harvester after the ESU is fully discharged. This implementation allows automatic system restart without maintenance effort. This functionality is very important for long term energy harvester deployment. This self-start circuit design uses a secondary solar cell/thermoelectric generator instead of secondary battery. In this way, the entire energy harvester is free of battery, and therefore the system lifetime is not constrained by the limited battery lifetime.

At the end of this chapter, a hybrid energy storage unit with super-capacitor and thin film battery (TFB) is also proposed in order to increase ESU capacity and reduce leakage current. The results of the hybrid ESU for indoor light EHM, tested under low indoor light intensity, are recorded and shown in the final sections. Consequently, the conclusion section summaries the ESU design considerations.

## 3.2 ESU Characterisations

The characteristics of these ESUs are of critical importance for energy storage design. Energy density is most common parameters used to define the performance of the ESU. It represents the static performance of the ESU. However, this parameter can only determine the theoretical maximum energy that can be stored in the ESU. The charge/discharge performance of the ESU cannot be estimated from these studies. More detailed characterization of ESU is conducted in this work. The super-capacitors used in these characterizations are the low cost Maxwell Ultra-Cap[77], low leakage Cap-XX [78] and low ESR AVX [75] super-capacitors which all have been reviewed in Chapter 2. The TFB characterized in this work is the infinite power solutions MEC-101/201 modules [74].

### 3.2.1 Equivalent Series Resistance

The first experiment conducted is concerning the Equivalent Series Resistance (ESR). The ESU equivalent circuit with ESR is shown in Figure 3.1.

In the literature review chapter, the power consumption pattern of the WSN mote was mentioned. The proposed WSN mote (Tyndall mote) consumes power in a duty cycling manner as shown in Chapter 2 Figure 2.3.

It shows that a relatively large current (20mA-30mA) is drawn during the active mode. When this current is drawn from an ESU with a high ESR it will result in a large voltage drop on the ESR of capacitor during active mode.

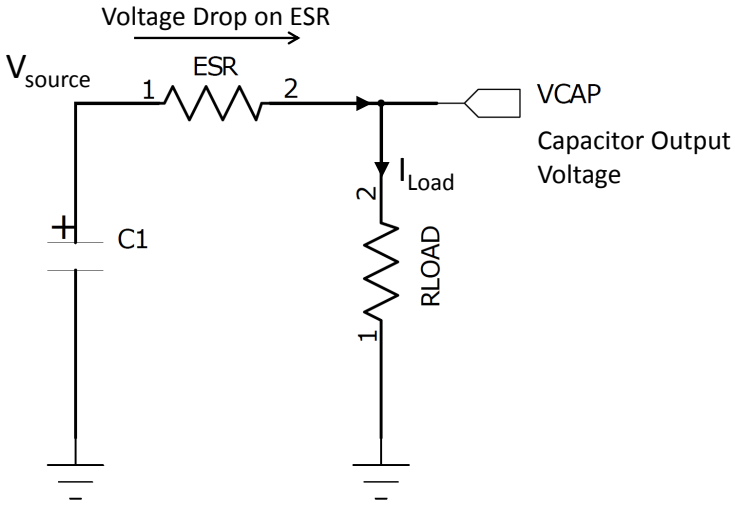



Figure 3.1: ESU ESR Equivalent Circuit

The WSN mote power supply minimal threshold voltage is 2.5V. For a fully charged 3.0V ESU, if the voltage drop across the ESR is larger than 0.5V (3.0V-2.5V), power failure will occur. When ESU is connected to an output regulator (boost or buck-boost converter), the power failure can be avoid since the threshold voltage is lower. However, the conduction power loss due the large ESR cannot be improved by integrating a regulator.

The impact of the high ESR on the TFB (IPS MEC-101 thin film battery with 50Ω ESR) output voltage is shown in Figure 3.2. This WSN mote operates with a 100 second duty cycle, the 26mA active mode current lasts less than 1 second. During the active mode, the 50Ω resistance generates a voltage drop approximately equal to 1.3V. The output voltage of the ESU is drawn down to 1.7-1.8V, lower than the required threshold voltage, 2.5V, of the WSN mote. Thus, the WSN mote is repeatedly disabled during the active mode.

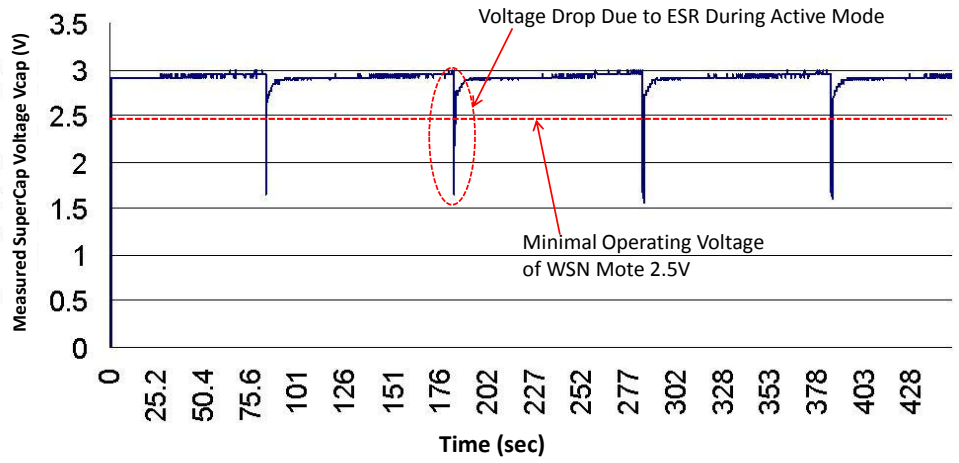



Figure 3.2: Measured Voltage Drop Due to ESR During (high current) Active Mode

To avoid this, it is essential to use low ESR super-capacitors (e.g. AVX Bestcap super-capacitors, which has an ESR of 50 mΩ) to supply the active mode current. So one alternative solution is to use a parallel connection of high energy density/large ESR TFB with lower energy density/lower ESR super-capacitor. For example, when the 10mF/50mΩ ESR AVX super-capacitors are connected with the TFB (50Ω ESR) in parallel, the voltage drop on ESU during WSN active mode can be kept less than 0.9mV. The voltage drop during active mode on the parallel connected super-capacitors are shown in Figure 3.3.

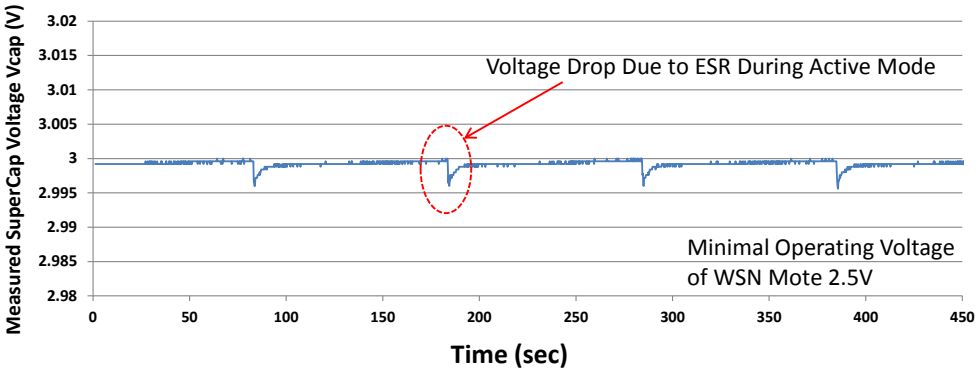



Figure 3.3: Measured Voltage Drop Due to Parallel Connected super-capacitors ESR During (high current) Active Mode

### 3.2.2 Leakage Current

Another consideration for the utilization of ESU is the leakage current. However, useful data on the leakage current is not always available in the manufacturer data sheets. In this work, the leakage characteristics of individual super-capacitors and TFB have been measured to identify this important parameter.

To determine the leakage current over 24 hours, self discharge tests were conducted on 4 different super-capacitors. All the super-capacitors were pre-charged to the same voltage level. They were then isolated and the voltage drop was monitored periodically by using a Pico Technologies ADC-11/12 data acquisition device. The data acquisition device has an output end impedance of 1MΩ during measurements and a 10MΩ impedance in idle mode, which effectively eliminated the current flow through the probe. The voltage drop is therefore only related to the self discharge of the super-capacitors. The 24 hours results of the self discharge tests are presented in Figure 3.4.

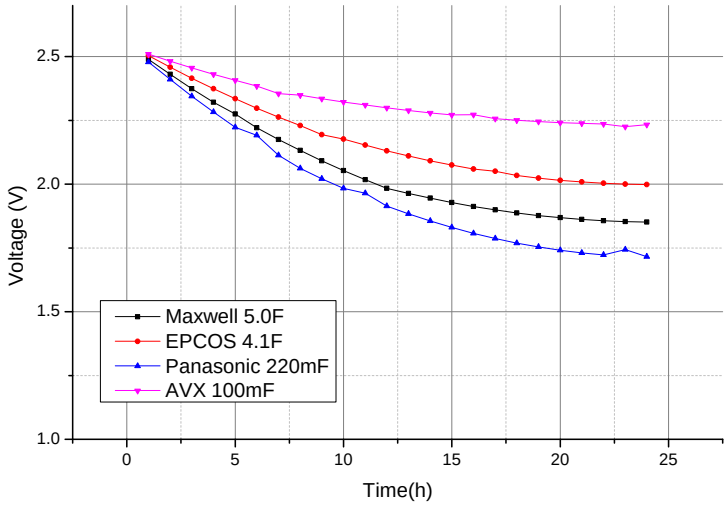



Figure 3.4: super-capacitors Discharge Test Over 24 Hours

These results confirm that the self discharge rates (SDR) of the super-capacitors are considerably higher than those of rechargeable batteries (5-10% monthly self discharge rate). The super-capacitors have SDR ranging from 45% to 15% every 24 hours. Therefore, without an intermittently available energy source every few days,

using the super-capacitors alone as a long term storage solution is not feasible. The 20-30$\mu$A leakage current of 5F super-capacitor is higher than the sleep mode current consumption of most WSN mote and is not negligible. The average self discharge current over the 24 hours period is calculated and shown in Table 3.1. The self discharge current stables after 24 hours, i.e. further voltage drop within the 24-48 hours is less than 5% of the voltage rating. Most energy loss due to leakage current ($> 90\%$) occurs during the first 24 hours based on the characterization results.

| Manufacturer | Capacitance Cs(F) | Average Leakage Current $I_{leak}(\mu A)$ | Leakage Correlation $\rho_{leak}$ $I_{leak}/C_s V(\mu A/V \cdot F)$ |
|---|---|---|---|
| Maxwell | 5.00 | 35.6 | 3.54 |
| EPCOS | 4.10 | 19.7 | 2.41 |
| Panasonic GoldCap | 0.22 | 2.02 | 4.50 |
| AVX Best-cap | 0.10 | 0.38 | 1.91 |
| IPS TFB | 4.70 | 0.48 | 0.02 |

Table 3.1: super-capacitor and TFB Average Leakage Current Over 24 Hours and Leakage Correlation $\rho_{leak}$

Based on these measurement results, a near linear correlation is found between super-capacitor leakage current $I_{leak}(t)$ and the product of $C_s \times V(t)$ at time t during the beginning of the discharge (first 24 hours) [1].

The analysis presented by Du et. al. in [90] also supports this finding. [90] suggests that the leakage current can be modeled as the discharge current of a parallel connected resistor on the ESU. During the beginning of the self discharge, the "leakage current resistor" is near constant and the leakage current is directly proportional to the capacitor voltage. In the later part of self discharge, due to the decreased ionic species concentration near carbon surface (explained in [89] in the last footnote), the leakage current resistance increases and leads to smaller leakage current.

The leakage correlation, $\rho_{leak}$, is between 1.91 to 4.5 in various capacitors. For

[1] The self discharge mechanism in the early phase of this experiment is dominated by Faradic redox reactions generated ionic species concentration near the carbon surfaces [88]. The self discharge due to this phenomenon significantly decreases after first 8-24 hours [89].

large super-capacitors (> 5F), the leakage current is of the same order as the current consumption of WSN modules. Clearly, the leakage characteristics of the super-capacitor have a significant impact on the operation time of the WSN mote.

Only a few previous studies have addressed the leakage issue of the super-capacitor. In a practical system design, how to minimize the leakage current is a critical issue that needs to be taken into consideration.

The same test was conducted on the TFB to estimate the self discharge rate. The testing results show little self-discharge over 24 hours test. The average self discharge current is less than 0.5$\mu$A in the first 24 hours. The super-capacitor with the same capacity has a leakage current 50 times higher.

### 3.2.3 Charge Efficiency Characterization

The charge efficiency is the ratio of successfully stored energy in ESU versus the total charging energy from the power source ($E_{stored}/E_{charge}$). This perspective of ESU has not been fully addressed in most of energy harvesting related work. However, charge efficiency determines the amount of energy required to charge a super-capacitor and has a direct impact on ESU performance and should not be ignored.

The charge efficiency can be attributed to three types of power loss [91]:

1. Electrochemical loss: a percentage of charge energy can not be stored in ESU but wasted in electrochemical side-reactions (in batteries and TFB) or insufficient electrochemical charge transfer (in super-capacitor), this type of power loss is referred as electrochemical loss [91]. This inherent loss only varies with temperature, number of cycles and lifetime of ESU [92].

2. Conduction loss: for an ideal capacitor with zero equivalent series resistance, the efficiency of charge acceptance is 100%. However, in a practical ESU with equivalent series resistance, R, irreversible dissipation of energy $I^2R$ loss takes place. Thus, the conduction efficiency is <100%.

3. Electromagnetic (charge-up) loss: this type of loss only occurs in capacitive energy storages. When capacitor is directly charged without current limiting circuit, high charge rate of current (and voltage) results in electromagnetic radiation [93]. A simple example of this electromagnetic loss is: 50% energy is lost when directly charging a capacitor from another identical capacitor [94]. However, this issue can be resolved with a transient RLC charging circuit (e.g. inductor based switching regulator). It has been proved that the radiated energy is negligible via a RLC charging circuit in [93]. In this work, the input power management circuit also functions as the RLC charging circuit to reduce the electromagnetic loss.

Both charging (input-end: power management module) and discharging (output-end: output voltage regulator) of the super-capacitor ESU will be regulated by inductor based switching regulator. This architecture with typical RLC charging/discharging circuits will only lead to negligible electromagnetic loss.

In energy harvesting applications, the ESU charge current is normally small. For example, with 1mA charge current at 1V and an internal resistance of 1Ω, the $I^2R$ loss is only 1$\mu$W, whilst the delivered energy is 1mW. The conduction loss is only 0.1% of the delivered energy. Thus, the charge efficiency is mainly dependent on the inherent electrochemical charge loss.

In this thesis, the electrochemical process and its impact on efficiency are beyond the scope of this research work. Instead of studying the physical principle of super-capacitors in detail, standard charge experiments were conducted to understand the charge efficiency behavior of super-capacitor.

To understand the charge efficiency, a Cap-XX 220mF 3.3V super-capacitor is tested with a Keithley 2400 source-meter. The source-meter is programmed to charge the super-capacitor from U = 0V with six constant currents, 0.3mA, 0.5mA, 0.6mA, 0.7mA, 0.75mA and 0.8mA, respectively. The charge time is set to 1000 seconds with a measurement resolution of 10 second per measurement. The measurement results of the standard charge experiment are shown in Figure 3.5. The

voltage of the super-capacitor is monitored to record the charge state.

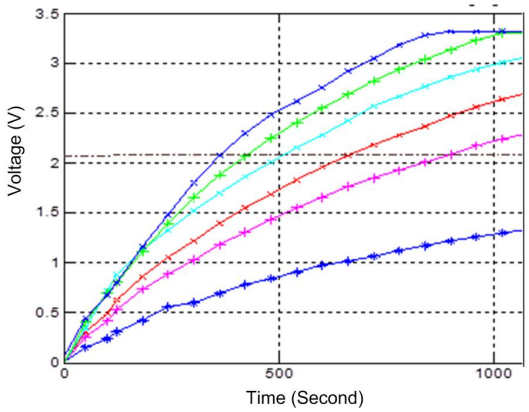



Figure 3.5: super-capacitor Charging Tests. From Bottom to Top: Charging Current Equals to 0.3mA, 0.5mA, 0.6mA, 0.7mA, 0.75mA and 0.8mA

The stored energy, E, in super-capacitor at a certain charge state can be calculated using Eq 3.1,

$$E = \frac{1}{2} \cdot CV_{soc}^2 \tag{3.1}$$

where C is the capacitance of super-capacitor, $V_{soc}$ is the voltage at certain state of charge. The voltage on the super-capacitor can be expressed in the basic equation of capacitor charging:

$$V_{soc} = \frac{1}{C} \cdot \int_0^t I_c(\tau) d\tau \tag{3.2}$$

where t is the charge time. $I_c$ is the charge current at time $\tau$. Since the source-meter provides a constant charging current I(t), the equation $I \cdot t = V \cdot C$ is valid in this case. It is necessary to consider the impact of leakage current during the charging phase. The "charged" energy is the sum of energy in the ESU, $E_{ESU}$, and the energy loss due to leakage current $E_{leak}$.

$$E_{char} \cdot \eta_{char} = E_{ESU} + E_{leak} \tag{3.3}$$

where $E_{char}$ is the total charge energy, $\eta_{char}$ is the charge efficiency. The leakage energy loss occurs during any stage of ESU (charging, discharging and idle). However, the charge efficiency loss only occurs during charge (transient) phase.

The equivalent charging current $I_{eqv}$ can be expressed as:

$$I_{eqv} = \frac{\sqrt{2 \cdot (E_{ESU} + E_{leak}) \cdot C}}{T_{char}} \tag{3.4}$$

where $T_{char}$ is the total charging time, which is the charge time for super-capacitor to reach 95% of voltage rating from zero. Cap-XX provided a super-capacitor SPICE model. The leakage current can be derived from this model. The SPICE model and the leakage current estimation are attached in Appendix 1. The equivalent charging current is then compared with the ideal charging current as shown in Figure 3.6.

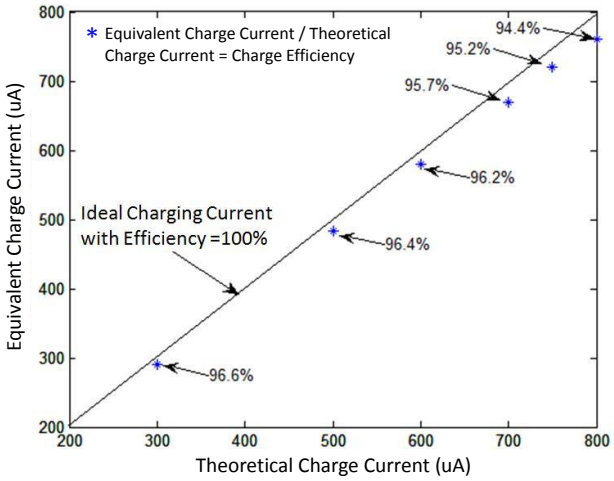



Figure 3.6: super-capacitor Charging Efficiency

The mathematical definition of charge efficiency is,

$$\eta_{char} = \frac{I_{eqv}}{I_{ideal}} \times 100\% \tag{3.5}$$

where $I_{eqv}$ is the equivalent charging current, $I_{ideal}$ is the theoretical charge current. In this illustration, the equivalent charging current is between 94% and 97% of the theoretical charging current. The charge efficiency loss is largely unreported in previous literature and apparently contributes to the total power loss.

A similar test was conducted on the Infinite Power Solution TFB with a wider charging current range. Due to the smaller voltage changes on the TFB voltage in different charge condition, a voltage amplifier circuit was built to monitor the

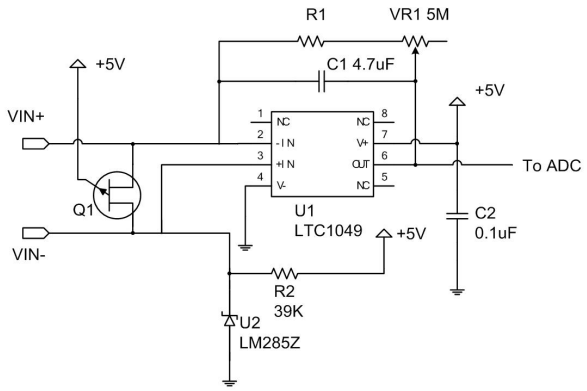



Figure 3.7: High Gain Amplifier Circuit for TFB Voltage Monitoring

changes on TFB voltage in order to achieve better accuracy. The monitoring circuit is shown in Figure 3.7.

The main rationale of the power loss during charging phase can be attributed to the conduction loss in ESR and the inherent electrochemical loss. The charge efficiency of TFB is illustrated in Figure 3.8. When compared with the super-capacitor, TFB has charge efficiency around 92%, obviously lower than the super-capacitors.

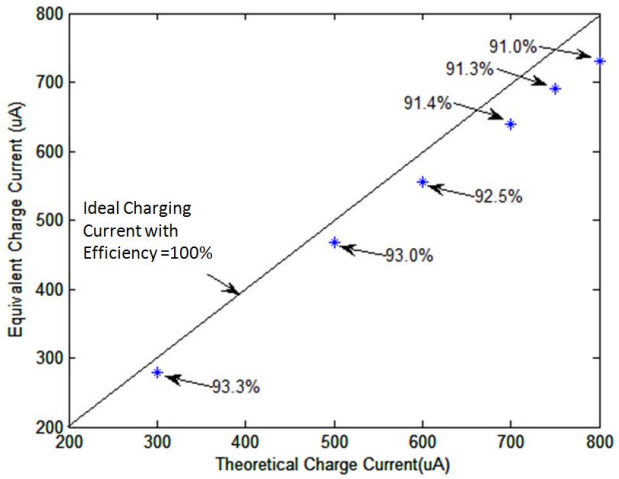



Figure 3.8: Charging Efficiency of TFB

In summary, Table 3.2 presents the characteristics related to the ESU design optimization. In next section, the charge and discharge model of the ESU based on these characterizations are presented. A Simulink model is then created to simulate

| | Maxwell Ultra-Cap P270 | Cap-XX H206 | IPS MEC101 |
|---|---|---|---|
| ESU Type. | super-capacitor | super-capacitor | TFB |
| ESR (30mA load current) | 0.29 Ω | 0.07 Ω | 50 Ω |
| Avg. Leakage Current (24 hours from voltage rating) | 28$\mu$A | 7 $\mu$A | 1$\mu$A |
| Measured Charge efficiency (0.5mA charge current) | 96% | 96.4% | 92% |

Table 3.2: Characterizations Summary of super-capacitors and Thin Film Battery

the performance of the ESU in various conditions.

## 3.3 ESU Simulation Model

In this section, a Matlab based model simulating energy storage unit is introduced. This is the first known Matlab model in literature concerning both the charge and discharge behaviours of super-capacitor. Section 3.3.1 addresses the charge/discharge model of ESU. Section 3.3.2 introduces the Matlab Simulink Implementation of this model and its verification.

### 3.3.1 Charge/Discharge Model

Figure 3.9 shows the equivalent circuit model for super-capacitor. The super-capacitor consists of four basic component: 1) ideal capacitor, 2) voltage controlled DC current source represents the leakage current, and 3) the equivalent series resistance ESR, 4) the ESU charge efficiency $\eta_{char}$. In addition, the solar cell is simulated by a current source. The WSN mote power consumption (load) is simulated using a variable resistor.

Both the capacitance and the ESR maintain constant values. The leakage current is a function of the constant capacitance, and the capacitor voltage, a variable. The voltage on the output end of the super-capacitor is the sum of the ideal capacitor

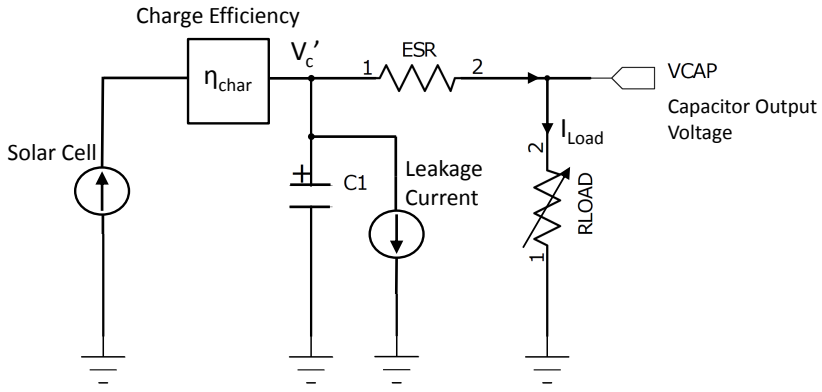



Figure 3.9: Simplified Equivalent Circuit of ESU

voltage and the voltage drop on the ESR.

$$V_{ESU} = V_{ESR} + V_C{}' \tag{3.6}$$

where the $V_{ESU}$ is the output voltage of ESU, $V_{ESR}$ is the voltage drop on the ESR and $V_C{}'$ is the theoretical voltage on the ideal capacitor. It is worth noting that the I-V characteristic of the photo-voltaic module is close to a voltage controlled current source. In the simulation, a constant current source is used to simulate the PV cell.

The commonly used capacitor charging equation with a constant input voltage and time constant in the RC circuit is not used in this case since the power source is a current source. Taking the leakage current into consideration, the leakage current can be expressed as,

$$I_{leak}(t) = \rho_{leak} \cdot C \cdot V_C{}'(t) \tag{3.7}$$

where $\rho_{leak}$ is the aforementioned leakage current coefficient, and is near constant for a certain super-capacitor. Taking the charge efficiency, $\eta_{char}$, into consideration, with current integral charging equation, the voltage on the ideal capacitor then can be modified into the following expression,

$$V_c'(t) = \frac{1}{C}\int_0^t I_{eqv}(t) - I_{leak}(t)dt = \frac{1}{C}\int_0^t \eta_{char} \cdot I_c(t) - \rho_{leak} \cdot C \cdot V_c'(t)dt \tag{3.8}$$

| | |
|---|---|
| $I_{act}$ | current consumption in active mode |
| $I_{sleep}$ | current consumption in Micro-controller sleep |
| $T_{act}$ | active mode period |
| $T_{sleep}$ | Micro-controller sleep period |
| $D_{act} = T_{act}/(T_{sleep} + T_{act})$ | duty cycle of active mode |

Table 3.3: Significance of terms in Equation 3.10

where $I_{eqv}$ is the equivalent charging current when the charging efficiency is considered. Derived from Eq 3.7 and Eq 3.8, the output voltage of ESU can be expressed as,

$$V_{ESU} = V_0 + \frac{1}{C}\int_0^t I_{eqv}(t) - I_{leak}(t)dt + I_c(t) \cdot R_{esr} \tag{3.9}$$

where $V_0$ is the initial voltage of super-capacitor. With only the charge model, the operation lifetime of the ESUs cannot be calculated. The second part discusses the discharge model of ESUs. When the ESU is fully charged and the load WSN is switched on, the load current is drawn with the duty cycling pattern that has been addressed previously.

The discharge time and voltage are directly affected by the WSN load current. The average current $I_{wsn}$ can be mathematically defined by,

$$I_{wsn} = I_{act} \cdot D_{act} + I_{sleep} \cdot (1 - D_{act}) \tag{3.10}$$

the terms used in Eq 3.10 is defined in Table 3.3. In this duty cycling WSN mote, the average current consumption is determined by the active mode current $I_{act}$, sleep mode current $I_{sleep}$ and the active mode duty cycle $D_{act}$.

### 3.3.2 Simulink Model Implementation

A simulink based Matlab model is then created to simulate the super-capacitor charging process. The model is created around a continuous time integrator with an external initial condition $V_0$ setting the initial voltage on the capacitor. The ESR, leakage current coefficient $\rho_{leak}$, and charge efficiency $\eta_{char}$ can be adjusted for different super-capacitors. The sleep/active mode power consumption and duty cycle of WSN mote can also be controlled in the model. Based on the parameters measured on the widely used and low cost Maxwell 2.5F 5.0V super-capacitor, the simulation parameters are adjusted accordingly. The charge efficiency is measured at 95%. The leakage current coefficient is 5.55E-6 A/V·F. The ESR is measured at 0.2Ω in DC condition (room temperature). The charging current is set to 350uA, similar to the current flow from a Sanyo AM1815 solar cell under 800lux fluorescent light intensity. The sleep mode current of Tyndall WSN mote is 10$\mu$A. The active mode current is 32mA. WSN mote operating duty cycle is 0.1%. The capacitor initial voltage is set at 0.5V. The output voltage of super-capacitor, the voltage drop on ESR, voltage on the ideal capacitor and the input current are monitored by "scopes". The complete simulink model is shown in Figure 3.10. The simulation results are shown in Figure 3.11 with simulation time resolution at 0.1Sec.

The simulation result is then verified by comparing with the experimental charging results of Maxwell 2.5F super-capacitor (measurement made on Pico Technology data acquisition device ADC-11/12). The simulation estimated time to reach 95% charge is only 5.6% longer than the measured charge time (see Figure 3.12).

One further test was conducted to understand the performance of the ESU when no input light is available for a prolonged period of time. The fully (95%) charged super-capacitor was discharged by a duty cycling power consumption programmed by a power analyzer Agilent N6740.

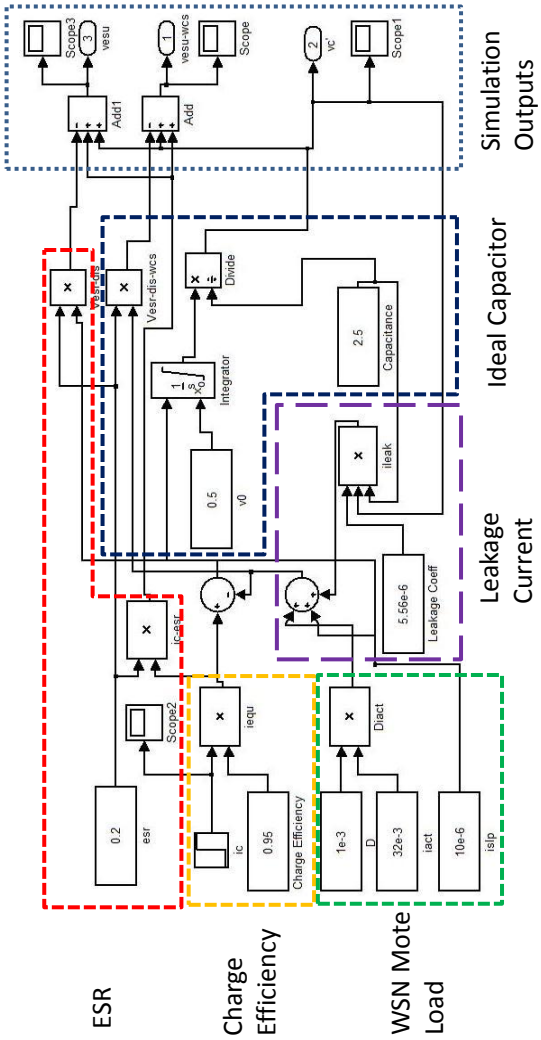



Figure 3.10: super-capacitor Charge/discharge Simulink Model

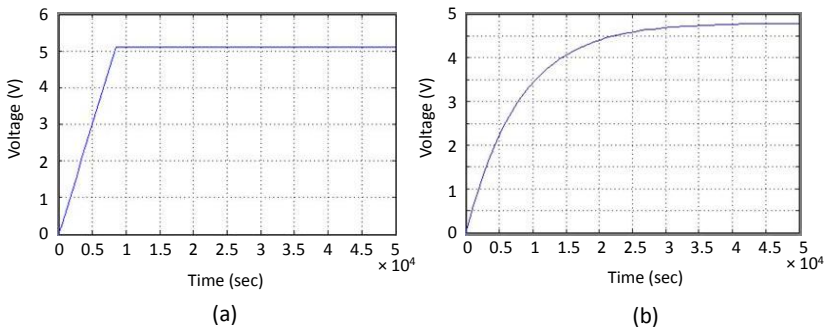



Figure 3.11: super-capacitor Simulink Model Simulation Results (Screen Capture) (a) Without Charge Efficiency and Leakage Current Effects; (b) Considering Charge Efficiency and Leakage Current Effects

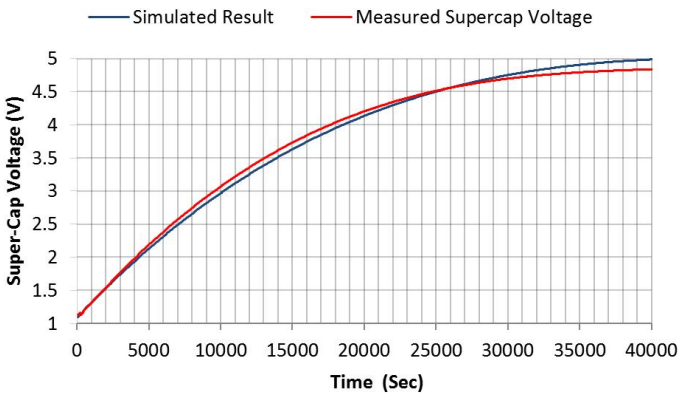



Figure 3.12: Super-capacitor Simulink Model Simulation Result Verification: Charging

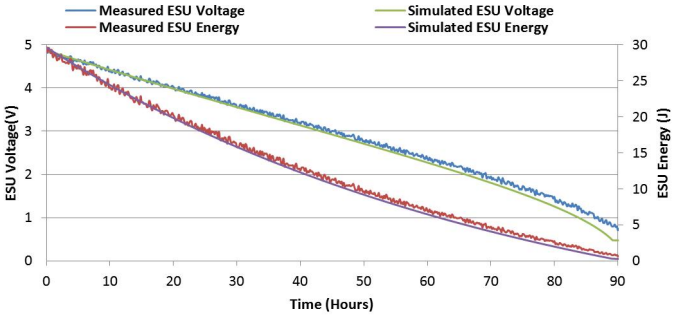



Figure 3.13: Super-capacitor Simulink Model Result Verification: Discharging

The measured energy storage voltage in the experiment shows it reaches the 0.5V (10% charge) at $94^{th}$ hour since the beginning of the experiment. The simulation estimation (see Figure 3.13) shows a highly consistent result with the actual measurement. The lifetime of 90.5 hours from the 95% charged ESU is shown in the simulation result. The error of the simulation (3.7 hours) is less than 4%.

The ESU model is essential to estimate the operating condition of energy harvester. With detailed ESU simulation model, the components selection and power management circuit design can also be optimized based on ESU conditions.

## 3.4 ESU Power Regulation

In addition to the ESU modeling, certain power regulation is important to effectively improve the utilization of the ESU. In this section, three circuits designed for

ESU power regulation are presented.

1) The first one is the output voltage regulation circuit to maximize stored energy utilization;

2) The second circuit is the fast charge circuit, it switches the charging circuit between parallel and series configurations to obtain maximum charging current in order to shorten the charging time;

3) The third circuit is the self-start circuit to automatically re-start the energy harvesting system when input power is available after the ESU is completely discharged.

### 3.4.1 Output Voltage Regulation

The output voltage regulation is necessary for the ESU to resolve the voltage mismatch issue between ESU and the required WSN voltage. In addition, it maximizes the useable energy in the ESU. It is especially important when the capacitive ESU is used, since the voltage fluctuates depending on its state of charge. In previous literature, the most common method of voltage regulation is to use a buck converter or low dropout (LDO) regulator [44],[45]. However, LDO has inherent low efficiency and the efficiency is even worse when applied with high voltage conversion ratio.

Assuming an ideal discharge process of a super-capacitor with a constant power dissipation and an ideal DC/DC converter with 100% conversion efficiency, the detailed discharge process simulation based on ESU model (Figure 3.10) is shown in Figure 3.14. When the ESU voltage drops from fully charged status, the cut off voltage (lower) threshold of the DC/DC converter determines the amount of energy that can be used in the ESU.

When the DC/DC converter is a buck converter or a LDO, the threshold voltage is the minimal operational voltage of the WSN mote, in this case, 2.7V (Mote micro-controller brown-out voltage detection threshold[2]) [95].

[2]A brown-out is an intentional or unintentional drop in voltage in an electrical power supply system. For a WSN mote micro-controller, a lower than the "brown-out" threshold supply voltage Vcc can cause out of control performance on micro-controller. In order to prevent it, the micro-controller usually has a circuit for brown-out shut down/reset. This circuit immediately shut down

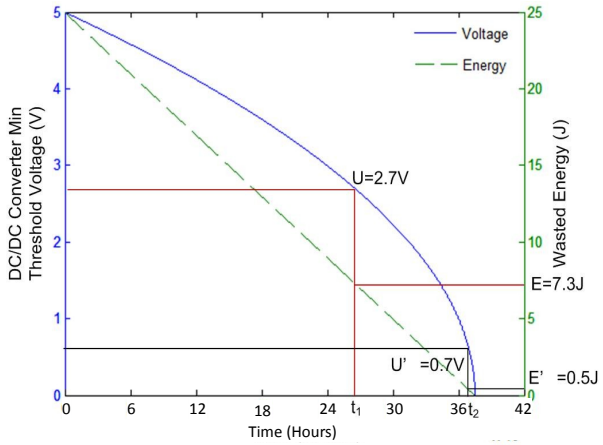



Figure 3.14: DC/DC Converter Voltage Threshold and Wasted Energy Analysis

When the ESU voltage further decreases after $t_1$ (26 hours) in the simulation, although a significant amount of energy is still stored in the ESU, it can not be utilized due to its lower-than-threshold voltage. As shown in Figure 3.14, 7.3J or 30% of energy is wasted due to that 2.7V is set to be the threshold voltage.

For ESU with lower voltage rating (e.g. 3.0V), only 19% of the stored energy can be utilized with the 2.7V mote minimal threshold voltage (81% of the energy is wasted). However, if the output voltage regulator has a step up function (assuming 100% conversion efficiency), the DC/DC converter minimal step-up voltage becomes the threshold voltage, e.g. 0.7V. The wasted energy becomes only 0.5J or 2% of the total stored energy (shown in Figure 3.14). More energy can be extracted from ESU by having the step-up function, thus a buck-boost converter is selected in the design for the output voltage regulation.

In Figure 3.14, an ideal DC/DC conversion is presumed; however, in the practical design, the efficiency is non-ideal.

In this work, TI TPS61220 is selected due to the high conversion efficiency, relatively low start up voltage threshold (0.5V) and buck/boost functions. It is worth noticing that the switching regulator energy conversion efficiency varies considerably with various input voltage and current.

the whole electronics when the voltage level drops below the "brown-out voltage detection threshold" and resets whole electronics when voltage level recovers.

More experiments are conducted to determine the conversion efficiency in various voltage/current conditions. The Keithley 2400 source-meter is used to simulate an ESU charging process with the TPS61220 buck/boost converter used as the output regulator. The layout of the experiment is shown in Figure 3.15.

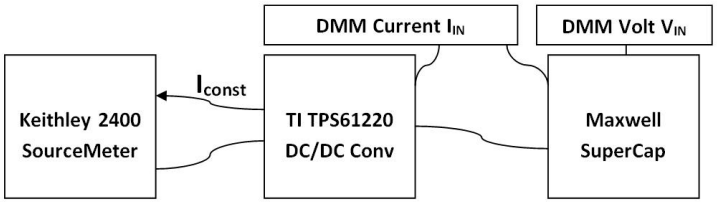



Figure 3.15: Sourcemeter Set-up for Conversion Efficiency Tests

The implementation of the schematics of the output regulator is based on Texas Instruments TPS61220 series DC/DC converter as shown in Figure 3.16.

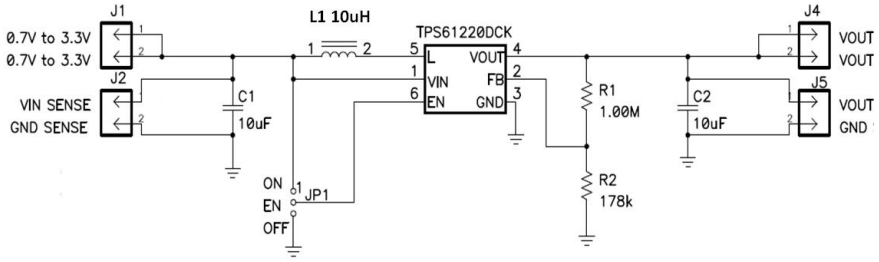



Figure 3.16: Output Regulation Schematic Using TI TPS61220

The tests of the output regulator are conducted with three constant output current, $I_{const}$ are 10$\mu$A, 100$\mu$A and 30mA, simulating the sleep, idle and active current consumption of the WSN module, respectively. The efficiency is defined as:

$$\eta_{dc/dc} = \frac{V_{out} \cdot I_{const}}{V_{in} \cdot I_{in}} \tag{3.11}$$

The test results on the conversion efficiency of the implemented output voltage regulator are shown in Figure 3.17,

As shown in Figure 3.17, when the DC/DC converter operates in the low voltage region (<1V), the conversion efficiency decreases considerably. The less than 50%

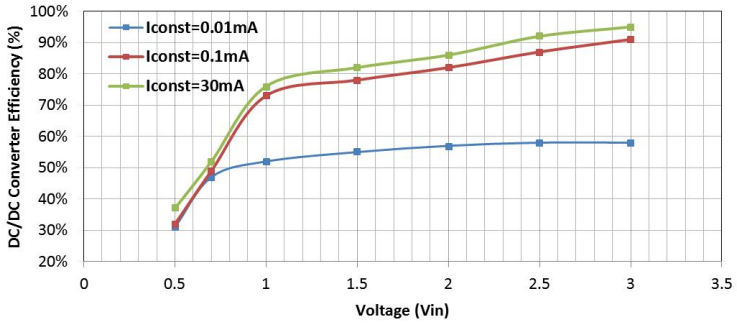



Figure 3.17: Measured DC/DC Converter Efficiency between 0.5V and 3V Input Voltage in 3 Current Consumption Modes

efficiency makes this power loss no longer negligible. The output regulator conversion efficiency needs to be considered.

Polynomial curve fitting is adopted to simulate the conversion efficiency and input voltage correlation. The active mode conversion efficiency is:

$$\eta_{dc-act}(V) = -0.08V^4 + 0.68V^3 - 2.09V^2 + 2.84V - 0.62. \tag{3.12}$$

The sleep mode conversion efficiency is:

$$\eta_{dc-slp}(V) = -0.12V^6 + 1.32V^5 - 5.76V^4 + 12.91V^3 - 15.62V^2 + 9.75V - 1.95. \tag{3.13}$$

To accurately calculate the conversion efficiency in both sleep mode and active mode, the current consumptions of the two modes of WSN are individually considered instead of using average current consumption. The energy consumption in a sleep mode and a active mode is defined in Eq 3.14,

$$E_{wsn} = \frac{I_{act} \cdot V \cdot T \cdot D}{\eta_{dc-act}(V)} + \frac{I_{slp} \cdot V \cdot T \cdot D}{\eta_{dc-slp}(V)} \tag{3.14}$$

where T is the total time of sleep mode time and active mode time, D is the active mode duty cycle. In this case, the sleep current and active current are 0.01mA and 30mA, respectively. The WSN operating duty cycle ($T_{act}/T_{total}$) is set to 0.1%, i.e.

activated for 90msec every 90 seconds (1.5 minutes) similar to the power consumption demonstrated in Figure 2.3.

Taking the conversion efficiency curve fitting into consideration, the analytical model for estimating energy consumption of the ESU in the discharge process is reprogrammed in the ESU model in Matlab. ESU is a 1F super-capacitor with 0.2Ω ESR and 5V voltage rating in the analysis. The results are plotted in Figure 3.18,

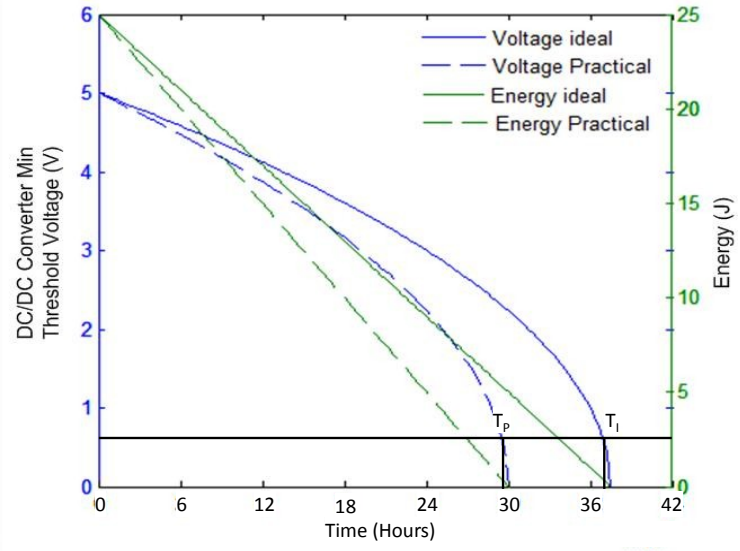



Figure 3.18: Revised DC/DC Converter Threshold Voltage and Wasted Energy Simulation with Consideration of Conversion Efficiency Variations

With the conversion efficiency of DC/DC converter considered, the improvement of the energy utilization from using DC/DC converter is partly compromised by the relatively low conversion efficiency. However, the energy utilization is still improved by 13.5%, i.e. the discharge time of ESU is $T_P$ =29.5 hours in Figure 3.18 instead of $T_1 = 26$ hours in Figure 3.14.

The energy conversion efficiency considered in this thesis is the "usable" energy that can be utilized by WSN mote. A new term, energy utilization ratio, $\eta_{ur}$, is introduced in this work to define the percentage of energy that can be used to power WSN mote (available energy $E_{avail}$ ) from a fully charged ESU (total stored energy $E_{total}$).

$$\eta_{ur} = E_{avail}/E_{total} = E_{avail}/(0.5 \cdot C \cdot V^2) \tag{3.15}$$

The result in Figure 3.19 shows a distinctive difference of energy utilization ratio between a buck converter based output regulator (e.g. previous works such as [44]) and a buck/boost converters (TI TPS61220 proposed in this work) output regulator. In Figure 3.19, the buck converter is considered as an ideal converter with 100% conversion efficiency. With smaller super-capacitor voltage rating, the energy utilization ratio of buck converter contracts considerably due to the much narrower voltage gap between ESU voltage rating and the minimal operative voltage of the WSN.

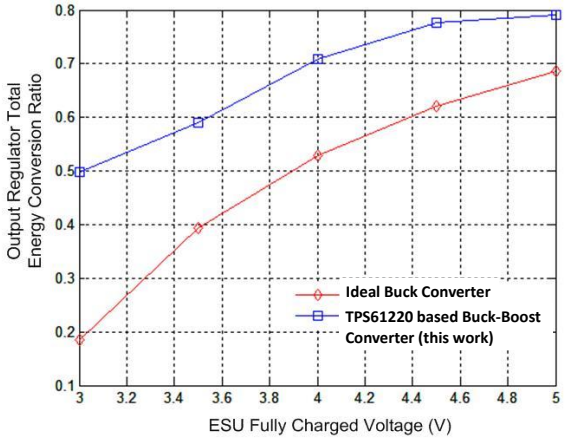



Figure 3.19: Buck and buck/boost Converters: Total Energy Utilization Ratio for Different ESU Voltage Rating (WSN load: D=0.1% duty cycle)

When the proposed buck-boost converter is used, overall, 80% of the stored energy can be extracted from the 5.0V voltage rating ESU; over 50% of the stored energy can be utilized from the 3.0V voltage rating ESU.

The efficiency of the buck converters in previous literature such as [44] and [50] are not presented in the publications. Thus this work compares the result to ideal buck converter with 100% conversion efficiency. This proposed TPS61220 buck/boost converter based approach shows an energy utilization ratio (50%) 2.5 times higher than an ideal buck converter (19%) when ESU voltage rating is 3.0V. For ESUs

with higher voltage rating at 5.0V, this proposed implementation still achieves energy utilization ratio 13.5% higher than the utilization ratio obtained in ideal buck converter configuration.

With the conversion efficiency in different current/voltage conditions considered, the Matlab based ESU model presents an analytic simulation tool which can more accurately estimate the correlation between WSN energy dissipation and charge condition in the ESU than previous work.

### 3.4.2 ESU Fast Charge Circuit

Typical WSN applications require large super-capacitors, e.g. $> 1$F. In order to shorten the charging time, a fast charge circuit is therefore proposed in this work.

It is worth noting that the super-capacitor is a capacitive ESU. The charging time of a capacitive ESU largely relies on the charging current as shown in Eq 3.16.

$$V_{soc} = \frac{1}{C} \cdot \int_0^t I_c(\tau) d\tau \tag{3.16}$$

The charging current can be maximized by changing the connections of PV cells.

One approach to fast charging capacitive load (maximize the charging current of the PV cells) is by switching between parallel and series connection of the PV cells. The principle of this fast charge is similar to the one proposed in [96]. The change of PV cells connection configuration is implemented by a switch array between separated PV cells. However, in [96], the power consumption of the design is approximately 1-2 orders of magnitude higher than the harvested power in this application. In order to apply this design concept in the ultra-low power devices, the fast charge circuits have been re-designed entirely.

As introduced in [96], the charging current is a variable depending on the number of PV cells, the PV cell charging voltage ($V_{CH}$), the voltage on the super-capacitor ($V_{SC}$), the energy harvester internal resistance (r) and super-capacitor equivalent

series resistance (ESR). The simulation of the parallel and series connections of the PV cells are shown in a PSPICE model as illustrated in Figure 3.20.

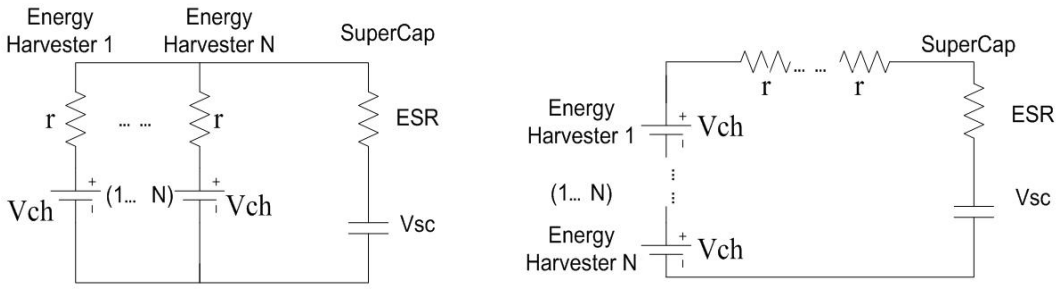



Figure 3.20: Parallel and Series Connection Configuration of PV cells

The charging currents in the above two configurations are calculated in Eq 3.17 and Eq 3.18.

$$I_{parallel} = \frac{N \cdot (V_{CH} - V_{SC})}{r + ESR} \tag{3.17}$$

$$I_{series} = \frac{N \cdot V_{CH} - V_{SC}}{N \cdot r + ESR} \tag{3.18}$$

where N is the number of solar cells connected in parallel or series, $V_{ch}$ is the equivalent charging voltage, $V_{sc}$ is the super-capacitor voltage, r is the internal resistance, ESR is the internal resistance of super-capacitor.

Figure 3.21 shows the simulation result of the charge current when the two types of connections are used. The simulation shows that, at the initial stage of the charge, the charging current will be higher when the PV cells are connected in parallel. In later stage, the charging current is higher for the series connection configuration.

The threshold voltage to swtich between parallel and series connection is when $I_{parallel} = I_{Series}$. The change from parallel connection to series connection occurs at a certain voltage $V_{sw}$. The switching voltage $V_{sw}$ is derived from Eq 3.17 and Eq 3.18,

$$V_{sw} = \frac{N \cdot r}{(N+1) \cdot r + ESR} \cdot V_{CH} \tag{3.19}$$

In order to achieve the switch from parallel connection to series connection, a voltage comparator is used to control the switching. The super-capacitor voltage $V_{SC}$ is monitored by the voltage comparator, and the required switch threshold voltage

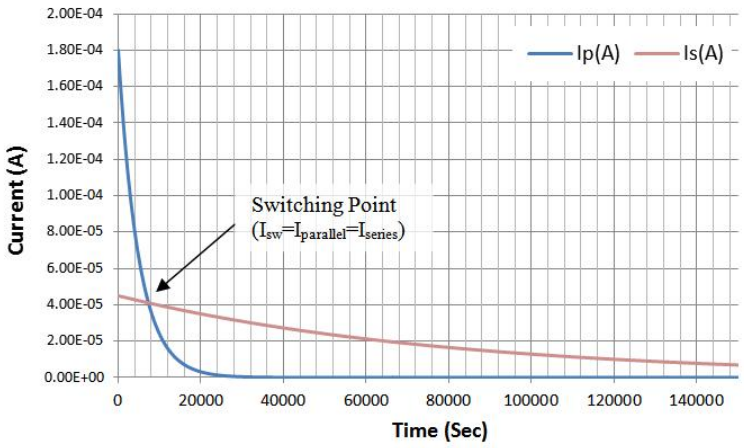



Figure 3.21: Charging current of Parallel and Series Configurations

$V_{sw}$ is compared with $V_{SC}$. Once $V_{SC} > V_{sw}$, the logic circuit will then switch off the parallel connection and change to series connection. Vice versa, if $V_{SC} < V_{sw}$, the series connection switches back to parallel connection. Figure 3.22 shows the design of the fast charge circuit.

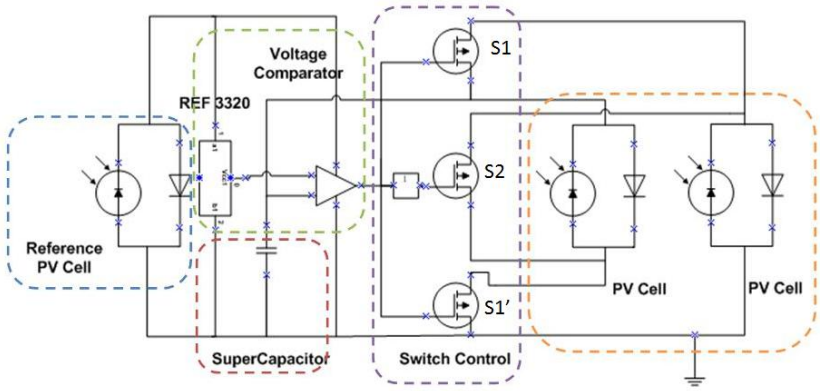



Figure 3.22: Fast Charge Circuit Schematics

The voltage comparator used in the circuit is a Seiko Instruments S-89530A [97]. To set the reference voltage $V_{sw}$, the reference PV cell and an ultra low power voltage reference IC (Texas Instruments REF3322) are used [98]. Together with the low power switches (Intersil ISL43L120 [99]) the average power consumption of the fast charge circuit is calculated at 25.7$\mu$W (continuous power consumption) which is 40 times smaller than the [96] solutions.

The fast charge circuits operate in these steps:

1) Reference PV cell generates a $> 1.5$V voltage to initialize voltage reference IC Texas Instruments REF 3322. Reference PV cell also functions as power supply for the ultra-low power voltage comparator Seiko Instruments S-89530A.

2) super-capacitor voltage and reference voltage from REF 3322 is compared on S-89530A. The output of the comparator is used to control the switch array. In the circuit implementation, two S-89530A comparators are used with inversed logic instead of the inverter shown in the illustration circuit in Figure 3.22.

3) The switch array connects PV cell 1 and cell 2 in parallel when super-capacitor voltage $V_{SC}$ is lower than the pre-programmed switch voltage $V_{sw}$ by switching on S1/S1'.

4) The switches array connects PV cell 1 and cell 2 in series when super-capacitor voltage $V_{SC}$ is higher than the pre-programmed switch voltage $V_{sw}$ by switching off S1/S1' and switching on S2.

The fast charge circuit is tested with 4 Schott ($10\text{cm}^2$ active area in total) PV cells. The amorphous silicon based single cell PV module has a 0.9V MPP voltage. In this implementation, the ESU is a AVX 1.0F 4.5V ultra-low ESR super-capacitor. The prototype is tested by Ecole Polytechnique Federale de Lausanne master student Luca Ribetto under the supervision of the author. The prototype is placed under fluorescent light with a constant 500lux light intensity. The result of charging the super-capacitor with the three configurations is shown in Figure 3.23.

The result shows that the switch from parallel to series connection occurs at $V_{sw} = 0.81$V. Before the switching occurs, the super-capacitor charging speed is nearly identical to the parallel connection charge speed. After the switch occurs, significantly higher charging current from the series connection accelerates the charge.

With the same light intensity and temperature conditions, from 0V to 90% of 3.6V ($4\times$ solar cell $V_{mpp}$ charging voltage 0.9V), the series connection charge time is 1.79E+5 seconds ($\approx 50$ hours), while the fast charge configuration charge time is 1.48E+5 seconds ($\approx 41$ hours). By using the fast charge configuration, the charging

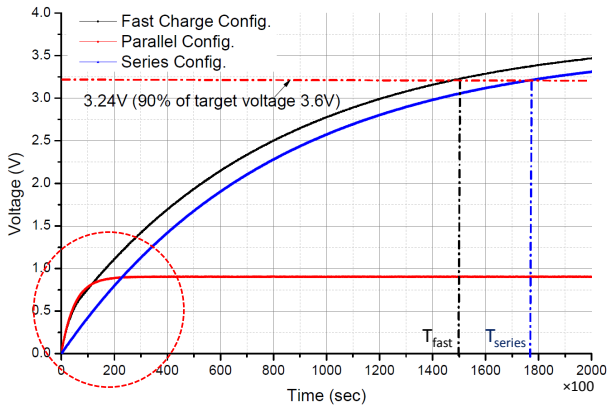



Figure 3.23: Fast Charge Experiment Charge Time Results (including the energy consumption of the switching circuits)

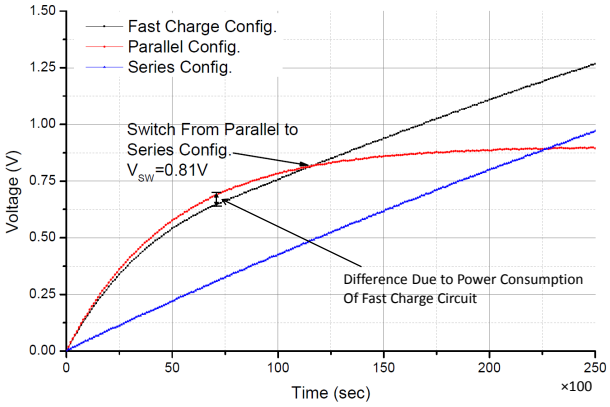



Figure 3.24: Initial Phase of Fast Charge Experiment (Difference between Fast Charge and Parallel Configurations is due to the power consumption of the switching circuits)

time is shortened by nearly 18% or 9 hours in this test.

However, it is worth noting that the super-capacitor voltage rating is relatively low (typically <5.0V for >1.0F capacitance super-capacitors). For PV cells with higher voltage (>3.0V or higher), series connection of a number of PV cells may generate a charging voltage significantly higher than the voltage rating of super-capacitor. The application of this fast charge circuit is particularly suitable for low voltage PV cells or single cell photovoltaic module with open circuit voltage less than 1.0V.

### 3.4.3 Self-Start Circuit for ESU

Different from previous literature such as [85] which only utilizes self-start circuit on the output voltage regulation, this work requires an additional self-start circuit for input power management. This is due to the input-end power management is also based on switching regulator as introduced in literature reviews.

The method for self-start circuit design is to build a circuit to prevent the input power management switching regulator and output power regulator from starting up before they reach the required voltage.

It is essential to obtain a self start circuit to achieve two targets:

1. the self start circuits provide logic control to switch on the enable pins of the switching regulators only when the input voltages exceed the switching regulator start-up voltage;

2. the self start circuits should provide a stable voltage supply for output power regulator, $V_{cc-opg}$, to continuously operate the output regulator until the ESU reaches minimum operational voltage;

The self start circuit is introduced in the Figure 3.25. This sub-system is largely separated from the rest of the energy harvester to ensure its reliability. A secondary PV cell is used in this self-start circuit design to function as an individual power supply. REF3312 is Texas Instuments voltage reference IC with 1.25V output reference voltage (when input voltage is higher than 1.5V).

With the ESU fully discharged and light intensity increases from zero, the detailed system restart are introduced in the following steps:

1. Secondary PV cell charges self start circuit capacitors $C_1$ and $C_2$ to approximately 1.5V and 1.2V. $D_1$ and $D_2$ are Vishay Semiconductors 95SQ015 Schottky diode with forward voltage drop approximately equals to 0.31V. The comparators used in the design are Maxim MAX934 quad channels low voltage

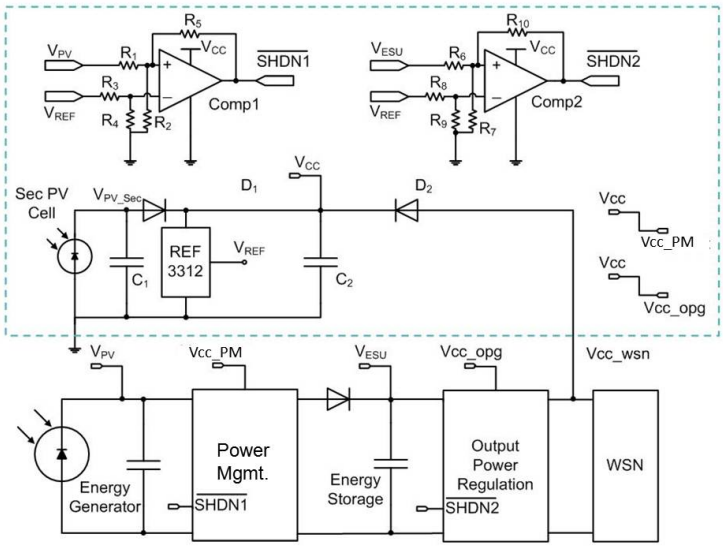



Figure 3.25: PV Cell Energy Harvester Self Start Circuits Schematics

comparators. The minimal operating voltage of the MAX934 is approximately 1V. When $C_2$ voltage is 1.2V, comparator 1 and 2 (Comp1 and Comp2 are powered from $V_{cc}$ as shown in Figure 3.25) enter the normal operation phase. The voltage supply $V_{cc}$ starts these two comparators (same IC, different channels), although the enable pins $\overline{SHDN1}$ and $\overline{SHDN2}$ are switched off from the comparators.

2. Voltage on the main PV cell $V_{EHU}$ starts to charge the main input capacitor and increase to the minimal operating voltage. The resistor divider (R1-R5) around Comp1 are set to compare $V_{EHU}$ with the voltage reference TI REF3312 (1.25V), and only turn on the DC/DC converter enable pin $\overline{SHDN1}$ by Comp1 when $V_{EHU}$ is higher than power management module minimal start up voltage (0.9V) instead of the minimal operating voltage, thus a controlled start-up. This effectively resolves the cold start issue for switching regulator. A small voltage headroom (0.2V) is introduced for the start up voltage threshold to achieve improved reliability. Selecting from the closest resistor value, the start up voltage threshold is approximately 1.09V. Thus, only when the main PV cell charges input capacitor to $V_{EHU} = 1.09$V, the enable pin $\overline{SHDN1}$ is activated and starts up the power management module.

3. After the power management module circuit is activated by the self start circuit, main PV cell starts to charge the ESU. Similar to the power management module switching regulator, Comp2 only turns on enable pin at its minimal start up voltage (0.9V for TI TPS61220). Once the output regulator starts to operate, the energy harvester system output voltage $V_{cc-wsn}$ reaches preset 3.3V. The $V_{cc-wsn}$ is connected via a diode to $C_2$ in the self start circuit and act as the main voltage supply for the system. The energy harvester enters normal operation mode, the restart is then complete.

The components parameters of the self start circuit is shown in Table 3.4, large resistors are chosen for low leakage current through the voltage divider arrays.

| | | |
|---|---|---|
| $R1$=1.5MΩ | $R2$=2MΩ | $R3$=1MΩ |
| R4=1MΩ | R5=5.1MΩ | R6=310kΩ |
| R7=710kΩ | R8=1MΩ | R9=1MΩ |
| R10=2.2MΩ | C1=10uF | C2=100uF |
| Comp1=MAX934 Channel 1 | Comp1=MAX934 Channel 2 | REF=TI REF3312 |

Table 3.4: Components Parameters of Self Start Circuit

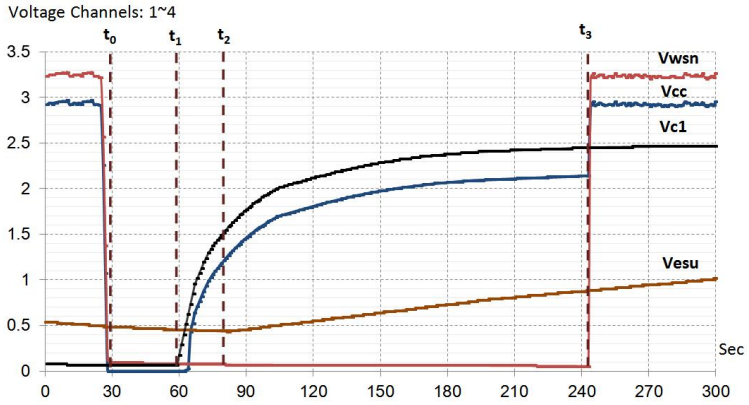



Figure 3.26: Screen Capture of Start Up Process in a PV Cell Energy Harvester Based on Self Start Circuits (measured with Pico Tech Data Logger)

The test results of the self start circuit are shown in Figure 3.26. The measurement is conducted with a Pico Technology data logger ADC-11/12. The self start circuit is firstly placed in 0lux light intensity when the ESU voltage $V_{ESU}$ is close to the output regulator minimal operating voltage. $V_{EHU}$ drops below the voltage threshold at $t_0$.

Both the power supply bus voltage $V_{cc}$ and the system output voltage $V_{wsn}$ drop to near zero volts at $t_0$. A fluorescent light source with 500lux light intensity is switched on at time $t_1$. The small input capacitor $C_1$ is then charged towards the required 1.5V. The minimal light intensity required for the start up is only 150lux with the 3.5cm$^2$ secondary PV cell ($\approx 10\mu$W).

When $V_{cc}$ is close to 1.2V, it activates the voltage reference and control comparators at $t_2$. The power management module circuit is then activated by comparator1 (Comp1) and the ESU starts to charge. The ESU is charged to 0.9V, the minimal start up voltage preset by the voltage divider, at $t_3$. Comparator 2 (Comp2) switches on the output regulator enable pin and system output recovers to a regulated $V_{wsn}$ . The system output voltage $V_{wsn}$ also starts to function as the voltage supply bus $V_{cc}$ at $t_3$. The self start procedure completes at $t_3$.

A self start circuit for thermoelectric generator energy harvester is also designed with a secondary thermopile and a charge pump. The difficulty to generate relatively high voltage ($> 1.4$V) on pilot thermopile is the main reason to adopt such charge pump.

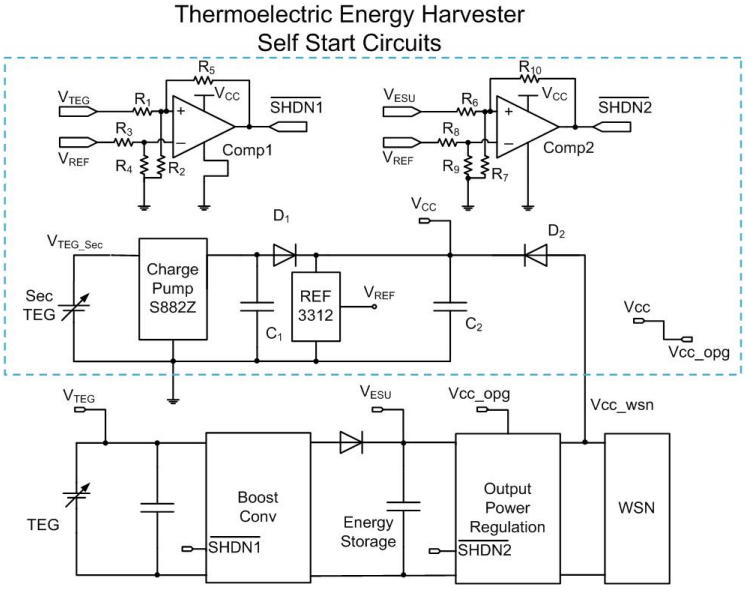



Figure 3.27: Thermoelectric Energy Harvester Self Start Circuits Schematics

The charge pump is a Seiko Instruments S-882Z with a 0.25V start up voltage.

With the output voltage set to 1.8V (fixed output voltage of S-882Z charge pump), the step up ratio is 7.2 times. The conversion efficiency of this charge pump is significantly lower than the switching regulator. Since the self start circuit is not frequently used, the inherent low conversion efficiency is not considered as a significant issue.

Similar to the PV cell based system, once the start up is complete, the regulated system output $V_{cc-wsn}$ supplies the power supply bus $V_{cc}$. The voltage divider resistor arrays are identical to the PV cell based self start system.

The self start time highly relies on the input energy and the capacitance selected in the system. The small input capacitor $C_1$ allows a short restart time within 30 seconds for the ICs. However, the majority of the self start time is due to ESU charging to reach the minimal start up voltage of the output regulator. In the case when large ESU is used, e.g. a 2F super-capacitor, the start up time extends to approximately 1.5 hours from 500lux indoor light.

## 3.5 Hybrid Energy Storage

The super-capacitor has been shown to be a suitable energy storage unit for energy harvesting systems. However, when comparing the super-capacitor to the TFB, several drawbacks exist. Although the long lifetime and large recharging cycle number make the super-capacitor suitable for long time deployment, the power loss due to self discharge in a super-capacitor is 20-50 times higher than that of a TFB. The low energy density of the super-capacitor also limits the further miniaturization of the EH device.

In contrast, the direct utilization of the TFB is also not practical in general WSN applications due to the large voltage drop on the ESR of TFB.

The concept of hybrid energy storage has been presented in the literature [100], [101], [102]. However, these proposed hybrid energy storage units all suggest the combination of super-capacitor and the conventional rechargeable battery. while this type of combination provides larger capacity and improved stability, the inherent

lifetime limitation of the conventional battery severely constrains the proliferation of system lifetime.

In this work, a novel hybrid energy storage unit with super-capacitor and thin film micro battery (TFB) is proposed with a power management circuit to optimize the performance. In order to exploit the low leakage current of the TFB and the low ESR in the super-capacitor, the hybrid ESU adopts a design effectively switching between two energy storage units during charging and discharging phase.

Based on the characterizations of the TFB and super-capacitor ESUs, the hybrid energy storage unit should be designed to 1) reduce the average super-capacitor voltage; 2) discharge the WSN active mode current from super-capacitor; 3) perform over-voltage and under-voltage protection for TFB.

The schematics designed for the hybrid ESU are shown in Figure 3.28. The super-capacitor is directly connected to the output voltage regulator. Three switches are used to connect/disconnect the TFB with the super-capacitor. These three switches are controlled by three out of four channels of a voltage comparator Maxim Max934. Max934 includes an internal reference which is set to 1.25V in this work. The total current consumption of the control logic circuits is less than $2\mu$A.

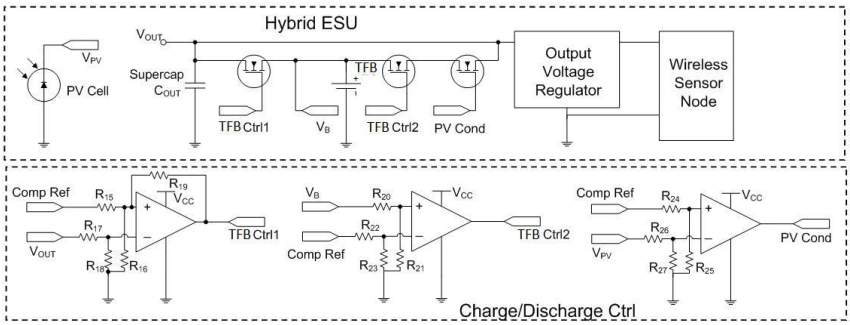



Figure 3.28: Schematics of hybrid ESU power management circuits

The control circuit limits the hybrid ESU voltage to a pre-set threshold of 4.2V in order to reduce the leakage current. Once the super-capacitor voltage is above the 4.2V threshold, "TFB Ctrl1" switch is turned on, the energy harvester will charge the additional energy into TFB for its low leakage current characteristics.

During the discharging, however, the TFB is always discharged first, and is connected with super-capacitor in parallel in order to minimize the ESR. This discharge only occurs when there is no input solar power. This is facilitated by "PV Cond" switch. The solar cell voltage, $V_{PV}$ is compared with reference voltage. "PV Cond" switch is only switched on when $V_{PV}$ is less than 1V, which indicates low light intensity condition. "TFB Ctrl2" switch is used to perform under-voltage protection of TFB. Once the TFB voltage $V_B$ is lower than 3.8V cut-off voltage, the discharge of TFB is switched off by "TFB Ctrl2" switch.

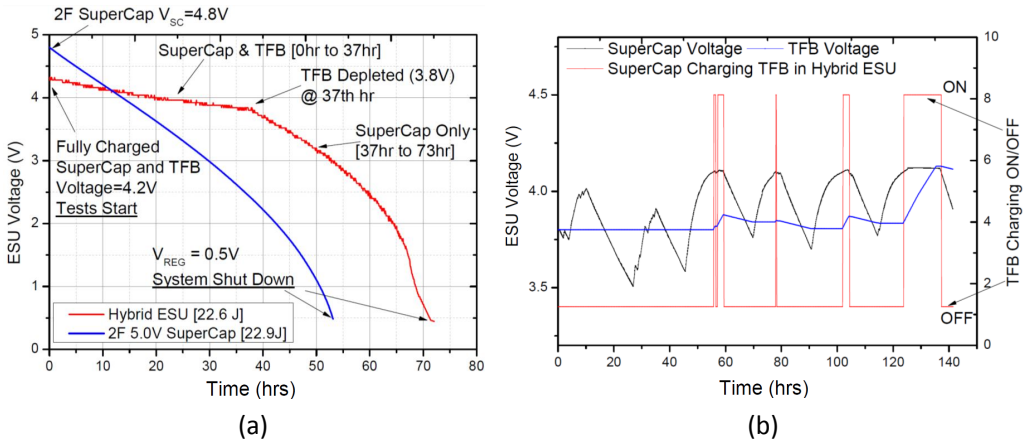



Figure 3.29: (a) Hybrid energy storage unit discharge experiment with a Tyndall WSN mote. (b) 1 week long charge/discharge test with 0.5mW PV cell and a Tyndall WSN mote. Black: super-capacitor Voltage; Blue: TFB Voltage; Red: super-capacitor charges TFB function ON/OFF

The prototype hybrid energy storage circuits are tested with a Maxwell 0.47F 5.0V super-capacitor and an Infinite Power Solutions TFB with 1mAh 4.2V capacity. The hybrid ESU prototype has been tested in two experiments shown in Figure 3.29. The first experiment shown in Figure 3.29(a) demonstrates the discharge process of the hybrid ESU when the load is the aforementioned Tyndall WSN module. The total operation time is 73 hours. The fully charged hybrid ESU has 22.6J capacity in total, with the super-capacitor and TFB (at 4.2V) store 8.2J and 14.4J energy, respectively. The power consumption of Tyndall WSN module and power loss in the proposed ESU is calculated at 0.088mW based on the 73 hours operation time. The average power consumption of Tyndall WSN module is 0.05mW when it operates

with 5 minutes measurement interval (shown in Table 2.2). Thus, average power loss due to ESU is calculated at 38$\mu$W.

A Maxwell 2F 5.0V super-capacitor is used as a stand-alone super-capacitor to compare the results with the hybrid energy storage unit as shown in Figure 3.29(a). It stores 22.9J energy when it is charged to 4.8V, which is 97% of its voltage rating. Its stored energy is similar to (1.3% more than) the 22.6J energy capacity of the proposed hybrid energy storage. The discharge process of this super-capacitor is also shown in Figure 3.29(a). The operation lifetime is measured at 52 hours. The average power consumption (leakage and mote power dissipation) is calculated at 0.119mW. The average leakage power of the stand-alone super-capacitor ESU is calculated at 69$\mu$W. The proposed hybrid ESU extends the operation lifetime by 40% (from 52 hours to 73 hours) in this experiment.

One week long charge/discharge experiments have been conducted to test the over/under-voltage protection functionality of the control circuits. The results are shown in Figure 3.29(b). The super-capacitor charges the TFB at Day 3/4/5 of the experiment when it is charged to the pre-set 4.2V over-voltage protection threshold and fully charges the TFB in Day 6. TFB is partially discharged during the night of Day 3/4/5 where no solar energy is available and the TFB voltage was kept higher than the 3.8V under-voltage protection threshold. In both over and under voltage protection scenarios, the hybrid energy storage control circuit is able to limit the TFB within the pre-set thresholds.

## 3.6 Conclusion

In this chapter, two types of energy storage units, i.e. super-capacitor and micro thin film battery (TFB), have been characterized for energy harvesting applications.

Based on these new criteria of energy storage units, the charging/discharging model of both super-capacitor and the TFB have been built. This Matlab based simulation model takes the self discharge, charge efficiency and ESR of the ESU into consideration. These parameters have not been fully considered in the previous

energy harvester design and simulation. This empirical data based model can estimate the charge condition of an ESU accurately. This is an essential tool to assist the design of energy harvester. It also can be used as a real-time evaluation tool to predict the state of charge for energy harvesting powered WSN.

The improvement of ESU cannot be achieved solely with the proper component selection through more accurate simulation. The output voltage mismatch, long charging time and self start, can only be resolved with careful power management circuit design.

Buck-boost converter output regulator has been designed in this work. Comparing with the LDO and buck converter introduced in previous literature, the energy utilization achieved in this work is 2.5 times higher (when ESU voltage rating is 3.0V, WSN mote threshold voltage is 2.5V). For ESU with lower voltage rating, the effect of this buck/boost converter is more obvious.

The novel fast charging circuit introduced in the chapter exploits a previous design which only exists in high power systems (in which the control circuit power budget was not a concern). Multiple PV cells are utilized to connect in parallel or series in order to constantly track the higher charging current, hence to effectively accelerate the charging speed. In this design, the power consumption of the control circuits is only 25$\mu$W with the ultra-low power comparator logic and switch circuits. By using the fast charge configuration, the charging time is shortened by 18% in this test.

The self start circuit introduced in this chapter features a secondary energy source, e.g. pilot PV cell or a pilot thermoelectric generator. The novel design employs simple Schmitt trigger type comparator control logic to avoid the zero start issue for boost converters. The low power design for the self start circuit and careful components selection have ensured a quick restart within several hours. The voltage supply bus adopted in the system provides a more reliable voltage supply. The start up circuit only requires 18$\mu$W from the pilot PV cell (3.5cm$^2$ with 150lux LED light).

The hybrid energy storage introduced in this work is the first known TFB and

super-capacitor hybrid ESU. The results show that low ESR and smaller leakage current can be achieved when the charge/discharge of TFB and super-capacitor ESUs are controlled. The control unit for the charge/discharge circuit delivers the harvested power to the hybrid ESU via a circuit nearly identical to the self start circuit, which allows this control circuit to utilize the same power management IC in the self start circuit. The hybrid ESU, with capacity equivalent to a 4.1V 2.46mAh battery, provides approximately 3 days (73 hours) of power for Tyndall WSN solely from the stored energy in the ESU. Comparing this with a standalone super-capacitor with same capacity, this hybrid energy storage solution prolongs the lifetime by 40% without compromising the performance of the WSN mote. This result surpass the thesis objective of 48 hours operation lifetime using only the stored energy.

# Chapter 4

# Thermoelectric Energy Harvesting

## 4.1 Introduction

For energy harvesting system applications in BEM WSN, thermal energy can often be found and potentially used as energy sources in many residential and commercial buildings. Many buildings contain a large number of water heaters, radiators, hot water pipes and solar water heating systems. If the wasted heat can be captured, thermoelectric energy harvesting can be used as a realistic method to continuously power WSN motes.

This chapter introduces a practical simulation model to estimate the output voltage and power of thermoelectric generator (TEG) in typical BEM applications. The surface temperature range of the heat source is between $50^{o}$C and $80^{o}$C (see example shown in Figure 2.14). The validation of the model is based on the TEG measurement results within this temperature range (TEGs are cooled by passive heatsink).

To utilize the harvested low voltage thermoelectric energy, a boost converter circuit is developed with a high ratio transformer. A charge pump and boost converter two stage dc-dc conversion solution is proposed in this work. The input impedance of the converter is measured and TEG internal resistance is designed to match the impedance.

## 4.2 Thermoelectric Module Characterizations

### 4.2.1 Thermoelectric Module Structures and Energy Transfer Model

A typical TEG features a structure shown in Figure 4.1. The P/N thermo-elements are electrically connected in series and thermally connected in parallel. Most TEGs adopted ceramic substrate. The equivalent circuit of TEG with resistive load is shown in Figure 4.1(b).

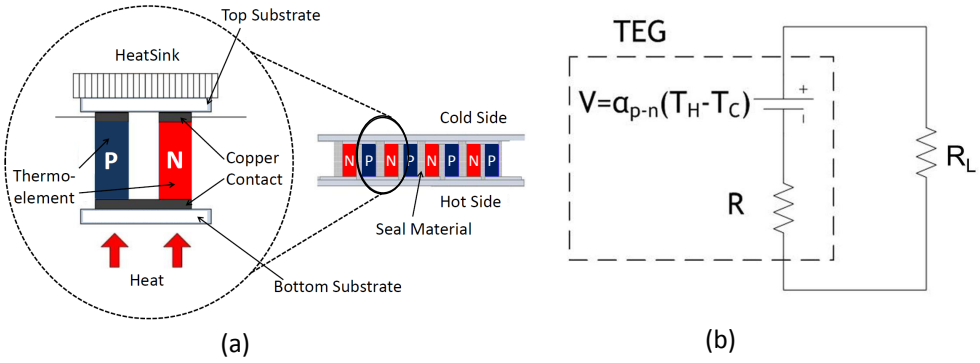



Figure 4.1: (a) Typical Thermoelectric Generator Structure and (b) Equivalent Circuit with resistive load

The voltage generated from the temperature difference is determined by the Seebeck equation.

$$V = \alpha_{p-n}\Delta T \tag{4.1}$$

where $\alpha_{p-n}$ is the Seebeck coefficient $\Delta T$ is the temperature difference between cold side and hot side of thermo-elements. The semi-conductor Seebeck coefficient is in a range of several hundreds of $\mu\text{V}\cdot K^{-1}$ to 1000 $\mu\text{V}\cdot K^{-1}$. For one pair of thermo-elements, the output voltage $V_L$ on the load is:

$$V_L = \alpha_{p-n}\Delta T \times \frac{R_L}{R_L + R} \tag{4.2}$$

where R is the internal resistance of TEG, $R_L$ is load resistance as shown in Figure 4.1 (b). The current flows through the TEG and the load is:

$$I = \frac{\alpha_{p-n}\Delta T}{R_L + R} \tag{4.3}$$

For a single pair of thermo-elements, the output power can be expressed as

$$P_L = R_L \cdot (\frac{\alpha_{p-n}\Delta T}{R_L + R})^2 \tag{4.4}$$

The thermoelectric modules are devices designed for thermoelectric energy generation. In most cases, thermoelectric module consists of large number of thermo-elements to increase the voltage and power output. The number of thermo-elements within a TEG ranges from tens and hundreds in conventional machined TEGs to several thousands in the MEMS based TEGs. Different from single pair of thermo-elements, several practical factors need to be considered in thermoelectric module.

First factor is the increased number of thermo-elements. In order to include several hundreds/thousands of thermo-elements, the layout shown in Figure 4.2 is commonly used in TEG designs. The connection of the P-element and N-element are through metal contact layers. Copper contact layers are most frequently used for its low resistivity. The copper contact layers are arranged in the way shown in Figure 4.2 in order to achieve series connections.

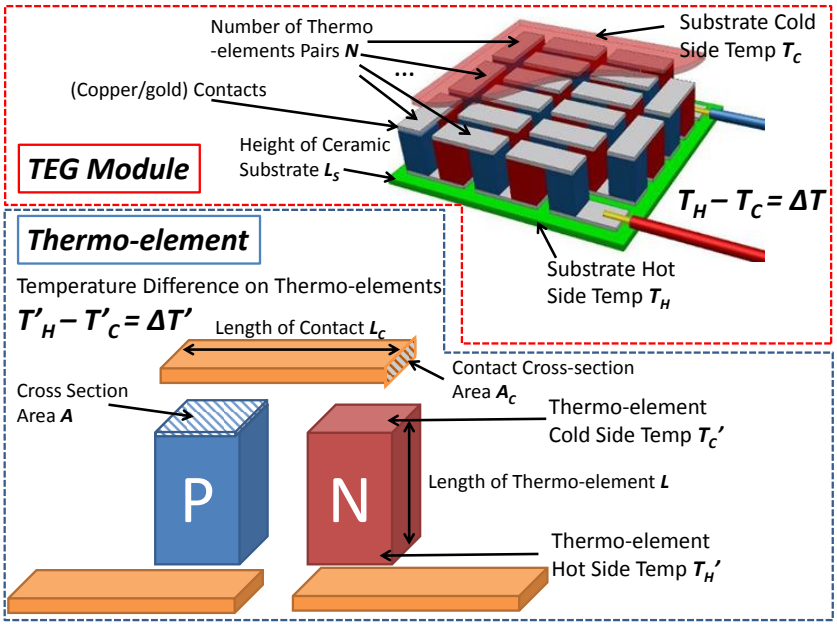



Figure 4.2: Thermoelectric Module Typical Structure and Key Parameters

The second factor is the ceramic thermal substrate. On both sides of the thermo-elements, a thin layer of ceramic is used to physically support the thermo-elements and metal contacts. In order to obtain enough structural strength to avoid physical damage to the device, the thickness of the ceramic layer normally exceeds 0.5mm. With total thickness higher than 1mm (two substrates, one on cold side, one on hot side), the impact on the heat transfer on the thermo-elements is no longer negligible. With significantly reduced thermo-element height (10-100 $\mu$m), the impact on the MEMS based TEG is particularly obvious (Substrate thickness is more than 10 times larger than the thickness of thermo-elements, i.e. substrate =500$\mu$m and thermo-elements=20$\mu$m [103]. For conventional TEG, substrate thickness is similar to the thickness of thermo-elements at approximately 1mm) and that impact will be investigated in characterizations in the following section.

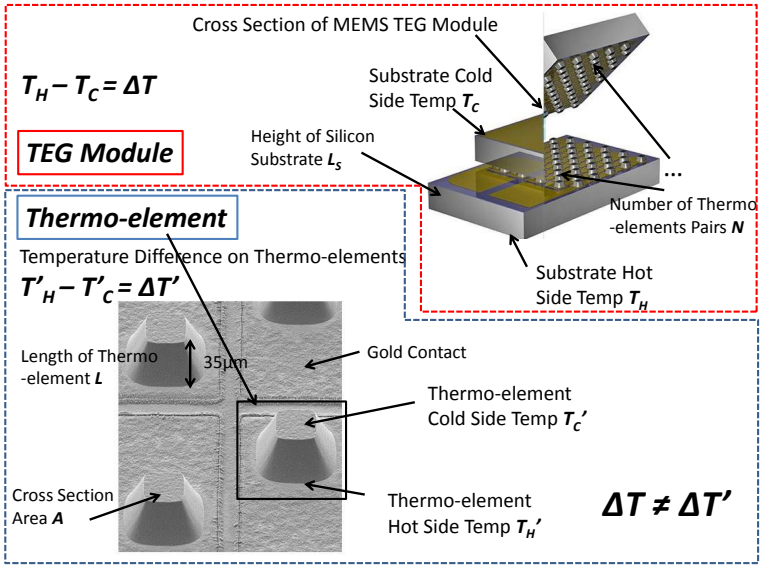



Figure 4.3: MEMS based TEG Microscope Photo and Illustrated Cross-Section [103] (Thermo-element length $\approx 35\mu$m)

The third factor is the increased internal electrical resistance. With large number of thermo-elements and metal connect layers, the internal resistance of the TEG also increased. Both the thermo-elements electrical conductivity and metal contacts conductivity are important to the output power. The main parameters of TEG are summarized in Table 4.1.

| Symbol | Definition |
|---|---|
| A | Thermo-elements Cross Section Area |
| $\alpha$ | Seebeck Coefficient |
| N | Number of Thermo-elements Pairs |
| L | Length of Thermo-elements |
| $L_S$ | Height of Ceramic Substrate |
| $L_C$ | Length of Contacts (between thermo-elements) |
| $A_C$ | Contacts Cross-Section Area |
| $\lambda$ | Thermo-element Thermal Conductivity |
| $\lambda_S$ | Substrate Thermal Conductivity |
| $\rho$ | Thermo-elements Electrical Resistivity |
| $\rho_C$ | Contacts Electrical Resistivity |
| $\Delta T$ | Temperature difference on the outside of substrates |
| $\Delta T'$ | Temperature difference on the inside of substrates |

Table 4.1: Symbol and Definition of Thermal Effect Parameters

The temperature variation in a steady-state (heat transfer q is constant) TEG module is shown in Figure 4.4. When the heat transfer on the substrate is considered, the definition of thermo-elements temperature difference changed. The more accurate estimation of temperature difference on the thermo-elements is the $\Delta T'$ value on the inside of the substrates.

Based on the heat transfer, the relationship between $\Delta T'$ and $\Delta T$ is expressed as:

$$\frac{\Delta T'}{\Delta T} = \frac{1}{1 + 2\frac{\lambda}{\lambda_S} \cdot \frac{L_S}{L}} \tag{4.5}$$

Different from previous literature such as [104], in this thesis, the heat transfers in the copper contacts are not considered due to its high thermal conductivity and consequently negligible impact on the heat transfer.

Based on the more accurately estimated heat transfer and temperature difference, the voltage output of N thermo-element pairs can be expressed as:

$$V_{load} = \frac{N \cdot \alpha \cdot \Delta T'}{R + R_L} \cdot R_L \tag{4.6}$$

where $V_{load}$ is the TEG output voltage, $\alpha$ is the combined P-N elements Seebeck coefficient, R is the internal resistance of TEG. The equivalent circuit of TEG and

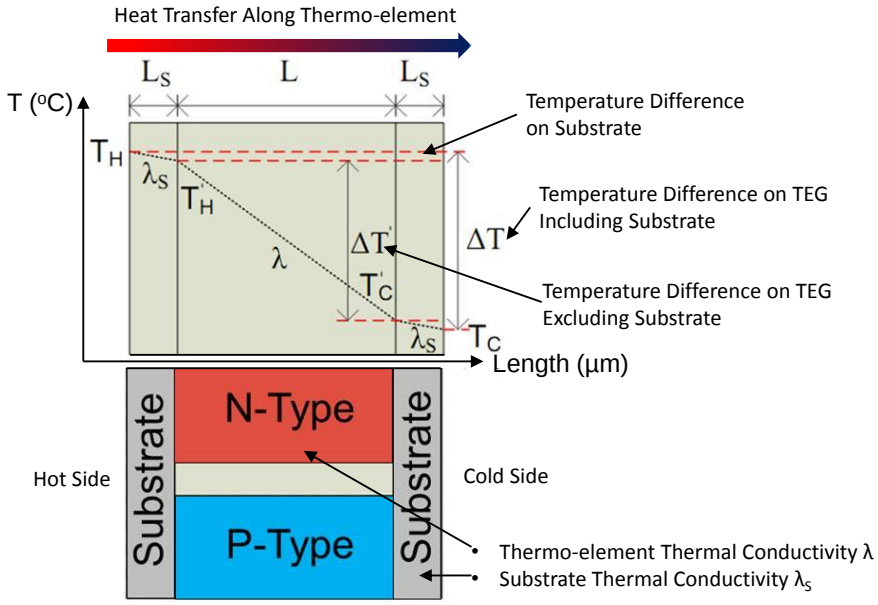



Figure 4.4: Temperature Variations on TEG and Substrates

load is presented in Figure 4.5.

The TEG internal resistance, R, can be mainly attributed to the thermo-element internal resistance, $R_{TE}$, and (copper) contact resistance $R_{CT}$,

$$R = R_{TE} + R_{CT} \tag{4.7}$$

Considering the electrical resistivity of thermo-element$\rho$, contact electrical resistivity, $\rho_C$, the length of thermo-element, L, the length of contact, $L_C$, the cross section area of thermo-element, A, and cross section area of contact, $A_C$, the internal resistance of the module is,

$$R = R_{TE} + R_{CT} = N \cdot (\frac{\rho \cdot L}{A} + \frac{2\rho_C L_C}{A_C}) \tag{4.8}$$

When TEG operates with a matched load i.e. $R = R_L$, with $\Delta T'$ derived from

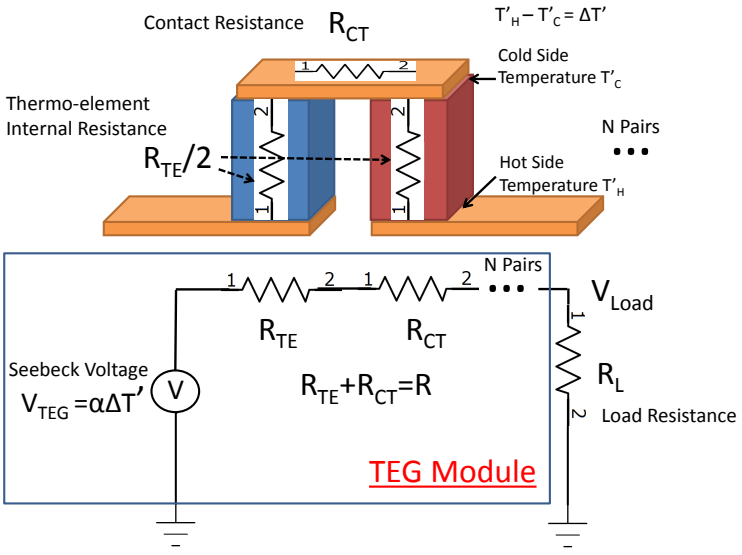



Figure 4.5: Equivalent Circuit of Thermoelectric Generator and Load

Eq 4.5, the TEG voltage output is:

$$V_{load} = \frac{N \cdot \alpha \cdot \Delta T}{1 + 2\frac{\lambda}{\lambda_S} \cdot \frac{L_S}{L}} \tag{4.9}$$

Derived from Eq 4.9 and Eq 4.8, the maximum output power at the matched load condition is:

$$P_{max} = \frac{N \cdot (\alpha \Delta T)^2}{(\frac{\rho L}{A} + 2\frac{\rho_C L_C}{A_C}) \cdot (1 + 2\frac{\lambda L_S}{\lambda_S L})^2} \tag{4.10}$$

When considering the case with MEMS (and nano-wire/tube) thermo-elements used in TEG, the thickness of thermo-elements L will decrease significantly whilst the substrate thickness $L_S$ remains at the same scale as in bulk material based design. This effect may substantially reduce the output voltage on TEG as shown in the voltage output equation Eq 4.9. Although a high number of thermo-elements N will be available in MEMS based TEG design, the internal resistance will be 1-2 orders of magnitude higher than that of the conventionally machined TEG. The output voltage (Eq 4.9) and internal resistance (Eq 4.8) simulations show a trade-off between high voltage and high internal impedance when number of thermo-elements increase. This trade-off is evaluated in the characterization of TEGs in the following section.

### 4.2.2 TEG Device Characterization

In this section, the thermoelectric modules are characterized in order to understand the device performance in typical indoor conditions. The heat source temperature selected in the tests range from $50^oC$ to $80^oC$ in order to simulate the temperature on the surface of typical radiator, water heater or hot water pipes. The tests are conducted on conventional machined TEGs provided by Thermonamic and MEMS based TEGs provided by MicroPelt. This test setup have been used to conduct accurate measurement of the temperature difference. The results are further analyzed to understand the consistency between the thermoelectric module energy conversion theories and the experimental measurements. At the end of this section, power density analysis at module level and device level are discussed to identify suitable TEG for indoor thermoelectric energy harvesting.

#### 4.2.2.1 Thermoelectric Characterization Test Setup

The basic test setup of the thermoelectric device characterization is shown in Figure 4.6. Instead of water cooling or liquid nitrogen cooling systems frequently adopted in most thermoelectric material studies, passive heat sink cooling is used in the setup. This is mainly because the passive heat sink is a more realistic cooling method in the BEM WSN application. The temperature is only controlled on the heat source side, but not on the cooling side. Two PT-1000 resistance temperature detectors (RTD) are attached to the outer surface of the ceramic substrates. The temperature measurements are made through a function generator (to generate voltage signal for RTD measurements) and data logger. The tolerance of the A-type PT1000 RTD is within $0.15^oC$ for room temperature. The maximum temperature error is less than $0.3^oC$ in the setup. The hotplate was heated to temperature between $50^oC$ and $80^oC$ and stabilized with a temperature variation typically less than $1^oC$ from the target temperature. The electrical output of the module is connected to various resistive loads. An oscilloscope was used to measure the output voltage and power. The output power measurement range is between 0mW and 500mW with a resolution around 0.1% of the maximum measurement.

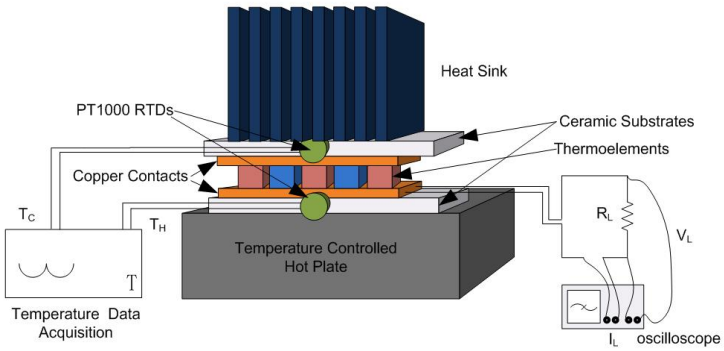



Figure 4.6: Test setup of thermoelectric module characterization

The ambient temperature was also measured to avoid environmental condition variation during the tests. The room temperature is measured before the experiment with less than $1^oC$ fluctuation.

#### 4.2.2.2 TEGs Thermoelectric Parameters

The MEMS based TEG manufactured by Micropelt was characterized first. The $Bi_2Te_3$ compounds (both N type and P type) are deposited onto the silicon substrate and formed the P-N thermo-elements array similar to the conventional bulk TEGs. The thickness of the silicon substrate is 0.525mm on both sides. The height of the thermo-element is approximately $20\mu$m. The prototype TEG tested in this work is MPG-D751 model with a 3.36mm by 3.38mm total area. The number of thermo-elements pairs is approximately 1100. The cross section area of a single thermo-element is $35\mu$m by $35\mu$m. Although the thermal conductivity of the $Bi_2Te_3$ compounds used in this TEG is not clarified in the datasheet, based on the previous published work by Micropelt [105], a thermal conductivity of 2W/mK is estimated. The Seebeck coefficient $\alpha$ and the electrical resistivity $\rho$ were not given in the product datasheet. However, Bottner et al. [105] present these parameters as power factor of the thermo-element. The power factor is an experimental measurement mainly for thermoelectric material quality control. It is defined as $\alpha^2/\rho$ (in the original document, it is shown as $\alpha^2 \cdot \sigma$, where $\sigma$ is the electrical conductivity and $\rho \times \sigma = 1$).

This implementation obtains $30\mu$W$\cdot$ cm$^{-1}$K$^{-2}$ power factor on the N type thermo-element and $40\mu$W$\cdot$ cm$^{-1}$K$^{-2}$ on the P type thermo-element.

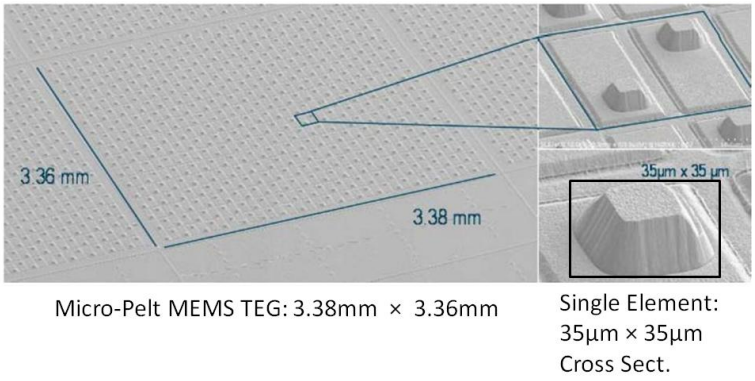



Figure 4.7: Wafer Photograph of Micropelt Thermo-elements [103]

The detailed resistivity of the contacts and thermal conductivity of substrates are presented in [106]. The copper contacts electrical resistivity is $2 \times 10^{-8}\Omega$·m [106]. The thermal conductivity of (pure) silicon substrate is $150W \cdot m^{-1}K^{-1}$ [107].

The cooling device used by the MEMS TEG is a 21 pin aluminium natural convection heat sink. The measured thermal resistance on the heat sink is around $7.1^{o}$C/W. Based on the datasheets, publications of Micropelt and measurement conducted on the MEMS TEG, Table 4.2 summaries the thermoelectric parameters of the TEG.

| Symbol | Definition | Value |
|---|---|---|
| A | Thermo-elements Cross Section Area | $1225\mu m^2$ |
| N | Number of Thermo-elements Pairs | 1100 |
| L | Length of Thermo-elements | $20\mu m$ |
| $L_S$ | Height of Ceramic Substrate | $525\mu m$ |
| $L_C$ | Length of Contacts (between thermo-elements) | 0.15mm |
| $A_C$ | Contacts Cross-Section Area | $750\mu m^2$ |
| $\lambda$ | Thermo-element Thermal Conductivity | $2W \cdot m^{-1}K^{-1}$ |
| $\lambda_S$ | Substrate Thermal Conductivity | $150W \cdot m^{-1}K^{-1}$ |
| $\rho_C$ | Contacts Electrical Resistivity | $2 \times 10^{-8}\Omega m$ |
| $\alpha_N^2/\rho_N$ | Power Factor - N type | $30\mu W/cmK^2$ |
| $\alpha_P^2/\rho_P$ | Power Factor - P type | $40\mu W/cmK^2$ |

Table 4.2: Micropelt Thermoelectric Module Parameters Summary

The conventional bulk thermoelectric module provided by Thermonamic is a

custom-designed module for low power generation. The reason Thermonamic module is selected is it can be made into customer defined configurations (cross-section area, number of thermo-elements pairs etc.). The module utilizes $Bi_2Te_3$ thermo-elements with $36\mu W/cmK^2$ power factor at 300K. For each thermo-element, the cross section area is $0.95mm^2$. A thin layer of ceramic substrate and a layer of heat-conductive foamed carbon thermal pad are applied on each side of the module. The carbon thermal pad is used to increase the heat transfer from the heat source to the module. The total thickness of the module is 3.4mm, while the thickness of ceramic layer and copper contacts is 0.9mm on each side. The height of the thermo-element is 1.6mm. In this basic unit, the total number of thermo-element pairs is 127 (16× 8 array with 2 thermo-elements removed to accommodate contact leads). This custom-designed module can be arranged into configurations with 16 pairs $\times N_{col}$, where $N_{col}$ is the number of columns and $N_{col}$ is a multiple of 2. The thermo-element obtains a thermal conductivity around 1.5W/mK. The power factor for both N type and P type thermo-element is approximately $36\mu W/cmK^2$. The ceramic substrates have a thermal conductivity around 180W/mK at room temperature.

| Symbol | Definition | Value |
|---|---|---|
| A | Thermo-elements Cross Section Area | $0.95mm^2$ |
| N | Number of Thermo-elements Pairs | 127 |
| L | Length of Thermo-elements | 1.6mm |
| $L_S$ | Height of Ceramic Substrate | 0.9mm |
| $L_C$ | Length of Contacts (between thermo-elements) | 1.7mm× 2 (upper and lower substrate) |
| $A_C$ | Contacts Cross-Section Area | $0.1mm^2$ |
| $\lambda$ | Thermo-element Thermal Conductivity | $1.5W\cdot m^{-1}K^{-1}$ |
| $\lambda_S$ | Substrate Thermal Conductivity | $180W\cdot m^{-1}K^{-1}$ |
| $\rho_C$ | Contacts Electrical Resistivity | $1.6\times 10^{-8}\Omega\cdot m$ |
| $\alpha_N^2/\rho_N$ | Power Factor - N type | $36\mu W/cmK^2$ |
| $\alpha_P^2/\rho_P$ | Power Factor - P type | $36\mu W/cmK^2$ |

Table 4.3: Conventional Machined Thermoelectric Module Parameters Summary

In this work, the temperature difference across the module is generated by passive heat sink cooling. Figure 4.8 shows the heat sinks used in this work based on recommendations from TEG manufacturers. While the pin type heat sink is used on MEMS based module(volume $=42cm^3$, thermal resistance $=7.1^oC/W$),

the fin type heat sink is used on bulk TEG module (volume =60cm$^3$, thermal resistance=6$^o$C/W). The correlation between heat source temperature (T) and tem-



Figure 4.8: Heat sinks for MEMS and Bulk TEG Modules

perature difference($\Delta T$) achieved cross the thermoelectric module due to heat sink cooling is shown in measurement results in Figure 4.9. The larger measurement error in MEMS TEG than conventional TEG is due to the location of the sensor. For the miniaturized MEMS TEG, the sensor can only be placed close to the substrates instead of on the substrates since the surface of TEG module substrate is occupied by the heat sink. In this work, detailed heat transfer study on the heat sink was not conducted due to it is not the main research focus.

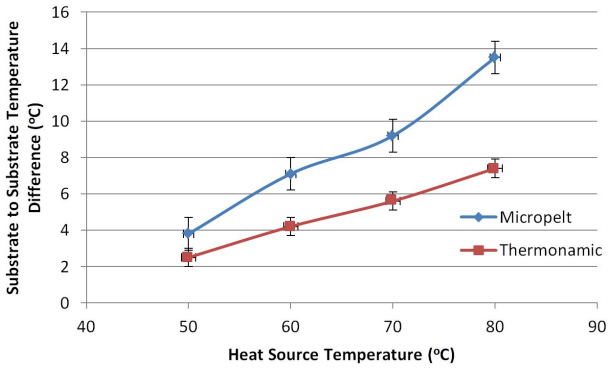



Figure 4.9: Temperature Difference on TEGs ($50 - 80^oC$ heat source) Due to Heat Sink Cooling; MEMS TEG: Micropelt; Conventionally machined: Thermonamic

The temperature difference is measured in 20$^o$C room temperature. The experiment condition is natural convection in a typical lab environment with negligible air flow. The thermal resistance and size/surface area of the heat sink determine the cooling efficiency and the temperature difference on the thermoelectric module. For the heat source temperature ranged between 50 and 80$^o$C, temperatures difference between 2.5$^o$C and 7$^o$C for Thermonamic module, between 4$^o$C and 13.5$^o$C for MEMS module. It suggests that the passive heatsink cools the MEMS TEG more

efficiently due to the smaller size of the MEMS TEG (3.36mm by 3.38mm) compare to the conventional TEG (40mm by 40mm).

#### 4.2.2.3 TEG Electrical Characterization

The I-V characteristics of the MEMS based Micropelt TEG are shown in Figure 4.10. The load resistances are between 10Ω and 50kΩ. Impedance matching is obtained by adjusting the resistive load. The matched load is obtained at approximately 1kΩ as shown in Figure 4.11.

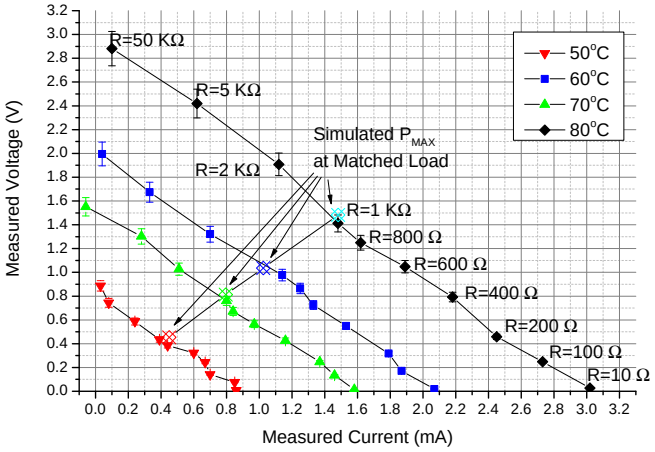



Figure 4.10: I-V Characteristics of MEMS TEGs for different load resistance

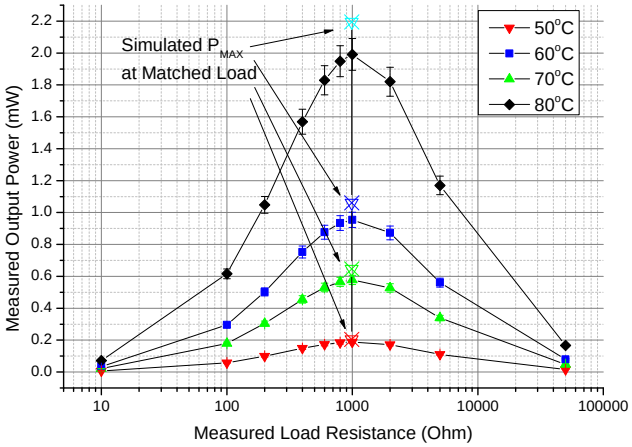



Figure 4.11: Power Characteristics of MEMS TEGs for different load resistance

The analytic model of the maximum output power and voltage in Eq 4.9 and

Eq 4.10 are used to calculate the TEG characteristics when it is operating with matched load. The parameters in Table 4.2 are used in the calculations. The measured and simulated results are shown in Figure 4.10 and Figure 4.11. Given the power factor at 30-40$\mu$W/cmK$^2$, the Seebeck coefficient is calculated at 300-320$\mu$V/K, the characterization and simulation results are shown in Table 4.4. The simulation result shows good consistency with the measured result, with a voltage and power simulation error less than +/-12%.

| Heat Source Temperature ($^oC$) | 50 | 60 | 70 | 80 |
|---|---|---|---|---|
| Module Temperature Difference ($^oC$) | 3.8 | 7.1 | 10.2 | 13.5 |
| Measured Voltage (V) | 0.434 | 0.760 | 0.977 | 1.411 |
| Simulated Voltage (V) | 0.453 | 0.812 | 1.036 | 1.482 |
| Measured Power (mW) | 0.189 | 0.577 | 0.954 | 1.991 |
| Simulated Power (mW) | 0.204 | 0.646 | 1.061 | 2.195 |
| Power Simulation Error (%) | +8.4% | +11.9% | +11.2% | +10.2% |

Table 4.4: Micropelt TEG Characterization and Simulation at Matched Load

One of the factors that leads to difference in simulation and measured result can be attributed to the temperature measurements on the module surface. PT-1000 sensors with +/-0.15 degree temperature measurement error may create error to the temperature measurement. In worst case scenario, the measurement error is 0.3$^o$C, e.g. ($T_H$+0.15$^o$C)-($T_C$-0.15$^o$C)= ($T_H$-$T_C$)+0.3$^o$C. By revisiting Figure 4.9, the 0.3$^o$C worst case temperature error is 6% of a 5$^o$C $\Delta T$.

The I-V characteristics of the bulk Thermonamic TEG are shown in Figure 4.12. The load resistance tested in the characterization is between 1Ω and 1kΩ. The matched load resistance is obtained at 8.5Ω. The output power characterization results are shown in Figure 4.13. The characterization and simulation of the TEG are summarized in Table 4.5. The simulation in the thermonamic TEG shows better consistency than the MEMS TEG. The power simulation errors are less than 5% of the measurement values.

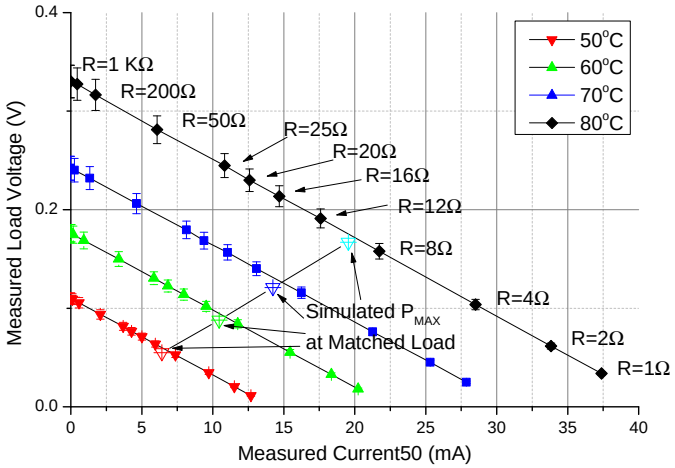



Figure 4.12: I-V Characteristics of Bulk Thermo-element TEG for load resistance between 1Ω and 1kΩ

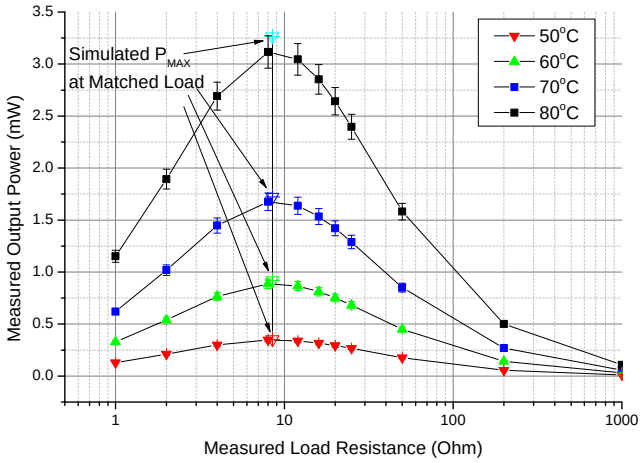



Figure 4.13: Power Characteristics of Bulk Thermo-element TEG

| Heat Source Temperature ($^oC$) | 50 | 60 | 70 | 80 |
|---|---|---|---|---|
| Module Temperature Difference ($^oC$) | 2.5 | 4.0 | 5.5 | 7.5 |
| Measured Voltage (V) | 0.053 | 0.084 | 0.116 | 0.158 |
| Simulated Voltage (V) | 0.055 | 0.088 | 0.121 | 0.167 |
| Measured Power (mW) | 0.346 | 0.886 | 1.676 | 3.117 |
| Simulated Power (mW) | 0.353 | 0.920 | 1.722 | 3.265 |
| Power Simulation Error (%) | +1.8% | +3.7% | +2.7% | +4.6% |

Table 4.5: Thermonamic Bulk TEG Characterizations and Simulation at Matched Load

The measured results (output power, cross section area, device/module volume

| | MEMS TEG | Bulk Material TEG |
|---|---|---|
| Output Power | 0.577mW | 0.886mW |
| Thermoelectric module cross section area | $15mm^2$ | $1600mm^2$ |
| Thermoelectric module volume | $\approx 12mm^3$ | $2560mm^3$ |
| TEG Device volume | $42cm^3$ | $60cm^3$ |
| TEG Device Power density | $13.7\mu W/cm^3$ | $14.8\mu W/cm^3$ |
| Matched Impedance (at MPP) | $1k\Omega$ | $8.5\Omega$ |

Table 4.6: TEG Module performance comparison at $60^oC$ source temperature

and matched impedance) of MEMS and conventional TEG modules and their device power density at $60^o$C heat source temperature are compared in Table 4.6.

The dimension of the heat sink and the power management circuits does not scale down with the MEMS TEG. When the heat sink and circuit board volume are considered in the power density calculation, the bulk TEG obtains a device power density similar to the MEMS based TEG.

The smaller internal resistance in the bulk material based TEG also simplifies the power management process and reduces the power loss in the conversion (see following section). For WSN application without strict limitation on the dimension of the device, the bulk material TEG is a more suitable device.

## 4.3 TEG Power Management

From the device characterization, one main issue discovered for the thermoelectric energy harvesting is: the voltage of the TEG output is one order of magnitude lower than the WSN operating voltage. A voltage step up circuit is required to boost the 100-500mV input voltage to 2.5-4.5V output voltage. This problem leads to two types of proposed power management methods, the first one uses ultra-low voltage boost converter; the second method uses low voltage charge pump and boost converter, a two-stage step up design.

### 4.3.1 Transformer Based Boost Converter

In the ultra-low voltage DC/DC converter, the performance of the single stage boost converter is limited due to the <500mV input voltage. A boost converter with a high turn ratio transformer is required for the application. The low voltage of the TEG is insufficient to provide a reliable power supply. A secondary start up voltage regulator is needed. At the start up phase, the impedance matching circuit is bypassed from the TEG output.

The circuit of a transformer based boost converter for the thermoelectric energy harvesting is shown in Figure 4.14.

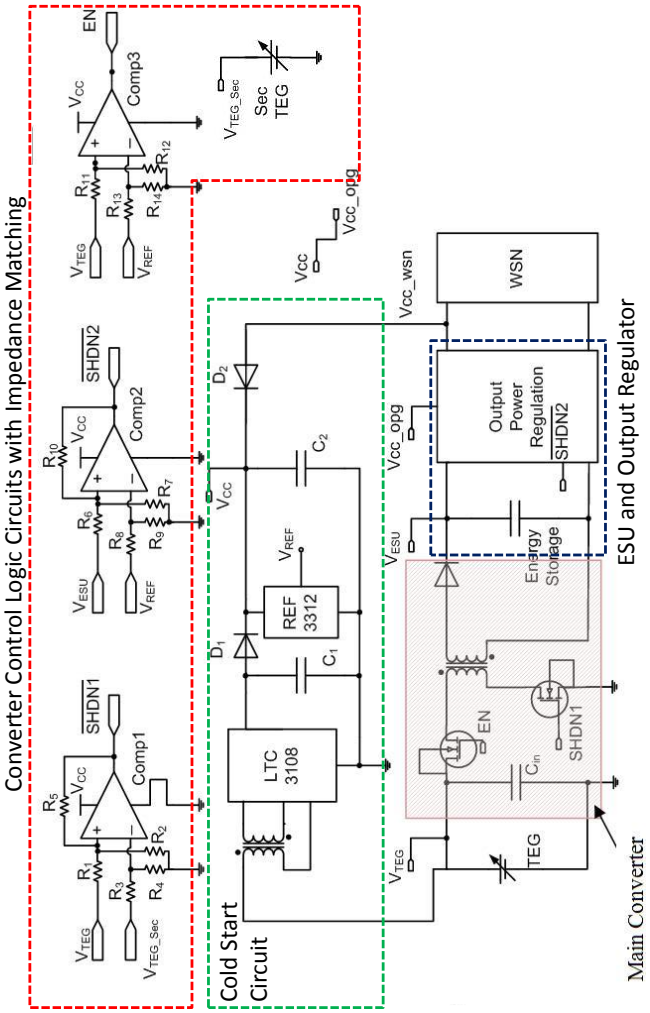



Figure 4.14: Conceptual circuit design of the thermoelectric energy harvesting power management

In this work, main boost converter uses a transformer with a 1:17 turn ratio, whilst the cold start Linear Technology LTC3018 converter features a 1:100 transformer [59]. The LTC3018 functions as the start up converter, whilst the 1:17 transformer ratio boost converter works as the DC/DC converter in normal operating mode.

The device operates in these steps:

1) Once the output voltage of LTC3018 on $C_2$ capacitor reaches the minimum operating voltage of the comparators, the $V_{CC}$ starts to power the control logic ICs.

2) When the output voltage of the main TEG on $C_{in}$ reaches the minimum start up voltage of the main boost converter, the comparator $Comp_3$ will enable EN pin and connect the main boost converter to the main TEG.

3) The voltage of the main TEG output on $C_{in}$ will be compared with the secondary TEG with a voltage divider to detect the 50% of open circuit voltage. The hysteresis comparator output $\overline{SHDN1}$ is then used to control the frequency of the MOSFET on the main boost converter. The duty cycle is then controlled to ensure $V_{TEG}$ always oscillating around half of the open circuit voltage.

4) Matched load output power is used to charge ESU. When ESU voltage is higher than pre-set minimum start up voltage of the output voltage regulator, the $\overline{SHDN2}$ is set to enable the output voltage regulation. The output power regulation generates a constant 3.3V output for WSN mote.

#### 4.3.1.1 Ultra-low Voltage Boost Converter

It is obvious that the main building block of the power management circuit is the ultra-low voltage boost converter. In this work, EnOcean/ Fraunhofer designed boost converter ME-PMA1 ASIC prototype IC is proposed and tested for the purpose of main boost converter. The schematic of the boost converter is illustrated in Figure 4.15. In this design, an N-JFET normally-on switch, a high turn ratio transformer, and two parallel connected switching transistors are used to form the main boost converter. Among the two parallel connected transistors, T1 is used to start the converter, while T2 is employed in steady state. The T1 JFET is chosen as

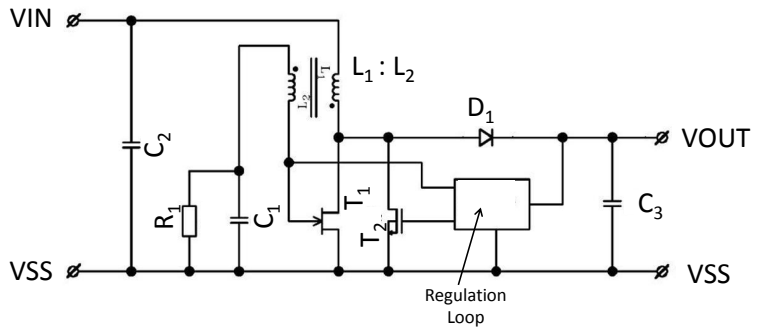



Figure 4.15: Ultra low voltage step up DC/DC converter [108]

start-up switch for the ultra-low gate voltage threshold. The high conduction losses due to large on-resistance($> 10\Omega$) in T1 makes it not suitable to be used as the main switching transistor. Therefore the n-MOS transistor T2 becomes the main switching element after the start-up phase. The parallel connection of both allows having low on-resistance during steady state, and low threshold gate voltage for start-up.

The regulation loop circuit, as in Figure 4.16, consists of starting aid circuit, MOSFET gate protection circuit and an output voltage regulation circuit. C3 and C4 are connected in parallel in the starting aid circuit. C3 is connected in series with a JFET T3. At startup, the gate-source voltage on T3 is 0 V and thus C3 is connected in parallel to C4. The larger capacitance due to the parallel connection initializes the oscillation at relatively low input voltages. JFET T3 is then switched-off during steady state operation and therefore only capacitor C4 (which has a lower capacitance than C3) is active which reduces the gate-source voltage of T2 and switching losses.

This Fraunhofer IIS designed boost converter was built in Tyndall using same parameters as in [108] in order to achieve 50mV start up voltage with discrete components. The boost converter was built by master student Matteo Piovanelli on protoboard under author's guidance.

The protoboard was tested with various input voltage/current to exam its start up performance and conversion efficiency. Figure 4.17 shows the start up performance of this boost converter.

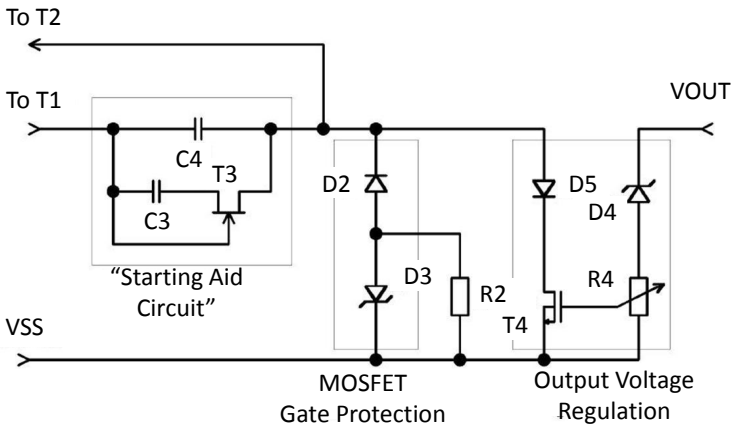



Figure 4.16: Regulation Loop of Ultra low voltage step up DC/DC converter [108]

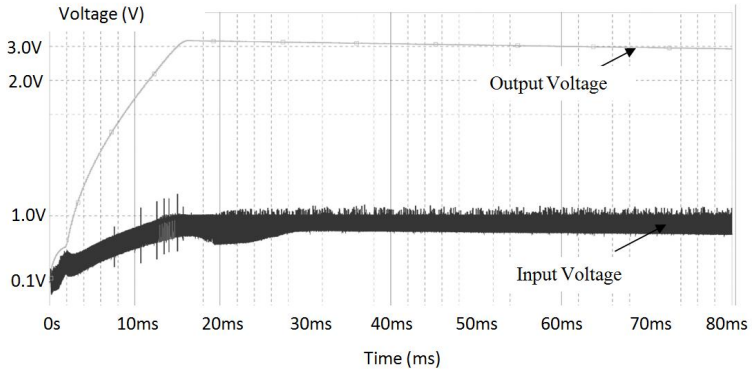



Figure 4.17: Ultra Low Voltage DC/DC Converter Start-up Process

The input capacitor was charged with 100mV input voltage at time 0s. Start up circuit $C_3$, $C_4$ and $T_3$ starts to oscillate around 100mV. The oscillation, however, is not large enough to switch on $T_2$. The gate voltage of $T_1$ follows $V_{C1}$, while $V_{C1}$ discharge through $R_1$. The oscillation increases when energy stored in $C_3$ and $C_4$ discharged into the $C_1$. Eventually, when the oscillation increased to 0.4V, $T_2$ is connected to the circuit, and output voltage reached the targeted 3.0V.

The efficiency test experiments selected four input voltage to simulate the temperature differences on the TEG. The four input voltages are set to 50mV, 70mV, 100mV and 200mV. The output voltage is set to 3.0V with output current ranges from 0.04mA to 80mA. The efficiency results of the experiment are shown in Figure 4.18.

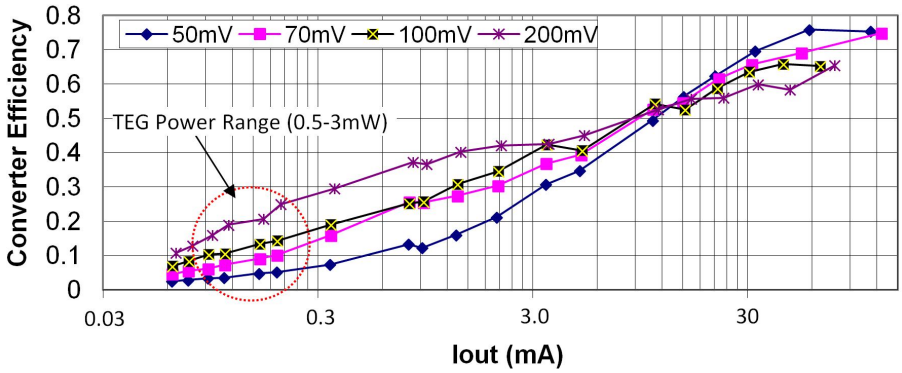



Figure 4.18: Ultra low voltage boost converter efficiency measurements

The boost converter achieved maximum conversion efficiency of 75% with 50mV input voltage. With an input voltage between 50mV and 200mV, the maximum conversion efficiency values all exceed 65%. However, the conversion efficiency is achieved with a 50mA output current. From the characterization of TEG in the last section, such a high current cannot be obtained from the miniature TEG modules.

The more realistic power output range is between 0.15mW and 0.5mW (0.05mA and 0.17mA output current). As shown in the experimental results plot, the conversion efficiency drops to less than 20% in this power range. For lower input voltage (50mV and 100mV), the conversion efficiency is as low as 5%. The conversion efficiency is considered as too low for this application.

This power management circuit also requires significant tuning to optimize the system operation, especially during the start up phase. The main issue associated to this is due to the lack of SPICE simulation model of the JFET $T_1$, and the correlation between transistor $T_4$ and $R_4$. The performance of the switching regulator can only be partly simulated before design and manufacture. This leads to uncertainties for the selection of components. The repeated component adjustments on the prototype to achieve improved performance further increases the cost and complexity of the design.

The low conversion efficiency at mW power level makes this solution less preferred in the design of thermoelectric power management. This method provides good conversion efficiency for 50mW TEG, but not suitable for 1mW applications. This

method was not adopted in the final TEG prototype design.

However, with improved simulation model to optimize the prototype in the future and dedicated IC implementation to reduce the power consumption at the 1mW power level, the design methodology is still very valuable to be further investigated in the future.

### 4.3.2 Charge Pump and Boost Converter Power Management

The previous method considers the utilization of one single stage switching regulator to manage the thermoelectric power. The high step-up conversion ratio of 1:50 to 1:100 (30mV-100mV: 3V-5V) significantly limited the conversion efficiency at 1mW power.

The second issue related to this type of power management is its very narrow peak efficiency voltage "zone" is due to the large and fixed transformer ratio as shown in Figure 2.21. In this example, the 1:100 ratio conversion achieves 40% conversion efficiency. However, for higher voltage e.g. 0.2V (with 1:15 ratio), the conversion efficiency is only 12%.

An alternative method proposed in this work is to include multiple stages of DC/DC converters with smaller conversion ratio and higher efficiency in each stage. The thermoelectric generator also needs to be re-designed in order to reduce the ratio between input voltage and output voltage from 1:100 to the 1:10/20 range. This requires a higher number of thermo-element pairs connected in series and inevitable higher series resistance.

The hypothesis in this section is to investigate if the multiple stages design can achieve higher conversion efficiency, i.e. the aggregated conversion efficiency improvement from the lower voltage conversion ratio can compensate the efficiency loss due to the introduction of multiple stage power conversion and the increased power loss due to the higher internal resistance of TEG as shown in Figure 4.19.

In addition to the multiple stage power conversion, impedance matching is also considered in this design. In the previous method, a dynamic impedance matching

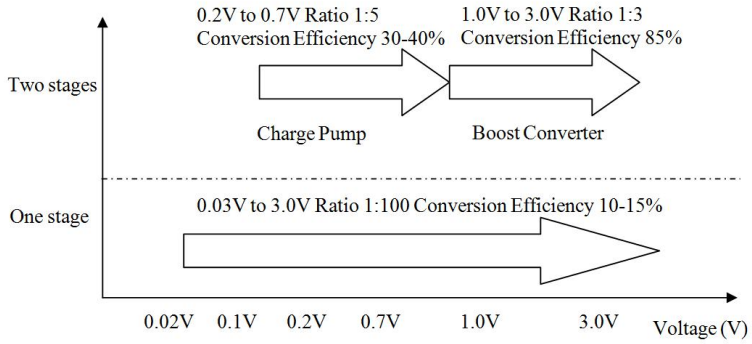



Figure 4.19: TEG Charge-Pump / Boost-Converter Two-Stage Power Management v.s. Boost Converter Single Stage Power Management

method was proposed. However, due to the low conversion efficiency obtained from the DC/DC converter, the value of such impedance matching is very limited. In this two conversion stages implementation, a different impedance matching is proposed.

A study confirmed $Bi_2Te_3$ materials have less than 5% temperature coefficient of electrical conductivity within $50 - 100^oC$ temperature range[109]. Revisiting the characterization of TEG internal resistance illustrated in Figure 4.13, from 50$^o$C to 70$^o$C, the internal resistance changes less than 3%. The internal resistance can be seen as mainly determined by the thermo-element configuration. When the configuration is determined, the TEG will obtain a near constant source resistance and constant open circuit voltage.

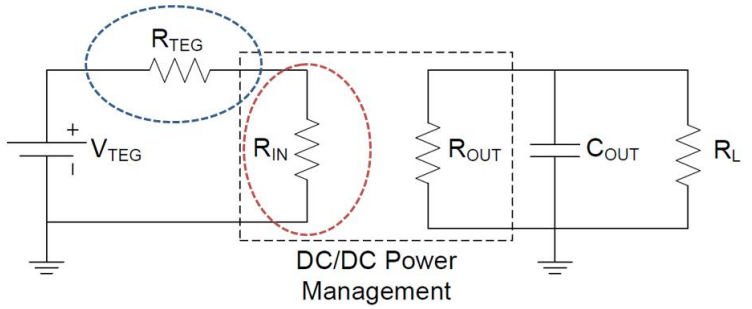



Figure 4.20: TEG Impedance Matching

With a near constant TEG source resistance, changes in the duty cycle of the boost converter can effectively adjust the input resistance of the power management module. By matching the input resistance and source resistance as shown in Figure

4.20, the energy transfer is at maximum efficiency. The DC/DC power management circuit input resistance of $R_{IN}$ can be measured from experiments.

By adjusting the bulk TEG configurations, the source resistance $R_{TEG}$ and TEG open circuit voltage $V_{TEG}$ can be optimized to match the $V_{IN}$ and $R_{IN}$ of the DC/DC converter. This impedance matching method was then implemented and presented in the next section.

#### 4.3.2.1 Charge Pump and Boost Converter

The power management circuit includes two stage of voltage conversion, the charge pump stage and boost converter stage. The schematics are shown in Figure 4.21.

The operation of the two stage conversion is: 1) The ultra-low input voltage of Seiko Instruments S-882Z enables a start up voltage at 150-250mV from the TEG voltage and the input capacitor. 2) The voltage on the output capacitor of the charge pump increases until it reaches the start up voltage of the boost converter at 900mV. 3) The Texas Instruments TPS61020 boost converter starts to operate. 3.3V output voltage is supply at the output end of the TPS61020 converter. The two-stage voltage regulator is then connected to the super-capacitors and output power regulator. The detailed component selection and value are given in Table 4.7.

| Component Name. | Value. | Component Name. | Value. |
|---|---|---|---|
| $C_{IN}$ | $47\mu F$ | $C_{SU}$ | $10\mu F$ |
| $C_{CP}$ | $1\mu F$ | $C_1$ | $47\mu F$ |
| $C_{SC}$ (super-capacitor) | $2.5F$ | $C_2$ | $10\mu F$ |
| $C_{OUT}$ | $47\mu F$ | $L_1$ | $22\mu H$ |
| $L_2$ | $4.7\mu H$ | $R_1$ | $510k\Omega$ |
| $R_2$ | $390k\Omega$ | $R_3$ | $1.6M\Omega$ |
| $R_4$ | $270k\Omega$ | $R_5$ | $1M\Omega$ |
| $R_6$ | $180k\Omega$ | $R_7 = R_8$ | $1M\Omega$ |

Table 4.7: Component Selection for Thermoelectric Energy Harvester

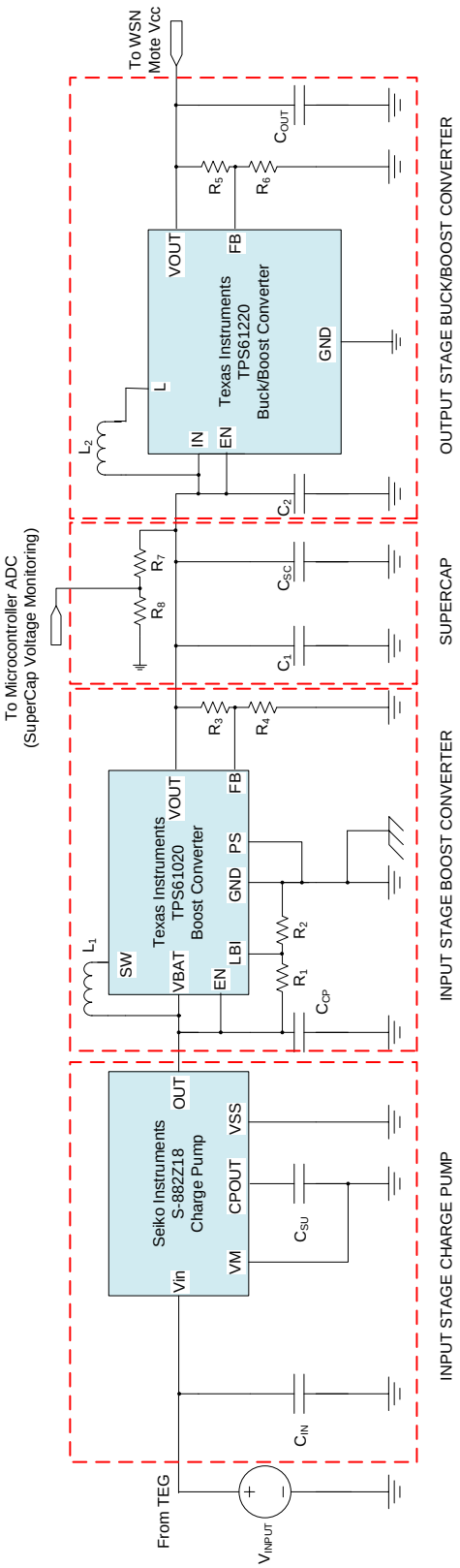



Figure 4.21: Schematics of Charge pump/Boost Converter Power Management

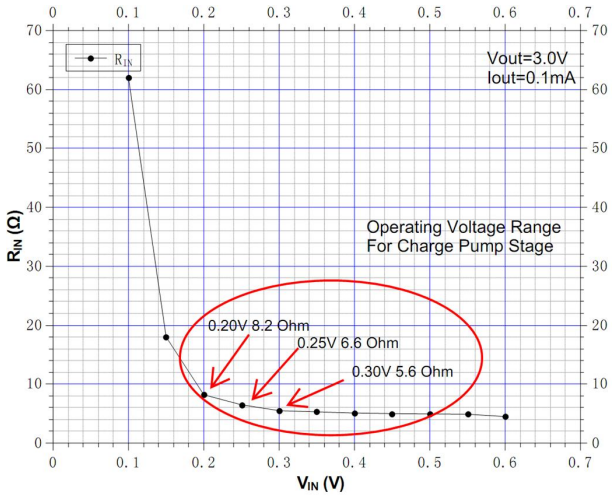



Figure 4.22: Equivalent Input Resistance of the two stage power management circuit

Experiments were conducted to measure the equivalent input resistance of the two stage power management circuit. The input voltage range for the charge pump is between 150mV and 500mV as shown in Figure 4.22.

This implementation obtains input resistance with relatively small variation as shown in Figure 4.22. With DC/DC converter input voltage changes from 200mV to 500mV, the input resistance changes from 8.2Ω to 5.1Ω.

#### 4.3.2.2 TEG Impedance Matching Configuration

In order to optimize the TEG configuration for impedance matching, the first step is to define the number of thermo-elements in the TEG. The number of thermo-elements is determined by the dimension of the TEG. Based on the size limitation stated in Chapter 1, the thermoelectric energy harvester should be smaller than 5cm×5cm.

The dimension of thermo-element is 0.95mm by 1mm by 1.6mm as shown in Table 4.3. The spacing between the thermo-elements is at least 0.5mm in the design rule provided by manufacturer. The maximum number of thermo-element pairs is approximately 600 for the 5cm by 5cm size limit.

Targeted at the 600 pairs total number of thermo-elements, the number 576 pairs

is selected, as the TEG can be arranged in a 16 pairs (in one row) by 36 column array.

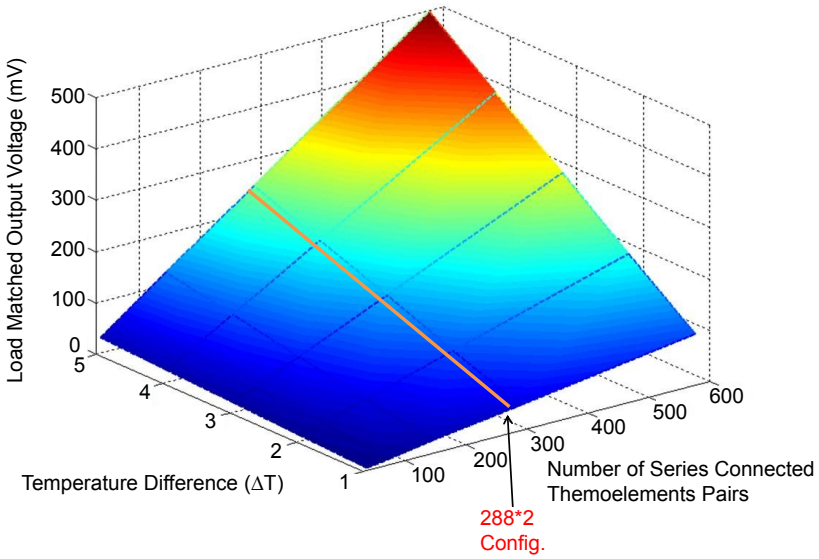



Figure 4.23: TEG Configurations Voltage Analytic Model Simulation Results

This configuration and the dimension of each thermo-element will give the TEG a near square shape (50mm by 54mm). The 36 columns allow the array to be connected in configurations: 1 column × 36 rows; 2 columns × 18 rows; 3 columns × 12 rows; 4 columns × 9 rows; 6 columns × 6 rows; 9 columns × 4 rows; 12 columns × 3 rows; 36 columns × 1 rows. The voltage analysis of the TEG configurations is based on Eq 4.9 and is presented in Figure 4.23.

The TEG internal resistance simulation is based on Eq 4.8. The result of the internal resistance and the charge pump/ boost converter input resistance are presented in Figure 4.24.

The result shows within the charge pump operating voltage range (0.15V-0.5V), the DC/DC converter input resistance and TEG internal resistance are matched in between $R_{IN}$ 8.2 Ω and $R_{TEG}$ 9.9 Ω with voltage between $V_{IN}$ = 200mV and $V_{TEG}$ = 220mV for $\Delta T = 4^oC$. The temperature difference of $\Delta T = 4^oC$ can be obtained from $60^oC$ hot surface in this TEG configuration.

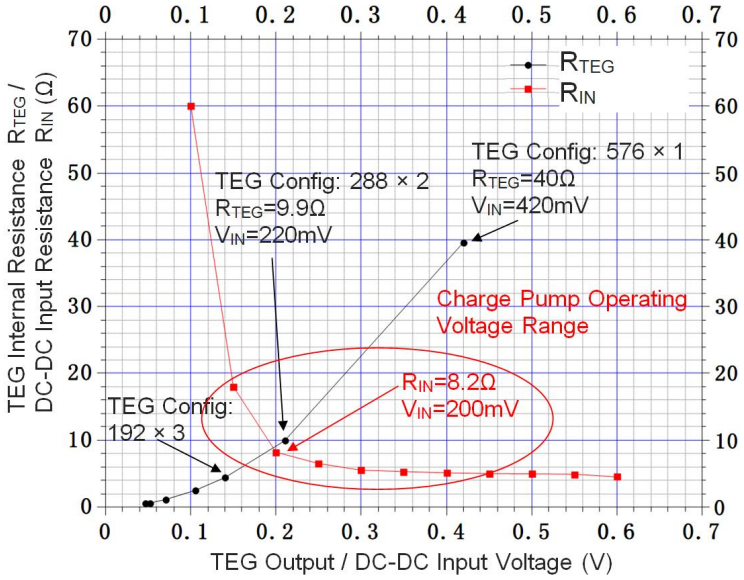



Figure 4.24: TEG Internal Resistance and Power Management Input Resistance Matching for $\Delta T = 4^oC$

With the configuration, parallel connecting two columns of 288 (16 pairs × 18 rows) series-connected thermo-elements pairs, the TEG internal resistance is close to the input resistance of DC/DC converter at the 220mV input voltage.

## 4.4 Prototype Implementation and Experimental Results

Based on the proposed TEG design, the device assembling and packaging were conducted. Four Thermonamic TEG modules with 144 thermo-element pairs (16×9 array) are used to assemble the TEG module. The prototype device is shown in Figure 4.25.

The prototype design also took the thermal dissipation on the PCB layer into consideration. The heat sink of the TEG is fastened to the PCB through a set of four long screws. This configuration allows typical indoor airflow to further cool the heat sink and generates higher temperature difference.

The viability of the TEG design and the application on WSN were tested through

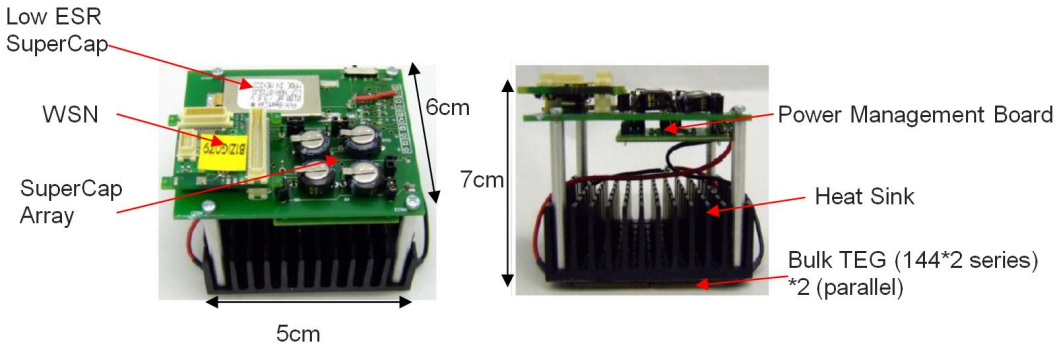



Figure 4.25: Thermoelectric Powered WSN Prototype

a set of experiments. The prototype was placed on hotplate in various temperatures to test the start up performance, continuous operation efficiency and energy storage charge time. The experiment result of the TEG start up at $60^oC$ is shown in Figure 4.26.

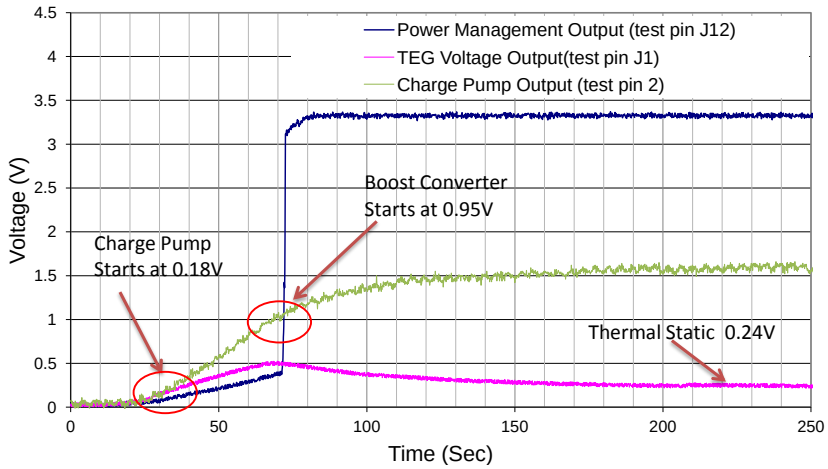



Figure 4.26: TEG Start-up Performance ($60^oC$ Hot Surface, $\Delta T = 4$ kelvin)

The charge pump S882-Z starts at 0.18V, both the input capacitor of charge pump $C_{IN}$ and the output capacitor of the charge pump $C_{CP}$ start to increase. The charge pump is moving towards the target voltage 1.5V. When $C_{CP}$ voltage reaches 0.95V, the boost converter starts to operate and steps up the 0.95V input to 3.3V.

When the start up process completes, the output voltage is stabilized at targeted 3.3V. The I-V characteristics of the TEG and the output of the power management

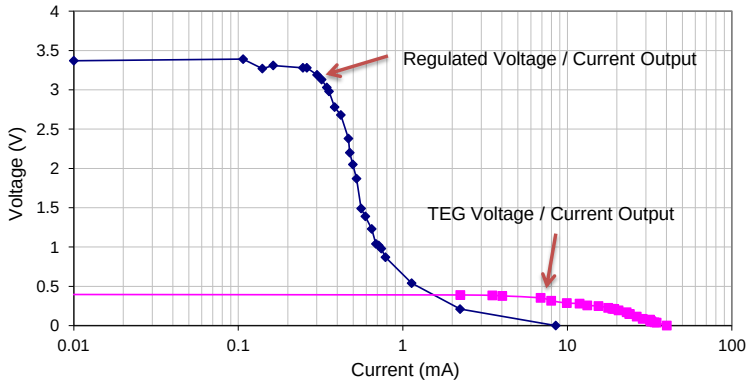



Figure 4.27: TEG I-V Characteristics ($60^oC$ Hot Surface, $\Delta T = 4$ kelvin)

are presented in Figure 4.27. The open circuit voltage of TEG before power regulation is at 0.45V. When the TEG enters the static state, the output voltage of TEG ($C_{IN}$ voltage) is stabilized at 0.24V, close to the theoretical maximum power point at half of open circuit voltage 0.225V (0.45V $\times$ 0.5). This proves the concept of impedance matching of the TEG source resistance and the input resistance of power management. The power-current correlations are plotted in Figure 4.28.

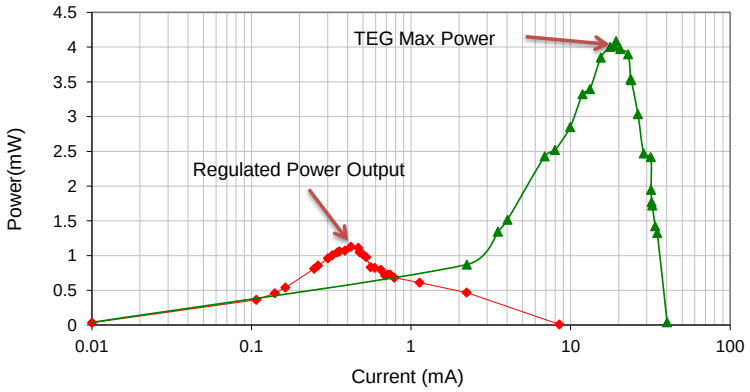



Figure 4.28: TEG Power-Current Characteristics ($60^oC$ Hot Surface, $\Delta T = 4$ kelvin)

The theoretical maximum power of TEG in this case is 4.08mW. The charge pump stage has a conversion efficiency of 28.9% in this measurement. The output power of the power management circuit is measured at 1.11mW. The input two-stage power management conversion efficiency is calculated at 26.8% (charge pump stage efficiency 28.9% $\times$ boost converter stage efficiency 92.9%). When the output power

regulator buck-boost converter TI TPS61220 is also included, the end-to-end conversion efficiency with a resistive load is 25.2% (input two-stage power management efficiency 26.8% × buck-boost converter efficiency 93.8%). The power transfer in each stage of the power management is shown in Table 4.8.

| Stage | Voltage (V) | Current (mA) | Power (mW) | Efficiency (%) |
|---|---|---|---|---|
| TEG Output | 0.25 | 17.0 | 4.08 | |
| Charge Pump Seiko S-882Z | 1.48 | 0.797 | 1.18 | 28.9% |
| Boost Converter TI TPS61020 | 3.25 | 0.338 | 1.097 | 92.9% |
| Buck/Boost Converter TI TPS61220 | 3.30 | 0.312 | 1.029 | 93.8% |
| End-to-end Conversion | 0.25→ 3.3V | 17.0→ 0.312mA | 4.08→ 1.029mW | 25.2% |

Table 4.8: TEG Power Management Energy Transfer

Whilst the boost converter stage achieves 92.9% conversion efficiency, the low start-up voltage charge pump can only obtain efficiency less than 30%. This factor significantly limits the overall conversion efficiency.

Super-capacitor charging experiments have been conducted to investigate the proposed power management circuit in practical applications. Since the energy storage are super-capacitors, the charging time of the super-capacitor relies on the converter equivalent impedance and the output power. Figure 4.29 shows the charging process of the 2.5F super-capacitor from 0V to 3.3V. The three curves (black, red, blue) illustrate the charging characteristics when TEG placed on various heat source temperatures, i.e. different input power.

When charging the capacitive load, the average charging power $P_{avg}$ during the complete charging phase (Charged from 0V to the target voltage $V_{target}$ 3.3V) can be calculated as,

$$P_{avg} = \frac{C_{SC} \cdot V_{target}^2}{2 \cdot T_{chrg}} \tag{4.11}$$

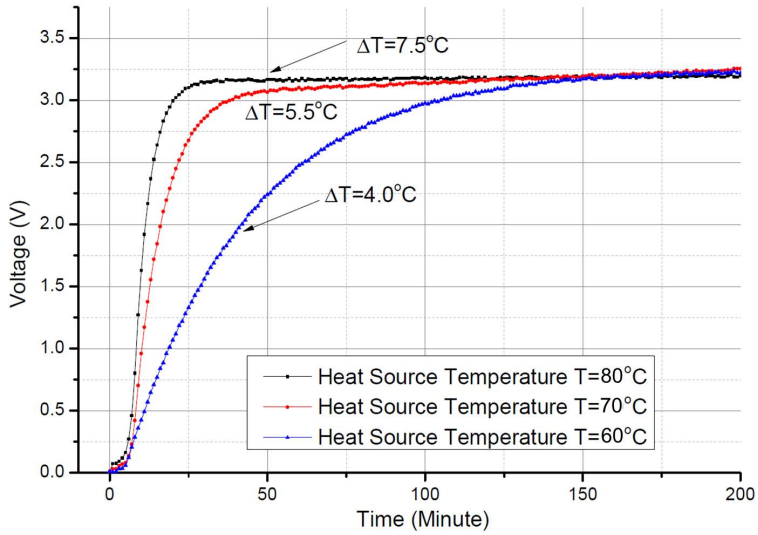



Figure 4.29: TEG Prototype Charges 2.5F Super-Capacitor

where $C_{SC}$ is the super-capacitor capacitance, $T_{chrg}$ is the total charging time. Based on the measured result shown in Figure 4.29, the average charging power is 0.95mW, 2.1mW and 4.35mW on 60$^o$C, 70$^o$C and 80$^o$C hot surfaces, respectively. When compared with the TEG generated maximum power, the efficiency of the conversions are 24%, 23% and 20%, respectively.

The measured conversion efficiency with super-capacitor load is 24% at 60$^o$C instead of 26.8% when the input two-stage power management is tested with resistive load. This further 2.8% (from 26.8% to 24%) power loss is mainly attributed to the charge efficiency of super-capacitor (introduced in Section 3.2.3 shown in Figure 3.6).

Full voltage range (200-700mV) tests have been conducted in this work to study the performance of the prototype. The end-to-end thermoelectric conversion efficiency (complete system including super-capacitor load and output regulation) is shown in Figure 4.30. The input stage conversion efficiency of this work (with resistive load) and state of the art Linear Technology ultra-low voltage boost converter LTC3108 are also compared in Figure 4.30.

The results show that although this proposed solution has lower peak conversion efficiency (LTC3108 40% vs. 29% in this work), the average conversion efficiency is

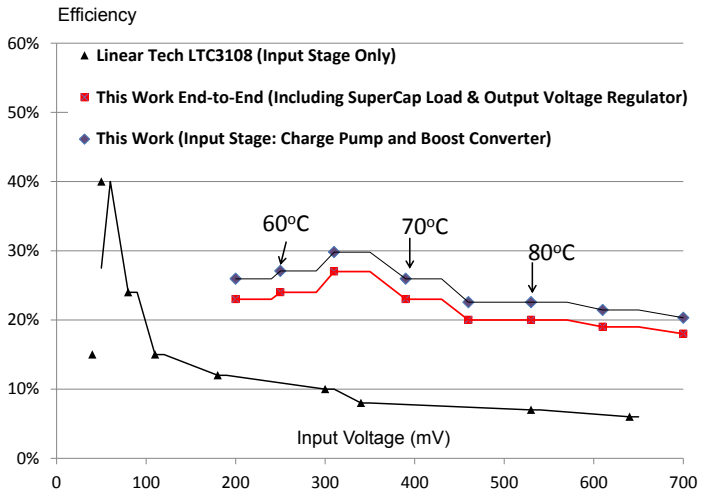



Figure 4.30: TEG power management circuit conversion efficiency (super-capacitor load) compares with Linear Technology LTC3108[59]

more than 2 times higher than LTC3108 when the input voltage is between 200mV and 700mV. This characteristic makes this proposed system suitable for wider range of TEGs and temperatures than LTC3108.

Further tests were conducted when the thermoelectric energy harvester is connected with operating WSN. The WSN mote is the aforementioned Tyndall mote. Its power consumption profile is summarized in Table 2.2. It is programmed with various operating duty cycles. The method for calculating the average power consumption is shown in Eq 2.3.

The WSN average power consumption and the energy storage leakage power are measured and illustrated in Figure 4.31. In order to continuously operate WSN mote from harvested power, the average power consumption must be lower than the thermoelectric energy harvester output power. For each thermoelectric energy harvester operating temperature, the harvested power has a minimal WSN mote measurements time interval and a maximum active mode duty cycle. The thermoelectric energy harvester powered WSN operation limits are shown in Figure 4.31.

For 60$^o$C hot side temperature, the minimal measurement time interval is 5.8

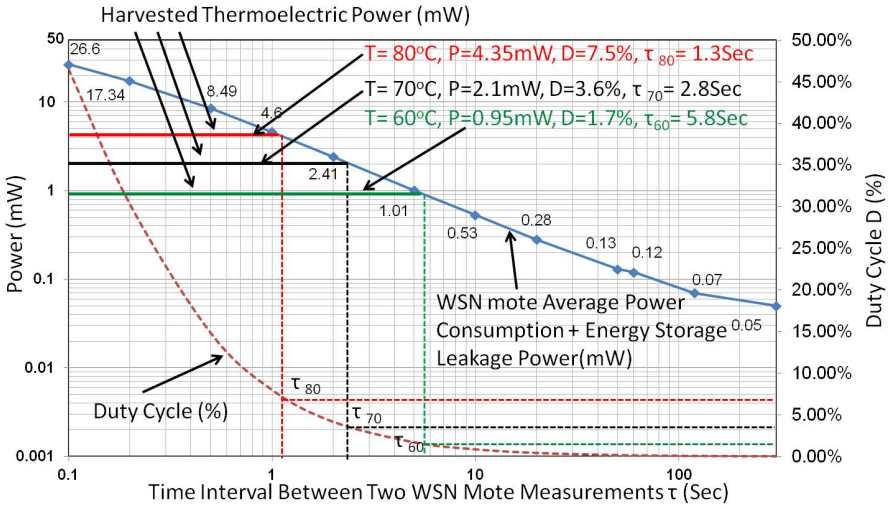



Figure 4.31: Duty Cycle Limits of WSN When Powered From Thermoelectric Energy Harvester

seconds, i.e. when placing the thermoelectric energy harvester on a $60^oC$ heat source, the generated power allows WSN mote to make a BEM measurement and transmit the data every 5.8 seconds. For higher hot side temperatures, the minimal measurement time intervals are shorter. Most BEM applications (light intensity, temperature, relative humidity sensing etc.) require measurements time interval between 1 and 10 minutes. The thermoelectric energy harvester proposed in this work can effectively provide a "power-autonomous" power supply for BEM WSN motes when thermal energy is available.

## 4.5 Conclusion

In this chapter, low temperature thermoelectric energy harvester is investigated for the use of powering wireless sensor networks.

An analytic model simulation of the TEGs is investigated in this work. The results show a less than 12% output power estimation error when applied on MEMS TEGs. Less than 5% output power estimation error is achieved when applied on conventional TEGs. This is the first known model to analyse the trade-off between MEMS and conventional TEGs for real world energy harvesting application. Due

to the similar power density when the cooling device is included and the smaller internal resistance, conventionally machined TEG is selected over MEMS TEG in this work.

A power management circuit was proposed to use a single stage boost converter to perform voltage step-up and dynamic impedance matching to achieve higher efficiency than devices such as Linear Tech LTC3108. The result is only partially successful. The implemented device achieved high conversion efficiency with low input voltage when the input power is >50mW. However, when the input power is limited to 0.5-3mW, as identified in the TEG characterization for $50 - 80^oC$ operational condition, the conversion efficiency only reaches 5-15% with maximum power transfer.

In order to obtain a regulated output voltage from 0.2-0.7V low voltage, another method is considered with multiple stage voltage regulation. The power management adopted the charge pump/switching regulator two-stage design to obtain lower conversion ratio on each stage. The charge pump starts up the voltage regulation when the TEG voltage is higher than 150mV, whilst the boost converter starts up at 0.95V.

Instead of using traditional approach, to adjust load impedance to match the TEG's internal resistance for MPPT, a new design concept is introduced in this work, i.e. configure TEG to match the input impedance of power management circuit to achieve MPPT.

It has been noticed that by adjusting the configurations of TEG, the source resistance and output voltage can be modified to match the power management circuit input impedance. Based on this method, the bulk TEG was re-configured with nearly matched resistance 9.9Ω with 220mV input at $60^o$C (compare to power management circuit input resistance of 8.2Ω at 200mV). The device implementation consists of four 144 thermo-element pairs TEG modules configured in the 288 × 2 thermo-elements layout. At $60^oC$, the output voltage of TEG (input voltage of power management) is measured at 0.24V, close to the 0.225V maximum power voltage (half of the open circuit voltage 0.45).

Although the charge pump runs in a relatively low conversion efficiency of 30%, the high conversion efficiency (approximately 93%) of the second stage voltage regulator TPS61020 from 1.0V to 3.3V allows the input stage (charge pump and boost converter) operate at efficiency between 20% and 29%. Although the peak conversion efficiency is lower than the state of th art, the average conversion efficiency results are more than 2 times higher than state of the art ultra-low voltage dc-dc converter Linear Technology LTC3108. When the super-capacitor and output regulator circuits are included, the system end-to-end conversion efficiency is between 19% and 26%.

Several experiments were conducted to measure the performance of the TEG at different temperatures. For tests with a heat source temperature higher than $60^oC$ in a room temperature environment, the power generated, regulated and supplied from the prototype device is sufficient to operate WSN mote running in low (0.1%) duty cycles and reach the target of power autonomous operation with thermoelectric energy harvesting in real world conditions, e.g. office wall-mounted heater.

# Chapter 5

# Low Intensity Light Energy Harvesting

## 5.1 Introduction

The photovoltaic power is impracticable to be efficiently harvested without maximum power point tracking (MPPT). The situation is even more severe when super-capacitor is adopted as the main energy storage. The several-farad super-capacitor pulls down the small PV cell voltage to the capacitor voltage when they are directly connected to each other. In this case, the charging voltage of PV cell drifts away from the maximum power point (MPP) and may lead to very low conversion efficiency. Without an effective MPPT, only a 20-50% of the MPP efficiency can be obtained [110].

In this chapter, high efficiency power management circuit design for low intensity light energy harvesting is investigated. Novel solutions derived from fractional open circuit voltage (FVOC) based maximum power point tracking for sub-mW PV cells power management are proposed in this work. The two main design goals of this indoor light energy harvester system are:

1. Maximizing the MPPT converter/output voltage regulator power conversion efficiency in sub-mW power level.

2. Minimizing the power consumption in the power management control logic circuits.

The proposed power management module consists of PV cell designated for indoor light energy harvesting, low power control logic circuits, discrete components based switching regulator, specific control scheme and energy storage unit with self start circuits introduced in Chapter 1 to achieve these two design goals. The complete energy harvester block diagram is shown in Figure 5.1.

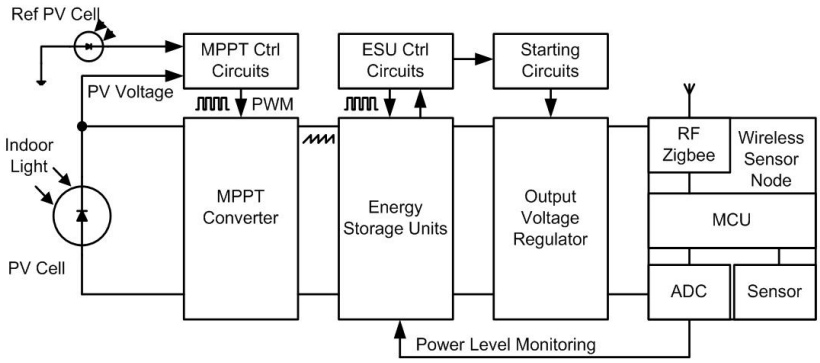



Figure 5.1: Indoor Light Energy Harvester for WSN System Block Diagram

The rest of this chapter is organized as follows: Section 2 introduces the indoor PV cell selection based on PV cell characterization results. Section 3 shows the maximum power point tracking for ultra-low power light energy harvesting, including 1) the buck converter based MPPT; 2) synchronized boost converter based MPPT. Both types of MPPTs are carefully simulated, prototyped and tested. The experimental results of these MPPTs are reported in this section.

Section 4 presents the energy model of the complete indoor light energy harvester prototype with energy storage unit. Long term experimental results are also presented in this section. The energy harvester performance is further discussed based on a case study with emphasis given on the deployment issues. The final section concludes the indoor light energy harvester designs and the evaluation of prototypes in long term WSN system deployments.

## 5.2 Indoor Light Photovoltaic Cell Characterization

### 5.2.1 Test Setup

Commercial off the shelf (COTS) PV cells and Tyndall designed PV cells have been tested with various light sources and light intensity conditions. The halogen illumination is generated from the Euromex EK-1 light illuminator. The low light intensity measurements are conducted with fluorescent lamp. The intensity of the light was measured with a light meter in an integrating sphere (in order to obtain an evenly distributed light scattering on the sample and light meter). Figure 5.2 shows the testing layout before the samples are placed onto the integrating sphere sample holder.

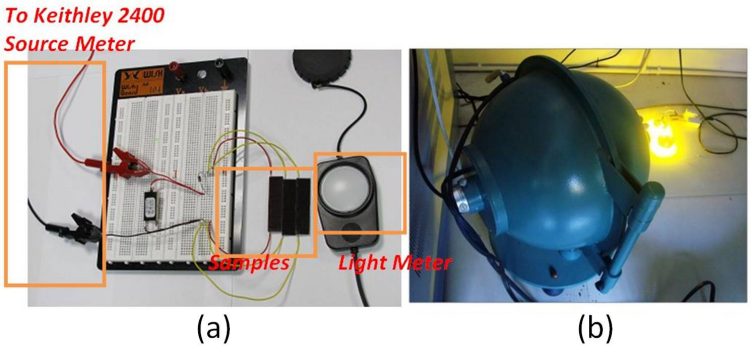



Figure 5.2: PV cell illumination tests: (a) Samples tests setup;(b) Integrating sphere with halogen lamp light source

The adjustable light sources can be programmed to simulate the indoor light (both halogen and fluorescent types) between 100lux and 10klux with +/-5% error. In this characterization, the PV cell power density at typical light intensities in a office is the main focus.

### 5.2.2 PV Cell Electric Model

The PV cell simulation model adopted in this work is the widely used Wolf and Rauschenbach two-diode model[111]. The evaluated I-V characteristics model will be applied in the energy harvesting system model introduced in the later part of

this chapter. Figure 5.3 shows the equivalent circuit of the proposed model for PV cells.

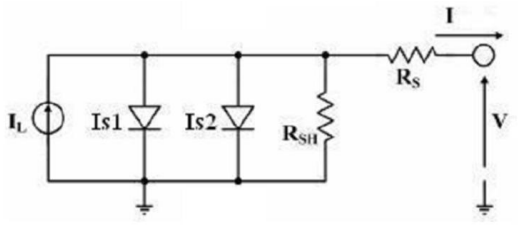



Figure 5.3: Equivalent Electric Circuit of PV cells [111]

The current $I_L$ represents the light generated current. The value of $I_L$ is equal to the short circuit current $I_{sc}$ under illuminance, and can be measured in I-V characterization [112].

Wolf and Rauschenbach observed a correlation between light generated current $I_L$, output current under illumination $I$ and dark current $I_{dark}$ [111].

$$I = I_L - I_{dark} \tag{5.1}$$

Practical measurements of I-V characteristics in illuminated conditions are difficult since small fluctuations in the light intensity often overwhelm the effects of the second diode. It is more common to analyze the double diode model in the dark.

The cell is placed in dark condition with zero light generated current $I_L$ and applied with voltage sweep (normally between zero and 2 times of open circuit voltage $V_{oc}$). Based on [111], the dark current based on double diode model is,

$$I_{dark} = I_{s1}[e^{\frac{q(V-R_s I_{dark})}{n_1 KT}} - 1] + I_{s2}[e^{\frac{q(V-R_s I_{dark})}{n_2 KT}} - 1] + \frac{V - R_s I_{dark}}{R_{SH}} \tag{5.2}$$

where $I_{dark}$ is the measured dark current flowing through the cell, $V$ is the voltage applied on cell, $R_s$ and $R_{SH}$ are the series and shunt resistances. q is the quantum of charge (1.602910E-19 C), k is Boltzman constant (k = 1.381910E-23 J/K), T is the cell temperature, (T=300K in this case). $I_{s1}$ and $I_{s2}$ are the reverse bias saturation current of diode 1 and diode 2, $n_1$ and $n_2$ are the ideality factor of diode 1 and 2.

The key parameters required for solar cell performance simulation are: $R_s$, $R_{SH}$, $n_1$, $n_2$, $I_{s1}$ and $I_{s2}$.

In this work, Kaminski method [113] is used to extract these parameters. This nonlinear regression method has the advantage of extracting parameters with only one dark I-V characterization. It also presents the advantage of being independent of the voltage step in contrary to the Lee method [114].

Kaminski method suggests diode 1 current $I_{s1}$ mainly contributes to the high voltage characteristic. Diode current $I_{s2}$ accounts for the lower voltages and around the maximum power point, where the shape of the overall I-V curve is affected by diode 1 and diode 2 fitting curves.

When the cell is applied with high voltage (larger than open circuit voltage $V_{oc}$), the I-V characteristic is dominated by diode 1 and the series resistance,

$$I_{dark-highV} \approx I_{s1}[e^{\frac{q(V-R_s I_{dark})}{n_1 KT}} - 1] \tag{5.3}$$

The verification of this method has been done on a GaAs cell developed in Tyndall. For Tyndall GaAs cell, diode 1 and series resistance curve fitting and measured dark I-V characteristics are presented in Figure 5.4. The measured dark current and diode 1 curve shows a good fitting result at high voltage (3V - 6V).

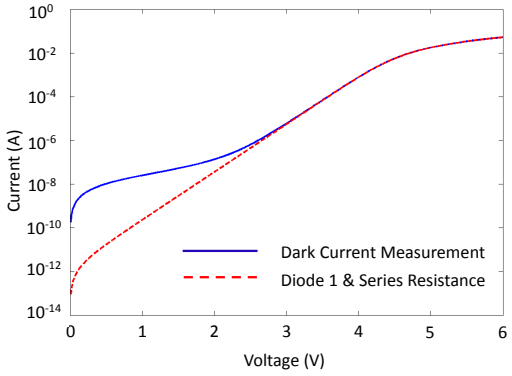



Figure 5.4: Diode 1 and series resistance curve fitting and measured dark I-V characteristics

When the cell is applied with low voltage (smaller than open circuit voltage $V_{oc}$),

the I-V characteristic is dominated by diode 2 and shunt resistance,

$$I_{dark-lowV} \approx I_{s2}[e^{\frac{q(V-R_sI_{dark})}{n_2KT}} - 1] + \frac{V - R_sI_{dark}}{R_{SH}} \tag{5.4}$$

Similar to diode 1 and series resistance curve fitting, diode 2 and shunt resistance curve fitting in Figure 5.5 also show a good consistency with the measured dark current.

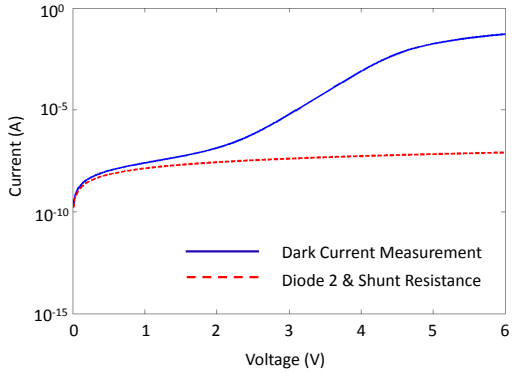



Figure 5.5: Diode 2 and shunt resistance curve fitting and measured dark I-V characteristics

When the two fitting curves are combined, the shape of the curve can be further adjusted by the shunt resistance value to achieve higher consistency. The overall comparison between photovoltaic model fitting curve and measured dark current is shown in Figure 5.6. The results are summarised in Table 5.1.

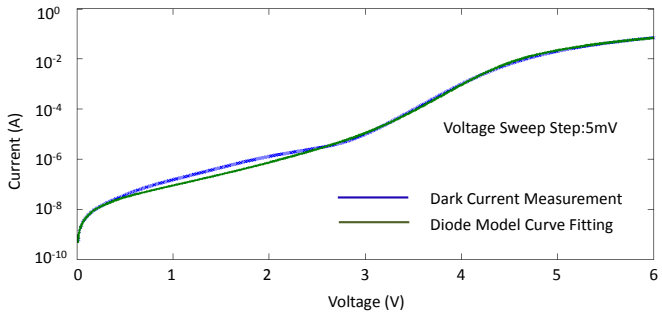



Figure 5.6: Simulated and measured dark I-V characteristics

With dark current characterization, PV cell diode model can be used to evaluate the I-V characteristics under illuminance. In this work, the Kaminski method was

| $R_s$ | $R_{SH}$ | $n_1$ | $I_{s1}$ | $n_2$ | $I_{s2}$ |
|---|---|---|---|---|---|
| 172mΩ | 7.7MΩ | 1.4 | $8.7pA$ | 2.9 | $3.9nA$ |

Table 5.1: Dark Characterization of Tyndall GaAs cells

performed with a non-linear regression software FitAll [1].

### 5.2.3 COTS Photovoltaic Cell Characterizations

In total, four COTS cells are tested to select the high performance PV cell in low light intensity indoor conditions. The main selection criteria are:

1. high output power density in indoor lighting conditions

2. suitable size and weight for the purposes of energy harvester

| | $R_s$ | $R_p$ | $n_1$ | $I_{s1}$ | $n_2$ | $I_{s2}$ | Active Area ($mm^2$) |
|---|---|---|---|---|---|---|---|
| Tyndall | 172mΩ | 7.7MΩ | 1.4 | 8.7pA | 2.9 | 3.9nA | 25 |
| Schott Solar | 20.5Ω | 58.8MΩ | 7.6 | 1.7pA | 20.7 | 3.4nA | 770 |
| SanyoAM1407 | 2.81kΩ | 18.4MΩ | 6.2 | 1.1pA | 41.5 | 27.9nA | 456 |
| SanyoAM1513 | 2.67kΩ | 22.0MΩ | 8.0 | 1.8pA | 46.6 | 14.2nA | 715 |
| Powerfilm | 40.8Ω | 18.6kΩ | 8.3 | 7.3pA | 29.8 | 9.9μA | 2368 |

Table 5.2: Measured Dark Characterization and Active Area Parameters Summary

Dark characterizations have been performed and their results are presented in Table 5.2. It shows a very small parallel resistance (18.6kΩ), $R_p$, in Powerfilm thin film cell. Based on the aforementioned [111] model (Section 5.2.2), it contributes to the low fill factor and low output power.

Table 5.3 summarizes the output power density in 500lux light intensity. The GaAs based Tyndall cell shows a relatively high power density when the light source is halogen type. However, when the light source is switched to fluorescent light, it only achieves 99.2nWmm$^{-2}$ power density, which is 58% less than the power density when applied with 500 lux halogen light.

[1] MTR FitAll curve fitting software www.fitall.com

| | Halogen | Fluorescent |
|---|---|---|
| Tyndall GaAs | 232.1nWmm$^{-2}$ | 99.2nWmm$^{-2}$ |
| Schott | 219.0nWmm$^{-2}$ | 218.9nWmm$^{-2}$ |
| Sanyo AM1407 | 244.7nWmm$^{-2}$ | 247.1nWmm$^{-2}$ |
| Sanyo AM1513 | 222.0nWmm$^{-2}$ | 230.5nWmm$^{-2}$ |
| Powerfilm | 36.6nWmm$^{-2}$ | 1.2nWmm$^{-2}$ |

Table 5.3: Power Density at 500 lux light intensity

For amorphous silicon based Schott and Sanyo cells, the power density is similar, with a difference less than 5%. No power density decline is observed when fluorescent light is used instead of halogen light source.

In modern office and residential buildings, fluorescent lightings have become the main type of light sources. The Sanyo AM series cells obtain power densities between 0.23 and 0.25$\mu$W·mm$^{-2}$ at around 500lux particular in the case of fluorescent lights, outperforms the rest of the measured cells. Thus, Sanyo AM series cells are selected in this work. Although Tyndall cell also obtains high power density in halogen spectrum, the poor performance in fluorescent light conditions eliminates the possibility of using this cell for indoor applications.

## 5.3 Maximum Power Point Tracking

PV cells have I-V (current-voltage) characteristics similar to voltage controlled current source[96]. As introduced in literature reviews, similar to the concept introduced in [115], the fractional open circuit voltage (FVOC) method is adopted in this design. This FVOC method often disconnects the PV cell to monitor the $V_{OC}$ momentarily and followed by adjusting the operative voltage to $V_{mpp}$ [46], [50]. The simple computation and low power consumption make this MPPT method suitable for small scale PV device.

The MPPT method in this work differentiates from previous literatures in six aspects:

1. Low-frequency MPPT is adopted in this work in order to reduce the switching

loss on the MOSFET.

2. Instead of operating in the converter continuous conduction mode, this MPPT converter operates in discontinuous conduction mode with lower inductor current. This is beneficial for reducing certain conduction loss on ESR.

3. The MPPT PMW control signal is generated from analog comparator instead of signal generator circuit in order to reduce the MPPT control logic power consumption.

4. A pilot PV cell (Sanyo AM1417) made from same technology of the main PV cell (Sanyo AM1815/16) is used as the voltage reference. Instead of disconnecting the PV cell to measure the $V_{OC}$, the pilot PV cell provides a reference $V_{OC}$ which is proportional to the open circuit voltage of the main PV cell. This method further reduces the complexity and power consumption of the MPPT controller.

5. Modelling and optimization for sub-1mW input power. The key parameter for power loss analysis including inductor current and the MPPT upper/lower voltage thresholds are optimized towards higher conversion efficiency with 0.5-1mW input power.

6. The efficiency evaluations are based on capacitive load instead of resistive load. This evaluation method can reflect the energy harvester efficiency more accurately in real-world deployment scenario.

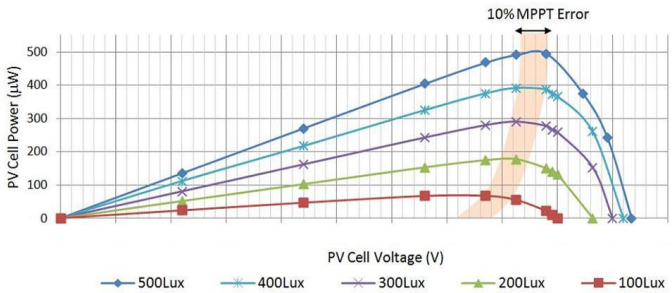



Figure 5.7: Measured I-V Characterizations and MPPT error (100-500 lux)

The I-V characteristics of the PV cell in indoor condition illustrate that a 10% MPPT error illustrated in Figure 5.7 only leads to $< 5\%$ of power loss due to MPPT

inaccuracy. Although the FVOC MPPT method has inferior dynamic tracking capability and tracking accuracy when compared to other methods, for low light intensity conditions, such parameters are less important. Reducing power consumption in the FVOC MPPT is the design priority for this small PV energy harvester.

### 5.3.1 Buck Converter FVOC MPPT

#### 5.3.1.1 MPPT Design

The maximum power is tracked with ultra-low power comparator based control logic. The frequency and duty cycle of a DC/DC converter are controlled by the logic in order to approach the voltage near the ideal maximum power point. The MPP tracker conceptual schematic is shown in Figure 5.8.

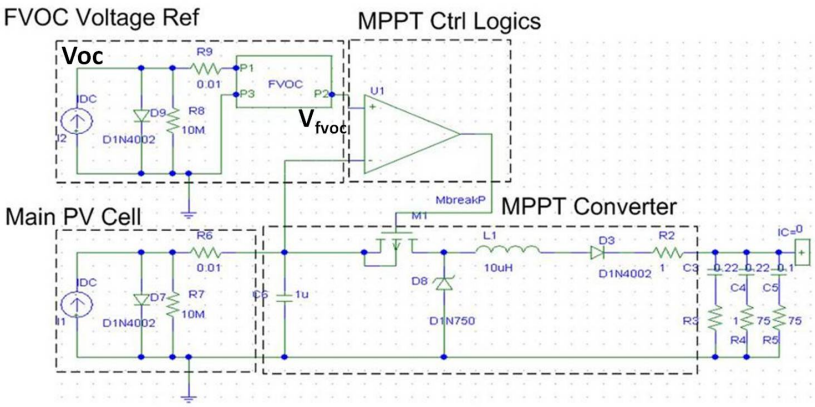



Figure 5.8: Buck Converter based MPPT

This MPP tracker consists of two main parts, namely, MPP tracking control unit and the MPPT converter. In the tracking control unit, a reference voltage is required to set $V_{fvoc}$. A secondary PV cell is used to obtain this reference voltage. By using the same photovoltaic technology as the main PV cell, the reference PV cell produces the same open circuit voltage $V_{OC}$. A pair of resistors is then used to divide the open circuit voltage Voc to the required $V_{fvoc}$. Hysteresis voltage comparators are used as control unit. It generates control signals to drive the MOSFET switch by comparing the reference $V_{fvoc}$ and the main PV cell operational voltage, $V_{pv}$. The

input capacitor $C_5$ provides a temporary energy buffer and allows the PV cell voltage to oscillate around the chosen optimal voltage.

By switching the MPPT converter, the output impedance changes significantly between On-stage/Off-stage and idle-stage. The impedance difference leads to charging and discharging of the input capacitor. Based on the changes of accumulated energy in the input capacitor, the PV cell voltage changes accordingly. By adjusting the hysteresis, the threshold voltage of the comparator and the oscillation can be changed, thus, the sensitivity of the MPP tracking can be adjusted. The controlled MOSFET can then approach the theoretical maximum power point voltage $K_{fvoc} \times V_{OC}$ by oscillating close to the required optimal voltage.

A buck converter structure MPPT is firstly adopted in the design. The simple structure of buck converter makes it relatively easy to simulate and implement. The simplified schematic of the proposed MPPT is shown in Figure 5.9.

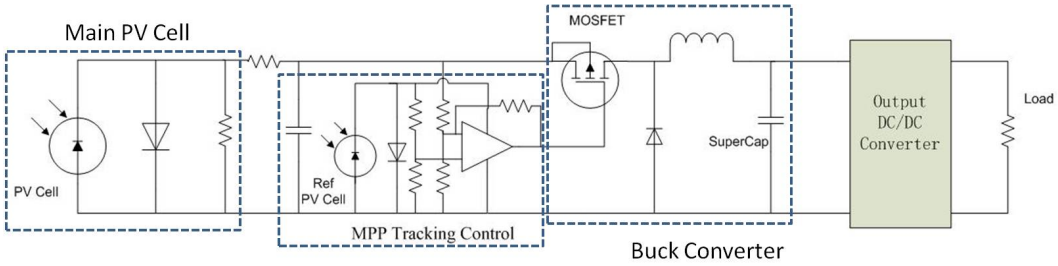



Figure 5.9: Simplified MPPT Implementation with Single Stage Buck Converter

Hysteresis comparator is adopted in the design to switch on transistor when input capacitor voltage (also the PV cell voltage) is higher than $V_{mpp} + V_{hyst}$. The comparator is arranged in a non-inverting Schmitt trigger layout with external hysteresis adjusted by the resistor array. The thresholds are shown in Figure 5.10.

The tracking process was considered in three stages: 1) idle stage 2) switch-on stage and 3) switch-off stage. In this design, a low frequency scheme is adopted in order to minimize the switching power loss. Due to the low frequency operation (long period $T_s$), the switching regulator is running in a discontinuous conduction mode (DCM).

The initial condition is the input capacitor starts at hysteresis lower threshold

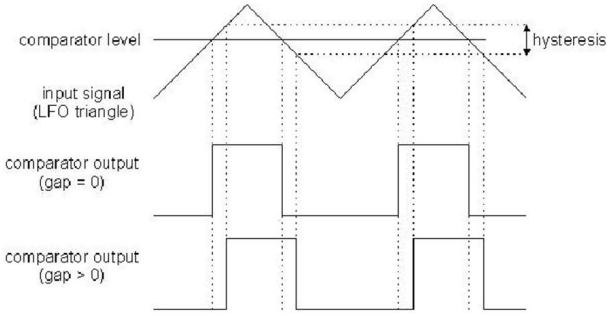



Figure 5.10: Upper and Lower Threshold of Proposed Comparator

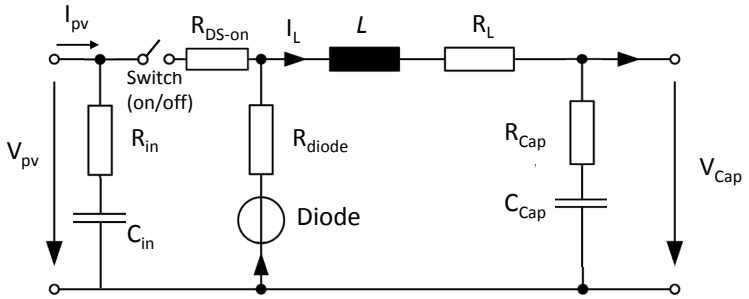



Figure 5.11: Buck converter based MPPT equivalent circuit

voltage $V_{HY-Low}$. The simplified circuit analysis illustrated in Figure 5.11 (when the system is stabilized) shows the operation of buck converter based MPPT in the following three steps:

**Idle-Stage:** During this phase, the input capacitor $C_{in}$ is charged by PV cell from lower hysteresis threshold $V_{HY-Low}$ to the higher hysteresis threshold $V_{HY-High}$. The time to charge input capacitor voltage $V_{pv}$ (including input resistance) from $V_{HY-Low}$ to $V_{HY-High}$ is $T_{idle}$. By applying Kirchhoff's current law and voltage law, KCL and KVL, the correlation between input voltage $V_{pv}$, idle time $T_{idle}$, PV cell current $I_{pv}$, input capacitance $C_{in}$ and input capacitor ESR $R_{in}$ is,

$$V_{HY-High} - V_{HY-Low} = \frac{1}{C_{in}} \int_{T_0}^{T_0+T_{idle}} I_{pv}(t)dt + R_{in}[I_{pv}(T_0) - I_{pv}(T_0+T_{idle})] \quad (5.5)$$

In this work, the voltage hysteresis $V_{HY-High} - V_{HY-Low}$ is inherently small in order to achieve small MPPT error (oscillating close to the MPPT voltage). The difference between $I_{pv}(T_0)$ and $I_{pv}(T_0 + T_{idle})$ from a 40cm$^2$ indoor PV cell is on the scale of

several $\mu$A. For 1mF input capacitor with ESR $R_{in}$ less than 1$\Omega$, the difference of voltage drop on input capacitor ESR is negligible. Thus, Eq 5.5 can be simplified into,

$$V_{HY-High} - V_{HY-Low} = \frac{1}{C_{in}} \int_{T_0}^{T_0+T_{idle}} I_{pv}(t)dt \tag{5.6}$$

$V_{HY-High}$ and $V_{HY-Low}$ are preset by the resistors array, $C_{in}$ is also known. Due to voltage controlled current source behavior of PV cell, the $I_{pv}$ is determined by light current $I_L$, $V_{pv}$ and dark characteristics of PV cells as in Eq 5.2. Thus, $T_{idle}$ can be derived from basic capacitor charge equation.

Since Figure 5.7 shows that within a 10% $V_{MPP}$ error, the variation of PV cell output current is less than 5%. In a further simplified analysis, $I_{pv}$ is considered as constant during $T_{idle}$. Thus, $T_{idle}$ can be expressed as,

$$T_{idle} = \frac{C_{in}(V_{HY-High} - V_{HY-Low})}{I_{pv}} \tag{5.7}$$

The energy loss in this phase is mainly due to the conduction loss on the input capacitor. The simplified conduction loss equation is,

$$E_{loss-idle} \approx I_{pv}^2 \cdot R_{in} \cdot T_{idle} \tag{5.8}$$

In this idle stage, converter switch is off, no energy transfer occurs in the buck converter. The idle stage time and energy loss are determined by the input capacitance, hysteresis voltages and charge current of PV cells.

**"ON" stage:** In this stage, energy transfers from input capacitor $C_{in}$ to inductor L. Inductor current $I_{L-on}$ increases to maximum value $I_{Lmax}$, whilst input voltage decreases back to the lower threshold $V_{HY-Low}$. The inductor current increases from 0 to $I_{Lmax}$ in a period of time $T_{on}$. The on stage duty cycle is $D_1$ as shown in Figure 5.12.

The linear correlation between time t and inductor current can be expressed as,

$$I_{L-on}(t) = \frac{I_{Lmax}t}{T_{on}} \tag{5.9}$$

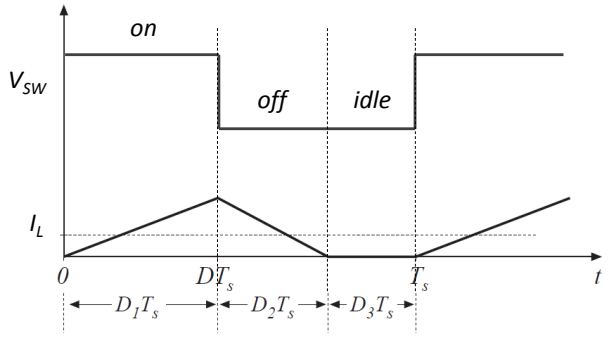



Figure 5.12: Buck converter based MPPT Inductor current

Based on capacitor discharge equation, the input capacitor voltage $V_{pv}$ can be derived,

$$V_{pv}(t) = V_{HY-high} - \frac{1}{C_{in}} \int_0^t I_{L-on}(t) - I_{pv} dt \tag{5.10}$$

derived from Eq 5.9 and Eq 5.10 we have,

$$V_{pv}(t) = V_{HY-high} - \frac{1}{C_{in}} \int_0^t \frac{I_{Lmax} \cdot t}{T_{on}} - I_{pv} dt = V_{HY-high} - \frac{1}{C_{in}} \cdot (\frac{I_{Lmax} \cdot t^2}{2 \cdot T_{on}} - I_{pv} \cdot t) \tag{5.11}$$

the input capacitor voltage $V_{pv}$ at time $T_{on}$ is,

$$V_{pv}(T_{on}) = V_{HY-low} = V_{HY-high} - \frac{I_{Lmax} T_{on}}{2C_{in}} + \frac{I_{pv} T_{on}}{C_{in}} \tag{5.12}$$

Based on the inductor charging model, the inductor current $I_{L-on}(t)$ can also be expressed as,

$$I_{L-on}(t) = \frac{1}{L} \int_0^t V_{pv}(t) - V_{cap} - (R_{ds,on} + R_L) \cdot I_{L-on}(t) dt \tag{5.13}$$

where $V_{cap}$ is the super-capacitor voltage, $R_{ds,on}$ is the switch resistance during "on" stage, $R_L$ is the inductor internal resistance. Derived from Eq 5.11, inductor maximum current at time $T_{on}$ is illustrated in Eq 5.14,

$$I_{Lmax} = \frac{1}{L} \int_0^{T_{on}} V_{HY-high} - \frac{I_{Lmax} t^2}{2C_{in} T_{on}} + \frac{I_{pv} t}{C_{in}} - V_{cap} - (R_{ds,on} + R_L) \cdot \frac{I_{Lmax} t}{T_{on}} dt \tag{5.14}$$

Eq 5.14 can be rewritten into polynomial function with two variables $I_{Lmax}$ and

$T_{on}$,

$$I_{Lmax} \cdot L = (V_{HY-high} - V_{cap}) \cdot T_{on} - \frac{(R_{ds,on} + R_L) I_{Lmax} \cdot T_{on}}{2} + \frac{I_{pv} T_{on}^2}{2C_{in}} - \frac{I_{Lmax} T_{on}^2}{6C_{in}} \tag{5.15}$$

Equation 5.12 can be re-written into this form,

$$I_{Lmax} = 2 \cdot [\frac{C_{in} \cdot (V_{HY-high} - V_{HY-low})}{T} + I_{pv}] \tag{5.16}$$

By combining Eq 5.16 and Eq 5.15, a cubic function of $T_{on}$ is illustrated,

$$\begin{aligned} \frac{5I_{pv}}{6C_{in}} \cdot T_{on}^3 + [(R_{ds,on} + R_L) I_{pv} + (V_{HY-high} - V_{HY-low}) - (\frac{V_{HY-high} - V_{cap}}{3})] \cdot T_{on}^2 \\ + [2I_{pv} L - (R_{ds,on} + R_L) \cdot C_{in} \cdot (V_{HY-high} - V_{HY-low})] \cdot T \\ - 2C_{in}(V_{HY-high} - V_{HY-low}) L = 0 \end{aligned} \tag{5.17}$$

The cubic function can be solved with Matlab function "roots", the function returns three roots of $T_{on}$, one real and two complex. The real root is the on stage time $T_{on}$.

Thus, maximum inductor current $I_{Lmax}$ can be derived from Eq 5.16. The conduction loss equation during "on" stage is presented in the following equation:

$$E_{loss-on} = \int_0^{T_{on}} I_{L-on}^2(t) \cdot (R_L + R_{rs,on} + R_{cap}) dt \tag{5.18}$$

The power loss in this stage is mainly attributed to the internal resistance of inductor and super-capacitor. Most inductors have a near linear correlation between the equivalent series resistance and the inductance. In this case, the correlation is around 1:6000 (i.e. 1mH inductor has 6Ω ESR).

The super-capacitor has a higher equivalent series resistance (ESR) than the input capacitor. However, different from the ESR in inductors, there is no obvious correlation between super-capacitor internal resistance and capacitance. The ESR of super-capacitor mainly relies on the manufacturing process. The super-capacitors with similar capacitance have considerable different ESR when manufactured from

different technologies. The super-capacitor adopted in this design features low ESR at around 1Ω for a 2.5F 5V model.

It is worth noting that, thin film batteries adopted in this work show ESR as high as 50Ω. When a TFB is used as main energy storage unit, the main contributor to the power loss during $T_{on}$ will shift from inductor conduction power loss to TFB conduction power loss.

**"OFF" stage:** During the off stage, converter switch is turned off. Energy stored in the inductor will charge the super-capacitor. The current in the inductor starts to decrease from $I_{Lmax}$ to 0. The time period of this stage is $T_{off}$. The converter switch then remains off after $t_{off}$ and enters idle stage, thus repeat the MPPT process from the beginning.

Based on the "on" stage analysis, the maximum inductor current $I_{Lmax}$ has already been derived. Assuming energy losses are: 1) $I^2R$ conduction loss $E_{cond}$ in components resistance; 2) energy loss in diode $E_{fd}$ due to forward voltage drop $V_{fd}$. The energy transfer model during "off" stage is,

$$E_L = \Delta E_{cap} + E_{cond} + E_{fd} \tag{5.19}$$

where $\Delta E_{cap}$ is the amount of energy delivered to the super-capacitor during "off" stage.

Based on inductor and capacitor energy capacity equations, Eq 5.19 can be re-written as,

$$\begin{aligned}\frac{L \cdot I_{Lmax}^2}{2} = \frac{1}{2} \cdot C_{cap} \cdot [(V_{cap} + \frac{1}{C}\int_0^{T_{off}} I_{L-off} dt)^2 - V_{cap}^2] \\ + \int_0^{T_{off}} I_{L-off}^2(t) \cdot (R_D + R_L + R_{cap}) + I_{L-off}(t) \cdot V_{fd} I dt\end{aligned} \tag{5.20}$$

we also assume the inductor current declines linearly with a correlation expressed as in,

$$I_{L-off} = I_{Lmax} \cdot (1 - \frac{t}{T_{off}}) \tag{5.21}$$

Eq 5.20 can be re-written into,

$$\frac{L \cdot I_{Lmax}^2}{2} = \frac{1}{2} \cdot I_{Lmax} \cdot V_{cap} \cdot T_{off} + \frac{I_{Lmax}^2 \cdot T_{off}^2}{8 \cdot C_{cap}} + \frac{1}{3} \cdot I_{Lmax}^2 \cdot (R_D + R_L + R_{cap}) \cdot T_{off} + \frac{1}{2} I_{Lmax} V_{fd} T_{off} \quad (5.22)$$

The "off" stage time $T_{off}$ can be calculated with Eq 5.23.

$$\frac{I_{Lmax}^2}{8 \cdot C_{cap}} \cdot T_{off}^2 + [\frac{1}{3} I_{Lmax}^2 (R_D + R_L + R_{cap}) + \frac{1}{2} I_{Lmax} V_{cap} + \frac{I_{Lmax}^2 L}{2}] \cdot T_{off} - \frac{I_{Lmax}^2 L}{2} = 0 \quad (5.23)$$

It is worth noting that the on stage duty cycle and off stage duty cycle, $D_{on}$ and $D_{off}$, are not constant even with same components settings. The duty cycles are also affected by super-capacitor voltage as indicated in Eq 5.23. The equations used to calculate the conventional buck converter input/output voltage ratio cannot be applied on this circuit, since the load is a large super-capacitor capacitive load instead of a resistive load.

The power loss analysis is further implemented based on a SPICE model created to understand the impacts from comparator frequency, hysteresis voltage bandwidth, input capacitor size and inductor size on the MPPT conversion efficiency.

The SPICE simulation model is shown in Figure 5.13. Ultra low power components are used to minimize the power consumption of the MPP tracker.

The PV cell is simplified as a current source with 0.23mA constant current output. This is used to simulate a 0.9mW output power with an $V_{MPP} = 3.81$V (Open circuit voltage $V_{OC} = 5.0$V, 0.23mA at 3.81V $V_{mpp}$ [2]) without any variation.

The voltage comparator is Linear Technology LTC1441, which consumes a typical $5\mu$W power. The MOSFET switch used in the circuit is an Intersil ISL43L120 with $< 1.0\Omega$ on resistance. The power consumption of this maximum power point tracker control logic is estimated at $28\mu$W.

[2] power output of two Sanyo AM1815 cells under 500 lux

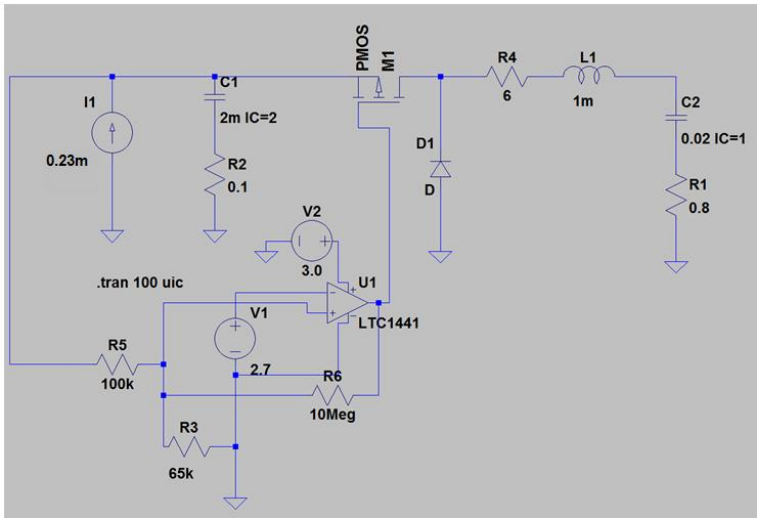



Figure 5.13: Buck Converter MPPT SPICE Model for Power Loss Analysis

In the buck converter simulation configuration, the inductance L is 1mH, input capacitor is $47\mu F$ with 0.1Ω ESR. The ESR of inductor is 6.0Ω. The diode forward drop voltage is 0.3V. The super-capacitor is 1F in capacitance and 1.0Ω in ESR.

The simulation results are shown in Figure 5.14, when the fractional MPP tracking circuit is used, the operational voltage of the PV cells oscillate around the proposed maximum power point voltage $V_{fvoc}$, which is proportional to the open circuit voltage $V_{OC}$, with $K_{fvoc} = 0.76$.

The simulation results show that the voltage on the PV cell output has an average value of 3.80V, with a positive error at +6.1% and a negative error at -6.7%. The simulated inductor current is captured in Figure 5.14, curve $I_L$. The simulated inductor current is 44mA, whilst the analytic calculation result is 48mA. The difference is less than 7%.

More simulations were conducted to verify the analytic model. The calculated and simulated inductor currents show high level of consistency. Simulations with various inductance and input capacitance are conducted to verify the model. The following table summarizes SPICE simulation results of the inductor current and the "on" stage time when inductance is 0.47mH. The analytical model conversion efficiency is calculated when super-capacitor voltage is 1.0V.

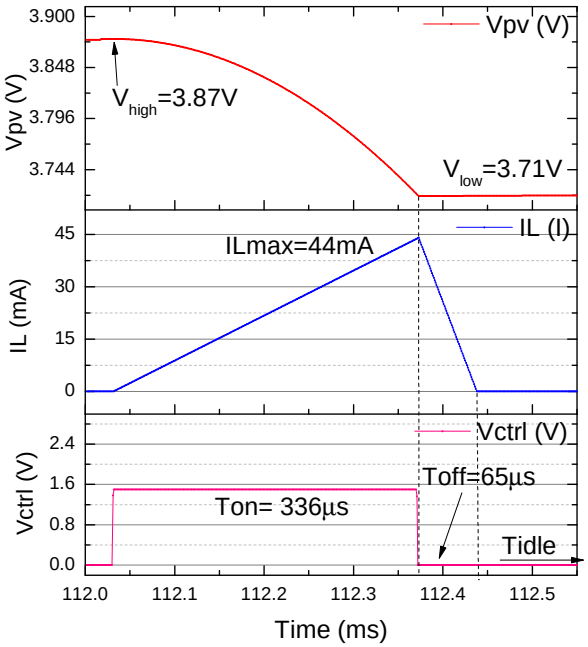



Figure 5.14: SPICE Simulation Results of Buck Converter MPPT PV voltage and Inductor Current(1mH inductor and $47\mu F$ input capacitor)

The simulation results confirm that the power loss mainly consists of ESR conduction loss and power loss due to diode forward voltage drop. The low frequency operation of MPPT only creates a negligible switching loss. The detailed power loss analysis in each component is shown in Table 5.5.

To understand the MPPT conversion efficiency, it is worth noting that, the efficiency estimation highly relies on the super-capacitor conditions. As shown in Eq 5.7, Eq 5.10 and Eq 5.12, the conversion efficiency is only a transient measurement at given super-capacitor voltage.

In this MPPT converter, the output load is a capacitive load, Figure 5.15 shows the conversion ratio increases when the super-capacitor is charged over time. During the charging process, capacitor voltage changes significantly (1.2V to 1.7V in this case, the yellow trace). Thus, the voltage conversion ratio is also not a constant in this case.

The variable conversion ratio leads to two effects:

| Input Capacitor | 0.01mF | 0.05mF | 1mF | 2mF | 10mF | 20mF |
|---|---|---|---|---|---|---|
| SPICE Simulated Inductor Current(mA) | 39.7 | 74.7 | 147.7 | 153.9 | 154 | 156.4 |
| Analytical Models Inductor Current(mA) | 36.5 | 72.4 | 139 | 143.4 | 145.2 | 146.6 |
| SPICE Simulated "ON" Time $T_{on}$(ms) | 0.08 | 0.21 | 2.16 | 4.15 | 20.78 | 41.6 |
| Analytical Models "ON" Time $T_{on}$(ms) | 0.09 | 0.25 | 2.43 | 4.95 | 26.2 | 46.4 |
| Analytical Models Conversion Efficiency (%) | 54.6% | 61.7% | 68.1% | 66.2% | 64.4% | 57.7% |

Table 5.4: Simulated Inductor Current and Control Signal Frequency with 0.9mW Input Power

| Total Input Power: | 100% | 0.900mW |
|---|---|---|
| Loss in Inductor ESR: | 14.2% | 0.128mW |
| Loss in Diode Forward Voltage Drop: | 5.3% | 0.048mW |
| Loss in MOSFET On Resistance | 2.5% | 0.023mW |
| Loss in SuperCap ESR: | 2.4% | 0.023mW |
| Switching Loss: | 0.4% | 0.003mW |
| Loss in input capacitor ESR | 0.2% | 0.002mW |
| Total Output Power: | 74.6% | 0.673mW |

Table 5.5: Power Loss Analysis in Buck Converter MPPT in 1 Duty Cycle (1mH inductor; $47\mu F$ input capacitor; super-capacitor voltage 2.0V)

1) the duty cycle of the buck converter is a variable even when the input voltage/current are constant

2) the efficiency of the buck converter is also a variable when the input voltage/current are constant

The transient conversion efficiency when super-capacitor is at certain voltage is not an accurate and appropriate merit for the system efficiency calculation. Other method which uses resistive load to evaluate the MPPT conversion efficiency as in [44] and [116] also cannot accurately show the system conversion efficiency, since in practical applications the capacitive load is used and its impact should not be ignored during the design. The more accurate measurement should be made on the overall efficiency during the entire charging process from 0V to fully charged condition of ESU. The converter efficiency $\eta_{conv}$ is then calculated by using Eq 5.24.

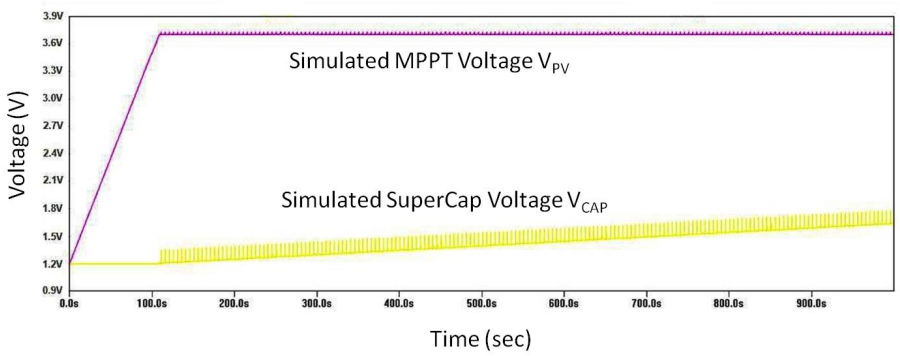



Figure 5.15: Input and Output Voltage Simulation Result (screen capture)

$$\eta_{conv} = (1 - \frac{\sum_{n=0}^{k} E_{loss}}{P_{mpp} \cdot T_{95\%}}) \tag{5.24}$$

where $T_{95\%}$ is the time period for the main super-capacitor to be charged from 0V to 95% of the voltage rating. The leakage current of the ESU is not considered in the simulation.

The MPPT conversion efficiency (with 47$\mu$F input capacitor and 1mH inductor configuration) in the super-capacitor charging process is illustrated in Figure 5.16.

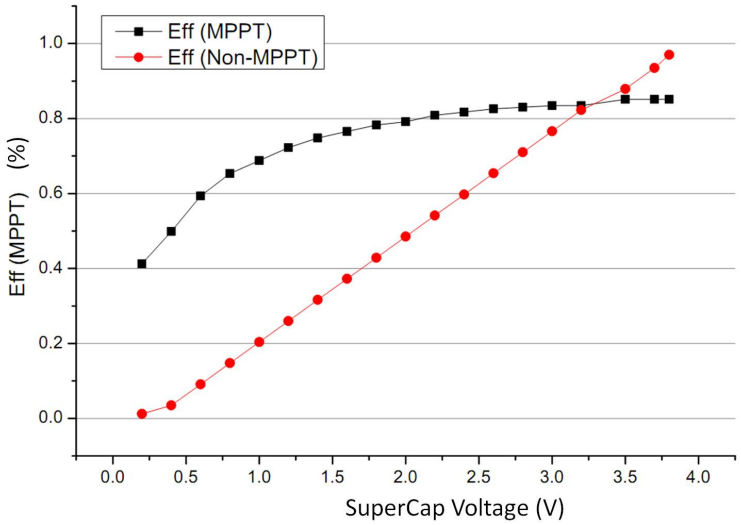



Figure 5.16: Buck MPPT conversion efficiency with different super-capacitor voltages

The overall (super-capacitor voltage charged from 0V to 95% of the voltage rating) conversion efficiency values based on the simulations are shown in Figure 5.17. Two sets of DC/DC converter inductors and six input capacitors are used in the simulations.

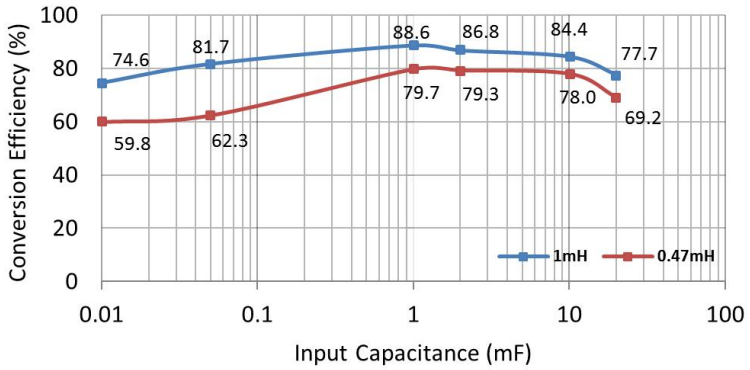



Figure 5.17: Buck MPPT input capacitance/inductance and Simulated conversion efficiency

The optimization between high frequency/low inductor current and low frequency/high inductor current is considered in the components selection. The lowest power loss (high conversion efficiency) is obtained when the input capacitance is near 1.05mF and the inductance is approximately 0.9mH. The maximum conversion efficiency achieved in this simulation is 88.6% at 1mF and 1mH component values.

The proposed concept and simulation is then implemented. Figure 5.18 shows the prototyped buck converter based maximum power point tracker.

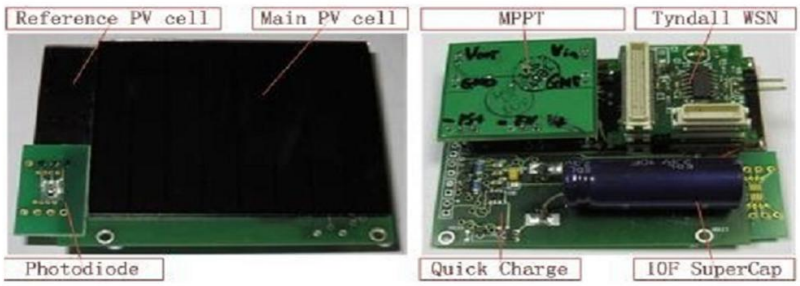



Figure 5.18: Buck converter MPPT and indoor light energy harvester implementation

Several experiments were conducted to validate the simulations and optimize the conversion efficiency with several component choices in realistic conditions. In this implementation, the main super-capacitor $C_{cap}$ is a 10F 2.5V super-capacitor. Two input capacitors 1mF and 20mF $C_{in}$ are tested to verify the simulation results.

The inductance is set at 1mH, near its optimal efficiency value. The main PV cell is Sanyo AM1816 (same Amorphous silicon technology as in AM1407 and AM1513 but with larger active area at 95mm×53mm). The secondary PV cell is Sanyo AM1417 with active area of 35.0mm×13.9mm. The implementation also includes a photodiode to record the light intensity information to the on-board micro-controller. The MPPT processes of the implementation are captured by a Pico data logging system. The results are shown in the Figure 5.19.

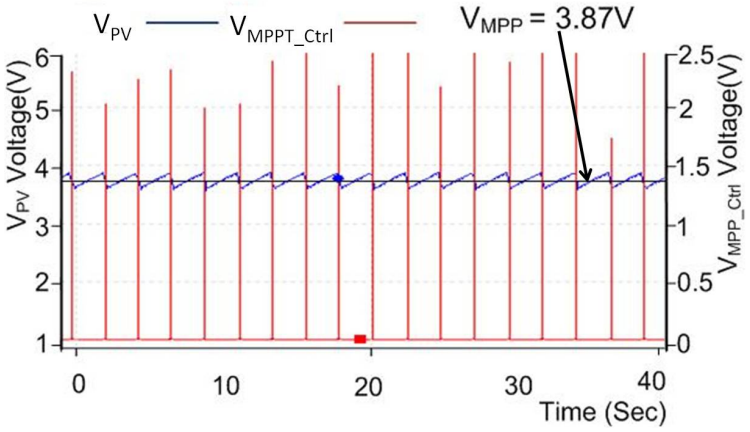



Figure 5.19: Buck converter MPPT Measurement Results: MPPT operation $V_{MPP} = 3.87V$ (1mF $C_{IN}$ configuration)

The MPPT control signal duty cycles are 0.9% when $C_{in}$=1mF. The MPPT charge frequencies in 500lux (≈ 0.9mW) is 0.46Hz. The proposed MPPT operates near the $K_{FVOC}$ at 78.6% of the open circuit voltage 4.92V with a maximum error less than 9.3%. This maximum power point tracking result $V_{MPP}$=3.87V is very close to the ideal $V_{mpp}$ 3.74V (76% of open circuit voltage 4.92V). The average error is less than 3% of the ideal MPP voltage.

In this work, average efficiency is measured by comparing the charged energy in super-capacitor to the total input light energy as expressed in the Eq 5.25.

$$\eta_{conv} = \frac{C_{cap} \cdot (V_{C1}^2 - V_{C0}^2)}{2 \cdot P_{PV} \cdot T_{Charge}} \cdot 100\% \tag{5.25}$$

One of the test capacitor charge experimental results are shown in Figure 5.20. By measuring the charge time T and calculating the theoretical maximum power, the system conversion efficiency is evaluated using Eq 5.25.

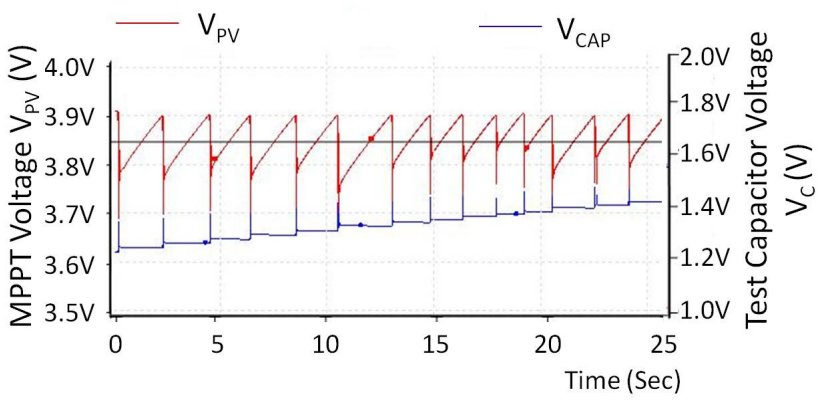



Figure 5.20: Buck converter MPPT Measurement Results: MPPT Circuit Charging Test Capacitor(100mF)

As illustrated in Figure 5.20, for 100mF test capacitor, the 25 seconds test charges it from $V_{C0} = 1.23$V to $V_{C1} = 1.41$V. Similar measurements were repeated with various test capacitors. Based on these measurement, the 1mF input capacitor with 1mH inductor configuration reaches average MPPT conversion efficiency at 79.6%.

By directly comparing the PV cell output powers during super-capacitor charging in two conditions: 1) with MPPT; and 2) without MPPT; leads to the following power gain results. In this condition, the theoretical maximum power for the $96mm \times 54mm$ AM1816 PV cell output poweris measured at 0.90mW.The MPPT power gain is defined by the following equation,

$$Power\ Gain = (\frac{P_{mppt}}{P_{non-mppt}} - 1) \cdot 100\% \tag{5.26}$$

With the 1mH inductor and 1mF input capacitor configuration, the average MPPT

output power (charge from 0% to 95% of the ESU) is 0.71mW, 79.6% of the theoretical maximum power. This MPPT implementation was the first known indoor light energy harvesting device suitable for sub-1mW PV cell applications when published in 2010 in ACM Journal of Emerging Technologies in Computing Systems [117].

In this configuration, the secondary PV cell only works as a reference cell and starts up the comparator logics. It does not supply power to the converter during normal operation. The conversion efficiency is entirely calculated on the main PV cell.

It is important to consider the power loss due to the energy storage unit leakage current. Derived from ESU leakage characterizations in Chapter 3, the average current loss for the 10F super-capacitor due to leakage current is between 20-35$\mu A$. By taking the aforementioned Maxwell UltraCap super-capacitor leakage factor into consideration, the power gain result is shown in Figure 5.21.

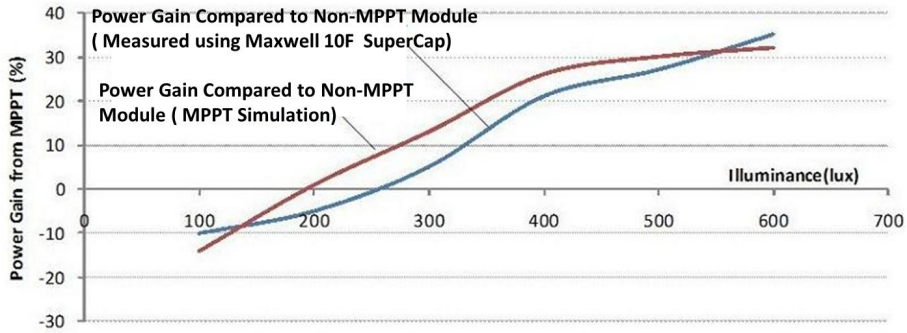



Figure 5.21: Power Gain from MPPT compared to Non-MPPT Configuration (Simulated vs. Measured Results) with 10F super-capacitor

By using the MPPT, the power gain is approximately 30% at the 550 lux light intensity condition. The minimum light intensity required for MPPT to improve the power output is approximately 245lux with this PV cell configuration (real-world condition with super-capacitor).

For light intensity lower than the minimum threshold, the power consumption of the MPPT offsets the power gain from the optimized output power. The buck converter based MPPT is particularly suitable for PV cell with high open circuit voltage and ESU with relatively low voltage rating. Without synchronous rectification, the

voltage drop of diode in the buck converter contributes a significant percentage of the MPPT power loss.

In addition, for indoor PV cells, the open circuit voltage may not always be higher than the ESU voltage rating. For small PV cells with low voltage and low power, the boost converter shows better design flexibility. In the next section, the boost converter based MPPT and synchronized rectifier switching for the ultra-low power MPPT are introduced for ultra-low power (<0.5mW) and low voltage indoor light energy harvesting.

### 5.3.2 Synchronized Boost Converter MPPT

The energy storage unit introduced in chapter 3 including super-capacitors and thin film batteries has voltage rating between 2.0V to 5.5V. To utilize the buck converter based MPPT described in Section 5.3.1, the PV cell voltage should be higher than the voltage rating. However, for miniature PV cells (less than credit card size approximately 50mm × 50mm), especially the single cell module, the open circuit voltage is less than 2.0V. The boost converter MPPT can be used for low voltage PV cells and high voltage rating ESU. In this section, boost converter MPPT is introduced for such applications.

In the power loss analysis of buck converter MPPT circuit, one obvious discovery is the body diode forward voltage drop contributes greatly to the total power loss. For switching regulation power system with low inductor current, the phenomenon is more evident. While lower current reduces the $I^2R$ loss exponentially, the near constant diode forward voltage drop only reduces the $I \cdot V_{fd}$ power loss linearly.

Synchronized rectifier switching regulation is frequently used to reduce the power loss in the diode forward voltage drop. The conventional synchronized rectification (SR) requires the use of specific SR control FET with Schottky diode, monitoring the inductor current by inserting a 10 to 30mΩ sense resistor in series with the inductor and auxiliary control system. The control system operates the two MOSFETs individually and often uses certain algorithms to maintain a short but compulsory

"dead time" and ensures "break-before-make". For the energy harvesting system, such complex power management is difficult to achieve with a small power budget. A new synchronized rectification method is introduced in this work to operate SR with pre-calculated dead time without complex control circuits and Schottky diodes offering a very low conduction loss.

The schematic of the synchronous boost converter based MPPT is shown in Figure 5.22. The MPPT consists of two main building blocks. 1) Comparator based MPPT controller; 2) synchronous boost converter. The boost converter is controlled by PWM signals generated from the ultra-low power comparators. A secondary PV cell is used to obtain a reference open circuit voltage $V_{PV-Ref}$ to set the theoretical $V_{MPP}$. Made from same photovoltaic technology as the main PV cell, the reference PV cell obtains open circuit voltage $V_{oc-ref}$ proportional to the main PV cell open circuit voltage.

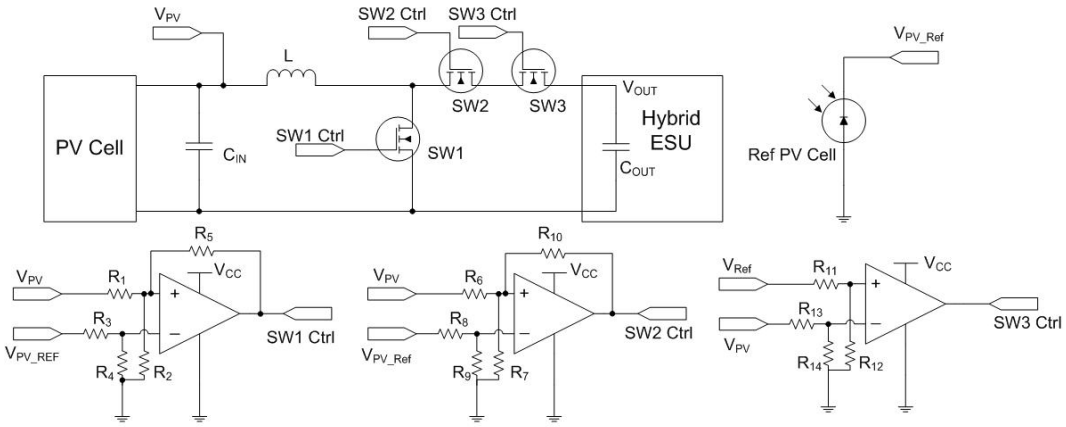



Figure 5.22: Schematics of Maximum Power Point Tracking

A SPICE model is created to simulate the boost converter MPPT. The captured simulation results show two cycles of the power tracking process in Figure 5.23.

Hysteresis is adopted in the design to switch on transistor SW1 when input capacitor voltage (PV cell voltage) is higher than $V_{MPP} + V_{hyst1}$. The input capacitor is then discharged whilst the inductor L is charged with variable current $I_L(t)$. Once the capacitor voltage drops to $V_{MPP} - V_{hyst1}$, the SW1 is turned off due to the hysteresis, the "ON" stage time is $t_0$ to $t_1$.

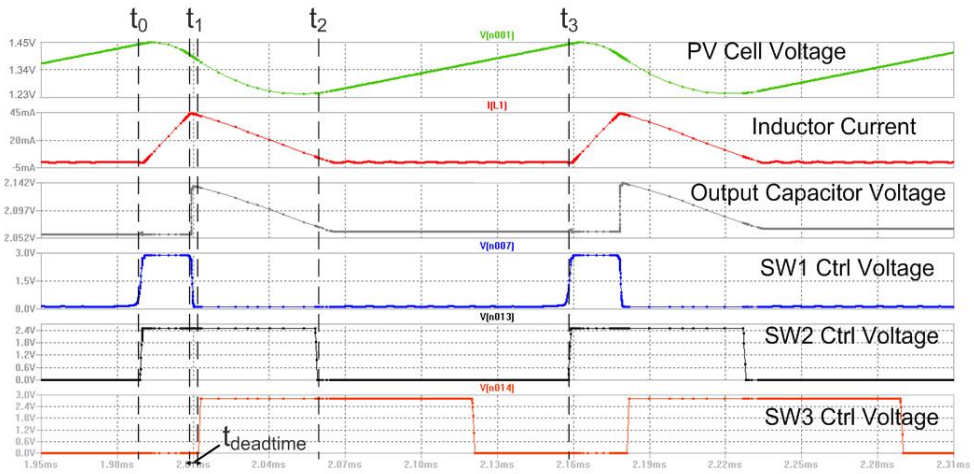



Figure 5.23: Converter SPICE simulation and control signals of SW1, SW2 and SW3

It is worth noting that the charging process in the simulation adopts small output capacitors in order to accelerate the charging speed and better illustrate the results. In actual cases, the time between $t_2$ and $t_3$ is 1-2 orders of magnitude longer than this simulation. SW2 is switched on when PV cell voltage is within $V_{MPP} + V_{hyst1}$ and $V_{MPP} - V_{hyst2}$. The hysteresis voltage $V_{hyst2}$ is larger than the hysteresis for SW1 $V_{hyst1}$.

SW3 is controlled with a voltage comparator without hysteresis as shown in Figure 5.13. SW3 is only switched on when PV cell voltage drops to $V_{MPP} - V_{hyst1} - V_{deadtime}$. The additional voltage difference $V_{deadtime}$ ensures SW3 only switches on after the SW2 is completely switched off. Thus, in a short period $t_{deadtime}$ (known as dead-time) both SW1 and SW3 are switched off to avoid shorting the output super-capacitor reversely through SW1. After SW3 is turned on, the energy stored in inductor, $L$, is discharged into the output capacitor, $C_{OUT}$, in this phase. The hysteresis can be easily adjusted by scaling the resistors in the voltage divider to amend the MPPT accuracy and frequency.

The adoption of the two switch SW2 and SW3 in series provides a means to better control the on/off time and dead-time with simple and low power comparator logics. SW2/3 and SW1 perform a synchronous rectification without output switch

drive. Similar to the hysteresis adjustment, the dead-time can then be changed with the resistance of comparator voltage divider. The power loss on the diode forward voltage drop is entirely eliminated in the design. As a result, the power conversion efficiency is improved.

In order to assess the concept and optimize the MPPT design, a SPICE simulation for power loss analysis is created with its equivalent schematics shown in Figure 5.24. The power loss model describes the three phases of the energy conversion. The converter "on-stage" when SW1 is switched on between $t_0$ and $t_1$ is shown in Figure 5.24 (a). The converter "off-stage" where SW1 is off, SW2 and SW3 are "on" between $t_1$ and $t_2$ is shown in Figure 5.24(b). The "idle-stage" when all transistors are switched off, while the input capacitor is charged from PV cell between $t_2$ and $t_3$ are also shown in Figure 5.24(b).

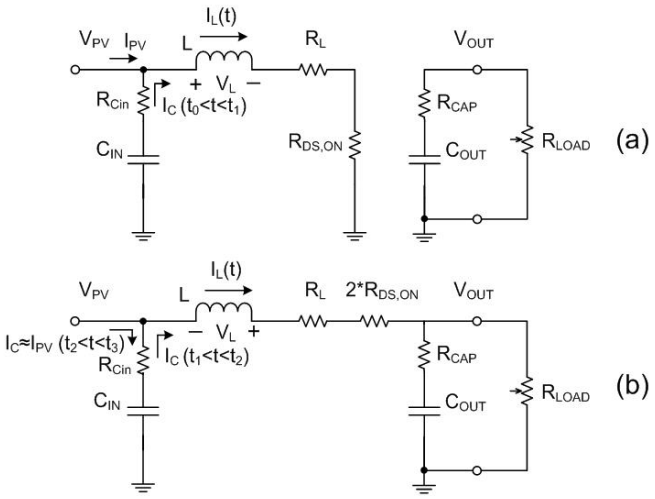



Figure 5.24: (a) On-stage ($t_0$-$t_1$) equivalent circuit (b) OFF-stage ($t_1$-$t_2$) equivalent circuit and Idle-stage ($t_2$-$t_3$) equivalent circuit

The power loss analysis in the following paragraphs are based on the equivalent circuit analysis in Figure 5.24 and the simulation results shown in Figure 5.23.

The power loss in the MPPT circuits consists of conduction loss, control IC power consumption and switching loss. The <1mW low input PV cell power can only charge the input capacitor at a relatively low speed, the magnitude of the cycle time $T_s$ is of the order of 10 milliseconds, the boost converter operating at a frequency

less than 1KHz. Due to the low frequency and the low current nature of the circuits, the switching loss is negligible. The main energy losses are due to conduction loss $E_{cond}$, MPPT error $E_{error}$ and control IC power consumption $E_{ctrl}$.

$$E_{loss} = E_{cond} + E_{error} + E_{ctrl} \tag{5.27}$$

The power consumption of control IC is near constant and mainly relies on the COTS comparator IC. The main variable in the power analysis is the conduction loss in the inductor, on-resistance of transistors and internal resistance of capacitors. As illustrated in Figure 5.23, the boost converter operates in discontinuous conduction mode (DCM mode). The power loss analysis is then divided into three stages: On-stage, off-stage and idle-stage.

**On-Stage:** At time $t_0$, the PV cell voltage, also the input capacitor voltage, $V_{PV}$ reaches the upper voltage limit of the preset MPPT hysteresis $V_{MPP}$+$V_{hyst1}$. SW1 is then switched on, the input capacitor transfers the stored energy into the inductor and the PV cell also charges the inductor in this stage. By applying Kirchhoff's voltage and current laws to the circuit, the voltage behaviour is shown in Eq 5.28.

$$V_L(t) = L\frac{di_{L,on}(t)}{dt} = V_{pv}(t) - (R_L + R_{ds,on}) \cdot I_{L,on}(t) \tag{5.28}$$

The inductor current, the main impact factor of the power loss, is shown in Eq 5.29. The inductor current increases until time $t_1$ and dissipates power on inductor internal resistance and the on resistance of the transistor.

$$\begin{aligned}\frac{1}{2}I_{Lmax}^2 L + \int_0^{T_{on}} I_{L,on}^2(t) \cdot (R_L + R_{ds,on} + R_{Cin})dt \\ = \frac{1}{2}C_{in}[(V_{mpp} + V_{hyst1})^2 - (V_{mpp} - V_{hyst1})^2] + P_{pv} \cdot T_{on}\end{aligned} \tag{5.29}$$

The on stage time $T_{on}$ is mainly determined by the hysteresis and input capacitor. Due to the near linear increases of the inductor current (also proved in the SPICE

simulation), the inductor current can be approximated by the following equation,

$$I_{L,on}(t) = \frac{I_{Lmax}}{T_{on}} \cdot t \tag{5.30}$$

With the presumed linear correlation between inductor current $I_{L,on}$ and time t, the energy transfer during on stage in Eq 5.29 is changed into,

$$\frac{1}{2} I_{Lmax}^2 L + \frac{1}{3} I_{Lmax}^2 (R_L + R_{ds,on} + R_{Cin}) T_{on} = 2 C_{in} V_{hyst1} V_{mpp} + P_{pv} \cdot T_{on} \tag{5.31}$$

In the input capacitor, the voltage decreases from $V_{MPP}+V_{hyst1}$ to $V_{MPP}-V_{hyst1}$, the voltage change can be expressed in the following equation,

$$V_{MPP} - V_{hyst1} = V_{MPP} + V_{hyst1} - \frac{1}{C_{in}} \int_0^{T_{on}} I_{L,on}(t) dt \tag{5.32}$$

The equation can be further simplified into,

$$2 V_{hyst1} = \frac{1}{2} \cdot \frac{I_{Lmax} T_{on}}{C_{in}} \tag{5.33}$$

By combining Eq 5.33 and 5.31, inductor maximum current $I_{Lmax}$ can be derived in the following equation,

$$\frac{1}{2} I_{Lmax}^3 \cdot L + \frac{4}{3} \cdot I_{Lmax}^2 \cdot (R_L + R_{ds,on} + R_{Cin}) \cdot V_{hyst1} \cdot C_{in} - 2 C_{in} \cdot V_{hyst1} \cdot V_{mpp} \cdot I_{Lmax} - 4 P_{pv} \cdot V_{hyst1} \cdot C_{in} = 0 \tag{5.34}$$

With Matlab "Roots" function, the only positive and real root of $I_{Lmax}$ is,

$$roots\ [\frac{1}{2} \cdot L,\ \frac{4}{3} \cdot (R_L + R_{ds,on} + R_{Cin}) \cdot V_{hyst1} \cdot C_{in},\ -2 C_{in} \cdot V_{hyst1} \cdot V_{mpp}, - 4 P_{pv} \cdot V_{hyst1} \cdot C_{in}] \tag{5.35}$$

Once $I_{Lmax}$ is known, the "on" stage time $T_{on}$ can be calculated using the following equation derived from Eq 5.33,

$$T_{on} = \frac{4V_{hyst1}C_{in}}{I_{Lmax}} \tag{5.36}$$

Once the input capacitor voltage (also the PV cell voltage) drops to $V_{mpp} - V_{hyst1}$, switch SW1 is turned off. The MPPT converter enters the "OFF" stage.

**off-stage:** From $t_1$ to $t_2$, the switches SW2 and SW3 are switched on, the energy accumulated in the inductor and input capacitor is discharged into the ESU. Based on the SPICE simulation, it is obvious that the MPPT converter is operating in a discontinues conduction mode. In the off-stage, the inductor current decreases from $I_{Lmax}$ to zero.

The voltage in input capacitor $C_{in}$ further decreases in this stage from $V_{mpp} - V_{hyst1}$ to $V_{mpp} - V_{hyst2}$ as shown in SPICE simulation. Hysteresis voltage $V_{hyst2}$ is also set by the comparator resistor array. The voltage change in the input capacitor can be used to express the relationship between the off stage time $T_{off}$, inductor current $I_{off}(t)$ and the hysteresis voltages,

$$V_{mpp} - V_{hyst2} = V_{mpp} - V_{hyst1} - \frac{1}{C_{in}} \int_0^{T_{off}} I_{off}(t)dt \tag{5.37}$$

Assuming a linear correlation between "off" stage time and inductor current,

$$I_{L,off}(t) = I_{Lmax} \cdot (1 - \frac{t}{T_{off}}) \tag{5.38}$$

Considering the linear correlation, the Eq 5.37 becomes,

$$V_{hyst2} - V_{hyst1} = \frac{1}{2} \frac{I_{Lmax}T_{off}}{C_{in}} \tag{5.39}$$

Since maximum inductor current $I_{Lmax}$ is known, $T_{off}$ is directly determined by hysteresis voltages and input capacitor.

In this stage, since the diode is replaced by synchronous switches, the $I_L \cdot V_{fd}$ diode

forward voltage drop power loss is replaced by the switch on resistance conduction loss $I_L^2 \cdot R$.

The equivalent resistance in the converter during this stage $R_{off}$ is comprised of ESR of inductor $R_L$, on resistance of SW2 and SW3 $R_{ds,on}$, input capacitor ESR $R_{Cin}$ and super-capacitor ESR $R_{cap}$,

$$R_{off} = R_L + 2 \cdot R_{ds,on} + R_{Cin} + R_{cap} \tag{5.40}$$

The energy transfer from input capacitor and inductor to the super-capacitor in this stage can be described as,

$$\frac{1}{2}I_{Lmax}^2 L + \frac{1}{2}C_{in}[(V_{mpp} - V_{hyst1})^2 - (V_{mpp} - V_{hyst2})^2] = \int_{t_1}^{t_2} I_{L,off}^2(t) R_{off} dt + \frac{1}{2}C_{cap}[(V_{cap} + \frac{1}{C_{cap}}\int_{t_1}^{t_1} I_{L,off}(t)dt)^2 - V_{cap}^2] \tag{5.41}$$

with a linearly decreasing inductor current, the energy transfer in Eq 5.41 becomes,

$$\frac{1}{2}I_{Lmax}^2 L + \frac{1}{2}C_{in}[(V_{mpp} - V_{hyst1})^2 - (V_{mpp} - V_{hyst2})^2] = \frac{1}{3} \cdot I_{Lmax}^2 \cdot R_{off} \cdot T_{off} + \frac{1}{2}C_{cap}[(V_{cap} + \frac{I_{Lmax}T_{off}}{2C_{cap}})^2 - V_{cap}^2] \tag{5.42}$$

In the implementation, the comparator which controls SW3 is carefully adjusted to include a short deadtime in order to avoid SW1, SW2 and SW3 simultaneously conducting current.

Comparing with buck converter which adopts rectifier diode instead of synchronous switches, the power loss is reduced in this configuration. The detailed power loss analysis is given in Table 5.6,

**Idle stage:** From time $t_2$ to $t_3$ the MPPT circuit enters an idle stage, SW1, SW2 and SW3 are switched off during this stage, the input capacitor voltage is charged from the lower hysteresis threshold to the upper threshold. In this work, the input current $I_{PV}$ is one to two orders of magnitude lower than the inductor current. The

| Total Input Power: | 100% | $500\mu W$ |
|---|---|---|
| Loss in Inductor ESR: | 10.6% | $53\mu W$ |
| Loss in Diode Forward Voltage Drop: | 0% | $0\mu W$ |
| Loss in MOSFET On-Resistance: | 2.8% | $14\mu W$ |
| Loss in SuperCap ESR: | 0.8% | $4\mu W$ |
| Loss in input capacitor ESR | 0.5% | $2.5\mu W$ |
| Switching Loss: | 0.8% | $4\mu W$ |
| Total Output Power: | 85.1% | $425.5\mu W$ |

Table 5.6: Power Loss Analysis in Boost Converter MPPT in 1 Duty Cycle (1mH inductor; $14\mu F$ input capacitor)

conduction power loss in this phase is negligible. However, from MPPT accuracy perspective, it is important to consider the PV cell voltage during this phase, since this relatively longer charging time $t_3 - t_2$ harvests most of PV energy in practical implementation as shown in Figure 5.23.

$$E_{pv} = P_{pv} \cdot (t_3 - t_0) \approx P_{pv} \cdot (t_3 - t_2) \tag{5.43}$$

The Sanyo AM PV cell power-voltage characteristics are evaluated with a numerical curve fitting which results in a voltage-power function $P_{pv} = F_{V-P}(V_{PV})$ to approximate the PV cell power at certain voltage $V_{PV}$. The energy loss due to the inaccuracy of the MPPT is then calculated in the following equation,

$$\eta_{error} = \frac{\int_{t0}^{t3} F_{v-p}(V_{mpp}) - F_{v-p}[V_{pv}(t)]dt}{\int_{t0}^{t3} F_{v-p}(V_{mpp})dt} \cdot 100\% \tag{5.44}$$

where $V_{MPP}$ is the ideal maximum power point voltage. With the PV cell I-V characteristics and considering 10% MPP voltage error, the energy losses due to the MPPT error are calculated using Eq 5.44 and summarized in Table 5.7.

Another important parameter of the idle stage is the frequency of the charging pulse. It is largely dependent upon the time period $t_3 - t_2$. The frequency, thus, is determined by the input capacitance $C_{in}$, PV cell current $I_{pv}$ and the pre-set hysteresis voltage range. As shown in Figure 5.25, if 2% MPP voltage error is used, the idle stage (solar cell charging the input capacitor) frequency must be higher than

| Light Intensity (lux) | PV Cell Theoretical Maximum Power $P_{MPP}$ ($\mu W$) | Power Loss Due to MPPT Error | Percentage of $P_{MPP}$ (%) |
|---|---|---|---|
| 100lux | $70\mu W$ | $1.05\mu W$ | 1.5% |
| 200lux | $155\mu W$ | $3.25\mu W$ | 2.1% |
| 300lux | $275\mu W$ | $6.33\mu W$ | 2.3% |
| 400lux | $410\mu W$ | $11.07\mu W$ | 2.7% |
| 500lux | $530\mu W$ | $16.96\mu W$ | 3.2% |

Table 5.7: Simulation Results of Energ Loss due to MPPT Error (Sanyo 1815 Cell 55mm × 40mm Cell)

3.5Hz. For 10% error, 1Hz frequency is required for 0.5mW solar power.

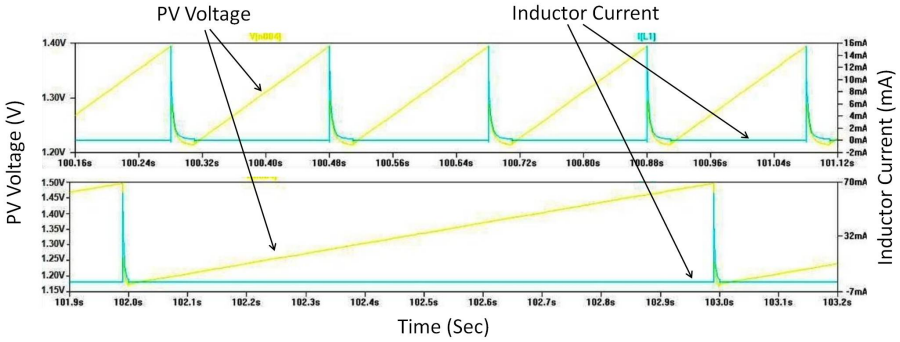



Figure 5.25: Boost Converter MPPT with (top) 2% MPP voltage error; (bottom) 10% MPP voltage error

The frequency of the MPPT converter can be adjusted by adopting various resistor array to control the hysteresis voltage range. Large hysteresis voltage leads to lower frequency. In the simulations, these parameters: 4.4Hz frequency, 2.5% MPPT error, 0.14mF input capacitor and 1mH inductor were selected due to their high conversion efficiency.

Two types of energy harvesters are designed and implemented. Prototype II implements the MPPT method proposed in this section. Prototype II-B is designed without MPPT optimization (for result comparison and verification purpose). The schematic of the proposed energy harvester powered WSN is presented in Figure 5.26. The control logics of MPPT and hybrid ESU charge/discharge are implemented with two 4-channels Maxim MAX934 ultra-low power comparators. The power consumption of the control logics during MPPT and ESU charge/discharge is measured at 29$\mu$W. The transistors adopted in this design are Vishay SiB914DK

with 0.28Ω on resistance at 1.5V Vgs and gate capacitance at 68pF.

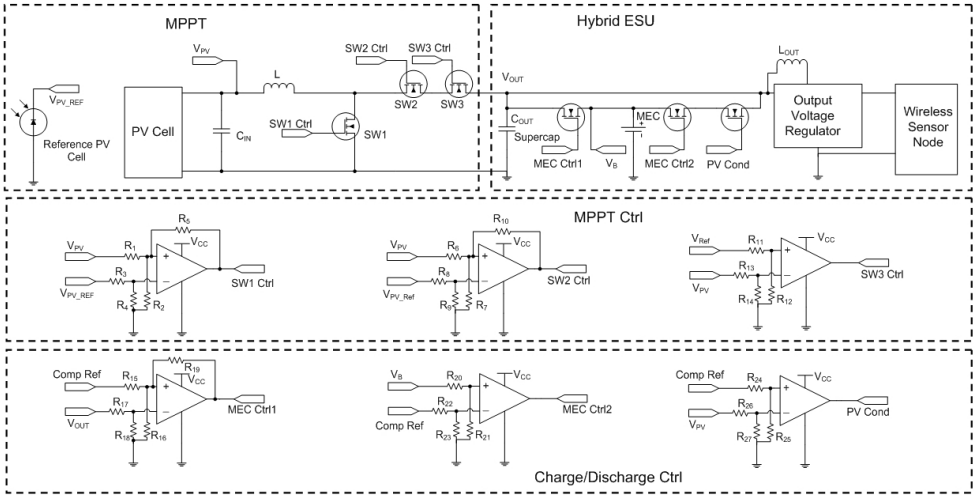



Figure 5.26: Indoor Photovoltaic Energy Harvester with Boost Converter MPPT and Hybrid Energy Storage Schematics

With Qg less than 1.5nC, the switching loss of the transistor is negligible. The inductance of the MPPT inductor is 1mH with equivalent series resistance of 6Ω. The input capacitor is 140$\mu$F with a 10$m\Omega$ ESR. The output capacitor is a Maxwell 2.5F super-capacitor with maximum voltage rating at 5V. The super-capacitor has an internal DC resistance around 2Ω. The TFB ESU is provided by Infinite Power Solutions with a 1.0 mAh capacity and 4.1-4.15 charging voltage.

The output voltage regulator is a Texas Instruments TPS61221 boost converter with a minimum input voltage threshold at 0.7V. The resistance of the voltage divider resistors are between 0.5MΩ and 10MΩ. The high resistance reduces the conduction loss in the dividers. The aforementioned power management system is implemented on a 39mm× 30mm PCB. The device is packaged with a polymer case printed by a 3D printer. The Sanyo amorphous silicon based PV cell has a form factor of 55mm×40mm. The overall device dimension is 88mm×60mm, slightly larger than a standard credit card. The prototype is shown in Figure 5.27.

The MPPT operation is shown in the captured oscilloscope waveform in Figure 5.28. The test is conducted under 500lux fluorescent lighting condition. In Figure 5.28 (a), the top waveform shows the achieved $K_{fvoc}$ is between 0.752-0.794 of the

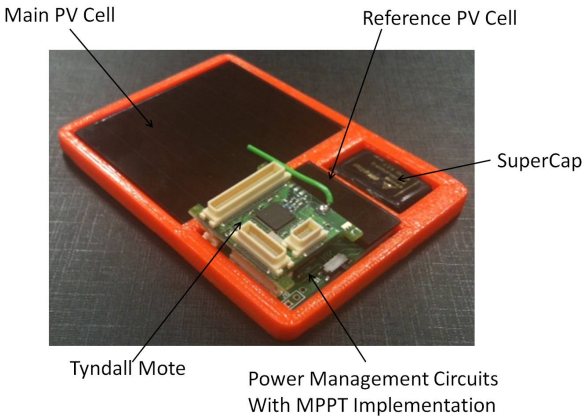



Figure 5.27: Picture of indoor light EH powered WSN prototype

ideal $V_{mpp}$. The MPPT error is less than 1.8% of the ideal MPP ratio of 0.760. The bottom waveform illustrates the shunt resistor voltage of the inductor current during MPPT. The MPPT circuit is operating in DCM with a low duty cycle at 0.8%.

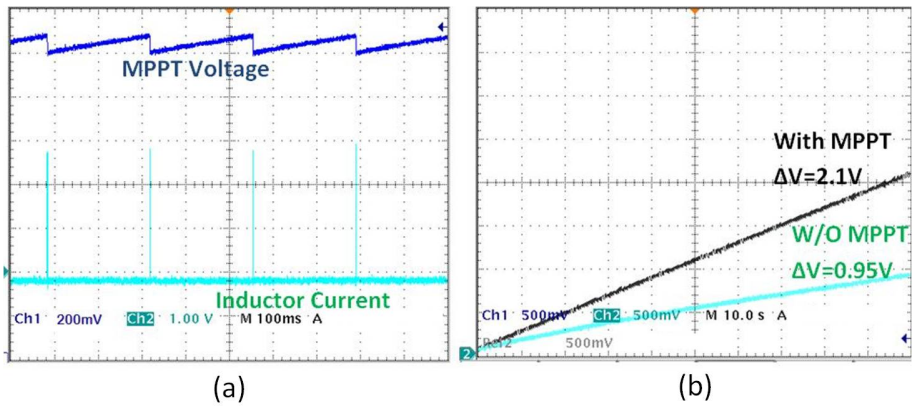



Figure 5.28: Boost Converter MPPT Results (Oscilloscope screen capture): (a) MPPT tracking PV cell voltage and charging current waveforms; CH1: MPPT Voltage: 200mV per vertical division. CH2: Inductor Current Measurement using 8Ω Shunt Resistor with 10× Amplification: voltage-current ratio 80:1. Horizontal: time: 100ms per division. (b) Comparison Charging Super-capacitor with/without MPPT; CH1 and CH2:500mV per vertical division. Horizontal: time: 10s per division.

Direct comparison was made to evaluate the performance difference between proposed method implemented in prototype II and energy harvesting without MPPT in prototype II-B. Figure 5.28(b) illustrates the charging performance at 500lux within

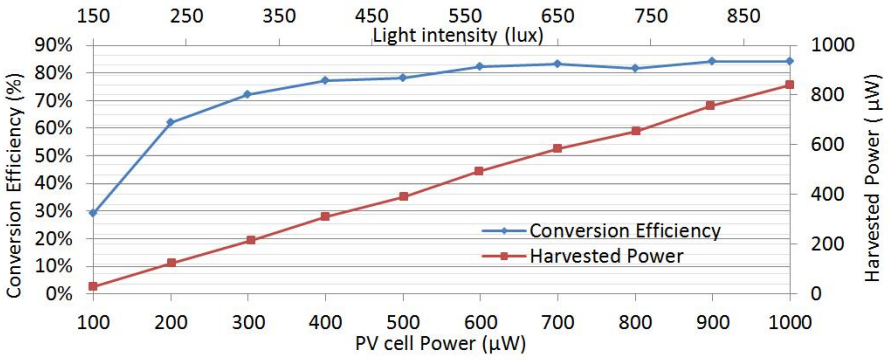



Figure 5.29: MPPT conversion efficiency in sub-1mW power conditions (100-1000 $\mu W$)

a time period of 100sec. Within this period of time, a 30mF super-capacitor is charged to 2.1V with the proposed MPPT method and only 0.95V without MPPT. The results clearly show that the charging performance is improved by adopting MPPT for the low power PV cell.

The energy conversion efficiency is calculated by using Eq 5.25. By using this proposed MPPT method, the input current and voltage variations are reduced, thus average current and voltage are used to calculate the input PV energy. It is worth noting that, in low light intensity conditions (due to the low output power), the leakage current of super-capacitor is no longer negligible. When energy leakage exceeds the charging energy, the PV cells cease to charge the ESU. Thus, the minimum operative light intensity highly relies on the ESU leakage current. In this implementation, the average leakage current of the 2.5F super-capacitor is approximately 25$\mu$A in 24 hours measurement. The conversion efficiency and the harvested power are shown in Figure 5.29.

In a typical office environment with light intensity at 480lux[3] (fluorescent), the theoretical maximum output power of this PV cell is approximately 490$\mu$W. The implemented EH device harvests 395$\mu$W in this condition and the energy conversion efficiency is 80.5%. The minimum operative light intensity (when output power equates power loss in energy conversion) is between 120-130lux ($\approx 80 - 90\mu W$). A

[3]EU guideline light intensity for office environment: $> 300lux$ and $< 750lux$ in office, optimal light intensity 450-500 lux. European Standard EN 15193:2007 Energy performance of buildings

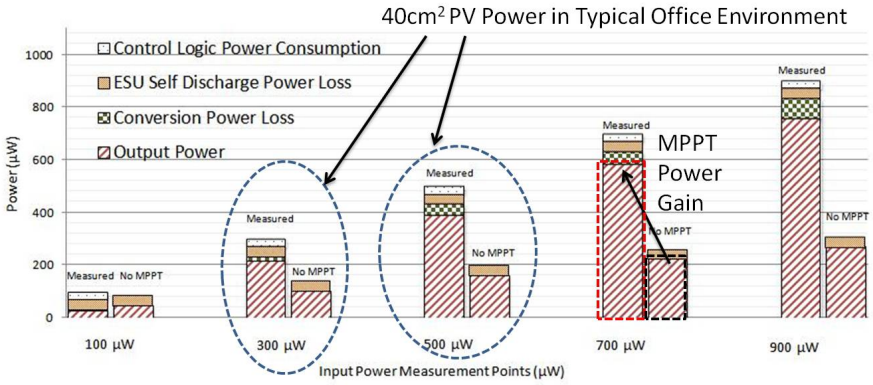



Figure 5.30: Measured Power Loss Factors and Output Power Results ($40cm^2$ PV cell in typical office environment)

detailed power analysis of the implementation is shown in Figure 5.30. Except the input power measurement point at 100 $\mu$W, the power measurements show that in spite of power losses in MPPT and control logics, the proposed MPPT outperforms the EHM without MPPT from energy harvesting efficiency perspectives.

For extremely low input power (e.g. $< 100\mu W$), the power gain from MPPT is offset by the inevitable power loss in MPPT based on this implementation. However, for typical office light intensity (400-500lux), this proposed MPPT can achieve 40%-150% power gain from a PV cell smaller than a credit card (0.3-0.5mW output power) as shown in Figure 5.30.

| | Wang[117] | Wang [118] | Tan [50] | Tan[51] | Chini [115] | Dondi[45] |
|---|---|---|---|---|---|---|
| Year | 2010 | 2012 | 2011 | 2012 | 2010 | 2008 |
| MPPT Converter | Buck | Boost | Buck | Buck | Boost | Buck |
| MPPT Control | PWM FVOC | PWM FVOC | PFM FVOC | PFM FVOC | PFM P&O | PWM FVOC |
| Input Power | 0.9mW | 0.5mW | 5mW | 0.4mW | 1.6mW | 50mW |
| Efficiency | 79.6% | 80.5% | 47% | 59% | 30% | 85% |

Table 5.8: sub-1mW to 50mW Input Power MPPT Results

Table 5.8 shows the comparison of efficiency among various maximum power point tracking circuits against their power levels. This boost converter based method proposed in this work has been published in [118]. The measured conversion efficiency

of 80.5% is the current state of the art in terms of sub-1mW MPPT circuits.

## 5.4 Indoor Photovoltaic EHM Powered WSN Operation Model

So far in this work, the energy storage Matlab simulink model, photovoltaic module I-V characterization, maximum power point tracking measurement result, output power regulator performance and power consumption of WSN have been studied individually. All main building blocks of the EHM powered WSN have been characterized. Based on the characterizations, a system operation model is proposed. The energy flow model can be simplified and summarized in Eq 5.45,

$$E_{stor}(t) = E_{init} + \int_0^t P_{EH} - P_{WSN} - P_{leak} dt \tag{5.45}$$

where $E_{Stor}(t)$ is the amount of energy in the storage unit at time t, $E_{init}$ is the energy in the storage unit at the beginning of the operation. $P_{EH}$, $P_{WSN}$ and $P_{leak}$ are the energy harvesting power, wireless sensor node power consumption and the energy storage leakage power, respectively. The state of charge and energy in ESU at time t $E_{stor}(t)$ is the key indicator of the system operation and for super-capacitor based ESU the voltage directly reflects the stored energy.

The energy "flow" between energy harvester, wireless sensor node and the energy storage unit are captured in the simulation. By adjusting the parameters of the system level simulation, the performance of the energy harvesting wireless sensor system can be estimated before the implementation. The limits of the WSN operation i.e. duty cycle, power mode, the energy harvester solar panel size and minimal light intensity over long period of time can be dynamically analysed. The simulation is on discrete time domain with time step of 1 second. Table 5.9 summarizes the inputs and outputs of the simulation. The system model is presented in Figure 5.31.

The Sanyo AM18 series PV cells characteristic lookup table is based on the curve fitting of I-V/P-V characterizations and simulations based on dark characterizations

| Name | Comments |
|---|---|
| pv_area | PV cell active area |
| lux | Light intensity in Lux unit |
| flk | MCU clock frequency |
| vcc | Mote Vcc |
| Tx_mode | Transmit power mode in dBm |
| drain_eff | Transmit drain efficiency |
| datapack | data packet length |
| ackpack | ACK packet length |
| Prx | receive mode power consumption |
| rr | transmit repeat rate |
| tinit | system initialization time |
| tcycle | full operation cycle time |
| sleep mode power consumption | $=43\mu W$ |
| ESU charge efficiency | $\approx 0.95$ |
| leakage current | ESU leakage current |
| esr | ESU equivalent series resistance |
| V0 | ESU Initial voltage |
| capacity | super-capacitor capacitance |

Table 5.9: System Simulation Parameters

parameters shown in Table 5.2. MPPT conversion efficiency lookup table is based on the characterization results of indoor energy harvesting module prototype II presented in Figure 5.29. Data processing, transmit and receive power lookup tables are based on the Tyndall mote power consumption characterizations presented in Appendix 2. The output regulator efficiency lookup table is based on measured converter efficiency between 0.5V and 3V input voltages with 2 current consumption modes(0.01mA and 30mA represents sleep and active mode current consumptions) as presented in Figure 3.17. The energy storage model is super-capacitor based on Figure 3.10. The simulation model verification is presented in a case study of WSN deployment in office environment.

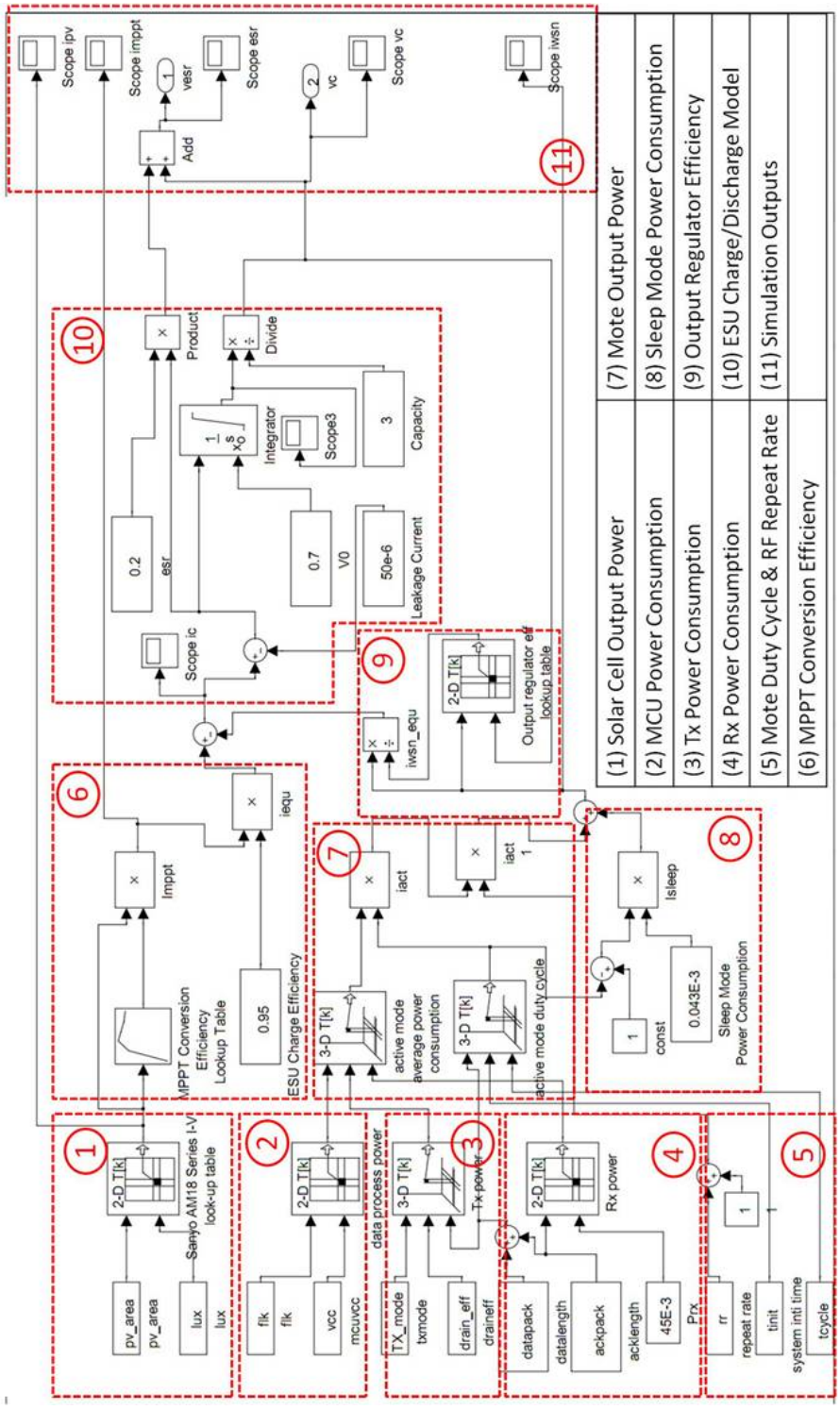



Figure 5.31: Simulink Simulation of Energy Harvesting Module Powered WSN System

### 5.4.1 Energy Harvesting WSN Case Study

A case study was conducted from March 14th 2012 to April 2nd 2012 for more than 2 weeks to test the operation of energy harvesting powered wireless sensor node in typical office conditions. The test location is in Tyndall Block A 3.31 Office Room (typical office environment). There is no direct sunlight at this location. Nearest window (northeast facing) is 5 metres away. The light source is provided by multiple groups of overhead fluorescent lamps. The configuration of typical office test is illustrated in Figure 5.32.

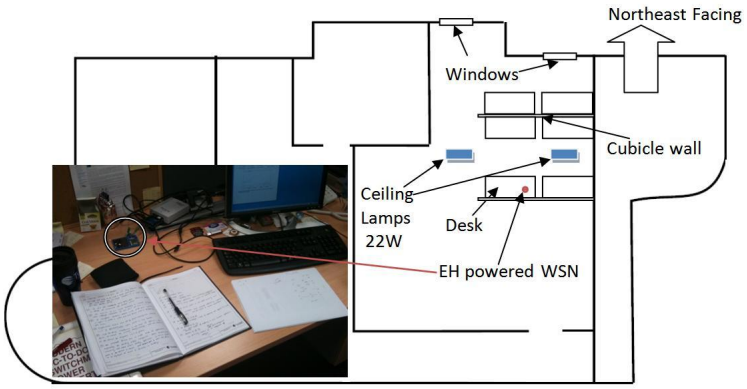



Figure 5.32: EH powered WSN Deployment Case Study

The lighting condition is within the range of 0lux (night) to maximum 600lux (day). A simulated light intensity is also created to study the system performance when the light intensity measurement is not available. The measured and simulated light intensity during the 14 days experiments are shown in Figure 5.33.

The simulation of the office light intensity is shown in the green curve. The simulation light intensity is 300lux for 4 hours, 450 lux for 8 hours and 0lux during the night. The overall product of lux and time is 4800 lux×hour in the simulation, whilst the measured light intensity in one day is also approximately 4800 lux×hour.

In the measured light intensity results, the northeast facing window contributes to some of the light intensity and was captured by the light sensor. The average light intensity during the daytime is measured at 410 Lux. The weekday and weekend light intensity are also different due to the usage profile. For example, at 144-hour

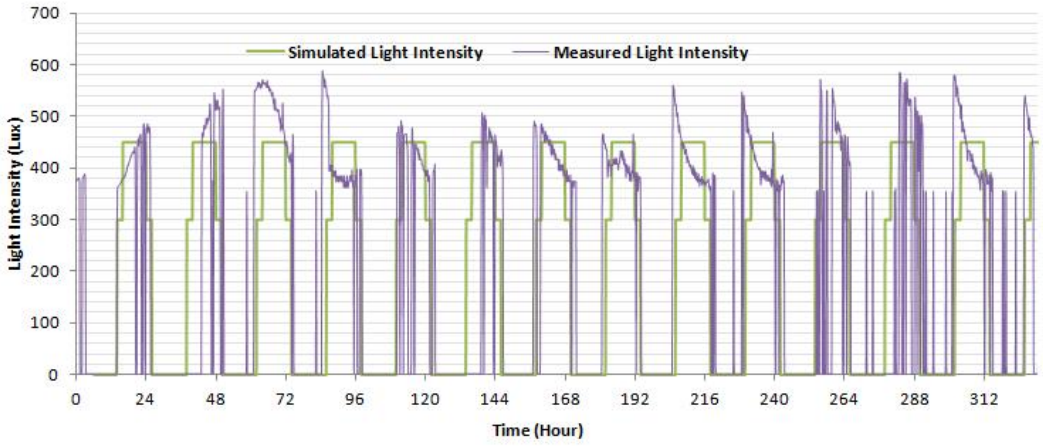



Figure 5.33: Light intensity measurement and simulation

mark, the light is measured during the weekend. The light intensity only increased to 520lux at 2.P.M. when the light is turned on, while the light is normally turned on around 8-9 A.M. during weekdays.

The EH device is tested with a Pico Tech Picolog data acquisition module Picolog-1206. It is capable of recording 3 million data sets (recording data for 33 days with 1 second resolution).

The indoor light energy harvesting module adopts a Sanyo AM18 series PV cell with an active area of $38cm^2$ (AM1815). The MPPT circuit is based on the synchronized boost converter design introduced in the previous section (prototype II). The output voltage regulator is based on TI TPS61220 buck/boost converter proposed in Chapter 3. The energy storage unit is a Maxwell PowerStor super-capacitor with a 5.0V voltage rating and 2.5F capacitance.

The WSN configuration used in this experiment is the standard setup for the environmental parameter measurements. The configuration of the EH powered wireless sensor node is summarized in Table 5.10.

The ESU voltage is measured for 340 hours ($\approx$ 14 days) and presented in Figure 5.34. Two simulation results are also presented in this figure. The black line indicates the measured ESU voltage. The blue line indicates the ESU voltage simulation with

| Name | Value | Comments |
|---|---|---|
| pv_area | $38cm^2$ | PV cell active area |
| lux | 0-600 lux | Light intensity in Lux unit |
| flk | 4MHz | MCU clock frequency |
| vcc | 3.3V | Mote Vcc |
| Tx_mode | 0dBm | Transmit power mode in dBm |
| drain_eff | 2.7% | Transmit drain efficiency |
| datapack | 50 bytes | data packet length |
| ackpack | 24bytes | ACK packet length |
| Prx | 52mW | receive mode power consumption |
| rr | 1% | transmit repeat rate |
| tinit | 0.25sec | system initialization time |
| tcycle | 300sec | full operation cycle time |
| sleep mode power consumption | $=43\mu W$ | n/a |
| ESU charge efficiency | $\approx 0.95$ | n/a |
| leakage current | avg. $50\mu W$ | ESU leakage current |
| esr | $0.2\Omega$ | ESU equivalent series resistance |
| V0 | 0.9V | ESU Initial voltage |
| capacity | 2.5F | super-capacitor capacitance |

Table 5.10: EH powered WSN System Configurations

measured input light intensity, whilst the red line indicates the ESU voltage simulation with simulated input light intensity (300/450 Lux at morning-evening/mid-day). The red bar (shadow area) illustrates the measured light intensity, whilst the blue bar illustrates the simulated light intensity.

The results show Tyndall mote operated for more than 14 days without power failure when it was solely powered from indoor light with energy harvesting module designed in this work. The ESU obtained a maximum voltage of 5.1V (2% higher than the super-capacitor voltage rating) and a minimum voltage of 0.83V. In the entire deployment, the voltage output of the energy harvester is always measured at 3.3V with variation less than 5%. In this experiment, the energy stored in the ESU accumulated over time and was always higher than the minimum operational voltage threshold in the entire deployment.

Both the measured light intensity and the typical office light intensity simulations show high consistency with the measurement results from the gathered deployment data. In both charge phase and discharge phase, this model is able to simulate the

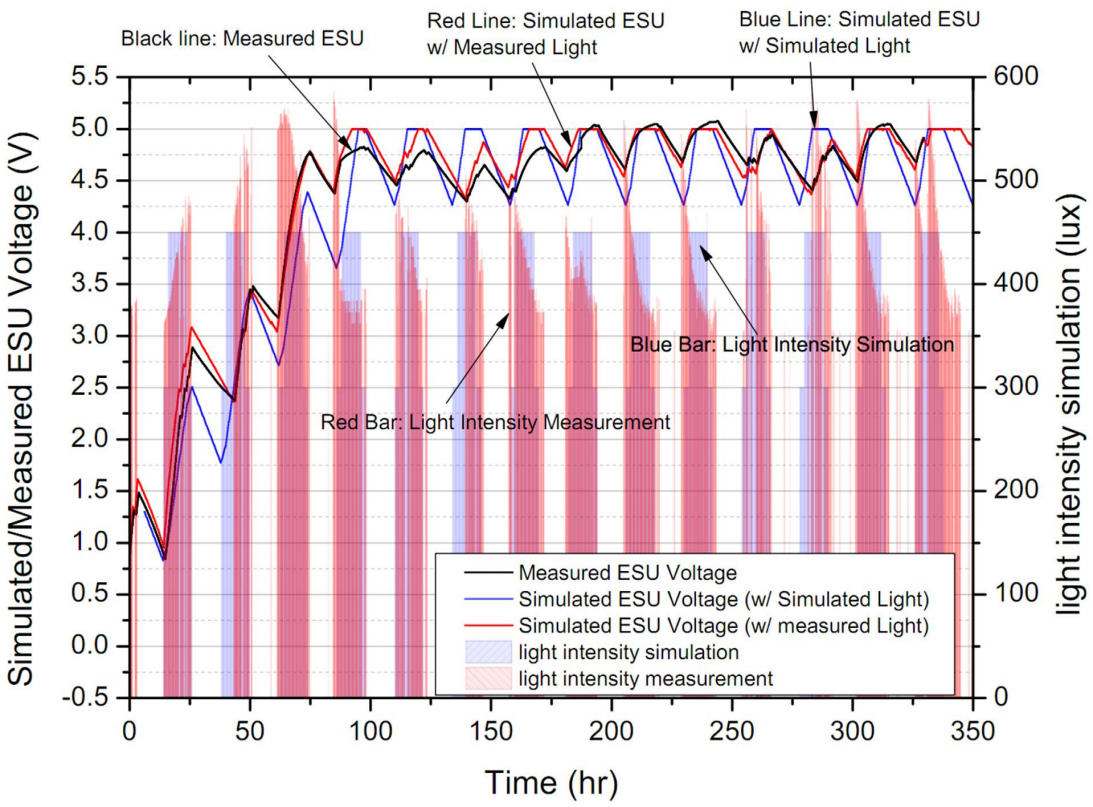



Figure 5.34: EH Powered WSN Deployment Measurement Results

power flow in the EH powered WSN. The average error between the measurement result and the simulation with measured light intensity is 5.8%, while the average error with simulated typical office environment is approximately 10%.

## 5.5 Conclusion

The concept of using fractional open circuit voltage method in the sub-1mW MPPT design for its superior ultra-low power consumption proved to be feasible and the implementation is suitable for WSN applications.

With MPPT efficiency as high as 79.6% at 0.9mW, the buck converter based MPPT prototype can provide a stable power supply when the input light intensity is only 245lux. This low frequency and simple comparator based buck converter MPPT energy harvester prototype was the first Zigbee wireless sensor node solely

powered by indoor light energy. This MPPT method was published in 2010 in ACM Journal of Emerging Technologies in Computing Systems [117].

It can be concluded that by replacing the high position diode by a synchronized switch and modifying the structure to boost topology, the boost converter based FVOC MPPT method further reduces the power loss in MPPT converter. It achieves power gain from input power as low as 80$\mu$W (120-130lux, credit card sized commercial off the shelf PV cells). With this MPPT design, Tyndall energy harvester prototype obtains 81% efficiency at 0.5mW. This conversion efficiency is higher than previous state of the art. Tan [51] reported 59% in similar condition. As of March 2013, the MPPT conversion efficiency and the minimum operating power of the power management circuitry are the current state of art for sub-1mW input power MPPT [118] (published in Sage Journal of Intelligent Materials Systems and Structures in 2012).

The system level energy model derived from sub-system simulation is one of the first Matlab Simulink based energy harvesting system modelling tools. It can be concluded that the simulation model can accurately estimate the operation performance of the energy harvester powered wireless sensor node in typical office condition over an extended period of time (at least 2 weeks in the case study). The main limitations of this model are: 1) while the components are interchangeable in this model, the system structure cannot be modified. 2) the WSN energy consumption part of this energy simulation tool is created based on curve fitting of subsystem characterizations, the input range of the model is limited to these characterizations.

The presented credit card sized indoor photovoltaic energy harvester supplies 0.2mW-0.4mW regulated power to the WSN mote when the solar cell is under 300-500lux indoor light. This generated power is sufficient for low duty cycle (0.1% or less) Tyndall WSN mote. It met the final target of long term WSN power autonomous operation in typical office/residential building environment. Over 100 prototypes have been built and used for real-world applications with Tyndall WSN mote since 2012. The prototypes have been provided to researchers in University of

California, Berkeley and Georgia Institute of Technology for various WSN applications.

# Chapter 6

# Conclusion and Future Work

Energy harvesting power management systems represent one of the most challenging technological barriers yet to be overcome in the widespread deployment of wireless sensor networks.

This thesis has been concerned with the design and optimization of indoor photovoltaic and thermoelectric energy harvesting systems for powering wireless sensor networks in typical office and commercial buildings.

The objective of this thesis is to design a continuous and maintenance-free power management system for energy harvester module in low duty cycle WSN applications. With a credit card form factor (less than 80mm $\times$ 50mm), the device should be able to supply the power for a low duty cycle (0.1%) WSN with (based on the characterization of Tyndall WSN, 0.05-0.5mW) regulated voltage from typical building environment.

In order to achieve this objective, several contributions to energy harvesting power management research are made in this work and presented as follows:

1) Maximum power point tracking circuit for low power PV cell was a very important but challenging issue under indoor light condition for WSN applications (1-2% power density of outdoor lighting). It can be concluded that the low power consumption fractional open circuit voltage MPPT solution is more suitable for the low power and stable indoor light condition than perturb and observe method.

The method proposed in this work is devised with 3 major improvements from previous MPPT methods: First, adopting an analog comparator based control logic

design. There is no obvious needs to use more power hungry and complicated micro-controller to control MPPT. The analog comparator with 1$\mu$A current consumption used in this work is more suitable for this application.

Second, low frequency and low inductor current MPPT converter design. The low frequency characteristics reduce the switching loss. The large inductor (1-10mH) reduces the inductor current and limits the conduction power loss. Both low frequency and low inductor current require a larger size of the inductor (up to 1cm$^2$). However, the 1cm$^2$ sized component does not present an issue for the credit card sized device.

With the first two improvements, the buck converter based MPPT achieves 79.6% conversion efficiency with 0.9mW input power. This result published in [117] outperforms the best reported low power MPPT circuit before 2011 (30% at 1.6mW [115]) in terms of efficiency.

Third, using synchronized boost converter. The synchronized switching instead of diode rectification reduces the conduction loss by 10-15%. It can be concluded that the boost converter high/low position switches are able to be controlled by the analog comparators. It reduces the control complexity of synchronized rectification. With this MPPT, the indoor PV energy harvesting is able to harvest energy on even lower light intensity (for a credit card sized form factor, the minimal light intensity is 250lux for the proposed buck converter MPPT ; for the proposed boost converter based MPPT is reduced to 120-130lux), extending the minimum operation conditions of PV energy harvester to 0.1mW level.

The above 3 main contributing technologies developed in this work are demonstrated in boost converter MPPT deign published in [118]. For a 40cm$^2$ PV cell with 0.5mW output power, the MPPT efficiency has been increased to 80.5%. It outperforms the previous state of the art [51] by 20% in similar test condition. The output power of the MPPT is close to 0.4mW which meets the objective of this thesis (0.05-0.5mW).

2) The characterization of TEG modules leads to two types of design for thermoelectric energy harvesting power management. It can be concluded that the one stage transformer based low voltage dc-dc converter achieves higher peak conversion efficiency at 40% but this efficiency is only available within a small voltage range. This issue is due to the large and fixed transformer ratio and difficult to resolve. The charge pump and boost converter two stage solution proposed in this work demonstrated a lower peak efficiency at 28% (input stage). However, the average conversion efficiency when the TEG is operating between a wide voltage range of 200-700mV is 2 times higher than the state of the art commercial solution Linear tech LTC3108.

A trade-off exists: when the TEG is operating at a constant temperature, transformer based dc-dc converter should be used with TEG output voltage designed at the peak efficiency voltage; however, when the TEG is operating with changing temperature, the charge pump and boost converter solution should be used for higher average efficiency.

In the TEG impedance matching, power management circuits are often optimized to match the output impedance of TEG module. In this work, it has been demonstrated that a TEG energy harvester system can be designed to match the power management circuits input impedance in order to maximize the output power.

3) The output power management using boost converter for energy storage unit enables continuous operation of WSN. The output voltage regulation also increases the useable energy by more than 30% for a 5V rating super-capacitor energy storage unit. The introduction of self-start circuit avoids maintenance effort required to cold start the EH system when capacitive energy storage unit is used.

The power management circuits for a novel hybrid energy storage unit using thin film batteries and super-capacitors have shown that it is practical to perform over/under voltage protection with sub-1mW input power. The analog comparator based control logic is able to switch between 2 different charge modes with only $1\mu$A power consumption. By reducing the super-capacitor voltage and using thin film battery as the secondary energy storage unit, the leakage current that occurs in the

0.47F 5.0V super-capacitor and 1mAh 4.2V thin film battery is 40% less than the 2F 5.0V stand-alone super-capacitor.

In terms of energy storage unit component, the analysis on charge efficiency, equivalent series resistance and leakage current of the energy storage unit has revealed power loss issues which have not been addressed previously. These parameters need to be considered during the design of an energy harvesting system.

4) An energy simulation model created for predicting the performance of an energy harvesting powered WSN system has been developed and utilized in this work. This model is the first known complete energy harvesting system level model built on Matlab simulink. It has been applied to simulate the real device and can accurately (average error less than 10%) reflect the actual energy flow from energy generation stage to energy storage and load. This model has been successfully used to determine component selection, operation configurations and energy related network layout.

## 6.1 Suggestions for Future Work

This thesis not only delivered several innovative energy harvesting solutions but also has revealed several potential avenues of research which remain open for further investigation.

It is possible to further improve the MPPT conversion efficiency by adopting an "adaptive MPPT" method. Due to the inevitable power consumption of MPPT, when the ambient light intensity is below a certain threshold, the power gained from MPPT will be entirely offset by the power consumption of MPPT. In this condition, applying MPPT will in fact lead to a negative impact on the PV cell output power. In the MPPT implementation presented in this work, the tracking is performed in any condition. In a future design, a control circuit to switch on MPPT only when it is possible to achieve power gain is recommended.

It is possible to further reduce the MPPT power loss and improve the output power regulation efficiency by integrating the two power management circuits into

a single integrated circuit. The existing power management with discrete components implementation cannot be optimized fully due to the significant mismatch in components parameters. Most of the power management ICs are designed for power systems with a power level one or two orders of magnitude higher (1-100mW instead of sub-1mW). By introducing the design concept and circuits developed in this thesis as well as IC level optimization, it is possible to significantly further increase the system conversion efficiency. Ultra-low power consumption and high conversion efficiency are critical for future "zero power" application. Several companies have started to invest more in the area of power management ICs for energy harvesting.

In this thesis, only part of the energy harvester model (MPPT, ESR power loss in energy storage and thermoelectric generator) is based on SPICE simulation and analytical model. The rest of the simulation (PV cell, charge efficiency and leakage current in ESU, and output voltage regulation) are based on measurement results of a certain type of device. The generality of the energy harvester system model is not complete.

Although the simulation results agree well with the existing system, changes on components will require further effort to characterize the components in order to obtain parameters needed for the simulation. Potentially, a system level circuit/SPICE model with all components simulated by analytic model is ideal. However, it is worth noting that the implementation of this further work may be challenging. Firstly, the circuit/SPICE models provided by component manufacturers are not entirely available on all components. The circuit/SPICE models on energy storage units is particularly limited. Secondly, in the available SPICE model, many parameters required for energy harvesting simulation are not included in the model, such as temperature variation impact on the capacity of ESU etc. Despite these difficulties, further investigation on the system level circuit/SPICE model will be beneficial for the understanding of overall system efficiency and potential methods for further efficiency improvement.

The hybrid energy storage solution can be further improved. In this thesis, the hybrid energy storage solution using super-capacitors and thin film batteries (TFB)

only uses the TFB as a secondary energy storage when the voltage in super-capacitor is higher than a certain threshold. However, it is possible to improve the discharging performance of the hybrid energy storage significantly. By only discharging from the thin film battery during the sleep mode and only discharging energy from super-capacitor during the active mode, the benefit of low leakage current in thin film battery and low ESR in super-capacitor can be fully realized. This requires a more complicated logic control to charge the super-capacitor to a voltage level to meet the active mode power consumption and return to a near zero voltage condition to minimize leakage current in the super-capacitor.

Based on the development level of the PV energy harvester, commercialization research is necessary to investigate the possibility of developing the system into a product. From this aspect, system operational lifetime and shelf life time become important, which, however, have not been included in this thesis. In further investigations, accelerated life cycle test in various temperature conditions is important. The cost effectiveness of the design also needs to be considered.

Finally, with the fast development of low power wireless sensor hardware and energy saving software, the power consumption of the node is decreasing significantly. The advances in IC design and semiconductor process allow the physical size of the wireless sensor node becoming further miniaturized. It is important to study "power miniaturized and form factor miniaturized" energy harvester in the foreseeable future. The research may start to investigate the energy harvesting technologies for sub-100$\mu$W power level WSN using 10cm$^2$ level form factor energy harvester instead of current 50cm$^2$ level form factor.

# Appendix A

## A.1 CAP-XX Super-capacitor Models and Design Aid Calculator

*CAP-XX Supercapacitor Models

*Last updated October 2007

*Tested at 20 degrees Celcius.

*Long term leakage simulated with 2M2 Ohm parallel resistor (RCp).

*Note these models are for a two terminal device only, in practice

*balancing is still required on the third terminal.

*CAP-XX assumes no responsibility for the accuracy of this model.

.SUBCKT GW209 1 2

+ PARAMS: precharge=0

L 2 3 9.67E-08

RLp 2 3 2.237171717

RCp 4 1 2.20E+06

R1 3 4 0.049077212

C1 4 1 0.004561071 IC=precharge

R2 4 5 0.008834749

C2 5 1 0.026885571 IC=precharge

R3 5 6 0.022730061

C3 6 1 0.05251849 IC=precharge

R4 6 7 0.15709697

C4 7 1 0.039165612 IC=precharge

R5 7 8 2.913272727

C5 8 1 0.014557041 IC=precharge

R6 8 9 133.9333333

C6 9 1 0.009203161 IC=precharge

.ENDS

.SUBCKT HS201 1 2

+ PARAMS: precharge=0

L 2 3 1.15E-07

RLp 2 3 1.9375

RCp 4 1 2.20E+06

R1 3 4 0.03227

C1 4 1 0.0022032 IC=precharge

R2 4 5 0.017125833

C2 5 1 0.0095346 IC=precharge

R3 5 6 0.037981667

C3 6 1 0.0522348 IC=precharge

R4 6 7 0.0746925

C4 7 1 0.120924 IC=precharge

R5 7 8 0.5091

C5 8 1 0.1024104 IC=precharge

R6 8 9 12.6

C6 9 1 0.0440136 IC=precharge

.ENDS

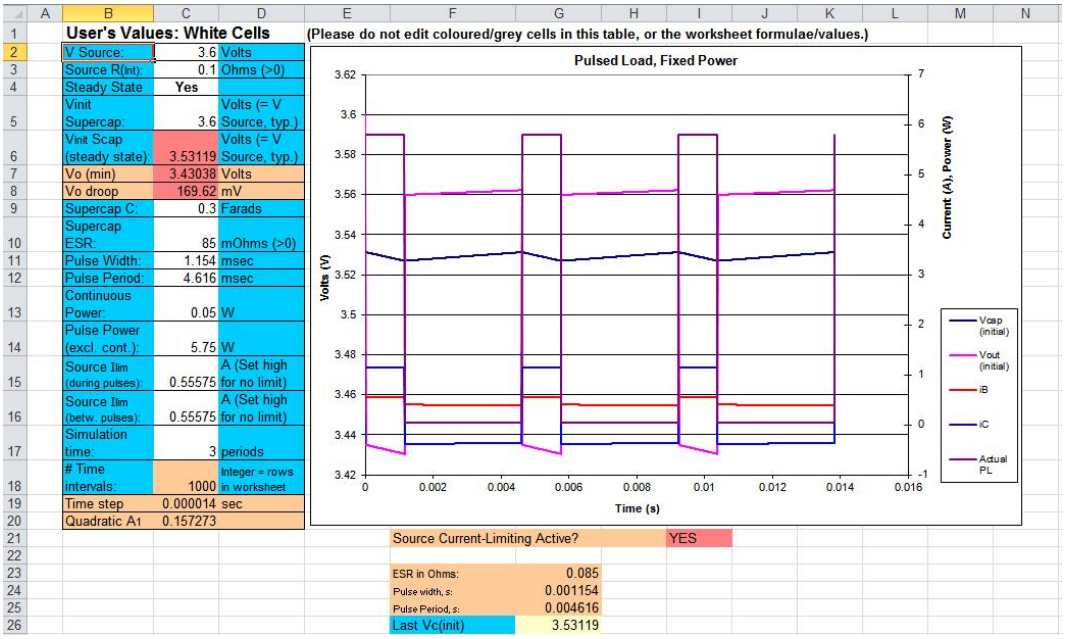



Figure A.1: Cap-XX Design-Aid Calculators

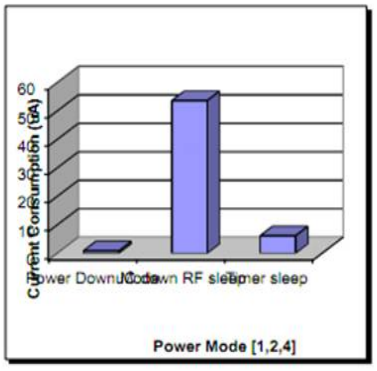
## A.2 Tyndall Wireless Sensor Node Power Consumption Test Results

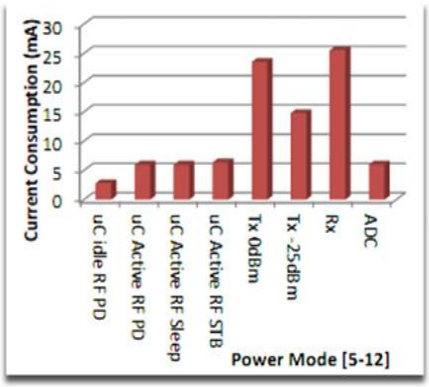
| MODE | Voltage on mote(V) | Rshunt | R(ohm) | I (uA) | Power (uW) | | |
|---|---|---|---|---|---|---|---|
| | 2.7 | voltage (uV) | | | | | |
| Mode. 1 | Power Down Mode | 8.8 | 9.9 | 0.89 | 2.403 | | |
| Mode. 2 | uC down RF sleep | 531.3 | 9.9 | 53.67 | 144.909 | | |
| Mode. 3 | uC down RF STB* | 4453 | 9.9 | 449.8 | 1214.46 | | |
| Mode. 4 | Timer sleep | 61.3 | 9.9 | 6.19 | 16.713 | I(mA) | Power (mW) |
| Mode. 5 | uC idle RF PD | 27875 | 9.9 | 2815.66 | 7602.282 | 2.82 | 7.602 |
| Mode. 6 | uC Active RF PD | 58869 | 9.9 | 5946.36 | 16055.17 | 5.95 | 16.06 |
| Mode. 7 | uC Active RF Sleep | 58920 | 9.9 | 5951.52 | 16069.1 | 5.95 | 16.07 |
| Mode. 8 | uC Active RF STB | 63210 | 9.9 | 6384.85 | 17239.1 | 6.38 | 17.24 |
| Mode. 9 | Tx 0dBm | 232953 | 9.9 | 23530.6 | 63532.65 | 23.5 | 63.53 |
| Mode. 10 | Tx -25dBm | 146435 | 9.9 | 14791.4 | 39936.81 | 14.8 | 39.94 |
| Mode. 11 | Rx | 252940 | 9.9 | 25549.5 | 68983.62 | 25.5 | 68.98 |
| Mode. 12 | ADC | 59398 | 9.9 | 5999.8 | 16199.46 | 6 | 16.2 |
| Mode. 13 | Duty Cycling | Go to spreadsheet 2:RF Operation | | | | | |

| | | MCU= | RF= | Tx= | Rx= | ADC= | Duty Cycle= |
|---|---|---|---|---|---|---|---|
| Mode. 1 | Power Down Mode | PD* | PD | PD | PD | PD | none |
| Mode. 2 | uC down RF sleep | PD | Sleep | Sleep | Sleep | PD | none |
| Mode. 3 | uC down RF STB* | PD | STB | STB | STB | PD | none |
| Mode. 4 | Timer sleep | Ext-Timer Sle | PD | PD | PD | sleep | none |
| Mode. 5 | uC idle RF PD | Idle | PD | PD | PD | Idle | none |
| Mode. 6 | uC Active RF PD | Active | PD | PD | PD | Idle | none |
| Mode. 7 | uC Active RF Sleep | Active | Sleep | Sleep | Sleep | Idle | none |
| Mode. 8 | uC Active RF STB | Active | STB | STB | STB | Idle | none |
| Mode. 9 | Tx 0dBm | Active | Active | Active 0dE | STB | Idle | none |
| Mode. 10 | Tx -25dBm | Active | Active | Active -25 | STB | Idle | none |
| Mode. 11 | Rx | Active | Active | STB | Active | Idle | none |
| Mode. 12 | ADC | Active | Sleep | Sleep | Sleep | Active | none |
| Mode. 13 | Duty Cycling | Active/Timer | Active/S | DC* | DC | DC | 1 cycle/min |

* PD=power down
*STB=standby
*External Timer control the wake up time
*DC=duty cycling

Repeat Mode 6. with CLK =8MH Vcc=2.7V/3.0V/3.3V
Repeat Mode 6. with CLK =8MHz



Repeat Mode 6 with clk=8MHz VCC=3.0

3.002

| | | | | | |
|---|---|---|---|---|---|
| 10.4 | 9.9 | 1.05 | 3.1521 | | |
| 567.2 | 9.9 | 57.29 | 171.98 | | |
| 4490 | 9.9 | 453.54 | 1361.5 | | |
| 63.2 | 9.9 | 6.38 | 19.153 | I(mA) | Power (uW) |
| 28175 | 9.9 | 2845.96 | 8543.6 | 2.84596 | 8.543572 |
| 59217 | 9.9 | 5981.52 | 17957 | 5.98152 | 17.95652 |
| 59123 | 9.9 | 5972.02 | 17928 | 5.97202 | 17.928 |
| 63705 | 9.9 | 6434.85 | 19317 | 6.43485 | 19.31742 |
| 233123 | 9.9 | 23547.78 | 70690 | 23.5478 | 70.69044 |
| 146435 | 9.9 | 14791.41 | 44404 | 14.7914 | 44.40381 |
| 253278 | 9.9 | 25583.64 | 76802 | 25.5836 | 76.80209 |
| 59401 | 9.9 | 6000.1 | 18012 | 6.0001 | 18.0123 |

Repeat Mode 6 with clk=4MHz Vcc=3.0

3

| | | | | | |
|---|---|---|---|---|---|
| 9.5 | 9.9 | 1.0666667 | 3.2 | | |
| 515.6 | 9.9 | 58.174359 | 174.52 | | |
| 4081.8 | 9.9 | 460.51282 | 1381.5 | | |
| 57.5 | 9.9 | 6.4820513 | 19.446 | I(mA) | Power (uW) |
| 25613.6 | 9.9 | 2889.7436 | 8669.2 | 2.88974 | 8.669231 |
| 53833.6 | 9.9 | 6073.5385 | 18221 | 6.07354 | 18.22062 |
| 53748.2 | 9.9 | 6063.8974 | 18192 | 6.0639 | 18.19169 |
| 57913.6 | 9.9 | 6533.8462 | 19602 | 6.53385 | 19.60154 |
| 211930 | 9.9 | 23910.051 | 71730 | 23.9101 | 71.73015 |
| 133122.7 | 9.9 | 15018.974 | 45057 | 15.019 | 45.05692 |
| 230252.7 | 9.9 | 25977.231 | 77932 | 25.9772 | 77.93169 |
| 54000.9 | 9.9 | 6092.4103 | 18277 | 6.09241 | 18.27723 |

Repeat Mode 6 with clk=8MHz Vcc=3.3

3.3

| | | | | | |
|---|---|---|---|---|---|
| 12.5 | 9.9 | 1.26 | 4.158 | | |
| 680.6 | 9.9 | 68.75 | 226.88 | | |
| 5388 | 9.9 | 544.24 | 1796 | | |
| 75.8 | 9.9 | 7.66 | 25.278 | I(mA) | Power (uW) |
| 33810 | 9.9 | 3415.15 | 11270 | 3.41515 | 11.27 |
| 71060.4 | 9.9 | 7177.82 | 23687 | 7.17782 | 23.68681 |
| 70947.6 | 9.9 | 7166.42 | 23649 | 7.16642 | 23.64919 |
| 76446 | 9.9 | 7721.82 | 25482 | 7.72182 | 25.48201 |
| 279747.6 | 9.9 | 28257.33 | 93249 | 28.2573 | 93.24919 |
| 175722 | 9.9 | 17749.7 | 58574 | 17.7497 | 58.57401 |
| 303933.6 | 9.9 | 30700.36 | 101311 | 30.7004 | 101.3112 |
| 71281.2 | 9.9 | 7200.12 | 23760 | 7.20012 | 23.7604 |

Repeat Mode 6 with clk=4MHz Vcc=3.3

3.3

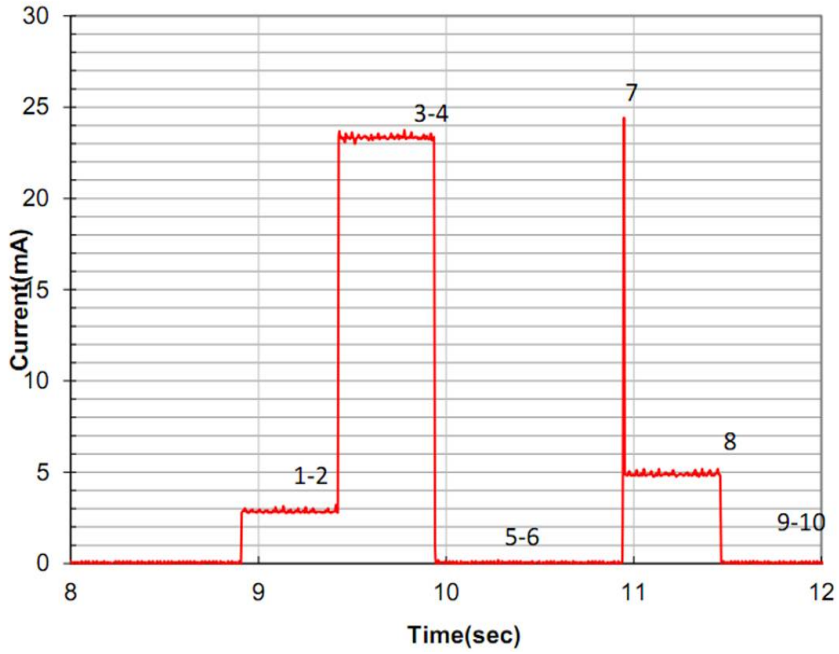
| | | | | | |
|---|---|---|---|---|---|
| 10 | 9.9 | 1.1460055 | 3.7818 | | |
| 541.4 | 9.9 | 62.501377 | 206.25 | | |
| 4285.9 | 9.9 | 494.76584 | 1632.7 | | |
| 60.4 | 9.9 | 6.9641873 | 22.982 | I(mA) | Power (uW) |
| 26894.3 | 9.9 | 3104.6832 | 10245 | 3.10468 | 10.24545 |
| 56525.3 | 9.9 | 6525.2893 | 21533 | 6.52529 | 21.53345 |
| 56435.6 | 9.9 | 6514.9311 | 21499 | 6.51493 | 21.49927 |
| 60809.3 | 9.9 | 7019.8347 | 23165 | 7.01983 | 23.16545 |
| 222526.5 | 9.9 | 25688.485 | 84772 | 25.6885 | 84.772 |
| 139778.8 | 9.9 | 16136.088 | 53249 | 16.1361 | 53.24909 |
| 241765.3 | 9.9 | 27909.421 | 92101 | 27.9094 | 92.10109 |
| 56700.9 | 9.9 | 6545.5647 | 21600 | 6.54556 | 21.60036 |

Repeat Mode 6 with clk=4MHz Vcc=2.7

2.7

| | | | | | |
|---|---|---|---|---|---|
| 8.9 | 9.9 | 0.9 | 2.43 | | |
| 486.2 | 9.9 | 49.11 | 132.6 | | |
| 3848.5 | 9.9 | 388.74 | 1049.6 | | |
| 54.2 | 9.9 | 5.47 | 14.769 | I(mA) | Power (uW) |
| 24150 | 9.9 | 2439.39 | 6586.4 | 2.43939 | 6.586353 |
| 50757.4 | 9.9 | 5127.01 | 13843 | 5.12701 | 13.84293 |
| 50676.8 | 9.9 | 5118.87 | 13821 | 5.11887 | 13.82095 |
| 54604.2 | 9.9 | 5515.58 | 14892 | 5.51558 | 14.89207 |
| 199819.7 | 9.9 | 20183.81 | 54496 | 20.1838 | 54.49629 |
| 125515.7 | 9.9 | 12678.35 | 34232 | 12.6784 | 34.23155 |
| 217095.4 | 9.9 | 21928.83 | 59208 | 21.9288 | 59.20784 |
| 50915.1 | 9.9 | 5142.94 | 13886 | 5.14294 | 13.88594 |

Motes operate measurement sequence:
1. System Initalization
2. Delay 200ms
3. RF Initalization
4. Rx for 500ms
5. RF Switch off
6. External Timer Dealy 1 second
7. Tx data in payload, payload=50byte
(repeat with payload=10 bytes/=30bytes/=103 bytes)
(Repeat with Tx=-25dBm/=-15dBm/=-7dBm/=3dBm/=10dBm)
8. RF idle
9. RF switch off
10. External Timer sleep for 15 seconds



# Bibliography


[1] G. Acosta-Marum and M. A. Ingram. Six time- and frequency- selective empirical channel models for vehicular wireless lans. *Vehicular Technology Magazine, IEEE*, 2(4):4–11, 2007.

[2] M. Weiser. The Computer for the Twenty-First Century. *Scientific American*, 265(3):94–104, 1991.

[3] I.F. Akyildiz, W. Su, Y. Sankarasubramaniam, and E. Cayirci. Wireless sensor networks: a survey. *Computer networks*, 38(4):393–422, 2002.

[4] J. Polastre, R. Szewczyk, C. Sharp, and D. Culler. The mote revolution: Low power wireless sensor network devices. In *Hot Chips*, volume 16, pages 22–24, 2004.

[5] C.S. Raghavendra, K.M. Sivalingam, and T.F. Znati. *Wireless sensor networks*. Springer, 2004.

[6] United States Department of Energy. International energy outlook 2011, website: www.iea.org/publications, 2011.

[7] K. Menzel, D. Pesch, B. O'Flynn, M. Keane, and C. O'Mathuna. Towards a wireless sensor platform for energy efficient building operation. *Tsinghua Science & Technology*, 13(Supplement 1):381–386, 2008.

[8] T. He, S. Krishnamurthy, J.A. Stankovic, T. Abdelzaher, L. Luo, R. Stoleru, T. Yan, L. Gu, J. Hui, and B. Krogh. Energy-efficient surveillance system using

wireless sensor networks. In *Proceedings of the 2nd international conference on Mobile systems, applications, and services*, pages 270–283. ACM, 2004.

[9] Department of Energy and Climate Change of U.K. The government's standard assessment procedure for energy rating of dwellings, website:www.bre.co.uk/filelibrary/sap, 2005.

[10] A. Arora, P. Dutta, S. Bapat, V. Kulathumani, H. Zhang, V. Naik, V. Mittal, H. Cao, M. Demirbas, M. Gouda, et al. A line in the sand: a wireless sensor network for target detection, classification, and tracking. *Computer Networks*, 46(5):605–634, 2004.

[11] J.A. Stankovic. Wireless sensor networks. *Computer*, 41(10):92 –95, 2008.

[12] R.H. Kori, A.S. Angadi, M.K. Hiremath, and S.M. Iddalagi. Efficient power utilization of wireless sensor networks: A survey. In *Advances in Recent Technologies in Communication and Computing, 2009. ARTCom '09. International Conference on*, pages 571 –575, Oct 2009.

[13] J. Yick, B. Mukherjee, and D. Ghosal. Wireless sensor network survey. *Computer Networks*, 52(12):2292 – 2330, 2008.

[14] R.J. Brodd, K.R. Bullock, R.A. Leising, R.L. Middaugh, J.R. Miller, and E. Takeuchi. Batteries, 1977 to 2002. *Journal of the Electrochemical Society*, 151(3):K1–K11, 2004.

[15] V. Shnayder, M. Hempstead, B. Chen, G.W. Allen, and M. Welsh. Simulating the power consumption of large-scale sensor network applications. In *Proceedings of the 2nd international conference on Embedded networked sensor systems*, pages 188–200. ACM, 2004.

[16] R. Niu, M. Moore, and D. Klamer. Decision fusion in a wireless sensor network with a large number of sensors. 2004.

[17] C.O. Mathuna, T. O Donnell, R.V. Martinez-Catala, J. Rohan, and B. O Flynn. Energy scavenging for long-term deployable wireless sensor networks. *Talanta*, 75(3):613–623, 2008.

[18] S. Roundy. On the effectiveness of vibration-based energy harvesting. *Journal of Intelligent Material Systems and Structures*, 16(10):809–823, 2005.

[19] S. Beeby, R.N. Torah, M.J. Tudor, P. Glynne-Jones, T. O'Donnell, C.R. Saha, and S. Roy. A micro electromagnetic generator for vibration energy harvesting. *Journal of Micromechanics and Microengineering*, 17(7):1257, 2007.

[20] I.N. Ayala, D. Zhu, M.J. Tudor, and S.P. Beeby. Autonomous tunable energy harvester. *Proc. PowerMEMS*, pages 49–52, 2009.

[21] S. Beeby and N. White. *Energy harvesting for autonomous systems*. Artech House Publishers, 2010.

[22] S. Roundy, P. Wright, and J.M. Rabaey. *Energy Scavenging for Wireless Sensor Networks: With Special Focus on Vibrations*. Kluwer Academic Publishers, 2004.

[23] C. Evans-Pughe. Close encounters of the magnetic-kind near field communications. *IEE Review*, 51(5):38–42, 2005.

[24] V. Leonov and R.J.M. Vullers. Wearable electronics self-powered by using human body heat: The state of the art and the perspective. *Journal of Renewable and Sustainable Energy*, 1:62–71, 2009.

[25] J.A. Paradiso and T. Starner. Energy scavenging for mobile and wireless electronics. *Pervasive Computing, IEEE*, 4(1):18–27, 2005.

[26] P. Schlyter. Radiometry and photometry in astronomy. In *Section 18, How bright are natural light website: stjarnhimlen.se/comp/radfaq.html*, 2006.

[27] Y. Li, N.J. Grabham, S.P. Beeby, and M.J. Tudor. Energy harvesting from solar cells under typical illumination conditions in buildings. Poster published in NanoEnergy Letters 2013., July 2013.

[28] Marlow Industries. Evergen energy harvesters for energy generation. In *EHA TEG Module: www.marlow.com/products/power-generators/energy-harvesting-kits-1.html*, 2009.

[29] T. Esram and P.L. Chapman. Comparison of photovoltaic array maximum power point tracking techniques. *Energy Conversion, IEEE transactions on*, 22(2):439–449, 2007.

[30] T. Azib, O. Bethoux, G. Remy, and C. Marchand. Structure and control strategy for a parallel hybrid fuel cell/supercapacitors power source. In *Vehicle Power and Propulsion Conference, 2009. VPPC'09. IEEE*, pages 1858–1863. IEEE, 2009.

[31] J.B. Goodenough. Rechargeable batteries: challenges old and new. *Journal of Solid State Electrochemistry*, 16(6):2019–2029, 2012.

[32] N.J. Dudney. Thin film micro-batteries. *The Electrochemical Society Interface*, 17(3):44, 2008.

[33] S. Mahlknecht. Energy-self-sufficient wireless sensor networks for the home and building environment. *Master Dissertation, Fakultät für Elektrotechnik, Technischen Universität Wien, Vienna*, 2004.

[34] R. Hahn and H. Reichl. Batteries and power supplies for wearable and ubiquitous computing. In *Wearable Computers, 1999. Digest of Papers. The Third International Symposium on*, pages 168–169. IEEE, 1999.

[35] G. Mao, B. Fidan, and B. Anderson. Wireless sensor network localization techniques. *Computer Networks*, 51(10):2529–2553, 2007.

[36] X. Zhao, T. Qian, G. Mei, C. Kwan, R. Zane, C. Walsh, T. Paing, and Z. Popovic. Active health monitoring of an aircraft wing with an embedded piezoelectric sensor/actuator network: part i: Wireless approaches. *Smart Materials and Structures*, 16(4):1218, 2007.

[37] A. Bodensohn, R. Falsett, M. Haueis, and M. Pulvermüller. Autonomous sensor systems for car applications. *Advanced Microsystems for Automotive Applications 2004*, pages 225–232, 2004.

[38] A. Baggio. Wireless sensor networks in precision agriculture. In *ACM Workshop on Real-World Wireless Sensor Networks (REALWSN 2005), Stockholm, Sweden*, 2005.

[39] G. Werner-Allen, P. Swieskowski, and M. Welsh. Motelab: A wireless sensor network testbed. In *Proceedings of the 4th international symposium on Information processing in sensor networks*, page 68. IEEE Press, 2005.

[40] S.A. Roen. Solar powered portable calculator, April 12 1977. US Patent 4,017,725.

[41] V. Raghunathan, S. Ganeriwal, and M. Srivastava. Emerging techniques for long lived wireless sensor networks. *Communications Magazine, IEEE*, 44(4):108–114, 2006.

[42] S. Farhan, S. Devyani, and P. Chou. Everlast: Long-life, supercapacitor-operated wireless sensor node. In *the 6th ACM conference on Embedded network sensor systems,(Sensys' 09), San Diego, California*, 2009.

[43] C. Park and P.H. Chou. Power utility maximization for multiple-supply systems by a load-matching switch. In *Low Power Electronics and Design, 2004. ISLPED '04. Proceedings of the 2004 International Symposium on*, pages 168 –173, Aug 2004.

[44] D. Brunelli, L. Benini, C. Moser, and L. Thiele. An efficient solar energy harvester for wireless sensor nodes. In *Proceedings of the conference on Design, automation and test in Europe*, pages 104–109. ACM, 2008.

[45] D. Dondi, A. Bertacchini, D. Brunelli, L. Larcher, and L. Benini. Modeling and optimization of a solar energy harvester system for self-powered wireless sensor networks. *Industrial Electronics, IEEE Transactions on*, 55(7):2759 –2766, July 2008.

[46] F. I. Simjee and P. H. Chou. Efficient charging of supercapacitors for extended lifetime of wireless sensor nodes. *Power Electronics, IEEE Transactions on*, 23(3):1526–1536, 2008.

[47] A. Bertacchini, D. Dondi, L. Larcher, and P. Pavan. Performance analysis of solar energy harvesting circuits for autonomous sensors. In *Industrial Electronics, 2008. IECON 2008. 34th Annual Conference of IEEE*, pages 2655 –2660, Nov 2008.

[48] D. Dondi, A. Bertacchini, L. Larcher, P. Pavan, D. Brunelli, and L. Benini. A solar energy harvesting circuit for low power applications. In *Sustainable Energy Technologies, 2008. ICSET 2008. IEEE International Conference on*, pages 945 –949, Nov 2008.

[49] D. Brunelli and L. Benini. Designing and managing sub-milliwatt energy harvesting nodes: Opportunities and challenges. In *Wireless Communication, Vehicular Technology, Information Theory and Aerospace Electronic Systems Technology, 2009. Wireless VITAE 2009. 1st International Conference on*, pages 11 –15, May 2009.

[50] Y.K. Tan and S.K. Panda. Optimized wind energy harvesting system using resistance emulator and active rectifier for wireless sensor nodes. *Power Electronics, IEEE Transactions on*, 26(1):38 –50, Jan 2011.

[51] Y.K. Tan and S.K. Panda. Energy harvesting from hybrid indoor ambient light and thermal energy sources for enhanced performance of wireless sensor nodes. *Industrial Electronics, IEEE Transactions on*, 58(9):4424 –4435, Sep 2011.

[52] CGI. Chilled groupage international, cold store facility. In *website:www.cgil.ie*, 2009.

[53] R. Vullers, R. Schaijk, H.J. Visser, J. Penders, and C.V. Hoof. Energy harvesting for autonomous wireless sensor networks. *Solid-State Circuits Magazine, IEEE*, 2(2):29–38, 2010.

[54] A. Elefsiniotis, D. Samson, T. Becker, and U. Schmid. Investigation of the performance of thermoelectric energy harvesters under real flight conditions. *Journal of Electronic Materials*, 2(2):1–5, 2013.

[55] K. Kadirvel, Y. Ramadass, U. Lyles, J. Carpenter, V. Ivanov, V. McNeil, A. Chandrakasan, and B. Lum-Shue-Chan. A 330na energy-harvesting charger with battery management for solar and thermoelectric energy harvesting. In *Solid-State Circuits Conference Digest of Technical Papers (ISSCC), 2012 IEEE International*, pages 106–108. IEEE, 2012.

[56] P.H. Chen, K. Ishida, X. Zhang, Y. Okuma, Y. Ryu, M. Takamiya, and T. Sakurai. A 120-mv input, fully integrated dual-mode charge pump in 65-nm cmos for thermoelectric energy harvester. In *Design Automation Conference (ASP-DAC), 2012 17th Asia and South Pacific*, pages 469–470, 2012.

[57] Ultra-Low Voltage Operation Charge Pump website: www.sii ic.com/. Ic for step-up dc-dc converter: S-882z series.

[58] N. Degrenne, F. Buret, F. Morel, S. Adami, D. Labrousse, B. Allard, and A. Zaoui. Self-starting dc: Dc boost converter for low-power and low-voltage microbial electric generators. In *Energy Conversion Congress and Exposition (ECCE), 2011 IEEE*, pages 889–896. IEEE, 2011.

[59] LTC3108 Datasheet. Linear technology corp, dc dc converter for thermoelectric energy harvesting. *website: www.linear.com/product/LTC3108*, 2010.

[60] D. Andrea. *Battery management systems for large lithium-ion battery packs*. Artech House, 2010.

[61] J.M. Tarascon and M. Armand. Issues and challenges facing rechargeable lithium batteries. *Nature*, 414(6861):359–367, 2001.

[62] E. Mengeritsky, P. Dan, I. Weissman, A. Zaban, and D. Aurbach. Safety and performance of tadiran tlr-7103 rechargeable batteries. *Journal of The Electrochemical Society*, 143(7):2110–2116, 1996.

[63] Tadiran battery gmbh. In *Tadiran Rechargeable Lithium-Ion Battery For Wireless Sensor Networks TLI series battery, product news letter: www.sourcetech411.com/2013/07/*, 2009.

[64] A.G. Pandolfo and A.F. Hollenkamp. Carbon properties and their role in supercapacitors. *Journal of Power Sources*, 157(1):11–27, 2006.

[65] M. Winter and R.J. Brodd. What are batteries, fuel cells, and supercapacitors? *ChemInform*, 35(50):no–no, 2004.

[66] P. Sharma and T.S. Bhatti. A review on electrochemical double-layer capacitors. *Energy Conversion and Management*, 51(12):2901–2912, 2010.

[67] K. Sahay and B. Dwivedi. Design and analysis of supercapacitors energy storage system for energy stabilization of distribution network. *Electrical Power Quality and Utilisation Journal*, 15(1):49–56, 2009.

[68] O. Tetervenoks, I. Galkin, and J. Armas. Autonomous power supply system for light sensor of illumination measurement test bench. *Electrical, Control and Communication Engineering*, 1(1):30–35, 2012.

[69] P.B. Aitchison, A. Bilyk, H. Nguyen, J. Chi, and W. King. A charge storage device, 2011. EP Patent 2,340,546.

[70] J. Yan, J. Liu, Z. Fan, T. Wei, and L. Zhang. High-performance supercapacitor electrodes based on highly corrugated graphene sheets. *Carbon*, 50(6):2179–2188, 2012.

[71] C. Liu, Z. Yu, D. Neff, A. Zhamu, and B.Z. Jang. Graphene-based supercapacitor with an ultrahigh energy density. *Nano Letters*, 10(12):4863–4868, 2010.

[72] P. Birke, F. Salam, S. Döring, and W. Weppner. A first approach to a monolithic all solid state inorganic lithium battery. *Solid State Ionics*, 118(1):149–157, 1999.

[73] J.B. Bates, N.J. Dudney, B. Neudecker, A. Ueda, and C.D. Evans. Thin-film lithium and lithium-ion batteries. *Solid State Ionics*, 135(1):33–45, 2000.

[74] Infinite Power Solutions. Thinergy thin film battery product: Mec202. In *www.digikey.com/product-detail/en/MEC202-22P*, 2009.

[75] Cooper Bussmann. Powerstor super-capacitor overview. In *website:www.cooperbussmann.com/datasheets/1640984.pdf*, 2009.

[76] P.C. Chen, G. Shen, Y. Shi, H. Chen, and C. Zhou. Preparation and characterization of flexible asymmetric supercapacitors based on transition-metal-oxide nanowire/single-walled carbon nanotube hybrid thin-film electrodes. *Acs Nano*, 4(8):4403–4411, 2010.

[77] Maxwell. Low cost high energy density pc series ultracapacitors. In *PC270 series www.maxwell.com/products/ultracapacitors/docs/datasheet-pc10-1003996.pdf*, 2009.

[78] Cap-XX. Pc series ultracapacitors. In *High Temperature Surface-mount Supercapacitor www.tecategroup.com/ultracapacitors-supercapacitors/*, 2010.

[79] Energizer. Ca5l li-ion battery. In *1120mAh cell phone battery www.farnell.com/energizer/ca5l*, 2010.

[80] D. Park and J.W. Park. Wireless sensor network-based greenhouse environment monitoring and automatic control system for dew condensation prevention. *Sensors*, 11(4):3640–3651, 2011.

[81] S. Bader and B. Oelmann. Enabling battery-less wireless sensor operation using solar energy harvesting at locations with limited solar radiation. In *Sensor Technologies and Applications (SENSORCOMM), 2010 Fourth International Conference on*, pages 602–608. IEEE, 2010.

[82] S. Mahlknecht and M. Roetzer. Energy supply considerations for self-sustaining wireless sensor networks. In *Wireless Sensor Networks, 2005. Proceeedings of the Second European Workshop on*, pages 397–399. IEEE, 2005.

[83] Texas Instruments. Tps61220 buck-boost converter for low voltage energy harvesting applications tps61220/1/2.

[84] Onsemi. Ncp1400, 100 ma, fixed frequency pwm step up micropower switching regulator.

[85] D. Zhu, S.P. Beeby, M.J. Tudor, and N.R. Harris. A credit card sized self powered smart sensor node. *Sensors and Actuators A: Physical*, 169(2):317–325, 2011.

[86] T.J. Kazmierski. *Energy Harvesting Systems: Principles Modeling and Applications*. Springer, 2011.

[87] A. Janek, C. Trummer, C. Steger, R. Weiss, J. Preishuber-Pfluegl, and M. Pistauer. Simulation based verification of energy storage architectures for higher class tags supported by energy harvesting devices. *Microprocessors and Microsystems*, 32(5):330–339, 2008.

[88] B.W. Ricketts and C. Ton-That. Self-discharge of carbon-based supercapacitors with organic electrolytes. *Journal of Power Sources*, 89(1):64–69, 2000.

[89] M.J. Guan and W.H. Liao. Characteristics of energy storage devices in piezoelectric energy harvesting systems. *Journal of Intelligent Material Systems and Structures*, 19(6):671–680, 2008.

[90] A. Du Pasquier, I. Plitz, S. Menocal, and G. Amatucci. A comparative study of li-ion battery, supercapacitor and nonaqueous asymmetric hybrid devices for automotive applications. *Journal of Power Sources*, 115(1):171–178, 2003.

[91] W.G. Pell, B.E. Conway, W.A. Adams, and J. de Oliveira. Electrochemical efficiency in multiple discharge/recharge cycling of supercapacitors in hybrid ev applications. *Journal of Power Sources*, 80(1):134–141, 1999.

[92] R. Kötz, P.W. Ruch, and D. Cericola. Aging and failure mode of electrochemical double layer capacitors during accelerated constant load tests. *Journal of Power Sources*, 195(3):923–928, 2010.

[93] A.M. Sommariva. Solving the two capacitor paradox through a new asymptotic approach. *IEE Proceedings-Circuits, Devices and Systems*, 150(3):227–231, 2003.

[94] C.K. Tse, S.C. Wong, and M. Chow. On lossless switched-capacitor power converters. *Power Electronics, IEEE Transactions on*, 10(3):286–291, 1995.

[95] E. Popovici, D. Boyle, S. O'Connell, S. Faul, P. Angove, J. Buckley, B. O'Flynn, J. Barton, and C. O'Mathuna. The s-mote: A versatile heterogeneous multi-radio platform for wireless sensor networks applications. In *Circuit Theory and Design (ECCTD), 2011 20th European Conference on*, pages 421–424. IEEE, 2011.

[96] S. S. M. Wolf and J. H. R. Enslin. Economical, pv maximum power point tracking regulator with simplistic controller. In *Power Electronics Specialists Conference, 1993. PESC '93 Record., 24th Annual IEEE*, pages 581–587, 1993.

[97] Seiko Instruments. S89530a/89531a series comparator website: datasheet.siiic.com/en/cmoscomparator/, June 2010.

[98] Texas Instruments. Ref3312 30ppm/c drift, 3.9ua, sot23-3, sc70-3 voltage reference website: www.ti.com/product/ref3320, 2007.

[99] Intersil. Isl43l120, ultra low on-resistance, single supply, dual spst analog switches, 2010.

[100] N.J. Guilar, T.J. Kleeburg, A. Chen, D.R. Yankelevich, and R. Amirtharajah. Integrated solar energy harvesting and storage. *Very Large Scale Integration (VLSI) Systems, IEEE Transactions on*, 17(5):627–637, 2009.

[101] J.R. Miller and P. Simon. Electrochemical capacitors for energy management. *Science Magazine*, 321(5889):651–652, 2008.

[102] G. Park, T. Rosing, M.D. Todd, C.R. Farrar, and W. Hodgkiss. Energy harvesting for structural health monitoring sensor networks. *Journal of Infrastructure Systems*, 14(1):64–79, 2008.

[103] T. Huesgen, P. Woias, and N. Kockmann. Design and fabrication of mems thermoelectric generators with high temperature efficiency. *Sensors and Actuators A: Physical*, 145:423–429, 2008.

[104] A. Beskok and G.E. Karniadakis. Simulation of heat and momentum transfer in complex microgeometries. *Journal of Thermophysics and Heat transfer*, 8(4), 2012.

[105] H. Bottner, J. Nurnus, A. Schubert, and F. Volkert. New high density micro structured thermogenerators for stand alone sensor systems. In *Thermoelectrics, 2007. ICT 2007. 26th International Conference on*, pages 306–309. IEEE, 2007.

[106] J. Nurnus. Thermoelectric thin film power generators-self-sustaining power supply for smart systems. In *Proc. of SPIE Vol*, volume 7362, pages 736205–1, 2009.

[107] C.J. Glassbrenner and G.A. Slack. Thermal conductivity of silicon and germanium from 3 k to the melting point. *Phys. Rev*, 134(4A):A1058–A1069, 1964.

[108] L. Mateu, M. Pollak, and P. Spies. Step-up converters for human body energy harvesting thermogenerators. *Technical Digest PowerMEMS*, 2007.

[109] H.J. Goldsmid. The electrical conductivity and thermoelectric power of bismuth telluride. *Proceedings of the Physical Society*, 71(4):633, 2002.

[110] X. Jiang, J. Polastre, and D. Culler. Perpetual environmentally powered sensor networks. In *Information Processing in Sensor Networks, 2005. IPSN 2005. Fourth International Symposium on*, pages 463 – 468, Apr 2005.

[111] M. Wolf and H. Rauschenbach. Series resistance effects on solar cell measurements. *Advanced Energy Conversion*, 3(2):455–479, 1963.

[112] G.E. Bunea, K.E. Wilson, Y. Meydbray, M.P. Campbell, and D.M. De Ceuster. Low light performance of mono-crystalline silicon solar cells. In *Photovoltaic Energy Conversion, Conference Record of the 2006 IEEE 4th World Conference on*, volume 2, pages 1312 –1314, May 2006.

[113] A. Kaminski, J.J. Marchand, A. Fave, and A. Laugier. New method of parameters extraction from dark i-v curve. In *Photovoltaic Specialists Conference, 1997., Conference Record of the Twenty-Sixth IEEE*, pages 203 –206, Sep 1997.

[114] T.C. Lee, S. Fung, C.D. Beling, and H.L. Au. A systematic approach to the measurement of ideality factor, series resistance, and barrier height for schottky diodes. *Journal of Applied Physics*, 72(10):4739–4742, 1992.

[115] A. Chini and F. Soci. Boost-converter-based solar harvester for low power applications. *Electronics Letters*, 46(4):296–298, 2010.

[116] D. Brunelli, C. Moser, L. Thiele, and L. Benini. Design of a solar-harvesting circuit for batteryless embedded systems. *Circuits and Systems I: Regular Papers, IEEE Transactions on*, 56(11):2519–2528, 2009.

[117] W.S. Wang, T. O'Donnell, N. Wang, M. Hayes, B. O'Flynn, and C. O'Mathuna. Design considerations of sub-mw indoor light energy harvesting for wireless sensor systems. *ACM Journal on Emerging Technologies in Computing Systems (JETC)*, 6(2):6, 2010.

[118] W. Wang, N. Wang, M. Hayes, B. OFlynn, and C. OMathuna. Power management for sub-mw energy harvester with adaptive hybrid energy storage. *Journal of Intelligent Material Systems and Structures*, 2012.